

Probing the nature of black holes with gravitational waves

Thesis by
Matthew Giesler

In Partial Fulfillment of the Requirements for the
Degree of
Doctor of Philosophy

The logo for the California Institute of Technology (Caltech), featuring the word "Caltech" in a bold, orange, sans-serif font.

CALIFORNIA INSTITUTE OF TECHNOLOGY
Pasadena, California

2020
Defended February 25, 2020

© 2020

Matthew Giesler

ORCID: 0000-0003-2300-893X

All rights reserved

ACKNOWLEDGEMENTS

I want to thank my advisor, Saul Teukolsky, for his mentorship, his guidance, his broad wisdom, and especially for his patience. I also have a great deal of thanks to give to Mark Scheel. Thank you for taking the time to answer the *many* questions I have come to you with over the years and thank you for all of the the much-needed tangential discussions. I would also like to thank my additional thesis committee members, Yanbei Chen and Rana Adhikari.

I am also greatly indebted to Geoffrey Lovelace. Thank you, Geoffrey, for your unwavering support and for being an invaluable source of advice. I am forever grateful that we crossed paths.

I also want to thank my fellow TAPIR grads: Vijay Varma, Jon Blackman, Belinda Pang, Masha Okounkova, Ron Tso, Kevin Barkett, Sherwood Richers and Jonas Lippuner. Thanks for the lunches and enlightenment. To my SXS office mates, thank you for all of the discussions – for those about physics, but mostly for the less serious digressions.

I must also thank some additional collaborators who contributed to the work in this thesis. Thank you Drew Clausen, Daniel Hemberger, Will Farr, and Maximiliano Isi.

Many thanks to JoAnn Boyd. Thank you for all that you have done over the years, but especially for our chats.

A special thank you goes to my family. Thank you Mom and Dad for your endless love. Lastly, without my brother, this thesis would not have been possible – my deepest thanks.

ABSTRACT

In this thesis, I present a number of studies intended to improve our understanding of black holes using gravitational waves. Although black holes are relatively well understood from a theory perspective, many questions remain about the nature of the black holes in our Universe. According to general relativity, astrophysical black holes are fully described by just their mass and spin. Yet, relying on electromagnetic-based observatories alone, we still know very little about the distribution of black hole masses or spins. Moreover, as merging black holes are invisible to these electromagnetic observatories, we cannot rely on them to provide us with information about the binary black hole merger rate or binary black hole formation channels. However, by observing gravitational wave signals from these inherently dark binaries, we will soon have some answers to these questions. Indeed, the Laser Interferometer Gravitational-Wave Observatory (LIGO) has already revealed a great deal of new information about binary black holes; giving us an early glimpse into their mass and spin distributions and placing the first constraints on the binary black hole merger rate. This thesis contributes to the goal of probing the nature of black holes with gravitational waves.

Binary black holes can form as an isolated binary in the galactic field or through dynamical encounters in high-density environments. Dynamical formation can significantly alter the binary parameters, which then become imprinted on the gravitational waveform. By simulating varying black hole populations in high-density globular clusters, we identify a population of highly eccentric binary black hole mergers that are characteristic of dynamical formation. Although these systems would circularize by the time they are visible in LIGO's frequency band, the future Laser Interferometer Space Antenna (LISA) is capable of distinguishing this population of eccentric mergers from the circular mergers expected of isolated field-formed binaries. As these dynamically formed binaries depend on the size of the underlying black hole population in globular clusters, we can utilize the dynamically formed merger rate to infer globular cluster black hole populations – allowing us to reveal information about binary black hole birth environments.

In order to properly estimate the parameters of binary black holes from detected gravitational wave signals, such as their masses and spins, high-accuracy waveforms are needed. The highest accuracy waveforms are those produced by numerical relativity simulations, which solve the full Einstein equations. Using the Spectral

Einstein Code (SpEC), we expand the reach of numerical relativity to simulate binary black holes with nearly extremal spins, i.e., black holes with spins near the maximal value $\chi = 1$. These waveforms are used to calibrate existing waveform approximants used in LIGO data analyses. This ensures that the systematic errors in these approximants are small enough that if highly-spinning systems are observed, the spins are recovered without bias. Although rapidly spinning binaries have remained elusive thus far, these waveforms ensure that the highest-spin systems can be detected in the quest to uncover the spin distribution of black holes.

The end state of a binary black hole merger is a newly born, single black hole that rings down like a struck bell, sending its last few ripples of gravitational waves out into the spacetime. Embedded in this ‘ringdown’ signal are a multitude of specific frequencies. Einstein’s theory of general relativity precisely predicts the ringdown frequencies of a black hole with a given mass and spin. The statement that a black hole is entirely described by just these two parameters is known as the no-hair theorem. For black holes that obey the laws of general relativity (and consequently, the no-hair theorem), these frequencies serve as a fingerprint for the black hole. However, if the objects we observe are not Einstein’s black holes, but instead something more exotic, the frequencies will not have this property and this would be a spectacular surprise. A minimum of two tones are required for this test, each with an associated frequency and damping time that depend only on the mass and spin. The conventional no-hair test relies on the so-called ‘fundamental’ tones of a black hole. A test relying on the fundamental modes is not expected to be feasible for another ~ 10 -15 years, after detector sensitivity has improved significantly. However, by analyzing the ringdown of high-accuracy numerical relativity waveforms, we show that modes beyond the fundamental, known as ‘overtones’, are detectable in current detectors. The overtones are short-lived, but this is countered by the fact that they can initially be much stronger than the fundamental mode. By measuring two tones in the ringdown of GW150914 we perform a first test of the no-hair theorem. While the current constraints are rather loose, this first test serves as a proof of principle. This is just one example of the powerful tests that can be employed with overtones using present day detectors and the even more precise tests that can be accomplished with LISA in the future.

PUBLISHED CONTENT AND CONTRIBUTIONS

- [1] Matthew Giesler, Maximiliano Isi, Mark Scheel, and Saul Teukolsky. “Black hole ringdown: the importance of overtones”. In: *Phys. Rev.* X9.4 (2019), p. 041060. DOI: [10.1103/PhysRevX.9.041060](https://doi.org/10.1103/PhysRevX.9.041060). arXiv: [1903.08284](https://arxiv.org/abs/1903.08284) [gr-qc].
M.G. conceived the project, carried out the analysis, and wrote the manuscript.
- [2] Maximiliano Isi, Matthew Giesler, Will M. Farr, Mark A. Scheel, and Saul A. Teukolsky. “Testing the no-hair theorem with GW150914”. In: *Phys. Rev. Lett.* 123.11 (2019), p. 111102. DOI: [10.1103/PhysRevLett.123.111102](https://doi.org/10.1103/PhysRevLett.123.111102). arXiv: [1905.00869](https://arxiv.org/abs/1905.00869) [gr-qc].
M.G. conceived the project, participated in the development of the analysis code, and contributed to the manuscript.
- [3] Swetha Bhagwat, Maria Okounkova, Stefan W. Ballmer, Duncan A. Brown, Matthew Giesler, Mark A. Scheel, and Saul A. Teukolsky. “On choosing the start time of binary black hole ringdowns”. In: *Phys. Rev.* D97.10 (2018), p. 104065. DOI: [10.1103/PhysRevD.97.104065](https://doi.org/10.1103/PhysRevD.97.104065). arXiv: [1711.00926](https://arxiv.org/abs/1711.00926) [gr-qc].
M.G. provided the single black hole metric perturbations used in the analysis and provided feedback on the manuscript.
- [4] Matthew Giesler, Drew Clausen, and Christian D. Ott. “Low-mass X-ray binaries from black-hole retaining globular clusters”. In: *Mon. Not. Roy. Astron. Soc.* 477.2 (2018), pp. 1853–1879. DOI: [10.1093/mnras/sty659](https://doi.org/10.1093/mnras/sty659). arXiv: [1708.05915](https://arxiv.org/abs/1708.05915) [astro-ph.HE].
M.G. conceived the project, carried out the analysis, and wrote the manuscript.
- [5] Geoffrey Lovelace, Mark A. Scheel, Robert Owen, Matthew Giesler, Reza Katebi, Bela Szilagyi, Tony Chu, Nicholas Demos, Daniel A. Hemberger, and Lawrence E. Kidder. “Nearly extremal apparent horizons in simulations of merging black holes”. In: *Class. Quant. Grav.* 32.6 (2015), p. 065007. DOI: [10.1088/0264-9381/32/6/065007](https://doi.org/10.1088/0264-9381/32/6/065007). arXiv: [1411.7297](https://arxiv.org/abs/1411.7297) [gr-qc].
M.G. provided new waveforms and feedback on the manuscript.
- [6] Mark A. Scheel, Matthew Giesler, Daniel A. Hemberger, Geoffrey Lovelace, Kevin Kuper, Michael Boyle, B. Szilagyi, and Lawrence E. Kidder. “Improved methods for simulating nearly extremal binary black holes”. In: *Class. Quant. Grav.* 32.10 (2015), p. 105009. DOI: [10.1088/0264-9381/32/10/105009](https://doi.org/10.1088/0264-9381/32/10/105009). arXiv: [1412.1803](https://arxiv.org/abs/1412.1803) [gr-qc].
M.G. developed improved methods, carried out some of the simulations, and contributed to the writing of the manuscript.

TABLE OF CONTENTS

Acknowledgements	iii
Abstract	iv
Published Content and Contributions	vi
Table of Contents	vii
List of Illustrations	ix
List of Tables	xxiv
Chapter I: Introduction	1
1.1 Our new view of the universe	1
1.2 General relativity	3
1.3 Gravitational waves	4
1.4 Binary black holes	7
1.5 Numerical relativity	9
1.6 Black holes in globular clusters	11
X-ray binaries	13
Eccentric mergers	14
1.7 Binary black holes with nearly extremal spins	15
1.8 Black hole ringdown	17
1.9 Testing Einstein’s theory	19
Chapter II: Low-mass X-ray binaries from black-hole retaining globular clusters	23
2.1 Abstract	23
2.2 Introduction	23
2.3 Methods	26
Model	27
Initial conditions	31
Evolution of the ‘test binary’	38
2.4 Simulations	48
Structural parameters	49
Galactic evolution	51
2.5 Results	54
Ejected black-hole binaries	54
Black-hole low-mass X-ray binaries	62
Merger events	74
Comparison with observations and previous results	81
2.6 Discussion and conclusions	85
Chapter III: Improved methods for simulating nearly extremal binary black holes	98
3.1 Abstract	98
3.2 Introduction	98
3.3 Techniques	101
Grid improvements	102

Control system improvements	103
3.4 Simulations	114
Equal-mass, aligned spins $\chi = 0.99$	115
Equal-mass, aligned spins $\chi = 0.994$	118
Unequal-mass, precessing	120
3.5 Results	122
Spin evolution during inspiral	122
Orbital hangup	126
Comparison with analytic approximants	128
3.6 Conclusion	134
Chapter IV: Black hole ringdown: the importance of overtones	145
4.1 Abstract	145
4.2 Introduction	145
4.3 Previous studies	147
4.4 Model	148
4.5 Results	149
QNM overtone fits	149
Characterizing the overtones	155
Observing overtones with GW detectors	161
4.6 Discussion and conclusions	165
4.7 Acknowledgments	167
Chapter V: Testing the no-hair theorem with GW150914	174
5.1 Abstract	174
5.2 Introduction	174
5.3 Method	176
5.4 Results	180
5.5 Discussion and prospects	181
5.6 Acknowledgments	183
5.7 Appendix: Technical Details	184
Time-domain likelihood	184
Other details	186

LIST OF ILLUSTRATIONS

<i>Number</i>	<i>Page</i>
1.1 A high-accuracy visualization of the moments before the merger of two black holes for a nearby observer. The black holes' extreme gravity is apparent in the distortion of of the background stars, as the path of the light emanating from the stars is bent by the black holes before reaching the observer, producing complex geometric features. This visualization is based on a simulation of the very first LIGO detection, GW150914. Credit: SXS	1
1.2 A view along one of the 4 km arms of the L-shaped LIGO detector in Livingston, Louisiana. A second detector resides across the country in Hanford, Washington. The two detectors operate together to identify coincident gravitational waves and to reject random noise fluctuations that can mimic astrophysical sources, as the noise should be uncorrelated between the two detectors. Credit: Caltech/MIT/LIGO Lab.	2
1.3 A visualization of warped spacetime for the Earth-Sun system. The green mesh represents the underlying spacetime fabric, which has noticeable curvature due to the massive objects. It is this curvature which tells light and matter how to move through space and time. Note that while spacetime is a four-dimensional construct, for illustrative purposes, it is represent here as a two-dimensional sheet. Credit: T. Pyle, Caltech/MIT/LIGO Lab	4
1.4 A simple illustration of how the Laser Interferometer Gravitational-Wave Observatory (LIGO) functions. A high-power laser passes through a beam splitter, sending light down each of the 4 km arms. Large mirrors at the end of each arm reflect the light back to the beam splitter, which redirects some light from each arm onto a photodetector. The photodetector is sensitive to how the light from each arm interacts with each other and allows for the detection of small changes in the arm lengths due to passing gravitational waves. Credit: T. Pyle, Caltech/MIT/LIGO Lab	5

- 1.5 An illustration of a quasi-circular binary black hole system and the seven fundamental intrinsic parameters that govern the evolution of the binary. Each angular momentum spin vector constitutes three parameters, with the seventh being the mass ratio, $q = M_1/M_2$, as the total mass, $M = M_1 + M_2$, scales out of the problem. 8
- 1.6 The top panel shows the underlying gravitational wave data in the Hanford detector for GW150914 and a waveform produced using numerical relativity that is consistent with the data. The illustration shows a rough separation of the waveform into the three key regions of the binary life: the inspiral, the merger, and the ringdown. The bottom panel shows the corresponding separation of the two black holes and the relative velocity of the two black holes as functions of time. Credit: LIGO [11] 9
- 1.7 An illustration of spacetime foliation used in numerical relativity simulations. The bottom hypersurface represents the space-like initial data at a fixed time. As time progresses, the evolution equations generate a sequence of non-intersecting space-like surfaces. A stack of these hypersurfaces represent the full spacetime, each slice being a three-dimensional surface, but with one suppressed spatial dimension for ease of illustration. Credit: H. Dimmelmeier 10
- 1.8 M80, also known as NGC 6093, is one of the densest known globular clusters in the Milky Way galaxy. The massive collection of stars is bound by their mutual gravity, leading to a compact, nearly-spherical, object. Clusters such as this are home to highly dynamical interactions because of the exceptionally high density of objects compared to the relatively sparse galactic field. Credit: NASA 12
- 1.9 The fraction of maximal rotation energy as a function of χ , where $\chi = 1$ corresponds to the maximum rotational energy. This illustrates how steeply the maximum rotational energy grows as the black hole spin increases. The inset zooms in to show a number of data points at $\chi \geq 0.9$, with $\chi = 0.9$ corresponding to $\sim 52\%$ of the maximum rotational energy of a black hole. The next highest point is the Bowen-York limit, $\chi = 0.93$, followed by $\chi = \{0.99, 0.994, 0.998\}$. These values of χ yield values for the fraction of maximum rotational energy of $\{59.1\%, 83.5\%, 87.1\%, 92.5\%\}$, respectively. 16

- 2.1 The He core mass (marked by circles) as a function of zero-age main-sequence mass from the MESA [52] runs, along with the fit (blue, dashed line) given by Equation 2.14. For the $\sim 70\%$ of BHs formed in binaries, we approximate the remnant BH mass with the He core mass of the progenitor. The remnant mass for the remaining $\sim 30\%$ of BHs is approximated by $0.9M_{\text{ZAMS}}$, which accounts for the hydrogen mass lost to stellar winds at low metallicity. 33
- 2.2 Radial number density profiles for the BH subgroup (solid lines) and the non-BH objects (dashed lines) in NGC 6656 for the three considered values of N_{BH} . The vertical line (red, dashed), at $r_c = 0.73$ pc, marks the core radius for this cluster. The non-BH objects are largely unaffected by the different numbers of BHs added to the cluster and the necessary modification to the velocity dispersion. For $N_{\text{BH}} = 20$, the BHs are concentrated in the core region, whereas to accommodate $N_{\text{BH}} \geq 200$, the modified velocity dispersion spreads the BHs throughout the cluster with a profile similar to that of the non-BH objects. 37
- 2.3 The distribution of non core-collapsed Milky Way GCs in a face-on view of the fundamental plane. The colour of each unmodelled GC (marked by circles) indicates the corresponding modelled GC (marked by stars) that serves as its proxy for determining the properties of the ejected binaries. The plane is defined by $\epsilon_2 = 2.05 \log_{10} E_b^* + \log_{10} L$ and $\epsilon_3 = c$, with the dashed line corresponding to the fit $\epsilon_3 = -12.5 + 0.13\epsilon_2$. Here c is the concentration, L is the total luminosity, and E_b^* is an additional parameter related to L (see section 2.4 for additional details). 50
- 2.4 Expected number of binary ejections $\langle N_{\text{ej}} \rangle$ as a function of the number of retained BHs N_{BH} , concentration c , and total cluster mass M_c . The number of binaries ejected over the life of the cluster is well described by the two characteristic variables of the fundamental plane, c and M_c , along with the number of BHs retained by the cluster. 56

- 2.5 The distributions of ejection velocities v_{ej} as a function of the total cluster mass M_c for the ejected binaries. Each vertical bar represents the distribution of v_{ej} for the corresponding mass M_c and is normalized such that the integral over $\log_{10}v_{ej}$ in each mass bin yields unity. The binary velocity fluctuates due to random encounters with other stars in the cluster until the binary acquires a high enough recoil velocity to exceed the minimum ejection velocity, which is determined by the cluster mass. The increase in the necessary velocity for escape is apparent in the increasing mean value of each v_{ej} distribution. 57
- 2.6 The distributions of the semi-major axes at ejection a as a function of the total cluster mass M_c for the ejected binaries. Each vertical bar represents the distribution of a for the corresponding mass M_c and is normalized such that the integral over $\log_{10}a$ in each mass bin yields unity. High mass clusters require a high velocity for escape, which a binary must acquire through three-body interactions in order to be ejected. The energy needed to escape is more easily gained once the orbital separation has decreased sufficiently (see Equation 2.41). As a consequence, the mean value of a at ejection shifts to smaller separation with increasing cluster mass M_c 59
- 2.7 The probability distribution for the ejected BH-NC binary semi-major axes from NGC 5694, a representative case, with a population of 20, 200, and 1000 BHs. An increase in the number of BHs requires spreading the BHs outside of the core, where they are more likely to form binaries with NC objects. In the outskirts, the energy necessary to escape is much smaller, allowing the binary to escape before it has had sufficient time to harden. These binaries escape with comparatively low magnitude binding energy and wide orbital separations. 60
- 2.8 The distributions of time of ejection t_{ej} as a function of the luminous central density ρ_L for the ejected binaries. Each vertical bar represents the distribution of t_{ej} for the corresponding core luminosity density ρ_L and is normalized such that the integral over $\log_{10}t_{ej}$ in each density bin yields unity. In higher density clusters, where encounters occur more frequently, many binaries are ejected after only a few Gyr, while in the lower density clusters most ejections occur near the end of the 10 Gyr evolution. 61

- 2.9 The distribution of the number of BH-LMXBs, $N_{\text{BH-LMXB}}$, produced from 10^4 realizations for the $N_{\text{BH}} = 200$ case and 5×10^3 realizations for the $N_{\text{BH}} = 1000$ case. The $N_{\text{BH}} = 20$ case produces a population of zero BH-LMXBs in 10^4 realizations. The expected values for the two producing cases are 25^{+10}_{-6} for $N_{\text{BH}} = 200$ and 156^{+26}_{-24} for $N_{\text{BH}} = 1000$, with the stated uncertainties bounding the 95% confidence interval. 62
- 2.10 The spatial probability distribution of the simulated population of BH-LMXBs from GCs with $N_{\text{BH}} = 1000$. The populations of Milky Way GCs (marked by black circles) and known BH-LMXBs (marked by orange stars) are included for reference. The map is a Mollweide projection of the (l, b) galactic coordinate system. The galactic centre is located near 0° latitude and 0° longitude, where the high density of objects explains the clustering of BH-LMXBs and GCs. 63
- 2.11 The spatial probability distribution of the simulated population of BH-LMXBs from GCs with $N_{\text{BH}} = 1000$ in the $R - z$ plane. The coordinate z specifies the distance perpendicular to the galactic plane and R is the in-plane distance from the galactic centre at the origin. The populations of Milky Way GCs (marked by black circles) and known BH-LMXBs (marked by orange stars) are included for reference. While many of the BH-LMXBs from GCs populate the galactic disc, the distribution extends well out of the galactic plane into the high- $|z|$ region. 66
- 2.12 The normalized cumulative distribution function of the absolute distance perpendicular to the galactic plane $|z|$. The included distributions are the BH-LMXBs produced in our GC simulations for the cases of $N_{\text{BH}} = 200$, $N_{\text{BH}} = 1000$, and the observed population. Note that in the case that GCs have minimal BH retention ($N_{\text{BH}} = 20$), no mass-transferring systems are produced. 67
- 2.13 The probability distributions of BH masses in BH-LMXBs for the observed population [82] and for the BH-LMXBs produced in our GC simulations for the cases of $N_{\text{BH}} = 200, 1000$. Note that in the case that GCs have minimal BH retention ($N_{\text{BH}} = 20$), no mass-transferring systems are produced. The discontinuous jumps in the distribution correspond to the mass bin minimum and maximum, with a power law distribution in-between determined by the evolved mass function. The lowest BH mass bin was truncated at $7M_\odot$ 68

- 2.14 The probability distributions of the companion masses in BH-LMXBs for the cases $N_{\text{BH}} = 1000$ and $N_{\text{BH}} = 200$. The observed population includes 12 of the 18 confirmed BH-LMXBs in BlackCAT [14] that have the necessary observational quantities (see section 2.5 for a description of the observed population) and are included for reference; the circles indicate the mean value, the line represents the uncertainty in the observations, and the inclusion of an arrow indicates that the uncertainty is only bounded on one side. The remaining 6 confirmed BH-LMXBs have companion masses above the range considered here, where the axis has been truncated to focus on the range of masses less than the MS turnoff-mass $m_{\text{to}} = 0.85 M_{\odot}$. The peaks in the simulated distributions are due to the sampling of companion masses from the evolved mass function (EMF) within each mass bin. 69
- 2.15 The probability distribution of orbital periods in the simulated BH-LMXBs from GCs for the two stellar companion sub-populations: WD and MS. The periods for the observed population of BH-LMXBs that are less than 13 h are included for reference and are identified by orange tick marks (18 of the 28 candidate BH-LMXBs from BlackCAT). To preserve the relative size of the MS and WD companion populations, each distribution is independently normalized and then multiplied by the factors $N_{\text{BH-MS}}/N$ and $N_{\text{BH-WD}}/N$, respectively, with $N = N_{\text{BH-MS}} + N_{\text{BH-WD}}$. This normalization is applied to each N_{BH} case independently. 70
- 2.16 Temperature-luminosity diagram for the BH-LMXB companion mass in the simulated population of BH-LMXBs from GCs with $N_{\text{BH}} = 1000$. The low-luminosity WD companions are excluded from the figure, leaving only the mass-transferring MS companions. Since the MS companions from GCs are unevolved stars, the companion temperature-luminosity diagram is essentially the portion of the Hertzsprung-Russell MS branch with $m_2 < m_{\text{to}}$ 71

- 2.17 The probability distributions for the space velocity v of the simulated BH-LMXB population for the two BHs retention values $N_{\text{BH}} = 1000$ and $N_{\text{BH}} = 200$. The BH-LMXB space velocity is $v = v_{\text{ej}} + v_{\text{GC}}$, where v_{ej} is the ejection velocity and v_{GC} is the velocity of the host GC. Since v_{ej} is approximately the GC escape velocity, the magnitude v is dominated by the relatively large contribution from v_{GC} . As such, the velocity distribution of BH-LMXBs is consistent with the velocity distribution of GCs, which is reflected in the high mean velocities. 73
- 2.18 The probability distributions of eccentricity for two populations of BH-BH binaries in GCs: BH-BH binaries which form and merge in cluster (BH-BH_m, black lines) and the BH-BH binaries which form and are ejected from the cluster (BH-BH_{ej}, blue lines). For each population, we show the eccentricity distribution at the time the binary forms, $e(t_0)$ (solid lines), and the distribution of eccentricities at the binary's final state (dashed lines). The final state of the in-cluster mergers is at a time t_m , the time at which the computed merger time is less than the cluster timestep. The final state for the ejected binaries is the time of ejection t_{ej} . A thermal eccentricity distribution, with probability density $f(e) = 2e$, is included for reference. 78
- 2.19 The eccentricity probability distributions for two populations of BH-BH mergers from GCs for the two detectors aLIGO and LISA. The two populations correspond to the BH-BH mergers occurring in-cluster (solid lines) and those that merge outside of the cluster, post-ejection (dashed lines). The black lines correspond to the eccentricity of each population when it reaches a corresponding gravitational wave frequency of $f_{\text{GW}} = 10$ Hz, the lower bound frequency of the aLIGO band at design sensitivity. The blue lines represent the eccentricity distribution at $f_{\text{GW}} = 1$ mHz, the proposed lower frequency bound for LISA. 79
- 3.1 The control error $Q(t)$ associated with one particular control system for two different $S_{0.994}^{++}$ simulations which differ only in the treatment of Q_t^{Max} for that control system. The black dashed curve shows the case in which Q_t^{Max} is a constant, given by Eq. (3.16), and the red solid curve shows the case in which Q_t^{Max} is chosen to be $0.05\Delta r_{\text{min}}$, with Δr_{min} given by Eq. (3.18). The former simulation crashes at $t \sim 50M$. 109

- 3.2 Flowchart illustrating how the control system for λ_{00} switches between horizon tracking (Q given by Eq. (3.7)) and characteristic speed control (Q given by Eq. (3.11)), and how the control system changes values of τ_d and v_T . The yellow diamonds labeled “ v in danger” and “ Δr_{\min} in danger” are illustrated in separate flowcharts in Fig. 3.3. Red final states indicate horizon tracking, purple final states indicate characteristic speed control, and the green final state indicates that no change is made. The algorithm is described in detail in § 3.3. 110
- 3.3 Flowcharts illustrating how the characteristic speed v (left) and the minimum distance between the horizon and the excision boundary Δr_{\min} (right) are deemed in danger of becoming negative. Each of these flowcharts is represented as a yellow diamond in Fig. 3.2. 111
- 3.4 Characteristic speed v and comoving characteristic speed v_c for two different $S_{0.994}^{++}$ simulations that differ only in the algorithm for treating the situation in which Δr_{\min} is deemed in danger while characteristic speed control is in effect and $v_c < 0$. The dashed red curve shows v for a simulation in which horizon tracking becomes active in this situation; the code crashes early, at only $t \sim 0.4M$. The solid red curve shows v for a simulation in which for this situation characteristic speed control remains in effect, but the target characteristic speed is reduced as described in the text. The quantity v_c is the same for both simulations. 113
- 3.5 The trajectories of the centers of the individual apparent horizons for the highest resolution of $S_{0.99}^{++}$ 115
- 3.6 Convergence test for $S_{0.99}^{++}$. Shown are gravitational-wave phase differences between Ψ_4 computed using different values of the numerical resolution parameter N . Several differences are shown, and labeled by the values of N that are compared, e.g. “3-2” means $N = 3$ versus $N = 2$. Waveforms are extracted at a finite radius $r = 465M$, and no alignment of waveforms was performed. 116
- 3.7 Spin magnitude as a function of time for $S_{0.99}^{++}$. At early times, the spin of one of the apparent horizons is shown at resolutions $N = 2$ (black solid), $N = 3$ (red dotted) and $N = 4$ (blue dashed). A closeup of early times is shown in the upper inset. At late times, the spin of the merged apparent horizon is shown as a function of time for the same resolutions, and a closeup of late times is shown in the lower inset. 117

3.8	Convergence test for $S_{0.994}^{++}$. Labels are the same as for Fig. 3.6. For $N \neq 5$, the simulations were started at $t_{\text{branch}} = 1414M$, using the $N = 5$ solution as initial data.	119
3.9	Convergence test for $S_{0.20}^{0.99}$. Labels are the same as for Figure 3.6. For $N \neq 4$, the simulations were started at $t_{\text{branch}} = 1362M$, using the $N = 4$ solution as initial data.	120
3.10	Coordinate trajectories (green and purple lines) of the black holes and coordinate shapes of the individual and common apparent horizons (surfaces) at the moment of merger, for $S_{0.20}^{0.99}$. The horizons are colored according to their vorticity [79].	121
3.11	Precession of the spins and orbital frequency for the highest-resolution simulation $N = 4$ of $S_{0.20}^{0.99}$. The unit vector spins, $\hat{\chi}_A$ and $\hat{\chi}_B$, and orbital frequency $\hat{\omega}_{\text{orb}}$ trace the precession on the unit sphere. The precession curves for $N = 2$ and $N = 3$ converge to the $N = 4$ curves shown here, and the curves for $N = 3$ and $N = 4$ are nearly indistinguishable.	122
3.12	Magnitude of dS/dt of one of the black holes from $S_{0.994}^{++}$. Shown are three numerical resolutions, Alvi's expression (Eq. (11) of [78]), the OPN expression, and the CPY expression [80, 81] to 1PN order. The inset zooms closer to the high-resolution numerical curve.	124
3.13	Magnitude of dS/dx , where $x \equiv (M\omega_{\text{orb}})^{1/3}$, of one of the black holes from $S_{0.994}^{++}$. The top horizontal axis shows t/M of the highest-resolution numerical simulation, for comparison with values of x	125
3.14	Magnitude of dm/dt of one of the black holes from $S_{0.994}^{++}$. Shown are three numerical resolutions, Alvi's expression (Eq. (11) of [78]), the OPN expression, and the CPY expression [80, 81] truncated to 1PN order. The inset zooms closer to the high-resolution numerical curve.	127
3.15	Magnitude of dm/dx , where $x \equiv (M\omega_{\text{orb}})^{1/3}$, of one of the black holes from $S_{0.994}^{++}$	128
3.16	The evolution of the derivative of the gravitational-wave frequency $\dot{\omega}_{22} = d\omega_{22}/dt$, for simulations $S_{0.99}^{++}$ and $S_{0.994}^{++}$ and (for comparison) simulations $S_{0.8}^{++}$ [41], $S_{0.85}^{++}$ [41], $S_{0.9}^{++}$ [41], $S_{0.95}^{++}$ [41], $S_{0.97}^{++}$ [37], and $S_{0.98}^{++}$ [24].	129

- 3.17 The number of gravitational-wave cycles as a function of the initial spin χ , measured after the initial relaxation, for simulations $S_{0.99}^{++}$ and $S_{0.994}^{++}$ and (for comparison) simulations $S_{0.8}^{++}$ [41], $S_{0.85}^{++}$ [41], $S_{0.9}^{++}$ [41], $S_{0.95}^{++}$ [41], $S_{0.96}^{++}$ [50], $S_{0.97}^{++}$ [37], and $S_{0.98}^{++}$ [24]. *Upper panel:* The number of gravitational-wave cycles of h_{22} accumulated between a gravitational-wave frequency $M\omega_{22} = 0.036$ and merger (i.e., the time when the amplitude of h_{22} peaks). The dashed line is a linear fit to the data. *Lower panel:* Fractional difference (“residual”) between our results and the linear fit, with uncertainties for simulations except $S_{0.85}^{++}$ (which we ran at only one resolution) estimated as differences between medium and high numerical resolutions. 130
- 3.18 Phase differences $\Delta\phi$ of h_{22} as a function of retarded time before merger for $S_{0.99}^{++}$. Shown are differences between the highest numerical resolution and several analytic approximants. Differences between the highest numerical resolution and other numerical resolutions are shown for comparison. The waveforms are aligned in the time interval delimited by the black triangles. 131
- 3.19 Phase differences $\Delta\phi$ of h_{22} between numerical and approximant data for $S_{0.994}^{++}$. Labels are the same as for Fig. 3.18. 132
- 3.20 Phase differences $\Delta\phi$ of h_{22} between numerical and approximant data for $S_{0.20}^{0.99}$. Labels are the same as for Fig. 3.18. Note that the Taylor models include precession but SEOBNRv2 does not. However, the precession of $S_{0.20}^{0.99}$ is mild so the numerical waveform still agrees reasonably well with SEOBNRv2. 133
- 4.1 Mismatches as a function of time for the eight models, each including up to N QNM overtones. The mismatch associated with each model at a given t_0 corresponds to the mismatch computed using Eq. (4.2), between the model and the NR waveform for $t \geq t_0$, where t_0 specifies the lower limit used in Eq. (4.3). Each additional overtone decreases the minimum achievable mismatch, with the minimum consistently shifting to earlier times. 150

- 4.2 Comparison between the plus polarization of the $\ell = m = 2$ mode of the NR waveform and the $N = 7$ linear QNM model. The QNM model begins at $t_0 = t_{\text{peak}}$. The upper panel shows both waveforms, and the lower panel shows the residual for $t \geq t_{\text{peak}}$. For reference, the lower panel also shows an estimate of the error in the NR waveform, $|h_{22}^{NR} - h_{22}^{\overline{NR}}|$, where h_{22}^{NR} refers to the highest resolution waveform of SXS:BBH:0305 and $h_{22}^{\overline{NR}}$ refers to the next highest resolution waveform for this same system. The two NR waveforms are aligned at $t_0 = t_{\text{peak}}$, in both time and phase. 151
- 4.3 The distribution of ϵ , Eq. (4.4), for a range of simulations in the SXS catalog. The distribution includes systems with mass ratios up to 8 and orbit-aligned component spins with $|\vec{\chi}| \leq 0.8$. The distributions shown are for $N = \{0, 3, 7\}$ overtones at the peak of the strain amplitude. For the best performing model, $N = 7$, the median value is 2×10^{-3} and the maximum error in estimating the mass and spin is $\sim 5 \times 10^{-3}$ 153
- 4.4 Mismatches for the $\ell = m = 2$ mode between NR and Eq. (4.1) for a grid of M_f and χ_f with $N = 7$ and $t_0 = t_{\text{peak}}$. The white horizontal and vertical lines correspond to the NR values and are in good agreement with the M_f and χ_f mismatch distribution using the maximum number of overtones considered. 154
- 4.5 The mismatches for the $\ell = m = 2$ mode between NR and Eq. (4.1) over a grid of χ_f and M_f with $N = 0$, the fundamental mode only, and $t_0 = t_{\text{peak}}$. The white horizontal and vertical lines correspond to the remnant values from NR. As the fundamental mode is subdominant at this time, this single-mode model is a poor probe of the underlying remnant mass and spin. Note that the mass and mismatch scales used in this figure are significantly different than Fig. 4.4, due to the discrepant single-mode fit at early times. 155

- 4.6 Mismatches for the $\ell = m = 2$ mode between NR and Eq. (4.1) for a grid of M_f and χ_f with $N = 0$, the fundamental mode, at a late time $t_0 = t_{\text{peak}} + 47M$. Here the fundamental mode is dominant, since the overtones have decayed away by this time. Again, the white horizontal and vertical lines correspond to the remnant values from NR and now, at this late time, we find good agreement between the true values and those recovered by using only the fundamental mode as a probe for M_f and χ_f 156
- 4.7 The root-mean-squared error, ϵ , defined in Eq. (4.4), for different sets of frequencies, as a function of number of included overtones N . The fits are performed on the spherical $\ell = m = 2$ mode at $t = t_0 = t_{\text{peak}}$. The label $\omega_{22n}(M_f, \chi_f)$ represents the set of frequencies consistent with perturbation theory, while $\tilde{\omega}_{22n}(M_f, \chi_f)$ represents the set of frequencies with the fundamental mode, $n = 0$, unmodified but with a slight modification to the overtone frequencies by a factor of $(1 + \delta)$. For each δ , there is an associated dashed line of the same color that corresponds to $\delta \rightarrow -\delta$. The faint grey lines correspond to frequencies with a random δ for each n , as explained in the last paragraph of Sec. 4.5. The results suggest there is information present in the overtones that contribute to extracting the remnant properties at the peak, as these outperform a similar set of functions, with the same degrees of freedom for each N , but with frequencies inconsistent with the asymptotic remnant. 157
- 4.8 A decomposition of the ringdown in terms of the overtones for $N = 7$. The evolution of the overtones is computed from the analytic decay rates with initial amplitudes at $t = t_0 = t_{\text{peak}}$ specified by the bottom row of Table 4.1. Notice that the fundamental mode does not dominate the ringdown of SXS:BBH:0305 until roughly $10M$ after t_{peak} 160
- 4.9 The numerically recovered amplitudes for the fundamental QNM and the first few overtones at each fit time, t (solid curves). Dashed lines are the same as the lines in Fig. 4.8. The numerically extracted amplitudes across t agree very well with the expected decay for the longest-lived modes, while modes that decay more quickly are more susceptible to fitting issues. Interestingly, the fundamental mode is in excellent agreement with the expected decay rate at times preceding the peak amplitude of the strain. 161

- 4.10 Remnant parameters inferred with different number of overtones, using data starting at the peak amplitude of the injected strain. Contours represent 90%-credible regions on the remnant mass (M_f) and dimensionless spin (χ_f), obtained from the Bayesian analysis of a GW150914-like NR signal injected into simulated noise for a single Advanced LIGO detector at design sensitivity. The inference model was as in Eq. (4.1), with ($\ell = m = 2$) and different number of overtones N : 0 (solid blue), 1 (dashed purple), 2 (dashed yellow), 3 (solid red). In all cases, the analysis uses data starting at peak strain ($\Delta t_0 = t_0 - t_{h\text{-peak}} = 0$). The top and right panels show 1D posteriors for M_f and χ_f respectively. Amplitudes and phases are marginalized over. The intersection of the dotted lines marks the true value ($M_f = 68.5M_\odot$, $\chi_f = 0.69$). 163
- 4.11 Remnant parameters inferred using only the fundamental mode, using data starting at different times relative to the peak amplitude of the injected strain. Contours represent 90%-credible regions on the remnant mass (M_f) and dimensionless spin (χ_f), obtained from the Bayesian analysis of a GW150914-like NR signal injected into simulated noise for a single Advanced LIGO detector at design sensitivity. For the blue contours, the inference model included no overtones ($N = 0$) and used data starting at different times after the peak: $\Delta t_0 = t_0 - t_{h\text{-peak}} \in [0, 3, 6, 10]$ ms (blue contours). For the red contour, the analysis was conducted with three overtones ($N = 3$) starting at the peak ($\Delta t_0 = 0$), as in Fig. 4.10. The top and right panels show 1D posteriors for M_f and χ_f respectively. Amplitudes and phases are marginalized over. The intersection of the dotted lines marks the true value ($M_f = 68.5M_\odot$, $\chi_f = 0.69$). 164

- 5.1 Remnant parameters inferred with different number of overtones, using data starting at peak strain amplitude. Contours represent 90%-credible regions on the remnant mass (M_f) and dimensionless spin magnitude (χ_f), obtained from the Bayesian analysis of GW150914. The inference model is that of Eq. (5.1), with different number of overtones N : 0 (solid blue), 1 (solid yellow), 2 (dashed purple). In all cases, the analysis uses data starting at peak strain ($\Delta t_0 = t_0 - t_{\text{peak}} = 0$). Amplitudes and phases are marginalized over. The black contour is the 90%-credible region obtained from the full IMR waveform, as described in the text. The intersection of the dotted lines marks the peak of this distribution ($M_f = 68.5M_\odot$, $\chi_f = 0.69$). The top and right panels show 1D posteriors for M_f and χ_f respectively. The linear quasinormal mode models with $N > 0$ provide measurements of the mass and spin consistent with the full IMR waveform, in agreement with general relativity. 178
- 5.2 Measured quasinormal-mode amplitudes for a model with the fundamental mode and two overtones ($N = 2$). The purple colormap represents the joint posterior distribution for the three amplitudes in the $N = 2$ model: A_0 , A_1 , A_2 , as defined in Eq. (5.1). The solid curves enclose 90% of the probability mass. A yellow curve in the A_0 - A_1 plane, as well as corresponding yellow dashed lines, represents the 90%-credible measurement of the amplitudes assuming $N = 1$. Similarly, blue dashed lines give the 90%-credible measurement of A_0 assuming $N = 0$. All amplitudes are defined at $t = t_{\text{peak}}$, where all fits here are carried out ($\Delta t_0 = 0$). Values have been rescaled by a constant to correspond to the strain measured by the LIGO Hanford detector. Assuming $N = 1$, the mean of the A_1 marginalized posterior lies 3.6 standard deviations away from zero, i.e. $A_1 = 0$ is disfavored at 3.6σ . Assuming $N = 2$, $A_1 = A_2 = 0$ is disfavored with 90% credibility. 179

- 5.3 Remnant parameters inferred only from the fundamental mode, using data starting at different times after the peak. Contours represent 90%-credible regions on the remnant mass (M_f) and dimensionless spin magnitude (χ_f), obtained from the Bayesian analysis of GW150914. For the blue contours, the inference model included no overtones ($N = 0$) and used data starting at different times after the peak: $\Delta t_0 = t_0 - t_{\text{peak}} \in [1, 3, 5]$ ms . For the yellow contour, the analysis was conducted with one overtone ($N = 1$) starting at the peak ($\Delta t_0 = 0$), as in Fig. 5.1. Amplitudes and phases are marginalized over. The black contour is the 90%-credible region obtained from the full IMR waveform, as described in the text. The intersection of the dotted lines marks the peak of this distribution ($M_f = 68.5M_\odot$, $\chi_f = 0.69$). The top and right panels show 1D posteriors for M_f and χ_f respectively. Around $\Delta t_0 = 3$ ms, the overtones have become unmeasurable and only the fundamental mode remains; consequently, at that time $N = 0$ returns a measurement of the final mass and spin consistent with both the full IMR waveform and the $N > 0$ models at the peak, in agreement with general relativity. 182
- 5.4 Measurement of the frequency and damping time of the first overtone, using data starting at the peak. The colormap represents the posterior distribution of the fractional deviations δf_1 and $\delta \tau_1$ away from the no-hair value $\delta f_1 = \delta \tau_1 = 0$ (gray dotted lines). The solid contour and dashed vertical lines enclose 90% of the posterior probability. All other parameters, including M_f and χ_f have been marginalized away. Fixing $\delta f_1 = \delta \tau_1 = 0$ recovers the $N = 1$ analysis in Figs. 5.1 and 5.3. 184

LIST OF TABLES

<i>Number</i>	<i>Page</i>
2.1 Evolved mass groups for NGC 6121 ($N_{\text{BH}} = 200$) with corresponding mass index, the lower boundary bin mass m_{min} , the upper boundary bin mass m_{max} , the average mass of the group \bar{m} , the fraction of the total mass in the cluster f_{m} , the number fraction with respect to the total number of objects in the cluster f_{n} , and the fraction of luminous objects in the group f_{L} . For reference, the BH masses occupy the top three mass groups with mean masses of $8.87 M_{\odot}$, $20.48 M_{\odot}$, and $57.18 M_{\odot}$	34
2.2 Summary of simulations. Listed are the 15 GCs modelled for evolution along with the total cluster mass M_{c} , squared velocity dispersion σ^2 , the luminous core density ρ_{L} , concentration c , and metallicity Z . The clusters are ordered by total mass. There are 39 independent models after taking into account the number of BHs retained by the cluster. Medium to high mass clusters can accommodate large BH populations without disrupting the listed structural parameters. The size of the BH population in lower-mass clusters is either (1) limited in number by the IMF or (2) by the ability of the cluster to maintain the model structural parameters in their presence; in these cases, the cluster is not used for evolutions and is omitted from the table. In the final column we list the total number of evolutions performed for each case.	44
2.3 Expected number of binary ejections. For each cluster and number of retained BHs, we list the exact number of BHs in the cluster along with the expected number of ejections over the cluster lifetime for three binary types: BH-NC, BH-NS, and BH-BH. The clusters follow the same order as Table 2.2, sorted according to increasing total cluster mass. The values of N_{BH} are non-integer values as a consequence of modelling the population with a smooth distribution function.	55

- 2.4 Expected number of mergers. For each cluster and number of retained BHs, we list the exact number of BHs in the cluster along with the expected number of mergers over the cluster lifetime. The number of expected mergers within a cluster are Poisson distributed. Denoting each expectation value λ , the standard deviation, σ , associated with each value in the table follows from Poisson statistics and is given by $\sigma = \sqrt{\lambda}$ 72
- 2.5 The contribution to the compact merger rate density from all GCs in the universe, stated in $\text{Gpc}^{-3} \text{yr}^{-1}$. Each row corresponds to the merger rate contribution from GCs with the simulated BH population specified by N_{BH} in $\langle R(N_{\text{BH}}) \rangle$. The merger rate densities are averaged over the life of the cluster, weighted by the GC mass function to account for the non-uniform mass distribution of GCs, and assumes a GC spatial density of $\rho_{\text{GC}} = 0.77 \text{Mpc}^{-3}$ 76
- 2.6 The rate of three-body mergers in GCs computed for the Milky Way galaxy and stated in $\text{MWEG}^{-1} \text{Myr}^{-1}$. Each row corresponds to the three-body merger rate in Milky Way GCs with the simulated BH population specified by N_{BH} in $\langle R(N_{\text{BH}}) \rangle$. The merger rates are averaged over the life of the cluster, weighted by the GC mass function to account for the non-uniform mass distribution of GCs, and assumes $N_{\text{GC}} \simeq 150$ for the number of GCs in the galaxy. 81
- 2.7 Properties of the five observed systems that are consistent with the properties of our simulated population of BH-LMXBs with GC origins. The columns refer to the primary BH mass M_{BH} , the companion mass m_2 , the orbital period p , and the absolute distance perpendicular to the galactic plane $|z|$. [0] Yamaoka et al. [95], [1] Kuulkers et al. [96], [2] Mata Sánchez et al. [97], [3] Corral-Santana et al. [98], [4] Shaw et al. [99], [5] Neustroev et al. [100], [6] Zurita et al. [101], [7] Cadolle Bel et al. [102], [8] Khargharia et al. [103], [9] Calvelo et al. [104], [10] Torres et al. [105], [11] Gelino et al. [106], [12] Casares et al. [107], [13] Beekman et al. [108], [14] Webb et al. [109], [15] Gelino and Harrison [110] 83

- 3.1 Summary of physical simulation parameters. Data are publicly available online [77] indexed by their Catalog ID. Quantities with an r superscript are reported at time $t = t_{\text{relax}}$, the time after the initial “junk radiation” transients have settled down: q is the mass ratio, m_H is the Christodoulou mass of an individual black hole (where H represents black hole A or B), $M\omega_{\text{orb}}$ is the orbital frequency (computed via $d^2\vec{\omega}_{\text{orb}} = \vec{d} \times \dot{\vec{d}}$, where \vec{d} is the coordinate separation between the black holes), χ_H is the dimensionless spin, θ_H is the angle between $\vec{\omega}_{\text{orb}}$ and $\vec{\chi}_H$, and ϕ_H is the angle between the separation vector and the component of $\vec{\chi}_H$ in the orbital plane. The remaining quantities are eccentricity e , number of orbits N_{orb} from $t = 0$ to merger, final Christodoulou mass M_f , and final spin magnitude χ_f 114
- 4.1 Best-fit estimates of the amplitudes A_n of the fundamental mode and overtones in the ringdown of NR simulation SXS:BBH:0305, with $t_0 = t_{\text{peak}}$. Amplitudes are computed for various values of N , the total number of overtones included in the fit. Also shown is the time t_{fit} where the fit is performed for each N , stated with respect to t_{peak} . A_n are always the amplitudes at $t = t_0 = t_{\text{peak}}$, even if the fit is performed at a later time. The amplitude values are truncated such that the last significant figure agrees with the the two highest resolutions for the NR simulation. 159

Chapter 1

INTRODUCTION

1.1 Our new view of the universe

Black holes are strange creatures of the cosmos. Their mysterious nature and peculiar properties have intrigued generations of physicists. Their properties are so unusual, it is somewhat surprising that they actually exist in nature. Yet recent achievements have confirmed their existence and observations continue to confirm these objects behave just as Einstein's general theory of relativity predicts.



Figure 1.1: A high-accuracy visualization of the moments before the merger of two black holes for a nearby observer. The black holes' extreme gravity is apparent in the distortion of the background stars, as the path of the light emanating from the stars is bent by the black holes before reaching the observer, producing complex geometric features. This visualization is based on a simulation of the very first LIGO detection, GW150914. Credit: SXS

Just over four years ago, the Laser Interferometer Gravitational-Wave Observatory (LIGO) detected gravitational waves emitted by two black holes as they spiraled in toward each other, driving them into a violent collision that resulted in a single, massive, ringing, black hole. As the newborn remnant settled into a stable state, the ringing grew quieter and the signal faded into the noise. The black hole universe didn't remain quiet for long. After the first two observing runs, the tally stood at

10 binary black hole mergers and one exceptionally scientifically rich observation of the merger of two neutron stars, which was followed up by a large number of electromagnetic-based observatories. This was the reward for decades of work by an enormous group of scientists, both theorists and experimentalists. To date, there are roughly 50 additional candidate detections, each being carefully analyzed. LIGO has been hailed for providing us with a new view of the universe, by allowing us to ‘see’ merging black holes through the gravitational radiation they emit. The pre-LIGO era was restricted to inferring properties of black holes by observing the emitted electromagnetic radiation (e.g. radio, infrared, X-ray) generated when black holes interact with their environment. We have gained an unprecedented amount of information about black holes from these first few LIGO detections. In the near future, upgrades to existing detectors and the flight of the future space based detector, the Laser Interferometer Space Antenna (LISA), will allow for even more precise detections. As we continue to sense the gravitational perturbations from the extreme objects throughout the universe, with LIGO and the soon-to-come LISA, unexpected results will undoubtedly be revealed.



Figure 1.2: A view along one of the 4 km arms of the L-shaped LIGO detector in Livingston, Louisiana. A second detector resides across the country in Hanford, Washington. The two detectors operate together to identify coincident gravitational waves and to reject random noise fluctuations that can mimic astrophysical sources, as the noise should be uncorrelated between the two detectors. Credit: Caltech/MIT/LIGO Lab.

1.2 General relativity

Einstein's general theory of relativity is the current theory of gravity, displacing Newton's laws of gravity, which had been in place for over 200 years. One of the major problems with Newton's formulation is that the gravitational force propagates instantaneously. A key insight by Einstein, which was at the heart of his theory of relativity, is the invariance of the speed of light and its role as a universal speed limit. In other words, the speed at which light propagates is independent of both the inertial reference frame of an observer and the motion of the source. A change in gravity is not felt until there has been sufficient time for the change to travel from the source to an observer – in contrast to Newtonian instantaneity.

One of the most prominent aspects of general relativity is the concept of a spacetime fabric. This fabric arises as a consequence of placing the time coordinate on equal footing with spatial coordinates. This was another one of Einstein's key insights – that time is not universal. The three spatial coordinates along with time allow us to view our universe as a four-dimensional spacetime fabric. In general relativity, one can write down a metric, often denoted g_{ab} , which represents the geometry of the spacetime fabric and provides the mathematical framework necessary to determine how objects behave within the spacetime fabric.

A measure of distance across an infinitesimal displacement, also known as the line element,

$$ds^2 = g_{ab} dx^a dx^b, \quad (1.1)$$

is a function of the metric g_{ab} , which specifies how time and distance are to be measured along any given direction of the spacetime. The line element, Equation 1.1, generalizes the familiar line element of Euclidean geometry,

$$ds^2 = dx^2 + dy^2 + dz^2, \quad (1.2)$$

to allow for curved geometry in both space and time. The full Einstein field equations can be written succinctly as:

$$G_{ab} = 8\pi T_{ab}, \quad (1.3)$$

where G_{ab} on the left-hand side is the Einstein tensor, containing the metric g_{ab} and describing the curvature of the spacetime. On the right-hand side is T_{ab} , the so-called stress-energy tensor, which represents the density and flux of energy and momentum in the spacetime. In essence, as John Wheeler concisely stated, “spacetime tells matter how to move; matter tells spacetime how to curve.”

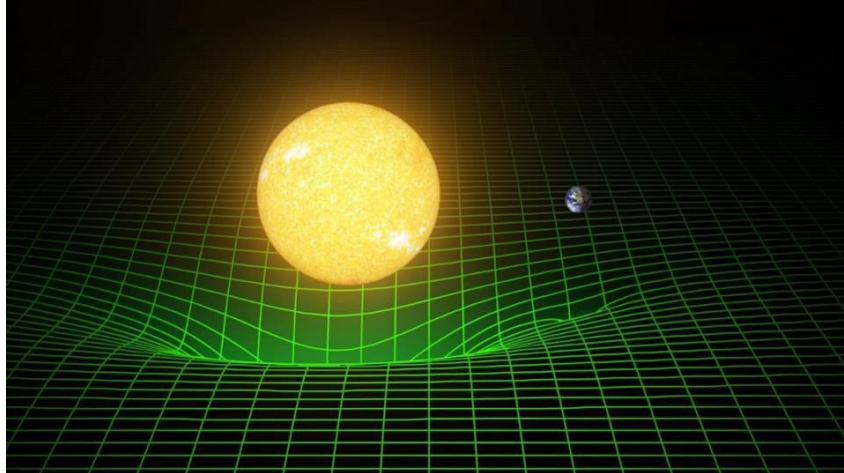


Figure 1.3: A visualization of warped spacetime for the Earth-Sun system. The green mesh represents the underlying spacetime fabric, which has noticeable curvature due to the massive objects. It is this curvature which tells light and matter how to move through space and time. Note that while spacetime is a four-dimensional construct, for illustrative purposes, it is represent here as a two-dimensional sheet. Credit: T. Pyle, Caltech/MIT/LIGO Lab

A simple example is one within our own solar system. The matter of the Sun causes the surrounding spacetime to become warped. The Earth orbits the Sun, attempting to maintain a ‘straight’ path, but a straight path on the warped spacetime forces the Earth to travel along a more circular trajectory. Similarly, the Earth’s matter causes the spacetime around it to bend as well, but to a much lesser extent than the Sun. Figure 1.3 provides a visual representation of the warping of the spacetime near both the Sun and the Earth. This is the modern picture of how gravity operates, a purely geometric formulation, where gravity does not emerge as a ‘pulling’ force as in Newton’s theory, but instead as one where mass modifies the spacetime fabric itself (see [1–4], for more detailed discussions of general relativity).

1.3 Gravitational waves

An interesting consequence of general relativity is its prediction of gravitational waves. In the previous section, the concept of a spacetime fabric was introduced. Gravitational waves are perturbations to this spacetime fabric, wrinkles in the spacetime that propagate at the speed of light. As gravitational sources accelerate, the change in the gravitational field propagates through the spacetime, like ripples in a pond. When a gravitational wave passes an observer, the observer’s local gravitational field is modified by these waves; the local metric is perturbed and the

line element, which is a function of the metric (see Eq. (1.1)) and determines how time and distances are measured, is consequently modified.

More formally, far from any sources, the local metric g_{ab} is just Minkowski space, or flat space, η_{ab} . However, in the presence of a gravitational wave, the local metric becomes

$$g_{ab} = \eta_{ab} + h_{ab}, \quad (1.4)$$

where h_{ab} is the small perturbation to flat space carried by the gravitational waves. Following [1], after linearizing the Einstein equations and some manipulation, it can be shown that small perturbations behave as

$$h_{ab} = A_{ab} \exp(ik^c x_c), \quad (1.5)$$

which describes a wave propagating at the speed of light (see [5, 6], for more detailed discussions of gravitational waves).

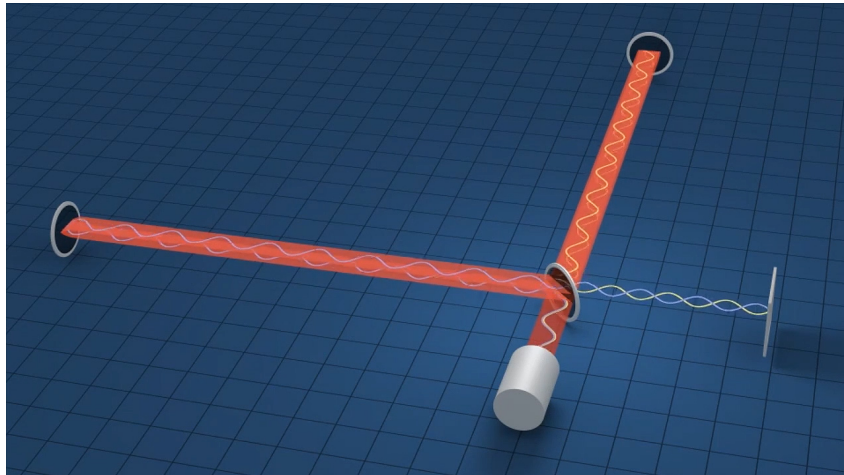


Figure 1.4: A simple illustration of how the Laser Interferometer Gravitational-Wave Observatory (LIGO) functions. A high-power laser passes through a beam splitter, sending light down each of the 4 km arms. Large mirrors at the end of each arm reflect the light back to the beam splitter, which redirects some light from each arm onto a photodetector. The photodetector is sensitive to how the light from each arm interacts with each other and allows for the detection of small changes in the arm lengths due to passing gravitational waves. Credit: T. Pyle, Caltech/MIT/LIGO Lab

The LIGO detectors were cleverly designed to detect gravitational waves by measuring these small modifications to our local gravitational field. High-powered lasers are directed down the two arms of the L-shaped detector, are reflected back by large mirrors, and are rejoined at a photodetector that monitors how the two beams interact.

If the local metric remains unmodified, the distance that light travels down each arm of the detector remains unchanged and so does the light interference pattern. When a gravitational wave passes through a detector, the distance that light travels down each arm is slightly longer or shorter, so that when the beams of light reconvene at the photodetector, the interference pattern is consequently modified.

However, this change in distance due to gravitational waves is incomprehensibly small. The ratio of the change of distance along one arm, ΔL , over the length of the arm, L , is referred to as the strain

$$h = \frac{\Delta L}{L}, \quad (1.6)$$

which is directly relatable to Eq. (1.5) [4]. Rearranging Eq. (1.6) and writing this as

$$\Delta L = h \times L, \quad (1.7)$$

we see that the change in length is directly proportional to the gravitational wave strain amplitude and the length of the arms. Given the knowledge of expected strain amplitudes from astrophysical source, the exceptionally long (4 km) LIGO arms were chosen with Eq. (1.7) in mind – bringing ΔL into a measurable regime.

To get an idea of how small the gravitational strain amplitude actually is, we can turn to the quadrupole formula, which was first derived by Einstein in 1918 [7]. The quadrupole formula provides us with a rough approximation for the strain amplitude of waves emitted from two equal mass objects with mass M [M_\odot], orbiting at a separation r [M], located at a distance R [Mpc] from a detector (with $G = c = 1$) [8]:

$$h \sim 5 \times 10^{-20} \left(\frac{1 \text{ Mpc}}{R} \right) \left(\frac{M}{M_\odot} \right) \left(\frac{M}{r} \right). \quad (1.8)$$

Let us assume that our source is two objects, each with the mass of ten suns, and it is located in one of the closest superclusters of galaxies, the Coma Supercluster, which is at a distance of roughly 90 Mpc away from Earth. This yields $h \sim 5 \times 10^{-21} \left(\frac{M}{r} \right)$. The minimum separation achievable by the two objects is approximately twice their radii. If we assume the objects are black holes, this gives rise to $r = 4M$ and we get an estimated strain of $h \sim 1 \times 10^{-21}$. This corresponds to a change in the length of the LIGO arms of $\Delta L \sim 5 \times 10^{-18}$ m, which is about 100 times smaller than the radius of a proton. Detecting changes in length at this scale is an unimaginable feat, earning LIGO the title of the most precise ruler ever constructed.

If we repeat the above, assuming the same total mass but replacing the source with two stars rather than compact black holes, the stars enormous sizes prevent them

from reaching the separations obtainable by black holes. With the radius of the sun being roughly 2×10^5 larger than a black hole of the same mass, the two stars would produce, at most, a change of $\Delta L \sim 2 \times 10^{-23}$ m in the LIGO detectors – this is smaller than the size of the smallest known quark. This difference in strain amplitude highlights why compact objects are the primary sources of gravitational waves. Although orbiting stars generate gravitational waves, we are currently only sensitive to those coming from the most extreme objects in space. Fortunately, compact objects are arguably some of the most mysterious objects in our universe, and LIGO has granted us the ability to study these strange beasts comfortably from Earth.

1.4 Binary black holes

The previous section described how gravitational waves from compact objects are the most promising sources for detection. While neutron stars are good candidates for gravitational waves – with one certain detection [9] and another recent candidate [10] – this thesis focuses solely on binary black hole sources. As black holes are more massive and more compact than neutron stars, the gravitational waves emitted by binary black holes are much louder (we say “louder” rather than “stronger” or “brighter” because stellar-mass black holes produce waves with frequencies corresponding to the audio band if they were sound waves). This loudness allows us to see binary black holes from much farther away than neutron star mergers. This increase in the detectable distance exposes us to a significantly larger volume of the universe, and consequently, a larger number of sources. The current count of LIGO detections reflects this, as the number of binary black hole mergers dominates over the current neutron star merger count.

Despite the exotic nature of black holes, binary black holes only depend on a handful of fundamental parameters. Each black hole is fully characterized by just its mass, M_i , and a dimensionless spin parameter, $\chi_i = S_i/M_i^2$, where S_i is the spin angular momentum of the hole, and the subscript simply labels each hole in the binary. In a binary, the orientation of each of the black holes’ spin becomes important, so each spin is properly described by a vector, \mathbf{S}_i . Figure 1.5 illustrates the typical parameters in a binary black hole system. It turns out that the total mass, $M = M_1 + M_2$, scales out of the equations, and instead only the ratio of the masses remains a fundamental parameter, $q = M_1/M_2$. In total, for a circular system, there are three components for each spin and the mass ratio – bringing the total dimensions of the binary black hole space to 7.

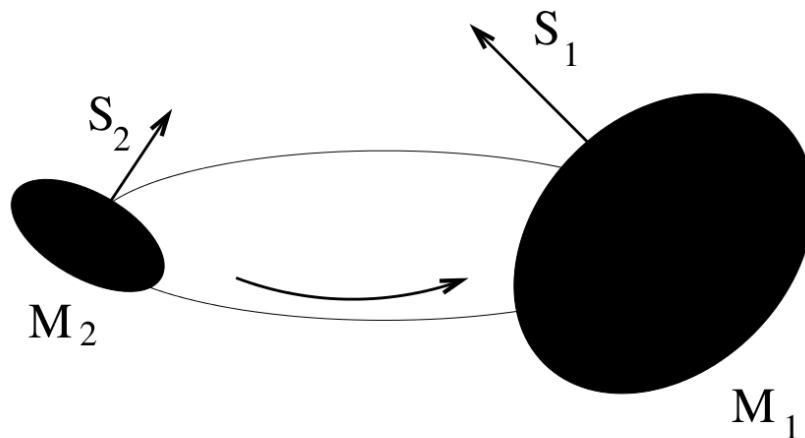


Figure 1.5: An illustration of a quasi-circular binary black hole system and the seven fundamental intrinsic parameters that govern the evolution of the binary. Each angular momentum spin vector constitutes three parameters, with the seventh being the mass ratio, $q = M_1/M_2$, as the total mass, $M = M_1 + M_2$, scales out of the problem.

The gravitational wave signal from orbiting black holes can be roughly separated into three segments, the inspiral, the merger, and the ringdown. The inspiral is the earliest stage of binary black hole evolution. During this stage, the black holes are widely separated and radiating weak gravitational waves that deplete energy from the system, causing the black holes to spiral in toward each other. Post-Newtonian theory is a perturbative scheme built around an expansion parameter that is the characteristic velocity of the binary over the speed of light (i.e., v/c). It is during the slow inspiral where this approximation is best suited. As the binary continues to radiate away gravitational waves, the holes are forced inward at an accelerating pace. During the last few orbits, the holes are traveling at a significant fraction of the speed of light, and consequently, post-Newtonian theory breaks down. Finally, as the two holes near each other, a new black hole forms, as the two black holes merge into one. The merger is the most dynamic moment for the binary, as the black holes are now moving at their highest velocity. The magnitude of gravitational radiation is nearly maximal. Once the new, more massive, black hole is formed it quickly begins evolving towards its final axisymmetric state. The perturbations to its final shape are quickly shed in the form of gravitational waves. This end-stage of the binary life is known as the ringdown, in analogy with the way a struck bell rings down.

They are comparable in the way that both radiate at frequencies that depend on the geometry of the object, and in the way that the amplitudes of the signals fade away as they each settle into a stable state. Figure 1.6 provides a nice visual summary of the three primary stages of the life of the binary, while also showing how the separation, relative velocity, and the waveform evolve in time.

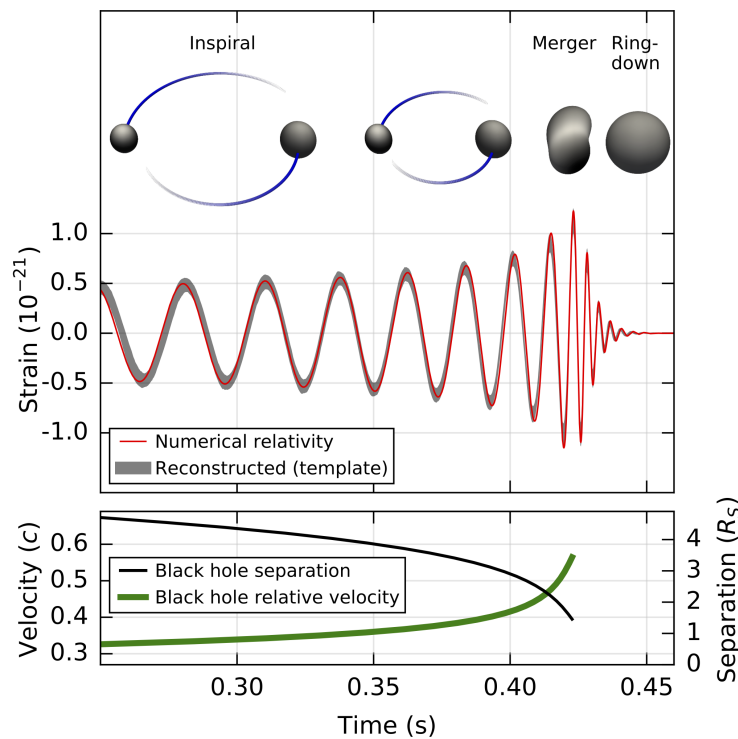


Figure 1.6: The top panel shows the underlying gravitational wave data in the Hanford detector for GW150914 and a waveform produced using numerical relativity that is consistent with the data. The illustration shows a rough separation of the waveform into the three key regions of the binary life: the inspiral, the merger, and the ringdown. The bottom panel shows the corresponding separation of the two black holes and the relative velocity of the two black holes as functions of time. Credit: LIGO [11]

1.5 Numerical relativity

The previous section described the key components of binary black hole evolution, but only briefly touched on modeling binary black holes. Unfortunately, there is currently no analytic solution to the generic two-body problem in general relativity. While there exists a large number of approximate models, including the post-Newtonian expansion briefly touched on in the previous section, these approximations all break down at some level. Waveform models are a critical part of LIGO data analyses

and will be equally important for LISA. Numerical relativity – solving Einstein’s equations on supercomputers – is an indispensable tool in waveform modeling and the most accurate waveform models are derived from numerical relativity simulations.

The first successful numerical relativity simulation of merging black holes [12] was achieved roughly a decade before the first detection of merging black holes, GW150914 [11]. There has been significant progress in the field of numerical relativity since the first successful simulation, including improved accuracy, newly identified observable phenomena, and most importantly, from a detection standpoint, an abundance of waveforms produced by a number of numerical relativity groups. The following is a short overview of numerical relativity, for a more in-depth discussion about the field of numerical relativity see Ref. [8].

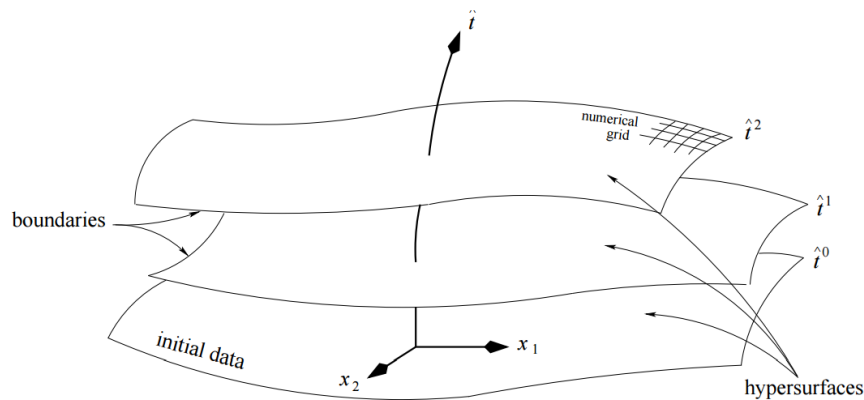


Figure 1.7: An illustration of spacetime foliation used in numerical relativity simulations. The bottom hypersurface represents the space-like initial data at a fixed time. As time progresses, the evolution equations generate a sequence of non-intersecting space-like surfaces. A stack of these hypersurfaces represent the full spacetime, each slice being a three-dimensional surface, but with one suppressed spatial dimension for ease of illustration. Credit: H. Dimmelmeier

The Einstein equations are a system of coupled, nonlinear partial differential equations, which are intractable with paper and pencil for systems like merging black holes. Numerical relativity recasts the Einstein equations in such a form that allows for the time evolution of some initial metric, ensuring that the equations remain satisfied at all times. The full spacetime for a binary black hole system is described by the four-dimensional metric g_{ab} . A slice of this four-dimensional spacetime results in a space-like hypersurface, with an induced metric g_{ij} resulting from the projection of g_{ab} onto one fewer dimension. The remaining information of the four-metric, after projection, is retained in the extrinsic curvature K_{ij} , which is related to the first

time derivative of g_{ij} and specifies the initial ‘velocity’ in the initial value problem, whereas g_{ij} can be interpreted as the specified initial ‘position.’ The Einstein equations then govern how the space-like surfaces evolve. Figure 1.7 provides a schematic representation of this foliation of spacetime.

In this thesis, all numerical relativity results were produced using the Spectral Einstein Code (SpEC) [13], developed by the Simulating eXtreme Spacetimes collaboration [14]. SpEC is unique in that it utilizes spectral methods for the simulations, rather than the standard finite-difference methods. The key benefit of spectral methods is the exponential convergence. This means a comparable change in the resolution (i.e. the number of grid points in the computational domain) produces much smaller computational errors in spectral methods versus finite-difference methods. SpEC has now produced over 2018 distinct gravitational waveforms [15], roughly a factor of 10 more than the previous release of SpEC waveforms [16]. These cover the space of mass ratios up to $q = 10$ and spin magnitudes up to 0.998 [17]. While numerical relativity is important for supplying high-accuracy waveforms, it is not limited to this sole task – it also serves as an accurate laboratory for exploring potential observables, which we can use to put general relativity to the test.

1.6 Black holes in globular clusters

Globular clusters are spherical, high-density collections of old stars. There are approximately 150 globular clusters within the Milky Way galaxy, largely residing in the halo of our galaxy. These are not unique to our galaxy, as almost every observed galaxy, with sufficient mass, has been found to harbor a collection of globular clusters. An important characteristic of globular clusters is that all of its constituents are of approximately the same age. This means that there has not been sufficient time for generations of stars to produce metals that typically enrich new stars. Consequently, stars in globular clusters are typically referred to as low-metallicity stars, because these stars are metal poor compared to stars like our own Sun. But perhaps the most intriguing property of globular clusters, is the astounding density of objects within them. There are only two stars, including our own sun, within about a parsec of us. The number of stars located within this same volume near the core of a globular cluster would be of order 10^4 . It is this high density of objects within globular clusters that make them a rich environment for highly dynamical interactions. The abundance of objects leads to numerous three-body interactions, where a binary’s orbital parameters can be significantly modified. This can result in a change in the original binary’s orbital parameters such as its separation or eccentricity, the binary

can be completely dismantled, or a new binary can form by ejecting one of the original partners. This is in contrast to standard binary formation that occurs in the galactic field, where the density is low enough that binaries form and evolve in nearly complete isolation.

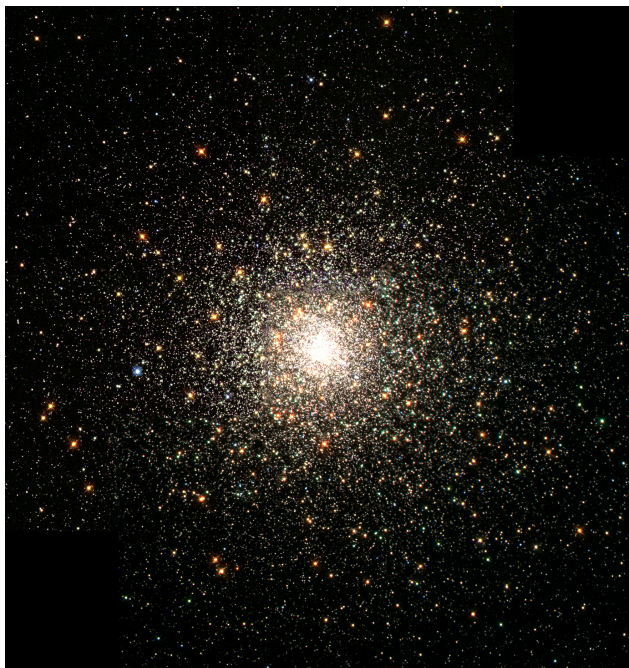


Figure 1.8: M80, also known as NGC 6093, is one of the densest known globular clusters in the Milky Way galaxy. The massive collection of stars is bound by their mutual gravity, leading to a compact, nearly-spherical, object. Clusters such as this are home to highly dynamical interactions because of the exceptionally high density of objects compared to the relatively sparse galactic field. Credit: NASA

The general behavior of globular clusters has been modeled very well by relatively simple methods for decades. However, the majority of previous studies have been conducted assuming a population of zero to, at most, a few black holes. This assumption is based on the idea that whatever population of black holes that might form throughout the history of the globular cluster will eventually migrate to the core. There, they are subject to a high rate of dynamical interactions that are likely to eject the black holes as singles or in binaries. It was long accepted that this process would lead to repeated ejections from the globular cluster, leaving a few to zero black holes. Historically, this was supported by the lack of observational evidence for a black hole within a globular cluster. However, black holes are difficult to observe unless they are actively accreting from a stellar companion and it wasn't until recently that observers discovered two black hole low-mass X-ray binaries in the Milky Way

globular cluster M22. Since this discovery, evidence has continued to mount for the case of significantly larger populations of black holes in globular clusters.

In Chapter 2 of this thesis, we consider varying sizes of black hole populations in globular clusters and identify key observables that might allow us to estimate the size of their black hole populations. As individual black holes are nearly impossible to detect because of their inherently dark nature, we rely on interacting black holes to inform us of the underlying population size. Black holes accreting from low-mass stellar companions emit in the X-ray spectrum, earning them the straightforward label: black hole low-mass X-ray binaries. Additionally, binary black holes emit gravitational waves that are potentially detectable by current and future gravitational wave detectors. In the following, we discuss these two promising observables characteristic of black holes originating in globular clusters.

X-ray binaries

As briefly discussed above, X-ray binaries are compact objects accreting from a stellar companion that produce radiation in the X-ray spectrum. Low-mass X-ray binaries are those where the stellar companion typically has a mass less than the primary accretor. The accretor in these systems is either a neutron star or a black hole. For such systems, the X-ray spectrum or a mass measurement can help distinguish between neutron star or black hole accretors. Hundreds of these systems have been identified within our own Milky Way galaxy and observations have been steadily increasing. These systems can form in the galactic field, where most of the matter in our galaxy resides. However, a large number of the systems have been observed at large distances above or below the galactic plane – requiring some explanation of how these systems escaped their birth environments. One potential explanation is a globular cluster origin. Globular clusters have a broad distribution throughout the Milky Way galaxy and spend much of their time in the galactic halo, at large distances out of the galactic plane. Given a population of black holes within a globular cluster, dynamical formation readily produces and ejects black hole low-mass X-ray binaries throughout the Milky Way galaxy.

This population of low-mass X-ray binaries from globular clusters retain a sort of fingerprint that allows us to deduce their origin. These are characteristically short orbital periods, low-metallicity companions, and a galactic spatial distribution that differs from that of low-mass X-ray binaries formed outside globular clusters. Crucially, the number of black hole low-mass X-ray binaries ejected from globular

clusters also depends on the size of the black hole population. Chapter 2 discusses, in much greater detail, the methods for simulating the population of X-ray binaries and identifies the relation between the population of black-hole X-ray binaries and the underlying globular cluster black hole population. Further, a number of observed systems are compared against the simulated systems and a number of X-ray binaries are identified as candidates for having a globular cluster origin. However, the most important trademark of a globular cluster origin is a low-metallicity companion, and unfortunately a measurement of the companion metallicity is lacking for the majority of these. But, as future data becomes available, these results can be used to place constraints on globular cluster black hole population sizes.

Eccentric mergers

While black hole low-mass X-ray binaries are a primary proxy for identifying black holes through electromagnetic observatories, gravitational wave detectors are a new way to shed some light on the invisible black hole population. The key to understanding the black hole population in globular clusters, though, is being able to distinguish them from binary black holes originating outside globular clusters.

A key finding of Chapter 2 is the result that binary black holes in globular clusters can form with very large eccentricities. The channel for this high-eccentricity formation is the three-body dynamics leading to the birth of these binary black holes. This large eccentricity causes the binary to merge more quickly, radiating away large bursts of energy at each periastron pass, while still inside the cluster. However, eccentric binary black holes are very efficient at circularizing. By the time these initially eccentric binaries have evolved to separations at which LIGO is sensitive to the gravitational waves being emitted by the system, the black holes are in a nearly perfect circular orbit. Globular clusters also eject a number of black hole binaries that will merge outside the cluster. These systems tend to have much smaller eccentricities and will also appear circular by the time they are observable by LIGO. For this reason, it is difficult to distinguish between binaries formed in the field versus globular clusters based on eccentricity alone. Future space-based detectors operate at much lower frequencies than LIGO, effectively observing the binary at much wider separations, where the eccentricity of the system is still measurable. The eccentricity in these signals would serve as a unique fingerprint for binaries formed in dense environments such as globular clusters. The number of eccentric mergers produced by globular clusters depends strongly on the underlying black hole population; thus, observations of these systems by LISA could serve to constrain the

black hole population in globular clusters.

This characteristic gravitational wave observable along with the uniquely produced black hole low-mass X-ray binaries could serve as independent measures of the black hole population in globular clusters, but can also serve to complement each other to place stricter constraints on the size of globular cluster black hole populations.

1.7 Binary black holes with nearly extremal spins

Black holes form after the collapse of massive stars. These massive stars are observed to be rotating and consequently black holes are expected to be born with some spin angular momentum. In Section 1.4, a Kerr black hole was described as having two key parameters, the mass of the black hole, M , and a dimensionless spin parameter, χ . This dimensionless spin parameter quantifies the amount of spin angular momentum associated with the black hole and is bounded between 0 and 1, where $\chi = 1$ is referred to as being *extremal*. For realistic astrophysical black holes, the Novikov-Thorne upper bound, $\chi \leq 0.998$, places an approximate limit on the spin of black holes spun up through the process of accretion from a thin disk. Observations of stellar-mass black holes in X-ray binaries have measured, albeit with large uncertainties, systems with black holes very near $\chi \sim 1$, lending more credence to the idea of astrophysical black holes reaching nearly-extremal spins.

Simulating nearly-extremal black holes in numerical relativity has proved to be challenging. Prior to the work presented in Chapter 3, the nearly-extremal region of parameter space was completely unexplored. A primary factor in the lack of high-spin waveforms was the difficulty in producing initial data for binary evolutions. The standard choice for producing spinning binary black hole initial data maxes out at $\chi = 0.93$, known as the Bowen-York limit. This limit arises from the assumption that the initial data solution is conformal to flat-space. However, conformally flat spacetimes cannot represent black holes with angular momentum. Consequently, conformally-flat spinning black hole initial data is out of equilibrium and spins specified above $\chi = 0.93$ quickly relax back down to the Bowen-York limit. By requiring the initial data to be conformal to two superposed Kerr metrics, one for each rotating hole, the Bowen-York limit can be overcome.

In addition to the difficulties producing initial data with sufficiently high black hole spins, evolving these systems also proves to be challenging. While the details of these challenges are perhaps too technical to discuss here, Chapter 3 explores the difficulties and how they can be overcome.

There is often some confusion about how large a χ value constitutes a nearly-extremal black hole, as $\chi = 0.93$ seems rather close to unity. One way to put this in context is to translate χ values into a fraction of the maximum rotational energy, where maximal rotation energy of unity corresponds to $\chi = 1$. Figure 1.9 shows the non-linear relation between rotational energy and χ , providing some guidance on how to interpret the extremality of χ . Note that a value of $\chi = 0.93$ only corresponds to roughly 59% of the maximum rotational energy. In Chapter 3, we present results from simulations with aligned binary spins of $\chi = 0.99$ and $\chi = 0.994$. These two values of χ result in disproportionate increases in the percent of maximal rotation energy, bumping from the Bowen-York associated 59% up to 83% and 87%, respectively.

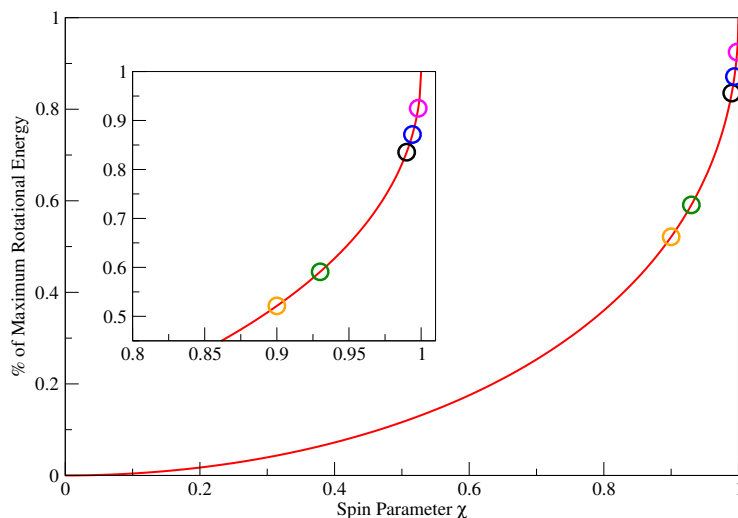


Figure 1.9: The fraction of maximal rotation energy as a function of χ , where $\chi = 1$ corresponds to the maximum rotational energy. This illustrates how steeply the maximum rotational energy grows as the black hole spin increases. The inset zooms in to show a number of data points at $\chi \geq 0.9$, with $\chi = 0.9$ corresponding to $\sim 52\%$ of the maximum rotational energy of a black hole. The next highest point is the Bowen-York limit, $\chi = 0.93$, followed by $\chi = \{0.99, 0.994, 0.998\}$. These values of χ yield values for the fraction of maximum rotational energy of $\{59.1\%, 83.5\%, 87.1\%, 92.5\%\}$, respectively.

The work in Chapter 3 presents the first waveforms generated in the nearly-extremal region of binary black holes. In this work, we compare existing waveform approximants against the numerical relativity produced waveforms to quantify the error in these approximants. These include post-Newtonian models and effective-one-body waveforms, the latter being a widely used model in LIGO data analyses. Effective-

one-body models rely on numerical relativity waveforms for calibration, ensuring that the accuracy of these models remains sufficient for LIGO, across all regions of the parameter space. As such, these numerically produced high-spin waveforms are critical in developing waveform models necessary for LIGO detections and parameter estimation.

1.8 Black hole ringdown

As previously discussed, the ringdown is the final stage of a binary black hole merger. When the two black holes collide, they merge into a single massive black hole that rings like a struck bell, sending out ripples in space and time. In general relativity, this newly formed black hole is described by just its mass, M , and dimensionless spin, χ . These are the only two parameters necessary to write down the metric for a single black hole. Although accurate numerical simulations of the ringdown phase of binary black holes have only become available relatively recently, the ringdown has been well studied for decades, by carefully understanding the behavior of small perturbations to the single black hole metric. These studies revealed that the geometry of the spacetime, fully described by the black holes mass and spin, produces a specific set of frequencies of gravitational waves, which are radiated away as the single black hole sheds its perturbations. The model that perturbation theory produces is a signal that behaves like a damped sinusoid, i.e.,

$$h \sim Ae^{-t/\tau} \cos(\nu t). \quad (1.9)$$

Here ν is the oscillatory frequency of the gravitational waves and τ dictates how quickly the amplitude of the radiation decays. In perturbation theory, these two quantities are often combined into a single complex frequency, $\omega = \nu - i/\tau$. Both ν and τ directly depend only on the underlying black hole mass and spin, i.e., $\omega(M, \chi)$. These perturbative solutions are known as quasinormal modes. The radiative modes are normal modes of the black hole spacetime, but, since they are non-conservative because of the escaping radiation, they do not entirely adhere to the normal mode definition, hence the *quasi* qualifier.

The first binary black hole observation, GW150914, was exceptionally loud and sparked significant interest in trying to study the ringdown portion of the data. Having access to a loud ringdown, along with the relatively simple model predicted by perturbation theory, provides a seemingly straightforward way to put general relativity to the test. By measuring the frequency and decay of the ringdown signal, we can compare how well these measurements agree with predictions from black

hole perturbation theory in general relativity. This test was carried out in Ref. [11], where a model with the form of Equation 5.1 was fit to the data to measure ν and τ . The recovered values are then compared to predicted values that are consistent with the best-fit parameters determined by analyzing the full gravitation wave signal. However, this test is problematic. It turns out that the results depend very sensitively on the assumption about where Equation 5.1 becomes a valid prescription. If it was employed at times near the peak of the waveform, there was noticeable disagreement. This disagreement became less pronounced as the analysis was started at later times, but then the signal gets weaker in time leading to a growth in the uncertainty. The conclusion was that the single black hole is initially swamped by non-linearities and that perturbation theory is only relevant at very late times, once the non-linearities have died out.

Since the measured signal is buried in noise, we can turn to high-accuracy numerical relativity waveforms as a cleaner testbed to understand the validity of perturbation theory, as these waveforms are essentially noiseless. In Chapter 4, we carry out an analysis focused on answering this question. We summarize the key points here.

The discussion about quasinormal modes above left out a few important details. Perturbation theory does not produce a *single* frequency for a given black hole. Instead, perturbation theory predicts a spectrum of frequencies, $\omega_n(M, \chi)$, where n labels each frequency. The n sorts the modes by how quickly they decay, with $n = 0$ corresponding to the longest-lived mode. The modes beyond $n = 0$ are referred to as overtones, while the $n = 0$ mode is known as the *fundamental* mode. We can include these modes in the prescription, so that the new model is one of the form

$$h \sim \sum_{n=0}^N A_n e^{-t/\tau_n} \cos(\nu_n t). \quad (1.10)$$

This is a simple superposition of all modes up to some cutoff, or maximum mode, N . By analyzing a high-accuracy numerical relativity waveform, consistent with the GW150914 parameters, we show that Equation 1.10 provides an excellent description for the region of the waveform going all the way back to the peak amplitude. Including up to $N = 7$ modes allows us to accurately match the post-peak region of the numerical relativity waveform, yielding residuals around the 10^{-4} level. The excellent agreement between the numerical waveform and this linear prescription indicates that non-linearities are very small. This was a surprising result, since the conventional wisdom was that the peak of the waveform corresponded to the *most* non-linear part of the merger. Additionally, allowing for the mass and spin to be free

parameters in the fit, we find that the best-fit mass and spin only differ by $\sim 10^{-4}$ from the numerical relativity measurements of mass and spin of the final black hole horizon. Repeating the analysis with only the fundamental mode, $n = 0$, reveals biased measurements of the black hole mass and spin unless the analysis is started at very late times. This is in agreement with the findings in Ref. [11]. However, our conclusion is that, rather than this region being contaminated by complicated non-linearities, the disagreement in the measurements is biased by the presence of the overtones that were excluded from the model.

Going one step further, we carried out a full analysis of a GW150914-like numerical relativity waveform injected into LIGO-like noise. Accurate measurements of the remnant black hole mass and spin can be obtained by including a sufficient number of overtones. Ignoring the overtones produces the expected bias, with the bias being reduced as the number of overtones included in the model is increased.

Although overtones were largely considered to be unimportant, the opposite appears to be true. While the overtones do indeed decay away rather quickly, the amplitudes of these modes can initially be much higher than the amplitude of the longest-lived fundamental mode. Consequently, ringdown analyses must include a sufficient number of overtones. Our results suggest that given the loudness of GW150914, an additional mode, the first overtone, should be resolvable. The bias present at early times in the initial ringdown analysis of GW150914 seems to also suggest the presence of this mode. The importance of measuring a second mode, along with the implications for testing general relativity – specifically testing the no-hair theorem – are discussed in Chapter 5 and summarized in the following section.

1.9 Testing Einstein’s theory

By now, we know that the merger of two black holes results in a single black hole that rings as it radiates away the distortions to the spacetime. This last bit of radiation, the ringdown signal, is composed of specific frequencies precisely predicted by general relativity. The hypothesis that a black hole is entirely described by just its mass and spin is known as the no-hair conjecture. This strangely titled conjecture is attributable to John Wheeler, stating ‘black holes have no hair,’ where the hair refers to any additional properties beyond its mass and spin, as all other information, or ‘hair’, is forever lost behind the black hole’s event horizon. For black holes that obey Einstein’s theory, the mode frequencies serve as a fingerprint for the black hole. A complementary statement is that if the objects we observe are not Einstein’s black

holes, but instead something more exotic, the frequencies will not have this property and this would be a spectacular surprise. Because merging black holes experience crushing gravity, studies of the ringdown allow for tests of general relativity under the most extreme conditions.

A minimum of two modes are required for a no-hair test, each with an associated frequency and damping time that depend only on the mass and spin. The conventional test relies on measuring two fundamental modes of a black hole, the fundamental of the dominant quadrupolar mode and the fundamental of a higher-order mode. However, modes beyond the dominant quadrupolar mode are weakly excited and have yet to reach the threshold for detectability. Consequently, a test relying on two fundamental modes is not expected to be feasible for another 10-15 years, after detector sensitivity has improved significantly.

However, as discussed in the previous section, overtones of the dominant quadrupolar mode are potentially measurable in current detectors and the overtones are present much earlier in the waveform than previous ringdown analyses had considered. As the overtones are present in a much louder part of the signal, we can access the higher signal-to-noise ratio to resolve these modes. Reanalyzing the first detection, GW150914, we were able to perform a first test of the no-hair theorem. By comparing the best-measured mass and spin at early times with one overtone, compared to a mass and spin obtained at late times solely with the fundamental mode, the remnant is consistent with a Kerr black hole as predicted by general relativity at the 10% level. An additional test, more in the spirit of the conventional test, is to allow the frequencies to be independent parameters in the fit. This test allows us to confirm that the spectrum is in agreement with the no-hair hypothesis to within $\sim 20\%$.

These first tests serve as a proof of principle and place the first, albeit loose, constraints on how far black holes can deviate from general relativity. The framework we have developed for analyzing ringdowns can be extended to coherently analyze multiple events, which would improve constraints on the current allowed deviations from black holes of general relativity. A system similar to the first, GW150914, at today's sensitivity would be an exceptional event, allowing for the measurement of 3 or 4 ringdown quasinormal modes – and would provide one of the most stringent constraints on the nature of black holes. The results presented in Chapter 5 just scratch the surface of the powerful tests that can be employed with overtones using present day detectors and the even more precise tests that can be accomplished with LISA. Once LISA is operational, we expect that several of the overtones

should be measurable, allowing for the most precise test of the no-hair theorem with considerably tighter constraints.

References

- [1] Bernard F. Schutz. *A First Course in General Relativity*. "Second". New York: Cambridge University Press, 2009.
- [2] James B. Hartle. *Gravity: An Introduction to Einstein's General Relativity*. New York: Addison-Wesley, 2003.
- [3] Sean Carroll. *Spacetime and Geometry: An Introduction to General Relativity*. New York: Addison Wesley, 2003.
- [4] Charles W. Misner, Kip S. Thorne, and John Archibald Wheeler. *Gravitation*. New York, New York: Freeman, 1973.
- [5] B.S. Sathyaprakash and Bernard F. Schutz. "Physics, Astrophysics and Cosmology with Gravitational Waves". In: *Living Reviews in Relativity* 12.2 (2009). DOI: [10.1007/lrr-2009-2](https://doi.org/10.1007/lrr-2009-2). URL: <http://www.livingreviews.org/lrr-2009-2>.
- [6] M Maggiore. *Gravitational Waves - Volume 1*. First. New York, NY: Oxford University Press, 2008.
- [7] E. Poisson and C.M. Will. *Gravity: Newtonian, Post-Newtonian, Relativistic*. Cambridge University Press, 2014. ISBN: 9781107032866. URL: <https://books.google.com/books?id=PZ5cAwAAQBAJ>.
- [8] Thomas W. Baumgarte and Stuart L. Shapiro. *Numerical Relativity: Solving Einstein's Equations on the Computer*. New York: Cambridge University Press, 2010. DOI: [10.1080/00107514.2011.586052](https://doi.org/10.1080/00107514.2011.586052).
- [9] B. P. Abbott et al. "GW170817: Observation of Gravitational Waves from a Binary Neutron Star Inspiral". In: *Phys. Rev. Lett.* 119.16 (2017), p. 161101. DOI: [10.1103/PhysRevLett.119.161101](https://doi.org/10.1103/PhysRevLett.119.161101).
- [10] B. P. Abbott et al. "GW190425: Observation of a Compact Binary Coalescence with Total Mass $\sim 3.4M_{\odot}$ ". In: (2020). arXiv: [2001.01761](https://arxiv.org/abs/2001.01761) [[astro-ph.HE](https://arxiv.org/abs/2001.01761)].
- [11] B. P. Abbott et al. "Observation of Gravitational Waves from a Binary Black Hole Merger". In: *Phys. Rev. Lett.* 116 (6 Feb. 2016), p. 061102. DOI: [10.1103/PhysRevLett.116.061102](https://doi.org/10.1103/PhysRevLett.116.061102). URL: <http://link.aps.org/doi/10.1103/PhysRevLett.116.061102>.
- [12] Frans Pretorius. "Evolution of binary black hole spacetimes". In: *Phys. Rev. Lett.* 95 (2005), p. 121101. DOI: [10.1103/PhysRevLett.95.121101](https://doi.org/10.1103/PhysRevLett.95.121101). arXiv: [gr-qc/0507014](https://arxiv.org/abs/gr-qc/0507014) [[gr-qc](https://arxiv.org/abs/gr-qc)].
- [13] <http://www.black-holes.org/SpEC.html>.

- [14] *Simulating eXtreme Spacetimes*. <http://www.black-holes.org/>.
- [15] Michael Boyle et al. “The SXS Collaboration catalog of binary black hole simulations”. In: *Class. Quant. Grav.* 36.19 (2019), p. 195006. DOI: [10.1088/1361-6382/ab34e2](https://doi.org/10.1088/1361-6382/ab34e2). arXiv: [1904.04831](https://arxiv.org/abs/1904.04831) [gr-qc].
- [16] Abdul H. Mroue et al. “A Catalog of 174 Binary Black Hole Simulations for Gravitational Wave Astronomy”. In: *Phys. Rev. Lett.* 111 (2013), p. 241104. DOI: [10.1103/PhysRevLett.111.241104](https://doi.org/10.1103/PhysRevLett.111.241104). arXiv: [1304.6077](https://arxiv.org/abs/1304.6077) [gr-qc].
- [17] Mark A. Scheel, Matthew Giesler, Daniel A. Hemberger, Geoffrey Lovelace, Kevin Kuper, Michael Boyle, B. Szilagyi, and Lawrence E. Kidder. “Improved methods for simulating nearly extremal binary black holes”. In: *Class. Quant. Grav.* 32.10 (2015), p. 105009. DOI: [10.1088/0264-9381/32/10/105009](https://doi.org/10.1088/0264-9381/32/10/105009). arXiv: [1412.1803](https://arxiv.org/abs/1412.1803) [gr-qc].

*Chapter 2*LOW-MASS X-RAY BINARIES FROM BLACK-HOLE
RETAINING GLOBULAR CLUSTERS

Matthew Giesler, Drew Clausen, and Christian D Ott

Monthly Notices of the Royal Astronomical Society, 477, 1853 (2018)

[arxiv:1708.05915](https://arxiv.org/abs/1708.05915)**2.1 Abstract**

Recent studies suggest that globular clusters (GCs) may retain a substantial population of stellar-mass black holes (BHs), in contrast to the long-held belief of a few to zero BHs. We model the population of BH low-mass X-ray binaries (BH-LMXBs), an ideal observable proxy for elusive single BHs, produced from a representative group of Milky Way GCs with variable BH populations. We simulate the formation of BH-binaries in GCs through exchange interactions between binary and single stars in the company of tens to hundreds of BHs. Additionally, we consider the impact of the BH population on the rate of compact binaries undergoing gravitational wave driven mergers. The characteristics of the BH-LMXB population and binary properties are sensitive to the GCs structural parameters as well as its unobservable BH population. We find that GCs retaining ~ 1000 BHs produce a galactic population of ~ 150 ejected BH-LMXBs whereas GCs retaining only ~ 20 BHs produce zero ejected BH-LMXBs. Moreover, we explore the possibility that some of the presently known BH-LMXBs might have originated in GCs and identify five candidate systems.

2.2 Introduction

The fate of the population of stellar-mass black holes (BH) in globular clusters (GCs) is still widely uncertain. It is expected that tens to hundreds and possibly thousands of BHs are formed in GCs, of which some fraction might be ejected early due to a kick at formation [1]. In the standard GC evolution picture, the remainder of the BHs should rapidly sink to the core due to mass segregation. There they are subject to a high rate of dynamical interactions that are likely to eject the BHs as singles or in binaries. It was long accepted that this process would lead to repeated ejections from the GC leaving a few to zero BHs (e.g., [2]; [3]). Historically, this was supported by the lack of observational evidence for a BH in a GC; however, BHs are difficult to

observe unless they are actively accreting from a stellar companion.

In order to explore the population of BHs within and outside of GCs, black-hole low-mass X-ray binaries (BH-LMXBs) can serve as an ideal proxy. In an evolved cluster, a main-sequence star (MS) will necessarily be less than the MS turnoff mass, yielding an abundance of potential low-mass companions. This, coupled with a high rate of encounters due to the high-density environment of GCs, makes GCs ideal BH-LMXB factories. However, this assumes that a significant number of BHs are retained by GCs and that the BHs avoid segregating completely from the lower-mass stars.

The discovery of two BH-LMXB systems in the Milky Way GC M22 [4] has led to a renewed interest in GC BH retention. This observation coupled with an estimate for the fraction of the BH population expected to be in accreting binaries [5] suggests that M22 may contain 5 – 100 BHs [4]. Additionally, [6] suggested a number of high-luminosity LMXBs residing in M31 GCs may harbour BH primaries, which was confirmed by [7]. Recent theoretical studies, including some detailed N -body simulations (e.g., [8]; [9]), support the idea that GCs are capable of retaining from a few to hundreds of BHs (e.g., [10]; [11]; [12]; [13]).

There is an increasing number of BH-LMXB candidates identified in the Milky Way galaxy. BlackCAT [14], a catalogue of BH-LMXBs, has to date identified 59 candidate Milky Way BH-LMXBs. An LMXB is identified as a candidate BH-LMXB if the X-ray spectrum rules out a neutron star (NS) as the compact accretor [15]. Of the 59 candidate BH-LMXBs in BlackCAT, 22 are currently considered to be ‘confirmed’ BH-LMXBs. A BH-LMXB labelled as ‘confirmed’ has a dynamical measurement of the primary mass or mass-function $f(M_{\text{BH}})$ (see, e.g., [16]).

Roughly one-fifth of the observed BH-LMXBs reside at an absolute distance $|z|$ perpendicular to the galactic plane greater than 1 kpc (e.g., [17]; [14]). The distribution of the candidate and confirmed BH-LMXBs within the Milky Way gives rise to the idea that BHs might be subject to high-velocity kicks at formation (e.g., [18]; [19]; [20]; [21]). In some cases, the velocity needed for the binary to reach large $|z|$ exceeds the contribution from a Blaauw kick [22]. This is the velocity imparted to a binary in the case of sudden mass loss, i.e. in the BH progenitor’s supernova explosion. The exceptional high-velocity BH-LMXB cases have led to the idea of high-velocity formation kicks, also known as ‘natal’ kicks, where the binary receives a large kick through an asymmetric explosion launched prior to BH formation ([23]; [24]). Due to the long-held assumption that GCs maintain a

near-zero population of BHs, the possibility that some of these systems originated in GCs has been largely ignored. BH-LMXBs sourced by BH-retaining GCs might help to explain some of the peculiar properties of the observed Milky Way BH-LMXB population. Although GCs are not likely to describe the entire population of BH-LMXBs, the halo-orbits of GCs in the Milky Way make GCs ideal candidate sources for the high- $|z|$ systems. In light of the recent studies that suggest GCs might harbour a large number of BHs, we revisit in this paper the possibility of GCs as a potential origination point for a subset of the observed BH-LMXB systems.

Although we are primarily concerned with the galactic population of BH-LMXBs evolving from initially non mass-transferring binaries ejected from GCs, BH-LMXBs can form within GCs through more exotic channels. These formation channels include mass-transfer following directly from a physical collision or triple-induced mass transfer coupled with exchange encounters or physical collisions [5]. The more recent work of [25], proposes a new BH population-dependent channel for the production of BH-LMXBs within GCs by means of grazing tidal encounters between a BH and a subgiant.

In addition to using BH-LMXBs as probes of BH retention in GCs, the BH-BH merger rates might also serve to place some constraints on GC BH retention. The recent success in observing merging BH-BH binaries by advanced LIGO (aLIGO) makes this a realistic possibility ([26]; [27]; [28]). Furthermore, binary BH mergers occurring in GCs may be characteristically eccentric due to dynamical formation channels. Although these eccentric systems are likely to have circularized by the time they are visible in the aLIGO frequency band, the eccentricity is potentially detectable at lower frequencies. The addition of a space-based gravitational wave observatory (e.g., LISA) in the future, designed for sensitivity at lower frequencies, further improves the prospect of using BH-BH mergers to probe GC dynamics.

In this study, we explicitly evolve ‘test’ binaries in a fixed cluster background subject to dynamical friction and single-binary interactions. Additionally, we include an updated prescription for allowing single BHs to exchange into existing binaries. The GCs are chosen to represent a realistic subset of Milky Way GCs with varying BH populations in order to investigate the effects of BH retention in clusters. Each GC background is described by an isotropic multi-mass King model. We produce a large number of realizations for each set of initial parameters to obtain statistical distributions of the number of ejected binaries and their relevant properties. Using the statistics from the GC simulations, we then perform Monte Carlo simulations to obtain

a population of BH-LMXBs produced by GCs. The GCs and the ejected binaries are evolved in time through the Milky Way potential while simultaneously accounting for the stellar evolution of the ejected binaries. The resulting mass-transferring systems make up a previously unexplored galactic population of BH-LMXBs from GCs. We investigate the distribution and properties of the resulting population and its dependence on BH retention in GCs. Specifically, we find that in the case of minimal BH retention ($N_{\text{BH}} = 20$) no observable BH-LMXBs are produced, while the $N_{\text{BH}} = 200$ and $N_{\text{BH}} = 1000$ cases respectively yield galactic populations of 25_{-6}^{+10} and 156_{-24}^{+26} BH-LMXBs. Furthermore, we use the resulting population to determine the most likely candidates for a GC origin in the population of observed Milky Way BH-LMXBs: the five systems that are compatible with our simulated population of BH-LMXBs from GCs are MAXI J1659-152, SWIFT J1357.2-0933, SWIFT J1753.5-0127, XTE J1118+480, and GRO J0422+32. One caveat is that four out of five of these systems are still lacking measurements of the companion metallicity. Due to the low metallicity environments of GCs, a measurement finding a metallicity significantly larger than typical GC metallicities would be a strong piece of evidence ruling out a GC origin for the system under consideration. The fifth system, XTE J1118+480, has had its metallicity measured twice. However, the findings of [29] and [30] currently provide conflicting claims regarding the companion metallicity. Future measurements will be necessary to increase support for a GC origin theory, but if we can confidently attribute a BH-LMXB to a GC, this would provide strong evidence for significant BH retention in GCs.

The remainder of this paper is structured as follows. In section 2.3, we describe our model for the GCs and the evolution of a test-binary in a static cluster background. In section 2.4, we lay out how we generate the present-day BH-LMXB population from our simulations of Milky Way GCs. In section 2.5, we review the properties of the ejected BH binaries along with the distribution and properties of the present-day BH-LMXBs from GCs. Additionally, we explore the effects of BH retention on the BH-BH merger rate in GCs. We conclude the section by comparing our results with observations and previous work. Finally, in section 2.6, we provide concluding remarks.

2.3 Methods

GCs typically contain $\sim 10^5 - 10^6$ stars, which makes them accessible to modern N -body simulations (e.g., [31]; [9]) that can track GC evolution. However, full N -body cluster evolution simulations are still very computationally expensive,

making this method poorly suited for studying many realizations of different GCs necessary for building statistics on the evolution of BH binaries inside clusters. Fokker-Planck methods are more approximate and describe GCs with a phase-space distribution function for its constituent stars that evolves via the Fokker-Planck equation, a Boltzmann equation with a small local collision term that modifies only velocities (see, e.g., [32]). The Fokker-Planck equation can be numerically integrated directly (e.g., [33, 34]) or, more commonly, integrated with Monte Carlo methods (see, e.g., [35, 36] and [13] for a comparison between N -body and the Monte Carlo approaches). However, here we are concerned with the evolution of BH binaries in GCs and not with the GC evolution itself. Hence, we adopt the approach of modelling the evolution of binaries in a fixed cluster background, pioneered in the early 90’s (see, e.g., [37–40]; and [41] for an overview of the theoretical models of GCs and the dynamics occurring within). We approximate the collision term in the Fokker-Planck equation analytically to model the effects of distant encounters as the binary evolves through the GC. Near encounters are accounted for by explicitly integrating the three-body equations of motion. We build up statistics by carrying out simulations of many random realizations of binaries for a given GC background model. In the following sections, we describe our method in detail.

Model

Our model, most closely based on [40], incorporates a number of assumptions that simplify the simulations and allow us to perform $\sim 10^4$ realizations for a given cluster model with relatively minimal computational needs. The three key assumptions are: (i) GCs are well described by a ‘lowered Maxwellian’ distribution function, (ii) the gravitational potential and distribution functions are stationary, and (iii) the effect of distant interactions is well described by the leading order terms in the Fokker-Planck equation. The ‘lowered Maxwellian’ distribution function, which eliminates the tail of the Maxwellian velocity distribution, introduces a maximum energy for stars within the cluster to remain bound. This maximum energy $\phi(r_t)$ implies a finite mass and a maximum radius r_t , commonly referred to as the ‘tidal’ radius, as stars beyond this distance are pulled from the cluster by the galactic tidal field. Models based on a ‘lowered Maxwellian’, commonly referred to as King models, readily describe many observed clusters ([42]; [43]; [32]).

We evolve a single ‘test binary’, initialized according to section 2.3, in a static cluster background described by an isotropic multi-mass King model [44] defined by single particle distribution functions $f_\alpha(\mathbf{r}, \mathbf{v}, m_\alpha)$ for a discrete set of mass groups. Here,

r and v are the radius and velocity in the cluster centre-of-mass frame and m_α is the representative mass of group α . The distribution function for a given mass group is given by

$$f_\alpha(\varepsilon) = \begin{cases} \frac{n_{0_\alpha}}{(2\pi\sigma_\alpha^2)^{3/2}} (e^{-\varepsilon/\sigma_\alpha^2} - 1) & \varepsilon < 0 \\ 0 & \varepsilon \geq 0 . \end{cases} \quad (2.1)$$

Here, ε is the energy per unit mass, $\varepsilon = v^2/2 - \Psi(r)$, and $\Psi(r) \equiv \phi(r_t) - \phi(r)$ is the gravitational potential relative to that at the tidal radius r_t . Additionally, σ_α is the group's velocity dispersion at the core of the cluster and n_{0_α} is a normalization factor. For an isotropic cluster, the velocity dispersion reduces to the one-dimensional mean-square velocity, such that $3\sigma_\alpha^2 = \bar{v}_\alpha^2$. The normalization factor in its full form is

$$n_{0_\alpha} = \eta_\alpha \frac{n_o}{e^{\Psi(0)/\sigma_\alpha^2} \operatorname{erf}\left(\sqrt{\frac{\Psi(0)}{\sigma_\alpha^2}}\right) - \sqrt{\frac{4\Psi(0)}{\pi\sigma_\alpha^2}} \left(1 + \frac{2\Psi(0)}{3\sigma_\alpha^2}\right)}, \quad (2.2)$$

where $\eta_\alpha = N_\alpha/N$ is the number fraction for mass group α and $n_o = n(0)$ is the central density.

The free structural parameters necessary to specify a model cluster, with specified mass groups, are the mean core velocity dispersion $\bar{\sigma}$, the core number density n_o , and the potential depth, which is specified by the dimensionless King parameter $W_o = \Psi(0)/\bar{\sigma}^2$. The remaining structural parameters, which are fully determined by the free parameters, are: total mass M_c , core radius r_c , tidal radius r_t , and concentration $c = \log_{10}(r_t/r_c)$. The core radius r_c is defined as the radius at which the surface brightness has dropped to half the value at the core.

For a given set of masses with corresponding distribution functions, the cluster satisfies Poisson's equation for the relative potential $\nabla^2\Psi(r) = -4\pi G \sum_\alpha \rho_\alpha$. Here, $\rho_\alpha = m_\alpha n_\alpha$, where n_α is the number density of mass group α given by

$$n_\alpha = \int_0^{v(r_t)} f_\alpha(r, v, m_\alpha) 4\pi v^2 dv . \quad (2.3)$$

The upper limit of the integral is the maximum allowed velocity $v(r_t) = \sqrt{2\Psi(r_t)}$, i.e. the escape velocity. The object masses m_α and number fraction η_{0_α} are determined by the evolved mass function, discussed in section 2.3. We generate a model cluster that satisfies Poisson's equation for the specified masses and number fractions in an iterative fashion. We begin by integrating Poisson's equation out to a radius r_t , implicitly determined by $\Psi(r_t) = 0$, with boundary conditions $\Psi(0) = W_o$ and $\nabla\Psi(0) = 0$, and take $\eta_\alpha = \eta_{0_\alpha}$ as our initial guess. The actual number fraction of

each mass group, $\eta_\alpha = N_\alpha/N$, is then calculated using

$$N_\alpha = \int_0^{r_t} n_\alpha(r) 4\pi r^2 dr , \quad (2.4)$$

along with $N = \sum_\alpha N_\alpha$. We then update our guess to $\eta_\alpha = (\eta_{\alpha_{\text{new}}} + \eta_{\alpha_{\text{old}}})/2$, where $\eta_{\alpha_{\text{new}}} \rightarrow \eta_{\alpha_{\text{old}}} \times (\eta_{0_\alpha}/\eta_\alpha)$. We repeat the above steps until $(\eta_{0_\alpha} - \eta_\alpha)/\eta_{0_\alpha} < \delta$ is satisfied for all mass groups, where we have made the somewhat arbitrary choice of $\delta = 6.25 \times 10^{-3}$ for our convergence threshold. This iterative procedure determines the normalization constant n_{0_α} and r_t . Once r_t is found, the concentration $c = \log_{10}(r_t/r_c)$ is determined and the total mass of the cluster M_c is obtained from

$$-\nabla\Psi(r_t) = \frac{GM}{r_t^2} . \quad (2.5)$$

The evolution of our ‘test binary’ in the cluster background is affected by long-range and short-range interactions, which modify the magnitude and direction of the binary’s velocity. The short-range encounters are accounted for by fully resolving the three-body interactions, detailed in section 2.3. We account for the velocity fluctuations due to long-range interactions with ‘field stars’, distant cluster stars, through the diffusion coefficients $D(\Delta v_i)$ and $D(\Delta v_i \Delta v_j)$ in the Fokker-Planck equation,

$$\frac{Df}{Dt} = \left(\frac{\partial f}{\partial t} \right)_{\text{enc}} = \sum_{i,j} \left\{ -\frac{\partial}{\partial v_i} (D(\Delta v_i) f) + \frac{1}{2} \frac{\partial^2}{\partial v_i \partial v_j} (D(\Delta v_i \Delta v_j) f) \right\} . \quad (2.6)$$

In this context, a diffusion coefficient $D(X)$ for a variable X , corresponds to the average change in X per unit time. Here, we focus on velocity changes per unit time as experienced by the binary due to interactions with the ‘field stars’. The form of the coefficients can be derived, for a simple case, by first considering the change in velocity of a mass m_1 , initially at rest, due to an encounter with a second mass m_2 at a relative velocity v with impact parameter p ,

$$(\Delta v)^2 = \frac{4m_1^2}{(m_1 + m_2)^2} \frac{v^2}{\left(1 + \left(\frac{p}{p_0}\right)^2\right)} , \quad (2.7)$$

where $p_0 \equiv G(m_1 + m_2)/v^2$ is a reference impact parameter which causes a deflection of $\pi/2$, consistent with close encounters (e.g., [32]). The average rate of change of the quantity in Equation 2.7, per unit time, due to encounters is then obtained by integrating over the possible impact parameters for a given density of field stars n ,

$$D(\Delta v^2) = 2\pi \int_0^{p_{\text{max}}} \Delta v^2 p n v dp , \quad (2.8)$$

up to a maximum allowable impact parameter p_{\max} . The maximum impact parameter is required to suppress the divergence of the integral and essentially determines the maximum distance of long-range encounters that contribute to the velocity perturbations. This maximum value, p_{\max} , is not explicitly specified, but finds its way into the coefficient calculations through the so-called Coulomb logarithm, $\ln \Lambda \equiv \ln(p_{\max}/p_0)$, which appears as a result of the integration.

We work out the details for the case of an isotropic velocity dispersion with a density of field stars given by Equation 2.3 and restate the relevant coefficients we use in our model (cf. [45]). These coefficients, which describe the average rate of change in the velocity of the binary due to long-range encounters, are used to update the velocity of the binary at each time step. The implementation is described further in section 2.3. A detailed derivation and a more general form of the coefficients can be found in [32].

By choosing a coordinate system in which one axis is aligned with the velocity of the binary, we can decompose $D(\Delta v_i)$ into a coefficient parallel to the binary's velocity $D(\Delta v_{\parallel})$ and two mutually orthogonal coefficients perpendicular to the velocity, $D(\Delta v_{\perp})_1$ and $D(\Delta v_{\perp})_2$. In an isotropic cluster, there is no preferred direction with regard to the two perpendicular components, so the contributions from $D(\Delta v_{\perp})_1$ and $D(\Delta v_{\perp})_2$ tend to cancel each other out. Their squares, $D(\Delta v_{\perp}^2)_1$ and $D(\Delta v_{\perp}^2)_2$, on the other hand, do not and are non-vanishing. Additionally, we include a quadratic term for the parallel component $D(\Delta v_{\parallel}^2)$ and in consideration of the symmetry we retain only the sum of the perpendicular components $D(\Delta v_{\perp}^2) = D(\Delta v_{\perp}^2)_1 + D(\Delta v_{\perp}^2)_2$.

The diffusion coefficient $D(\Delta v_{\parallel})$ parallel to the binary's motion is by analogy often referred to as the coefficient of dynamical friction as it opposes the binary's direction of motion,

$$D(\Delta v_{\parallel}) = - \sum_{\alpha} \gamma_{\alpha} \left(1 + \frac{m_b}{m_{\alpha}}\right) \int_0^v \left(\frac{v_{\alpha}}{v}\right)^2 f_{\alpha}(v_{\alpha}) dv_{\alpha} . \quad (2.9)$$

Here, m_b is the mass of the binary and $\gamma_{\alpha} \equiv (4\pi G m_{\alpha})^2 \ln \Lambda$, where we have chosen to set $\ln \Lambda = 10$, a value typical for GCs [32]. The two remaining coefficients,

$$D(\Delta v_{\parallel}^2) = \sum_{\alpha} \frac{2}{3} v \gamma_{\alpha} \left\{ \int_0^v \left(\frac{v_{\alpha}}{v}\right)^4 + \int_v^{\infty} \left(\frac{v_{\alpha}}{v}\right) \right\} f_{\alpha}(v_{\alpha}) dv_{\alpha} \quad (2.10)$$

and

$$D(\Delta v_{\perp}^2) = \sum_{\alpha} \frac{2}{3} v \gamma_{\alpha} \times \left\{ \int_0^v \left[3 \left(\frac{v_{\alpha}}{v} \right)^2 - \left(\frac{v_{\alpha}}{v} \right)^4 \right] + 2 \int_v^{\infty} \left(\frac{v_{\alpha}}{v} \right) \right\} f_{\alpha}(v_{\alpha}) dv_{\alpha} , \quad (2.11)$$

are strictly positive. These coefficients are responsible for the stochastic perturbations to the parallel and perpendicular components of the velocity, which take the binary on a random walk through velocity space and compete with the slowing due to dynamical friction. We implement these ‘random kicks’ as discrete changes to the binary’s velocity by sampling from a normalized distribution of the velocity perturbations, described in section 2.3.

Initial conditions

Evolved mass function

We obtain an initial distribution of masses in the range $0.08 M_{\odot} < m < 120 M_{\odot}$ from the broken-power-law initial mass function (IMF)

$$\xi(m) \propto \begin{cases} m^{-1.3} m_x^{0.3-x_*} & m < m_x \\ m^{-1.0-x_*} & m \geq m_x , \end{cases} \quad (2.12)$$

with $x_* = 1.35$ and $m_x = 0.55 M_{\odot}$ chosen to incorporate a Salpeter IMF [46] for masses above m_x and a Kroupa ‘correction’ [47] to masses below m_x along with a normalization factor for continuity. Stars with masses below the main-sequence turn-off, which we set to $m_{\text{to}} = 0.85 M_{\odot}$ [48], are assumed not to evolve significantly on the timescale of the simulations, while masses above m_{to} are assumed to be completely evolved according to a specified evolved mass function (EMF). The evolved mass m_e is determined by the EMF

$$m_e = \begin{cases} m_{\text{MS}} = m & 0.08 M_{\odot} < m \leq m_{\text{to}} \\ m_{\text{WD}} = 0.45 + 0.12(m - 1) & m_{\text{to}} < m < 8 M_{\odot} \\ m_{\text{NS}} = 1.4 & 8 M_{\odot} \leq m < 20 M_{\odot} \\ m_{\text{BH}} = m_{\text{BH}}(m, f_{\text{SBH}}) & 20 M_{\odot} < m < 120 M_{\odot} , \end{cases} \quad (2.13)$$

where the mass subscripts label the object type and refer to main sequence (MS), white dwarf (WD), neutron star (NS), and black hole (BH). We occasionally refer to the set of MS and WD objects as the non-compact (NC) population. The MS stars below the turnoff mass are set to their zero-age main-sequence (ZAMS) mass,

the WD stars are a linear function of their ZAMS mass [49], NS are simply set to $1.4 M_{\odot}$. Following the work of [50], the BHs are assumed to have formed from two possible channels: stars with companions that significantly affect the evolution of the star and those stars that are ‘effectively single.’ Effectively single is used to describe stars that evolve in isolation as well as those stars that evolve in wide binaries with minimal interaction. [50] estimate that $\sim 70\%$ of massive stars will have their final state impacted by a companion, which motivates setting $f_{\text{SBH}} = 0.3$ for the fraction of BHs that formed in isolation. This fraction of BHs that evolve from ‘effectively single’ stars are void of the complexities of binary stellar evolution and are assumed to lose a significant fraction of their hydrogen shells to stellar winds before collapsing to a BH. For the low metallicities typical of GCs, we approximate the mass loss, as $\sim 10\%$ of the initial mass and set $m_e = 0.9m$. The remaining 70% of BHs formed will have evolved with a companion and likely passed through a common envelope phase, stripping the stars down to their helium (He) cores [50, 51]. Using MESA [52] to evolve masses in the range $20 M_{\odot} < m < 120 M_{\odot}$, we obtained the He core mass as a function of the ZAMS mass in order to determine the remnant mass for the remaining $(1 - f_{\text{SBH}})$ fraction of BHs

$$m_e = m_{\text{He}} = 0.2312(m_{\text{ZAMS}})^{1.1797} M_{\odot} . \quad (2.14)$$

The stellar evolution performed using MESA version 6794, follows the procedure laid out in [53]. Figure 2.1 displays the resulting He core mass as a function of the ZAMS mass from the MESA runs with metallicity $Z = 5 \times 10^{-4}$, along with the power-law fit of Equation 2.14. This metallicity corresponds to the higher peak in the bimodal, GC metallicity distribution [54]. In order to properly account for the range of metallicities in our sample of clusters (see Table 2.2), we repeat the same process with $Z = 5 \times 10^{-3}$, corresponding to the secondary peak in the GC metallicity distribution. However, as this order of magnitude difference in metallicity produces He core masses differing by $\lesssim 10\%$, we rely on Equation 2.14 as a good approximation for the remnant masses in all modelled clusters.

In addition to specifying the evolved masses, it is also necessary to specify the number of NS and BH objects retained by the cluster in its static state. We specify the retained population of compact objects, comprised of NSs and BHs, through the retention fractions f_{INS} and f_{IBH} , respectively. This is necessary since we are modelling the cluster in its evolved state, a time at which many of the NS and BHs formed within the cluster have already been ejected due to formation kicks. Studies of the proper motion of pulsars suggest that NSs receive kicks in the range of

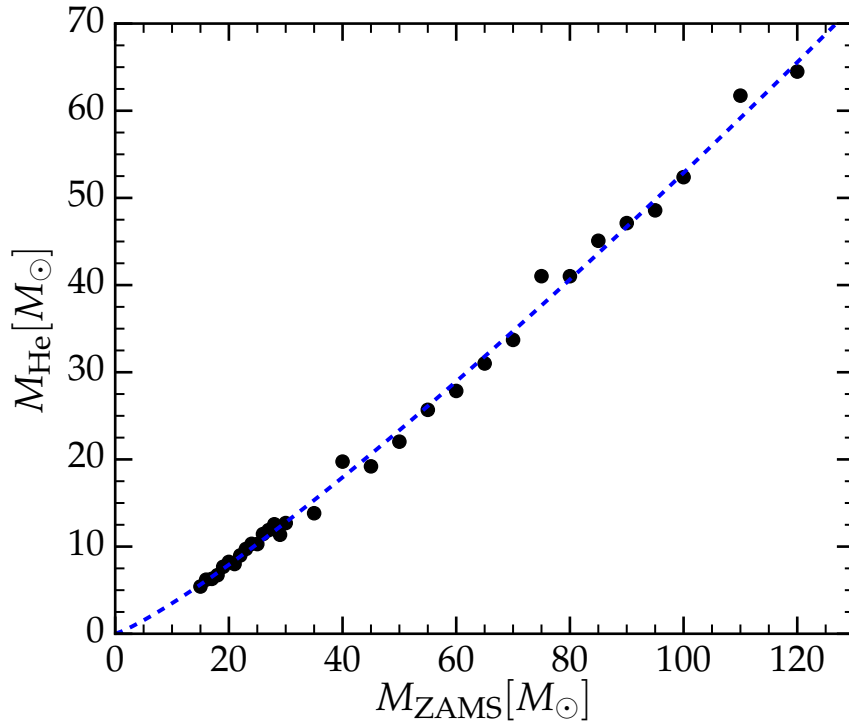


Figure 2.1: The He core mass (marked by circles) as a function of zero-age main-sequence mass from the MESA [52] runs, along with the fit (blue, dashed line) given by Equation 2.14. For the $\sim 70\%$ of BHs formed in binaries, we approximate the remnant BH mass with the He core mass of the progenitor. The remnant mass for the remaining $\sim 30\%$ of BHs is approximated by $0.9M_{\text{ZAMS}}$, which accounts for the hydrogen mass lost to stellar winds at low metallicity.

$200 - 450 \text{ km s}^{-1}$ [55], easily exceeding the typical escape velocity of clusters, which is on the order of tens of km s^{-1} . However, the observations of pulsars in GCs implies a ‘retention problem,’ since the observed fraction retained is inconsistent with the average natal kick velocities being significantly greater than GC escape velocities. This issue is somewhat reconciled by assuming some NSs form in binaries, which dampen the kick and allow the GC to maintain a hold on the NS and companion [56]. In consideration of these observations, for the case of NSs, we retain a constant fraction, $f_{\text{NS}} = 0.1$, of those produced by the IMF ([40]; [56]; [57]). In the BH case, the distribution of natal kicks is highly uncertain. Rather than take the retention fraction f_{BH} to be a constant across clusters, as in the NS case, we utilize this fraction as a free parameter in our models to control the number of retained BHs in each modelled GC.

Once we have determined the evolved masses from the IMF, the masses are binned

Mass group	$m_{\min} [M_{\odot}]$	$m_{\max} [M_{\odot}]$	$\bar{m} [M_{\odot}]$	f_m	f_n	f_L
0	0.08	0.200	0.12827	0.17531	0.42853	1.0000
1	0.20	0.350	0.26596	0.17757	0.20933	1.0000
2	0.35	0.450	0.40704	0.13954	0.10748	0.7552
3	0.45	0.600	0.51190	0.24921	0.15264	0.5763
4	0.60	0.700	0.64624	0.10020	0.04861	0.7644
5	0.70	0.850	0.76855	0.11027	0.04499	0.8233
6	0.85	1.000	0.91758	0.01161	0.00397	0.0000
7	1.00	1.200	1.08980	0.01005	0.00289	0.0000
8	1.20	1.500	1.29547	0.00527	0.00128	0.0000
9	1.50	10.00	8.87443	0.00143	0.00005	0.0000
10	10.0	40.00	20.4808	0.01261	0.00019	0.0000
11	40.0	120.0	57.1851	0.00693	0.00004	0.0000

Table 2.1: Evolved mass groups for NGC 6121 ($N_{\text{BH}} = 200$) with corresponding mass index, the lower boundary bin mass m_{\min} , the upper boundary bin mass m_{\max} , the average mass of the group \bar{m} , the fraction of the total mass in the cluster f_m , the number fraction with respect to the total number of objects in the cluster f_n , and the fraction of luminous objects in the group f_L . For reference, the BH masses occupy the top three mass groups with mean masses of $8.87 M_{\odot}$, $20.48 M_{\odot}$, and $57.18 M_{\odot}$.

into 12 groups. The small number of bins allows for a proper representation of the true distribution while keeping the computational costs to a minimum. Poisson's equation is then integrated to determine the final structural parameters as discussed in section 2.3. For illustrative purposes, the evolved mass distribution for NGC 6121 with 200 retained BHs is given in Table 2.1. The bins for each mass group, the mean mass in each bin, and the fraction of luminous objects are constant across simulations, however the mass fraction and number fraction depend on the structure of the cluster and the number of BHs.

Core density

As discussed in section 2.3, one of the free parameters in our model when specifying a cluster's structure is the core number density n_0 . However, because this parameter is not easily observable, a GC's density is often reported in terms of a central luminosity density ρ_L . For each mass group we determine a central luminous number density $n_{L\alpha} = f_{L\alpha} \bar{n}_{\alpha}$, where $f_{L\alpha}$ and \bar{n}_{α} are the fraction of luminous objects and the core density, respectively, of mass group α . The central luminosity density is then given by $\rho_L = \sum_{\alpha} L_{\alpha} n_{L\alpha}$. In order to account for the variability in the mass-luminosity relation with stellar mass, we use a parameterized luminosity for each group of the

form $L_\alpha = a(m_\alpha)^b$, with luminosity coefficients $a = 0.23, b = 2.3$ for $m_\alpha < 0.43 M_\odot$ and $a = 1.0, b = 4.0$ for the remaining luminous objects [58]. To ensure that our clusters appropriately model the Milky Way GCs of interest, we compute ρ_L for each integrated cluster and adjust n_0 accordingly to match the observed quantity.

Binary fraction

In order to account for the uncertainty in the size of the binary population within a cluster, we allow for a specifiable binary fraction. The fraction of objects that are binaries is

$$f_b = \frac{N_b}{N_s + N_b}, \quad (2.15)$$

where N_s and N_b are the number of single objects and binary objects, respectively, and the total number of objects in our model clusters is then $N = N_s + 2N_b$. Observations of the binary fraction are limited to the luminous objects within the cluster. Due to this restriction, we take the observed fraction to be determined solely by the MS star binary fraction $f_{\text{obs}} = N_{\text{MS}_b} / (N_{\text{MS}_s} + N_{\text{MS}_b})$, where, as above, we respectively refer to N_{MS_s} and N_{MS_b} as the number of single and binary MS stars. Using the above definitions along with the fraction of all binaries that are MS-MS binaries, $f_{\text{MS}_b} = N_{\text{MS}_b} / N_b$, and the fraction of objects that are MS stars, $f_{\text{MS}} = N_{\text{MS}} / N$, we convert the observed binary fraction into a uniform total binary fraction for use in our models through the relation

$$f_b = \left(\frac{f_{\text{MS}_b} (f_{\text{obs}} + 1)}{f_{\text{MS}} f_{\text{obs}}} - 1 \right)^{-1}. \quad (2.16)$$

The number of MS stars N_{MS} is determined solely by the IMF and for the simulations in this study we use $f_{\text{MS}_b} = 0.23$ [59]. We perform our simulation with f_{obs} covering a range of values, consistent with theoretical findings, between 5 to 10% [60], and with observational constraints, between 5 to 20% [61]. We complete an approximately equal number of simulations for f_{obs} taking values from the set $\{0.05, 0.10, 0.20\}$. However, we find that this parameter has a negligible effect on the quantities of interest, so for conciseness, it is not specified in the simulation parameters.

Modified black-hole velocity dispersion

Recent studies of BH retention in GCs have shown clusters initially retain between 65 – 90% of the BHs formed in cluster, with the remainder being lost due to formation kicks [62]. This is in contrast to the long-standing belief that present-day GCs should

be nearly void of BHs. In addition to the increase in retention, [62] also found that the retained BHs remain well-mixed with the non-BH population. Follow-up studies support the idea of a large population of BHs that are spread throughout the cluster and are consistent with a recent 10^6 N -body simulation [13].

In the standard King model, it is common to assume that the mass groups satisfy an equipartition of energy. Specifically,

$$m_\alpha \sigma_\alpha^2 = \bar{m} \bar{\sigma}^2, \quad (2.17)$$

where m_α and σ_α are the mass and velocity dispersion of mass group α , \bar{m} is the mean mass of all objects in the cluster, and $\bar{\sigma}$ is the mean velocity dispersion. However, with this equipartition of kinetic energy amongst all mass groups, the heavier objects then necessarily have lower random velocities compared to the lighter objects and become trapped deep in the gravitational potential at the core of the cluster. With an equipartition of kinetic energy in place, the much more massive BHs densely populate the central region of the cluster, driving the core radius to a small fraction of the tidal radius. This disparity between the core radius and tidal radius leads to concentrations that deviate from observations, limiting the modelled clusters to supporting only a small number of BHs. In order to generate clusters with a significant BH population that are still representative of observed GCs, motivated by [62], we implement a velocity dispersion for the BHs away from energy equipartition. We maintain an equipartition of energy among the lower-mass objects and use a modified energy partitioning for the BHs of the form

$$m_\beta \sigma_\beta^2 = \frac{\sum m_\beta}{\sum m_\alpha} \frac{1}{f_s} \bar{m} \bar{\sigma}^2, \quad (2.18)$$

where the indices β and α label the mass groups corresponding to BHs and non-BHs, respectively. Here, f_s is a specifiable scale factor of order unity. The f_s parameter is enough to rescale the velocity dispersion for the BHs, however, the factor involving the mass ratio contributes substantially and f_s remains of order unity and does not vary wildly across the GCs we consider.

With this modified BH velocity dispersion in place, we find that we can match the observed structural parameters of a specific cluster for zero BHs up to ~ 20 BHs, in the case of more massive clusters up to ~ 100 BHs, and in the most massive clusters up to ~ 1000 BHs. We vary the number of BHs residing in the cluster by adjusting the scale factor f_s in Equation 2.18 and the fraction retained, f_{TBH} , introduced in section 2.3. To illustrate the spreading of the BHs, we present in Figure 2.2 the

radial density profiles for the BHs and the non-BH objects for different populations of retained BHs in the cluster model representing NGC 6656. In the case of minimal BH retention, the BH number density falls off quickly outside of the core, which for our model of NGC 6656 is located at $r_c = 0.73$ pc and is marked by a vertical line in Figure 2.2 for reference. However, in the case of many BHs, the modified velocity dispersion extends the number density profile radially, spreading the BHs throughout the cluster, without affecting the central density. The distribution of non-BH objects is largely unaffected by the change in BH numbers.

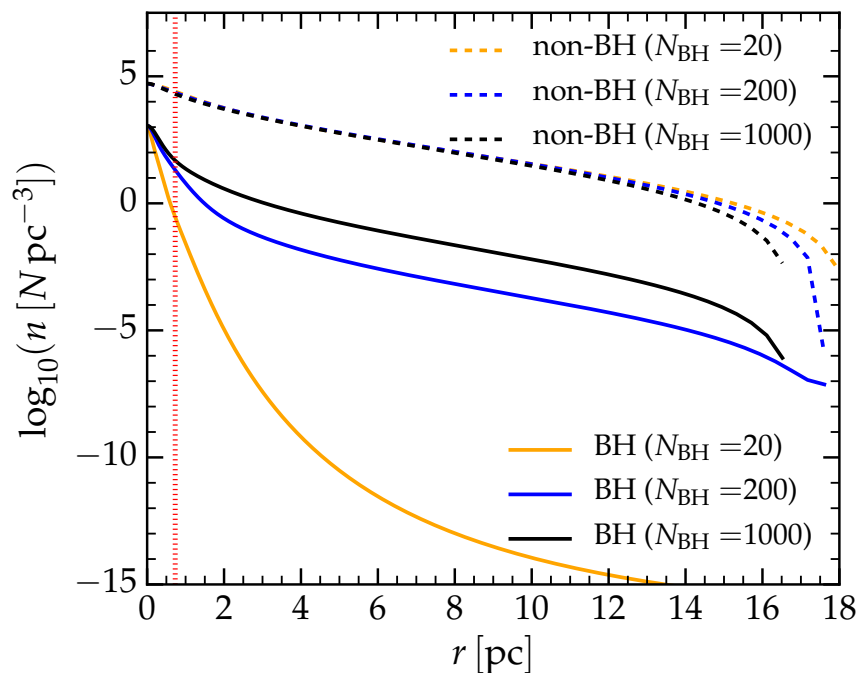


Figure 2.2: Radial number density profiles for the BH subgroup (solid lines) and the non-BH objects (dashed lines) in NGC 6656 for the three considered values of N_{BH} . The vertical line (red, dashed), at $r_c = 0.73$ pc, marks the core radius for this cluster. The non-BH objects are largely unaffected by the different numbers of BHs added to the cluster and the necessary modification to the velocity dispersion. For $N_{\text{BH}} = 20$, the BHs are concentrated in the core region, whereas to accommodate $N_{\text{BH}} \geq 200$, the modified velocity dispersion spreads the BHs throughout the cluster with a profile similar to that of the non-BH objects.

Binary initialization

We choose the initial masses for our ‘test binary’ by randomly sampling from the evolved mass distribution and reject those that do not contain at least one BH. If

one of the component masses falls within a mass bin with a non-zero luminous population, we then sample from the luminous mass fraction to determine whether the low-mass object is an MS star or WD. Additionally, if the selected mass is in the turnoff group, $0.63 M_{\odot} \leq m \leq 0.8 M_{\odot}$, then the object is chosen to be a giant with probability $P = 0.095 f_L$, where f_L is the luminous fraction for the turnoff-mass group. The probability for giants is adopted from [40] and represents the approximate fraction of the cluster age that giants in this mass range survive. Once the masses and object types are established, the BH radii are set to the Schwarzschild radius $R_{\text{BH}} = 2GM/c^2$, while the stellar radii are determined as described in [40]. The eccentricity of the binary e is specified by sampling from the probability density function $f(e) = 2e$ [63], commonly referred to as a ‘thermal’ eccentricity distribution. The semi-major axis a is obtained from a distribution uniform in $\log_{10} a$ in the range $-3 \leq \log_{10}(a \text{ au}^{-1}) \leq 1$. To avoid an immediate merger of the objects in our initial binary, we enforce $a > f_{\text{tid}}(R_1 + R_2)/(1 - e)$, where R_i are the radii of each component of the binary and $f_{\text{tid}} = 3.1$, by letting $a \rightarrow 2a$ until this condition is satisfied. The factor f_{tid} is chosen based on the separation at which tidal effects would induce a merger [64]. Once the binary parameters are set, we sample the primary-mass number density profile $n_{\alpha}(r)$ to determine the binary placement within the cluster and obtain a velocity from the primary-mass velocity distribution function at r .

Evolution of the ‘test binary’

Once we have an appropriate model, which satisfies the structural parameters for a specific cluster and an initial binary, we then evolve this single binary within the cluster background. In addition to the static potential, we include the interaction terms discussed in section 2.3. To account for dynamical friction, the diffusion coefficient $D(\Delta v_{\parallel})$ is added to the potential gradient to create a smooth effective acceleration $\mathbf{a}_{\text{eff}} = \nabla\Psi(r) + D(\Delta v_{\parallel})$. This smooth force is integrated using a 4th order Runge-Kutta integrator, which is discussed in detail in section 2.3. The quadratic scattering terms, or random ‘kicks’, are implemented by discretely updating the corresponding velocity components at each time step Δt . As discussed in section 2.3, the diffusion coefficient for Δv^2 , of the form $D(\Delta v^2)$, represents the change in this quantity per unit time, i.e. $\Delta v^2/\Delta t$. We update the velocity at each time step by

sampling from the normal distribution of kicks through

$$\begin{aligned}
 \Delta v_{\parallel} &= X \sqrt{D(\Delta v_{\parallel}^2) \Delta t} , \\
 \Delta v_{\perp 1} &= Y \sqrt{\frac{1}{2} D(\Delta v_{\perp}^2) \Delta t} , \\
 \Delta v_{\perp 2} &= Y \sqrt{\frac{1}{2} D(\Delta v_{\perp}^2) \Delta t} ,
 \end{aligned}
 \tag{2.19}$$

where X and Y are random numbers with mean values of zero and standard deviations of one.

At each time step, we also consider the evolution of the binary’s semi-major axis a and its eccentricity e due to gravitational wave (GW) emission. If the BH is in a binary with another compact object — which includes BHs, NSs, and WDs — then we implement the evolution of a and e according to the gravitational radiation formalism of [65]. In these cases, we also calculate the time until coalescence t_d due to the decay of a , and if this will occur within the current time step, $t_d < \Delta t$, we consider this a GW merger. If the merger is of a BH-BH or BH-NS binary, we add a recoil velocity, or ‘kick’, based on the fits to numerical relativity simulations given by [66] with initial spin magnitudes and orientations assigned as in Clausen, Sigurdsson, and Chernoff [67].

Short-range encounters

As the binary moves throughout the cluster, at each time step, we check for the possibility of a short-range encounter with a single star. Since the effects of long-range interactions are accounted for by the diffusion coefficients (section 2.3), here we focus on capturing the effects due to strong three-body interactions with much smaller impact parameters. We limit the range of encounters to include only those three-body interactions that result in a resonance, exchange, ionization, or the occasional flyby. We accomplish this by choosing the maximum impact parameter to be

$$p = a[B + C(1 + e)] , \tag{2.20}$$

where we have set $B = 4$ and $C = 0.6$ following [68]. The choice of these coefficients is intended to limit the number of weak encounters that have minimal impact on the binary, as these still require full resolution of the encounter, which is one of the more computationally intensive tasks during evolution. However, the coefficients only provide an approximate contour in the space of initial conditions, hence the

occasionally flyby. The cross section for an encounter to take place between the binary and a star of mass m_α with velocity \mathbf{v}_α is

$$\sigma(\mathbf{v}, \mathbf{v}_\alpha) = \pi p^2 + \frac{2\pi G(m_b + m_\alpha)p}{|\mathbf{v} - \mathbf{v}_\alpha|^2}, \quad (2.21)$$

(see, e.g., [32]). We then calculate the expected encounter rate between the binary and each mass group

$$\Gamma(r, v, \alpha) = \int \sigma(\mathbf{v}, \mathbf{v}_\alpha) |\mathbf{v} - \mathbf{v}_\alpha| f_\alpha(v_\alpha) dv_\alpha, \quad (2.22)$$

and from this assign the probability of interacting with mass group α to be

$$P_\alpha = \Gamma(r, v, \alpha) \Delta t. \quad (2.23)$$

An encounter is deemed to have occurred, based on a random generated number Z from a uniform distribution between 0 and 1, if Z is less than the total probability $P = \sum_\alpha P_\alpha$. The total probability is implicitly constrained to be less than unity by controlling the time-step size Δt , which is discussed in more detail in the subsequent section. In the case that $Z < P$, we select the third star m_3 based on the relative probabilities P_α and initiate our three-body integration scheme explained in section 2.3.

Time stepping

We use a 4th order Runge-Kutta integrator to evolve the effective acceleration introduced in section 2.3 as well as the three-body interactions described in section 2.3. During integrations, we utilize a time step reduction scheme requiring that the accuracy of the solution does not vary by more than a tolerance of $\epsilon_{\text{rk}} = 10^{-5}$ when the time step is halved. The initial integration time step $\Delta t = \lambda(1+r)/(1+v)$ is dynamically determined to account for the position and velocity of the binary in the cluster, with $\lambda = 0.1$ chosen to produce a time step that is a fraction of the core dynamical time $r_c/\bar{\sigma}$ for a binary at rest in the core. This time stepper accounts for the higher density in the core and the enlarged cross section at small velocities. Although this choice of time step is usually sufficient, some extra care needs to be taken when using Δt in Equation 2.23 to determine the encounter probability, so that the total probability does not exceed unity. To ensure that we correctly sample the encounter probabilities, by satisfying the constraint $P \ll 1$, we set $P_{\text{max}} = 0.1$ and enforce $P < P_{\text{max}}$ by reducing the time step Δt when necessary. For the case $P > P_{\text{max}}$, we decrease the succeeding time step by letting $\lambda \rightarrow 0.9(P_{\text{max}}/P)\lambda$.

During the subsequent step, if $\lambda < \lambda_0$, where $\lambda_0 = 0.1$ is the fiducial value, and $P < P_{\max}$, we allow the time step to increase slowly by setting $\lambda \rightarrow 1.1\lambda$. Once $\lambda > \lambda_0$ and the probability is satisfactorily small, which often occurs once the binary migrates out of the problematic dense region, we reset the time step factor to $\lambda = \lambda_0$.

Three-body interactions

In the case of an encounter, the relative probabilities described in section 2.3 determine the mass and velocity of the third object. We take this sampled velocity v_3 to be the velocity of the third body at infinity and calculate the relative velocity at infinity for the encounter from $v_\infty = |\mathbf{v} - \mathbf{v}_3| = \sqrt{v^2 + v_3^2 - 2vv_3 \cos\chi}$. Given v and the sampled m_3 and v_3 , the relative velocity at infinity is determined up to the $\cos\chi$ term, which for an isotropic King model distribution function can be sampled from an analytic expression for $\chi \in [0, \pi]$ as in [40]. With the mass of the third body and the relative velocity known, the maximum impact parameter is obtained from the cross section for the encounter

$$\pi p_{\max}^2 = \sigma(\mathbf{v}, \mathbf{v}_3) = \pi p^2 \left(1 + \frac{2G(m_b + m_3)}{pv_\infty^2} \right), \quad (2.24)$$

with p defined in Equation 2.20. The actual impact parameter for the encounter is sampled from a uniform distribution in the area spanned by the maximum impact parameter πp_{\max}^2 . The angles that comprise the remaining free variables necessary to specify the initial conditions are the projected true anomaly f of the binary at the time that the incoming third body reaches pericentre, two angles θ and ϕ specifying the initial location of the third body with respect to the binary centre-of-mass, and the impact orientation ψ , which specifies the angle of the impact parameter in a plane transverse to the incoming velocity of the third body. These four angles are sampled in a manner consistent with [68]. With the initial conditions specified, the explicit integration is performed with a modified scheme based on [69].

We modify the original method of a fixed initial distance of the third star, at $R_{\text{in}} = 20a$, to one of variable distance to improve efficiency and to prevent the case of long three-body interactions that can exceed the cluster time step. The addition of massive BHs introduces the possibility for wide binaries with orbital separations much greater than those for which the previous method was suited to handle. With a fixed choice for the distance of the third star from the binary, interactions such as distant flybys, which are the quickest to resolve computationally and have little impact on the binary, often take a time that exceeds the cluster evolution time step and leads to the possibility of missing other probable encounters.

To represent the three-body system as an isolated one, and to reduce excessive time spent integrating long approaches, we require that $R_{\text{in}} \leq R_{\text{max}}(n)$, where $R_{\text{max}}(n) = (4\pi n/3)^{-1/3}$ is the ‘interparticle’ distance and is a function of the local density $n(r)$. Once R_{in} is specified, we determine the relative velocity v_{in} at R_{in} based on the relative velocity at infinity. With these two quantities specified, we approximate the time for a flyby as $\delta t = 2R_{\text{in}}/v_{\text{in}}$. For the case in which $\delta t > \Delta t$, we let $R_{\text{in}} \rightarrow (\Delta t/\delta t)R_{\text{in}}$, calculate v_{in} at the new initial distance and recompute the new estimated time. We repeat this procedure until the estimated time is roughly the same as the cluster time step, $0.9 < \delta t/\Delta t < 1.1$. One important caveat is that this could lead to placing the third object too close to the binary, spoiling the assumption of an object at infinity approaching a well defined binary. To address this issue, we maintain one extra condition on the initial distance specification, a consideration for which we are willing to forgo our time step restrictions: that $(a/R_{\text{in}})^3 \leq 0.01$.

To increase the speed of the three-body integration, we move from a constant integration time step to one that is dynamical. We choose a maximum time step δT_{max} to be an arbitrarily small fraction $\epsilon = 6.25 \times 10^{-3}$ of the binary period T_{b} , i.e. $\delta T_{\text{max}} = \epsilon T_{\text{b}}$. At the end of each integration step, we update the time step to $\delta T = \epsilon(r_{\text{min}}/v_{\text{max}})$, where r_{min} is the minimum separation between any pair of the three objects and v_{max} is the largest velocity of the three bodies. This sets the time step to the maximum allowable value in consideration of the need to resolve the dynamics of the three objects or any potentially bound pair. In some instances, a resonance can form a temporarily bound triple system, causing the integrator to reach the maximum number of steps $N_{\text{max}} = 2 \times 10^6$ or to exceed the arbitrarily specified maximum allowable time of $5\Delta t$. Under these rare circumstances, we reinitialize the system with newly sampled initial angles and restart the integration. In addition to the occasional long-lasting semi-stable triples that form, there are also instances when a binary makes its way to the core where the average timescale necessary to resolve the three body encounters begins to approach the timescale for the evolution of the binary in the cluster. Since we calculate three-body encounters decoupled from the binary’s evolution in the cluster, we are forced to terminate the run in such cases. As the cluster timescale is inversely proportional to the cluster density, this situation is most likely to occur in the densest clusters. As a result of this timescale termination criterion, although a similar number of realizations are performed for each cluster, the highest density clusters have noticeably fewer runs than the lower density clusters, as is observable in the rightmost column of Table 2.2. For standard encounters, which are often much shorter than the cluster time step, we

periodically check whether the interaction has resolved — according to the criteria discussed in the following section — and in the case that a new binary has formed, even temporarily, we update δT_{\max} with the period of this new binary.

Encounter resolution

We first identify a potential binary among the triple system composed of the original binary, m_1 and m_2 , and the third mass m_3 , by selecting the pair with the largest gravitational binding energy. We refer to the masses in the potential binary as \bar{m}_1 and \bar{m}_2 , which may no longer correspond to the original binary composed of m_1 and m_2 . The remaining object, which is not part of the potential binary, is labelled \bar{m}_3 which is distinct from m_3 . All unbarred variables represent the initial configuration where the third object is incoming, while barred variables refer to the system where a binary has been identified and the encounter is nearly resolved. The encounter can be resolved in three ways: (I) there is a well defined bound binary system with the third object unbound and moving off to infinity, (II) a merger has occurred or (III) the system is completely ionized.

For case (I), we terminate the integration once the following criteria are all satisfied: (i) the third body has achieved the minimum required separation from the binary, $|\bar{r}_3 - (\bar{m}_1\bar{r}_1 + \bar{m}_2\bar{r}_2)/(\bar{m}_1 + \bar{m}_2)| > \max\{R_{\max}(n), 1.1 R_{\text{in}}\}$, (ii) the eccentricity \bar{e} of \bar{m}_1 and \bar{m}_2 is less than unity, (iii) \bar{m}_1 and \bar{m}_2 are bound, specifically $\bar{E}_b < 0$, and (iv) \bar{m}_3 is unbound, i.e. $\bar{E}_3 > 0$. Here, \bar{E}_b is the total energy of the final binary and \bar{E}_3 is the total energy of the third body. In addition to the above requirements, to determine the final state of the ‘isolated’ binary, we continue the integration until the total potential energy between \bar{m}_3 and each mass in the binary is a fraction of the total energy of the system E , specifically

$$\frac{G\bar{m}_1\bar{m}_3}{|\bar{r}_1 - \bar{r}_3|} + \frac{G\bar{m}_2\bar{m}_3}{|\bar{r}_2 - \bar{r}_3|} > 0.05E . \quad (2.25)$$

In case (II), two of the bodies merge and the third body is either unbound or forms a new binary with the merger product. The criteria for mergers is based on the distance of nearest approach d between two bodies during the three body encounter. In the case of a potential merger between two BHs, the merger criterion is $d \leq R_1 + R_2$. For the remaining merger situations, the criterion remains $d = f_{\text{tid}}(R_1 + R_2)$, as adopted from [40], using the same value for f_{tid} as introduced in section 2.3. Our choice for f_{tid} was selected as it approximately separates the boundary of where hydrodynamical effects become important (e.g., [64]; [70]). When this criterion

Name	M [M_{\odot}]	σ^2 [cm^2s^{-2}]	ρ_L [$L_{\odot}\text{pc}^{-3}$]	c	Z	N_{BH}	N_{runs}
Pal 13	5.12×10^3	8.10×10^9	1.45	0.66	2.6×10^{-4}	20	15232
NGC 6838	3.67×10^4	5.29×10^{10}	6.76×10^2	1.15	3.3×10^{-3}	20	18364
						200	20430
NGC 6535	5.93×10^4	5.76×10^{10}	5.19×10^2	1.33	3.2×10^{-4}	20	35865
						200	33561
NGC 6362	1.17×10^5	7.84×10^{10}	1.95×10^2	1.09	2.0×10^{-3}	20	32544
						200	33798
NGC 5053	1.66×10^5	1.96×10^{10}	3.47	0.74	3.8×10^{-5}	20	69058
						200	74681
NGC 6121	2.25×10^5	1.60×10^{11}	4.37×10^3	1.65	1.4×10^{-3}	20	14429
						200	17884
						1000	24667
NGC 5694	2.92×10^5	3.36×10^{11}	8.91×10^3	1.89	2.1×10^{-4}	20	14029
						200	13382
						1000	17445
NGC 6093	3.67×10^5	1.54×10^{12}	6.17×10^4	1.68	3.6×10^{-4}	20	7435
						200	7019
						1000	4645
NGC 5286	4.80×10^5	6.56×10^{11}	1.26×10^4	1.41	4.1×10^{-4}	20	6761
						200	10032
						1000	8196
NGC 6656	5.36×10^5	6.08×10^{11}	4.27×10^3	1.38	4.0×10^{-4}	20	12539
						200	20993
						1000	14832
NGC 1851	5.61×10^5	1.08×10^{12}	1.23×10^5	1.86	1.3×10^{-3}	20	7189
						200	6950
						1000	4563
NGC 6205	6.27×10^5	5.04×10^{11}	3.55×10^3	1.53	5.9×10^{-4}	20	13444
						200	24899
						1000	23583
NGC 6441	1.30×10^6	3.24×10^{12}	1.82×10^5	1.74	7.0×10^{-3}	20	2388
						200	2439
						1000	2463
NGC 104	1.45×10^6	1.21×10^{12}	7.59×10^4	2.07	3.8×10^{-3}	20	9545
						200	10467
						1000	8559
NGC 5139	2.64×10^6	2.82×10^{12}	1.41×10^3	1.31	5.9×10^{-4}	20	13197
						200	17466
						1000	23513

Table 2.2: Summary of simulations. Listed are the 15 GCs modelled for evolution along with the total cluster mass M_c , squared velocity dispersion σ^2 , the luminous core density ρ_L , concentration c , and metallicity Z . The clusters are ordered by total mass. There are 39 independent models after taking into account the number of BHs retained by the cluster. Medium to high mass clusters can accommodate large BH populations without disrupting the listed structural parameters. The size of the BH population in lower-mass clusters is either (1) limited in number by the IMF or (2) by the ability of the cluster to maintain the model structural parameters in their presence; in these cases, the cluster is not used for evolutions and is omitted from the table. In the final column we list the total number of evolutions performed for each case.

is met, we assume a tidal encounter takes place. The merger is assumed to be a momentum conserving, impulsive, completely inelastic collision with no mass loss [71]. When a merger occurs between the BH companion and the third body, if the merger product remains bound to the BH, this dynamically formed binary becomes our new ‘test binary’, which we continue to follow and evolve within the cluster. Similarly, if the BH merges with a third body and we still have a bound binary system, we again continue to follow this binary. However, if the BH becomes unbound by merging with another body or becomes unbound from a merger product, we handle the newly single BH as described in the subsequent section. In each of these cases, the position of the new binary, or single BH, is updated by continuing along the original binary trajectory and the velocity is updated by converting from the three-body centre-of-mass frame, where the three-body integration is performed, back to the cluster frame.

The result of the encounter can also end in complete ionization, case (III). Ionization occurs in the case of ill-defined binaries that will inevitably be unbound if, given that all previous criteria are satisfied, either (a) the eccentricity of \bar{m}_1 and \bar{m}_2 satisfies $1 - \bar{e} < 1 \times 10^{-7}$ or (b) $|\bar{r}_1 - \bar{r}_2| > R_{\max}(n)$ is satisfied. Additionally, ionization occurs if $\bar{m}_i \bar{v}_i^2 > 2(\bar{m}_i \bar{m}_j / |\bar{r}_i - \bar{r}_j| + \bar{m}_i \bar{m}_k / |\bar{r}_i - \bar{r}_k|)$ is true for all masses at any time, with $i \neq j \neq k$ taking on values $\{1, 2, 3\}$. This last criterion is a straightforward definition for a totally unbound triple. In addition to these choices for ionization during three-body encounters, there is one other instance in which the binary can be dissociated. For very wide binaries, the encounters are dominated by repeated grazing encounters with low mass stars, which tend to further widen the orbital separation. As a result, strong interactions become less likely and the binary will inevitably be dissociated by the increasing occurrence of these slowly ionizing encounters. For this reason, we use the encounter rate to define a maximum semi-major axis of dynamically formed binaries as

$$a_{\max}(\Gamma) = \left(\frac{Gm_b}{3(2\pi\Gamma)^2} \right)^{1/3}, \quad (2.26)$$

which is equivalent to requiring a minimum of three orbits between encounters. Here, the total encounter rate $\Gamma = \sum_{\alpha} \Gamma(r, v, a)$ is a sum over the rate associated with each mass group defined by Equation 2.22). The final criterion for ionization is then $a > \min\{a_{\max}(\Gamma), R_{\max}(n)\}$.

Single black holes

As described in the previous section, a BH can become single due to three-body dynamics such as exchange, merger, or through the dismantling of a binary that exceeds our large a or large e criteria. In the case of a single BH, we allow for the solitary BH to form a new binary by interacting with existing binaries within the cluster.

In order to accomplish this, we need to know the probability for the following encounter,

$$(m_1, m_2) + m_{\text{BH}} \rightarrow (m_{\text{BH}}, m_2) + m_1, \quad (2.27)$$

in which the BH exchanges with m_1 into a binary originally composed of masses m_1 and m_2 . We also consider the possibility that m_{BH} and m_2 undergo an exchange, which contributes to the total probability that the BH will exchange into the binary. However, for conciseness in deriving the probability of exchange, we will focus specifically on the encounter described by Equation 2.27, later adding the contribution from the reaction where the subscripts are interchanged. Unfortunately, we can no longer compute the probability for encounter as in section 2.3, since we do not possess a distribution function for binaries. However, by considering the reverse reaction of Equation 2.27, given by

$$(m_{\text{BH}}, m_2) + m_1 \rightarrow (m_1, m_2) + m_{\text{BH}}, \quad (2.28)$$

and relating this to the one of interest, we can obtain the encounter probability for the BH to exchange into an existing binary in the same way that we compute encounters for a binary composed of a BH and a companion.

We use the seminumerical fit of [72],

$$\bar{\sigma}_{1,2} = \left(\frac{M_{23}}{M_{123}}\right)^{1/6} \left(\frac{m_3}{M_{13}}\right)^{7/2} \left(\frac{M_{123}}{M_{12}}\right)^{1/3} \left(\frac{M_{13}}{M_{123}}\right) g(2, 3, 1), \quad (2.29)$$

as the dimensionless cross section for a generically labelled single mass m_3 to exchange into a binary of masses m_1 and m_2 to form a new binary composed of m_3 and m_2 , with m_1 being ejected. In this notation, uppercase masses represent the sum of the mass subscripts, i.e. $M_{ij} = m_i + m_j$. The coefficient $g(2, 3, 1)$ is a numerical fitting factor designed to improve the analytically derived fit. This dimensionless cross section $\bar{\sigma}_{1,2}$ is related to the dimensionful cross section for exchange $\Sigma_{1,2}$ through

$$\bar{\sigma}_{1,2} = \frac{2|\mathbf{v}_{1,2} - \mathbf{v}_3|^2}{\pi G M_{123} a_{1,2}} \Sigma_{1,2}. \quad (2.30)$$

The existing binaries that the BH is likely to encounter, which have remained intact in the cluster over long timescales, can be considered ‘hard’. These ‘hard’ binaries are characterized by having a binding energy U_{bin} that exceeds the average energy of the other stars in the cluster $|U_{\text{bin}}| > \frac{1}{2}\bar{m}\bar{\sigma}^2$ and this is what allows them to stay intact over such long timescales. In this case, we approximate the total encounter cross section by the dominant gravitational focusing term in Equation 2.21, explicitly:

$$\sigma_{1,2} \simeq \frac{2\pi GM_{123}a_{1,2}}{|\mathbf{v}_{1,2} - \mathbf{v}_3|^2} . \quad (2.31)$$

Finally, relating Equation 2.30 and Equation 2.31 allows us to express the cross section for exchange in terms of the total encounter cross section $\sigma_{1,2}$ through

$$\Sigma_{1,2} = (\bar{\sigma}_{1,2}/4)\sigma_{1,2} . \quad (2.32)$$

Evidently, the dimensionless cross section for exchange is related to the fractional probability that the total encounter ends in the specific exchange we previously described. Considering Equation 2.31 and assuming the relative velocities are similar for the forward and reverse reactions, we can relate the forward and backward total cross sections through $\sigma_{1,2} = (\frac{a_{1,2}}{a_{2,3}})\sigma_{2,3}$. Since the energy given to the binary is comparable to the energy required to destroy it, $m_1m_2/a_{1,2} \sim m_2m_3/a_{2,3}$, we can recast the relation in terms of the masses alone:

$$\sigma_{1,2} = \left(\frac{m_1}{m_3}\right)\sigma_{2,3} . \quad (2.33)$$

The cross section for the specific exchange of m_3 for m_1 in terms of the total encounter cross section of the original binary is found by substituting Equation 2.33 into Equation 2.32, yielding

$$\Sigma_{1,2} = \left(\frac{\bar{\sigma}_{1,2}m_1}{4m_3}\right)\sigma_{2,3} . \quad (2.34)$$

By writing the exchange probability in terms of the post-exchange binary, we can now utilize the same procedure described in section 2.3. In this formalism, m_3 represents the BH and we return to referring to this body as m_{BH} , while m_1 goes to m_α , a variable companion used for computing the relative probabilities for each mass group α . First we select a companion object m_2 for the BH on the left-hand side of Equation 2.28. We obtain m_2 by sampling from the local number density and determine a and e for the binary as in section 2.3. The probability of the encounter described by Equation 2.27, where the BH exchanges places with m_α in a binary composed of m_2 and m_α is then,

$$P_{\alpha,2} = \Delta t \int \left(\frac{\bar{\sigma}_{\alpha,2}m_\alpha}{4m_{\text{BH}}}\right)\sigma_{2,\text{BH}}(\mathbf{v}, \mathbf{v}_\alpha)|\mathbf{v} - \mathbf{v}_\alpha|f_\alpha(v_\alpha)dv_\alpha . \quad (2.35)$$

The usefulness of the manipulations in this section is most clearly seen by writing this in terms of Equation 2.23:

$$P_{\alpha,2} = \left(\frac{\bar{\sigma}_{\alpha,2} m_{\alpha}}{4m_{\text{BH}}} \right) P_{\alpha}, \quad (2.36)$$

which in practice makes computing the exchange probabilities as easy as rescaling our standard encounter computations by the parenthetical factor. Since we also allow for the BH to exchange with m_2 , we also consider the probability $P_{2,\alpha} = \left(\frac{\bar{\sigma}_{2,\alpha} m_2}{4m_{\text{BH}}} \right) P_2$.

We apply one final rescaling to account for the density of binaries that are of type m_2 and m_{α} . We assume that the fraction of objects that are binaries f_b is constant throughout the cluster with the value specified by Equation 2.16. The density of binaries is then $n_b(r) = \left(\frac{f_b}{1+f_b} \right) n(r)$, which is derived from Equation 2.15. Additionally, we also assume that the fraction of binaries of a given type is constant at all cluster radii, $n_{ij}(r) = f_{i/j} n_b(r)$. Here, $f_{i/j}$ represents the fraction of binaries that have a star of type i and a star of type j , e.g. $f_{\text{NS/MS}}$ is the fraction of all binaries that are composed of an NS and an MS star. For binaries composed of only MS or WD we use values of $f_{\text{MS/MS}} = 0.23$, $f_{\text{MS/WD}} = 0.44$, and $f_{\text{WD/WD}} = 0.32$ [59]. The remaining one percent of binaries contain at least one BH or NS, for which we compute the binary fraction through $f_{i/j} = 0.01 \left(\frac{N_i}{N} \right) \left(\frac{N_j}{N_{\text{BH+NS}}} \right)$, where i can be any object type, j is limited to BH or NS, N is the total number of objects in the cluster, and $N_{\text{BH+NS}}$ is the total number of BHs and NSs.

The final total probability for the BH to exchange into a binary, given the sampled mass m_2 , is then

$$P_{\text{exch}}(r) = \sum_{\alpha} n_{\alpha 2}(r) \left(\frac{P_{\alpha,2}}{n_{\alpha}(r)} + \frac{P_{2,\alpha}}{n_2(r)} \right). \quad (2.37)$$

Here we divide out the respective local density picked up in the integration of the distribution function in order to enforce our assumption of a uniform binary fraction. If an exchange is determined to occur based on this total probability, we select a specific binary for the encounter based on the relative probabilities of exchange for each mass group m_{α} . With a binary in hand, we initiate our three-body system, which is run until we get the proper outcome dictated by the encounter cross section — i.e. that m_{BH} exchanges with the appropriate mass in the binary.

2.4 Simulations

We present 698,486 realizations from 15 GC models with total masses in the range of $5.12 \times 10^3 - 2.64 \times 10^6 M_{\odot}$, velocity dispersions covering $9 \times 10^4 - 1.8 \times 10^6 \text{ cm s}^{-1}$, core densities of $1.45 - 1.23 \times 10^5 \text{ pc}^{-3}$, and concentrations spanning 0.66 – 2.07.

The simulations are summarized in Table 2.2, which includes the catalogue name for the modelled cluster, total mass, velocity dispersion squared, central luminosity density, concentration, metallicity, the number of retained BHs in the model, and the total number of completed runs. The simulations are run for $t = 10^{10}$ years or until the single/binary is ejected from the cluster, when $r > r_t$.

Structural parameters

In our framework, a GC's structure is determined by four parameters: the total cluster mass M_c , the core velocity dispersion σ , the core luminosity density ρ_L , and the concentration c . [73] finds that GCs described by single-mass isotropic King models are fully defined by four independent physical parameters: the mass-to-light ratio $\Upsilon_{v,0}$, total binding energy E_b , central concentration c , and total luminosity L . Furthermore, [73] shows that Milky Way GCs lie in a ‘fundamental plane’ and thus can be fully described by just two independent parameters, c and L . A face-on view of the fundamental plane is defined by the axes $\epsilon_2 = 2.05 \log_{10} E_b^* + \log_{10} L$ and $\epsilon_3 = c$. The apparent dependence on the third quantity $\log_{10} E_b^*$ is due to a rotation in the larger three dimensional space in order to remove projection effects. However, this is reconciled by showing that this third parameter, E_b^* , is fully described by the luminosity, such that $E_b^*(L)$ [73]. With the space of physical clusters reduced to the fundamental plane, we determine a representative group of 15 Milky Way clusters by sampling from the two-dimensional distribution. A face-on view of the fundamental plane is given in Figure 2.3, which includes all GCs from the Harris catalogue [54, 2010 edition] for which observed concentrations are available. We omit clusters identified in the catalogue as core-collapsed, since these are not generally well described by King models. This includes those with $c = 2.5$, an arbitrary value assigned to clusters in the catalogue with central density cusps indicative of core collapse. There are 125 Milky Way GCs remaining after core-collapse pruning; of these, 15 GCs are chosen as representative models, in an attempt to properly cover the fundamental parameter space. The 15 Milky Way GC models representative of the 125 Milky Way GCs are described in Table 2.2 and represented by stars in Figure 2.3 to visualize our coverage of the fundamental parameter space.

As stated in section 2.3, our input parameters for specifying the structure of a cluster are the core velocity dispersion $\bar{\sigma}$, the central density n_o , and the King parameter W_o . The mean core velocity dispersion $\bar{\sigma}$ is chosen to be the observed value listed in the Harris catalogue. The core number density n_o is adjusted until the central luminosity density ρ_L is consistent with observation. Finally, the King parameter W_o , which sets

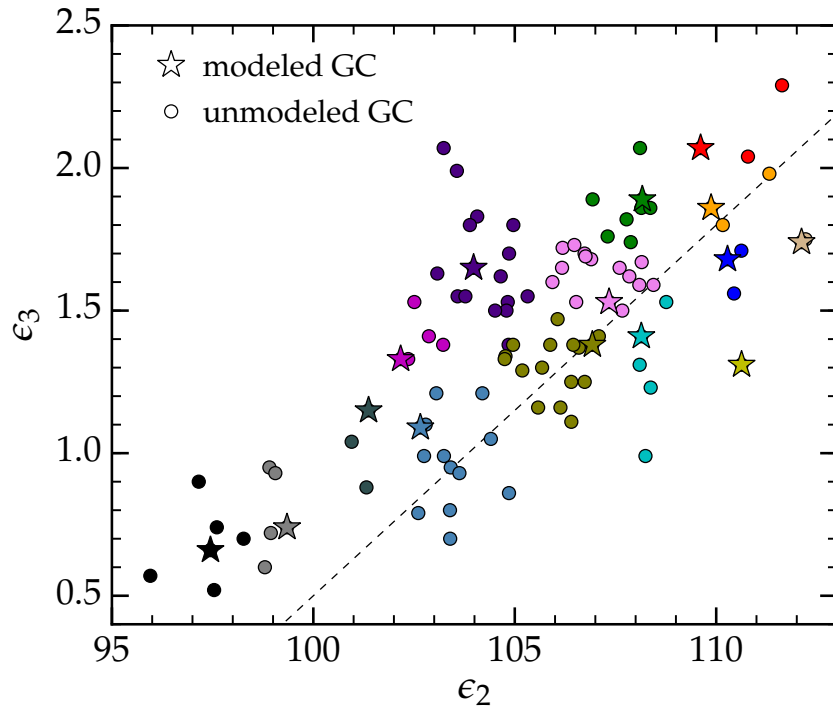


Figure 2.3: The distribution of non core-collapsed Milky Way GCs in a face-on view of the fundamental plane. The colour of each unmodelled GC (marked by circles) indicates the corresponding modelled GC (marked by stars) that serves as its proxy for determining the properties of the ejected binaries. The plane is defined by $\epsilon_2 = 2.05 \log_{10} E_b^* + \log_{10} L$ and $\epsilon_3 = c$, with the dashed line corresponding to the fit $\epsilon_3 = -12.5 + 0.13\epsilon_2$. Here c is the concentration, L is the total luminosity, and E_b^* is an additional parameter related to L (see section 2.4 for additional details).

the depth of the potential, is varied until the cluster has the desired total mass M_c and concentration c . Once we have a model for a given GC, we add BHs by increasing the fraction of retained BHs f_{TBH} , where a value of unity corresponds to retention of all BHs produced according to the IMF. For a given number of BHs in the cluster, we use the parameter f_s in Equation 2.18 to adjust the BH velocity dispersion such that the overall structure of the cluster is unaffected by the presence of a significant number of BHs. However, we find that there is a limit to the number of BHs each cluster can harbour. For the lowest-mass clusters, such as Pal 13, setting the retention factor to unity, $f_{\text{TBH}} = 1$, in order to maximize the number of BHs retained by the cluster produces a peak number of ~ 20 BHs. In this case, the number of BHs retained by the cluster is inherently limited by its structure. More generally, for lower-mass clusters that allow for more BHs, the large number of BHs can become problematic as they become a more significant part of the total mass of the cluster. As the fraction

of the total mass in BHs increases, the BHs begin to affect the structural parameters such that no set of initial parameters exists that satisfy the observed structure of the GC. We find that for many of the lower-mass clusters we are only able to simulate populations of 20 or 200 BHs (cf. Table 2.2).

Galactic evolution

The GC evolution models, described in detail in section 2.3, compute the properties of the BH binaries at the moment they are ejected from a GC. Determining the present day properties of potentially observable, ejected BH binaries requires further modelling that tracks both the evolution of ejected binaries in the Milky Way potential and the internal evolution of each binary. In this section, we describe Monte Carlo models for the subsequent evolution of the ejected binaries that are seeded with results from our GC models.

Globular cluster orbits

We first build a sample of GCs to include in our galactic evolution simulations. The orbit of a cluster is specified by its location on the sky (right ascension and declination), distance from the Sun D_{\odot} , radial velocity v_r , and proper motion μ_{α} and μ_{δ} . Of the 125 non core-collapsed GCs in the Harris catalogue [54, 2010 edition], we are able to find literature values for the orbital parameters of 106 of these clusters in the catalogues of [74] and [75]. For clusters appearing in both catalogues we use the values given in Moreno, Pichardo, and Velázquez [74].

To begin each realization in our Monte Carlo ensemble, we initialize the GC orbits by sampling the uncertainty in their current positions and velocities. We assume normally distributed errors and use the quoted uncertainties in v_r , μ_{α} , and μ_{δ} . Following Krauss and Chaboyer [76], we assume a 6% error in D_{\odot} . After the orbit is specified, we integrate it 10 Gyr backward in time, corresponding to the duration of our GC dynamical simulations.

The orbits of the GCs, and the ejected binaries, are integrated using the python galactic dynamics library `galpy`¹ [77]. We model the Milky Way gravitational potential using the built in `MWPotential2014`. The potential includes contributions from the galactic bulge, disc, and halo, which have been fit to observational data to provide a realistic model of the Milky Way potential. The physical scale of the potential is set using the distance from the centre of the Galaxy to the Sun and the

¹<http://jobovy.github.io/galpy/>

circular velocity of the Sun, which we set to 8 kpc and 220 km s⁻¹, respectively. For all calculations, we use the `dopr54_c` integrator, a fast implementation of a high order Dormand-Prince method included with `galpy`.

Now that we have calculated the positions and velocities of the Milky Way GCs during the past 10 Gyr, the next step is to determine the properties of any potential BH-LMXBs ejected by these clusters. Since our dynamical simulations only include a subset of the galactic GCs, we use the results from the 15 GCs simulated in Table 2.2 as proxies for the ejected binary populations produced by the remaining 110 clusters in our galactic evolution models. For each of the unmodelled clusters, a proxy cluster is selected by finding the nearest simulated cluster in the fundamental plane (see section 2.4). Specifically, we find $\min \left[(\epsilon'_{2,i} - \epsilon'_{2,j})^2 + (\epsilon'_{3,i} - \epsilon'_{3,j})^2 \right]$, where the i index runs over all 106 clusters in the galactic evolution models, the j index runs over the 15 clusters included in our GC dynamics models, and the primes denote the normalized versions of ϵ_2 and ϵ_3 restricted to the range $[0, 1]$. Figure 2.3 shows the proxy cluster chosen for each GC, by assigning the same colour marker to each GC as the colour of the proxy cluster used, which are marked by coloured stars. To ensure the robustness of this method for choosing a proxy cluster, we assign a proxy by two additional methods. One secondary method is to assign the proxy cluster based on the minimum distance in the fundamental plane using the unnormalized axes ϵ_2 and ϵ_3 . The second alternative is by identifying the most similar cluster using the structural parameters M_c , σ , and ρ_L weighted according to the strengths of the correlations between these parameters and the ejected binary populations, which are explored in 2.5. Selecting the proxy cluster by any of these three methods gives similar results in our galactic evolution models. In fact, all three methods will select the same proxy cluster for all but ~ 15 of the 110 unmodelled GCs in our study. In what follows, we discuss models that use the scaled distance in the fundamental plane to assign the proxy cluster.

The ejected binaries

The output of our GC dynamical simulations describes the properties of the BH-binaries ejected from GCs. To model the present day population of BH-LMXBs that are ejected from GCs, we use as inputs for our galactic evolution models: the ejection time t_{ej} , ejection velocity v_{ej} , and the properties of the binary, the semi-major axis a , eccentricity e , the mass of the BH primary m_1 , and the mass of the companion m_2 . This is accomplished by constructing empirical cumulative distribution functions

(CDFs) of these quantities for each of the 37 sets of parameters listed in Table 2.2, and then sampling these distributions in our Monte Carlo models. We assume that the ejection time, ejection velocity, and binary properties are independent and sample the marginal distributions of each.

In the GC dynamical models, a , e , t_{ej} , and v_{ej} are treated as continuous variables. As such, we are able to sample the CDFs for these quantities directly. We fit cubic splines to the empirical CDFs and invert the distributions by interpolation. The GC dynamical models treat m_1 and m_2 as discrete quantities, which fall into the mass bins shown in Table 2.1. In our galactic evolution models, however, we want to consider continuous masses. To accomplish this, we first determine an object’s mass bin by sampling the discrete CDF output by the dynamical simulations. Next, we sample the mass distribution within that bin using the evolved mass function described in section 2.3. Using these CDFs, we are able to generate sample populations of the BH-binaries ejected by the 106 GCs in our galactic evolution simulations.

During each realization, for each cluster, we first determine the number of binaries that the cluster will eject during the 10 Gyr simulation by sampling a Poisson distribution with rate parameter $\langle N_{\text{ej}} \rangle$ (third column of Table 2.3). Once we have determined the number N_{bin} of ejected binaries, we draw N_{bin} samples from the a , e , m_1 , m_2 , t_{ej} , and v_{ej} distributions.

Since the internal evolution of a binary is independent of its orbit in the Galaxy, we separately compute the full internal evolution of the binary using the rapid binary population synthesis code BSE described in [78] with the updates described in [79] and [80]. BSE combines interpolated stellar evolution models with recipes for mass-transfer and other binary evolution processes to enable rapid modelling of a binary system’s lifetime. Binary population synthesis calculations employ parameterized models to describe poorly understood processes in binary evolution. In our BSE runs, we assume that stable mass transfer is conservative. Additionally, we use a common-envelope efficiency parameter of 1.0 and include the effects of tidal circularization.

We use each set of a , e , m_1 , m_2 as the initial conditions for a BSE run. When handling the binary stellar evolution to determine which ejected binaries become mass-transferring, we discard a small number of binaries that would have begun mass-transfer within the cluster. The internal evolution of these tight binaries are coupled to their dynamical evolution within the cluster in a complex manner. Since these effects are not accounted for in our code, we do not include them in our results.

For the remaining binaries, we set the companion star’s metallicity to that of its parent GC and its age to t_{ej} . The latter has little effect because most of the ejected stars have lifetimes that exceed 10 Gyr. The binary is evolved for $t_{\text{evol}} = 10 \text{ Gyr} - t_{\text{ej}}$, i.e., to the present day. Systems are discarded if the companion star is not overflowing its Roche-lobe and transferring mass to the BH at the end of the simulation. For each mass transferring binary, we determine the position \mathbf{r}_{GC} and velocity \mathbf{v}_{GC} of its parent GC at t_{ej} . We initialize an orbit for the ejected binary at \mathbf{r}_{GC} and $\mathbf{v}_{\text{GC}} + \mathbf{v}_{\text{ej}}$, assuming that the binaries are ejected isotropically. With the initial conditions determined, we then evolve these binaries using `galpy` to determine their positions at the present day.

Our galactic evolution models consider three BH-retention scenarios. In the first, we assume that most BHs are ejected and use the results from our GC dynamics models with $N_{\text{BH}} = 20$. We refer to this set of models as MIN. In the second case, referred to as 200, we assume moderate BH retention, using the results from our GC dynamics models with $N_{\text{BH}} = 200$. Finally, in a case denoted MAX, we consider significant BH retention by utilizing the GC dynamics models with $N_{\text{BH}} = 1000$. In cases where we are unable to generate a background cluster model with the appropriate N_{BH} , we use the results from the model with nearest N_{BH} simulated for that same cluster. We compute 10^4 realizations for the MIN and 200 cases and 5×10^3 realizations for the MAX case.

2.5 Results

Our simulations of binary-single star interactions in GCs provide us with statistical properties of the ejected BH binaries they produce including ejection time t_{ej} , ejection velocity v_{ej} , the orbital properties a and e , and the component masses m_1 and m_2 . Combining these results with the methods described in section 2.4, we obtain predictions for the distribution and properties of the galactic population of BH-LMXBs produced by GCs. Additionally, the simulations allow us to explore merger events involving BHs such as gravitational radiation driven mergers, both in the cluster and post-ejection, as well as those mergers that occur during three-body encounters. We describe these results in detail below.

Ejected black-hole binaries

We find that the number of ejected binaries and the properties of these binaries are strongly affected by the GC structure and the number of retained BHs. In Table 2.3, we list the expected number of ejected BH binaries over the life of each cluster, listed

Name	N_{BH}	BH-NC	BH-NS	BH-BH
Pal 13	19.64	3.14	7.74×10^{-3}	1.40×10^{-1}
NGC 6838	20.61	6.33×10^{-1}	3.59×10^{-2}	5.08×10^{-1}
	174.55	2.56×10^1	2.39×10^{-1}	2.67
NGC 6535	19.89	2.35×10^{-1}	1.72×10^{-2}	3.64×10^{-1}
	198.95	5.12	1.24×10^{-1}	2.08
NGC 6362	20.22	1.61×10^{-1}	6.83×10^{-3}	2.31×10^{-1}
	199.33	1.07	2.36×10^{-2}	1.55
NGC 5053	21.71	2.04×10^{-2}	3.14×10^{-4}	7.31×10^{-2}
	199.65	1.79×10^{-1}	2.67×10^{-3}	4.96×10^{-1}
NGC 6121	20.70	3.11×10^{-1}	6.31×10^{-2}	4.96×10^{-1}
	200.53	1.74	3.03×10^{-1}	2.66
	1039.16	1.02×10^2	1.43	8.17
NGC 5694	20.49	2.29×10^{-1}	1.18×10^{-1}	7.49×10^{-1}
	200.39	1.54	1.02	4.19
	1001.94	3.21×10^1	2.87	1.54×10^1
NGC 6093	19.85	1.01×10^{-1}	4.81×10^{-2}	3.42×10^{-1}
	198.31	1.13	3.67×10^{-1}	2.66
	1004.51	1.23×10^1	2.38	1.31×10^1
NGC 5286	12.29	6.00×10^{-2}	2.36×10^{-2}	1.91×10^{-1}
	198.28	9.29×10^{-1}	5.93×10^{-2}	2.08
	787.45	4.42	3.84×10^{-1}	5.48
NGC 6656	19.80	6.79×10^{-2}	1.42×10^{-2}	2.57×10^{-1}
	205.86	4.22×10^{-1}	8.83×10^{-2}	1.74
	1000.35	3.10	2.02×10^{-1}	5.09
NGC 1851	20.76	8.37×10^{-2}	4.91×10^{-2}	4.74×10^{-1}
	203.71	8.79×10^{-1}	4.98×10^{-1}	3.09
	1039.94	1.98×10^1	1.82	1.03×10^1
NGC 6205	20.10	6.13×10^{-2}	1.79×10^{-2}	2.62×10^{-1}
	199.58	4.25×10^{-1}	5.61×10^{-2}	1.70
	998.62	1.61	1.27×10^{-1}	5.36
NGC 6441	20.98	3.51×10^{-2}	1.76×10^{-2}	3.16×10^{-1}
	212.57	9.59×10^{-1}	8.72×10^{-2}	1.57
	1010.37	3.69	8.20×10^{-1}	4.72
NGC 104	22.49	6.60×10^{-2}	3.06×10^{-2}	4.49×10^{-1}
	222.95	1.09	4.47×10^{-1}	2.89
	979.55	3.09	2.52	8.41
NGC 5139	20.84	0.00	0.00	2.53×10^{-2}
	207.50	1.19×10^{-2}	0.00	1.19×10^{-1}
	1009.04	0.00	0.00	2.57×10^{-1}

Table 2.3: Expected number of binary ejections. For each cluster and number of retained BHs, we list the exact number of BHs in the cluster along with the expected number of ejections over the cluster lifetime for three binary types: BH-NC, BH-NS, and BH-BH. The clusters follow the same order as Table 2.2, sorted according to increasing total cluster mass. The values of N_{BH} are non-integer values as a consequence of modelling the population with a smooth distribution function.

in order of increasing mass, including the exact number of BHs in each cluster. The ejected BH-binary expectation value is well described by the number of retained BHs N_{BH} and the two characteristic variables that define the fundamental plane of GCs (see Figure 2.3), namely the total cluster mass M_c and the concentration c . In Figure 2.4, we plot the expected number of ejected BH binaries as a function of the three characteristic variables: N_{BH} , M_c , and c .

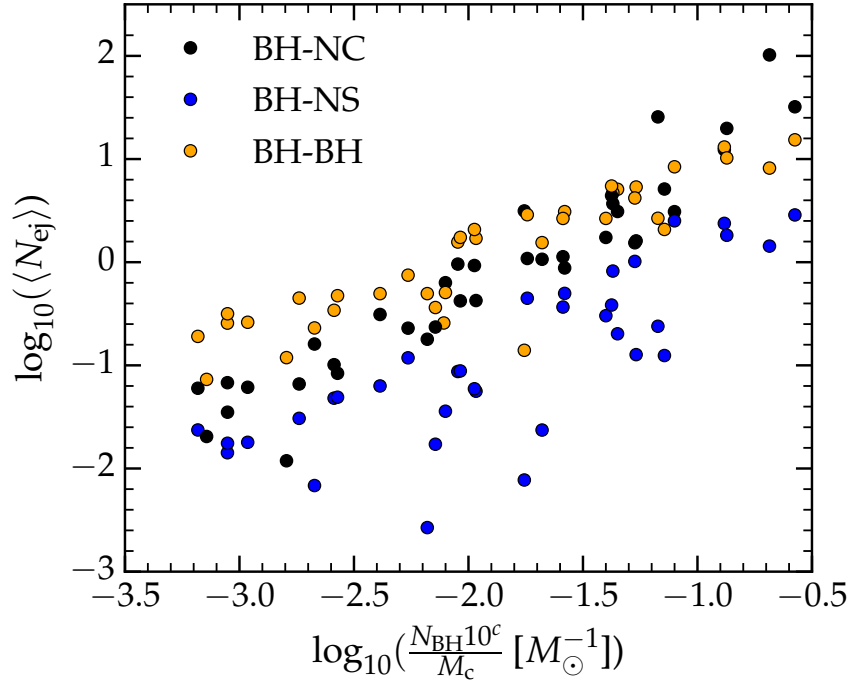


Figure 2.4: Expected number of binary ejections $\langle N_{\text{ej}} \rangle$ as a function of the number of retained BHs N_{BH} , concentration c , and total cluster mass M_c . The number of binaries ejected over the life of the cluster is well described by the two characteristic variables of the fundamental plane, c and M_c , along with the number of BHs retained by the cluster.

The most important structural variable that impacts the ejected binary properties is the cluster mass. The total cluster mass enforces a minimum energy needed to escape, which the binary must gain through repeated encounters. In order for a binary to escape from the cluster, it must acquire a recoil velocity from a final three-body encounter high enough to climb out of the cluster gravitational potential. In Figure 2.5, we show the distribution of the ejected binary velocities as a function of cluster mass, where the influence of the mass of the cluster on the ejection velocity is apparent. The expected number of ejections is then higher for lower-mass clusters

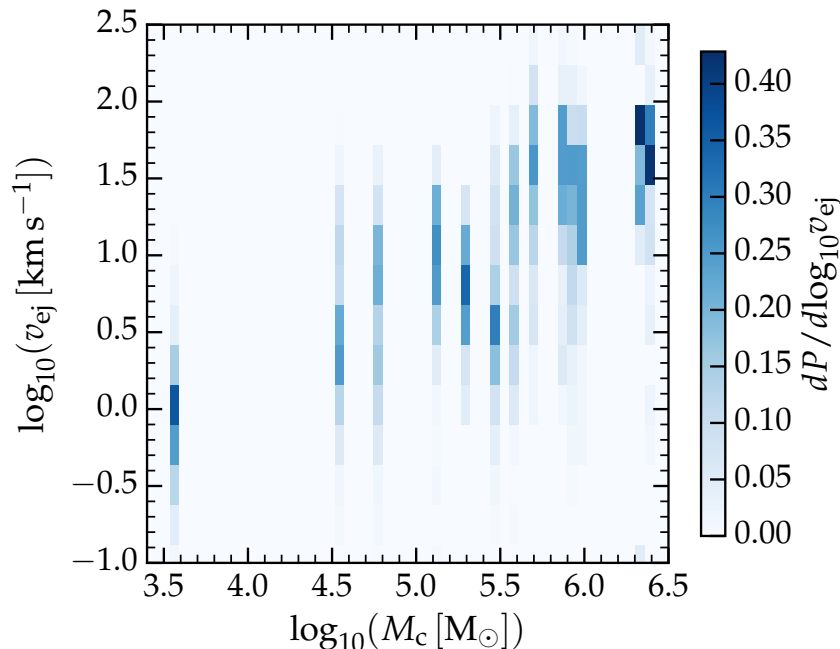


Figure 2.5: The distributions of ejection velocities v_{ej} as a function of the total cluster mass M_c for the ejected binaries. Each vertical bar represents the distribution of v_{ej} for the corresponding mass M_c and is normalized such that the integral over $\log_{10} v_{\text{ej}}$ in each mass bin yields unity. The binary velocity fluctuates due to random encounters with other stars in the cluster until the binary acquires a high enough recoil velocity to exceed the minimum ejection velocity, which is determined by the cluster mass. The increase in the necessary velocity for escape is apparent in the increasing mean value of each v_{ej} distribution.

due to the lower escape velocities associated with these clusters, as is visible in Figure 2.4. To decouple this statement from the additional variables in Figure 2.4, it can also be observed in Table 2.3 (which is ordered by increasing mass) that for a fixed number of retained BHs, the expected number of ejections scales with the cluster mass.

The mechanism through which the binary converts binding energy to kinetic energy is easiest to understand in the three-body centre of mass frame, where we perform our integration for encounters. After an encounter, the final relative velocity at infinity is given by

$$\bar{v}_{\infty}^2 = \frac{m_3(m_1 + m_2)}{\bar{m}_3(\bar{m}_1 + \bar{m}_2)} v_{\infty}^2 + \frac{2M_{123}}{\bar{m}_3(\bar{m}_1 + \bar{m}_2)} (U_{\text{bin}} - \bar{U}_{\text{bin}}), \quad (2.38)$$

where $U_{\text{bin}} = -\frac{Gm_1m_2}{a}$ is the binding energy of the binary and all unbarred quantities represent the initial binary before encountering m_3 , while barred quantities represent

the final binary and \bar{m}_3 is the ejected mass. In the case of no exchange, and utilizing $\Delta a \equiv \bar{a} - a$, Equation 2.38 reduces to

$$\bar{v}_\infty^2 = v_\infty^2 - \frac{2M_{123}}{m_3 m_b} \left(\frac{Gm_1 m_2 \Delta a}{a^2} \right). \quad (2.39)$$

In this frame, the binary velocity is related, through conservation of momentum, to the relative velocity simply by $v_b = \frac{m_3}{M_{123}} v_\infty$. The change in the kinetic energy, $\Delta T \equiv \bar{T} - T$, of the binary is then

$$\Delta T = -\frac{Gm_1 m_2 m_3}{M_{123}} \left(\frac{\Delta a}{a^2} \right). \quad (2.40)$$

The amount by which the semi-major axis changes in an average encounter, where the semi-major axis is reduced without exchange, is proportional to the semi-major axis, $\Delta a \approx -\epsilon a$, with ϵ in the range $\sim[0, 0.6]$ [69]. Using this relation, and assuming a binary with constant m_1 and m_2 , Equation 2.40 reduces to

$$\Delta T \propto \frac{m_3}{M_{123}} \frac{\epsilon}{a}, \quad (2.41)$$

yielding a simple relation that describes the gain in kinetic energy in terms of the constant fractional change in the semi-major axis ϵ and the ratio of the third body to the total mass of the three-body system. Additionally, Equation 2.41 shows that this change in kinetic energy becomes more efficient as the semi-major axis decreases, converting more energy from binding to kinetic after each encounter that shrinks the binary's orbit. After repeated interactions, the increase in velocity due to the decrease in a becomes more substantial and the binary can eventually reach the necessary velocity to escape.

We can directly relate the necessary gain in kinetic energy to the change in binding energy $\Delta U = \bar{U}_{\text{bin}} - U_{\text{bin}}$, by simply rearranging Equation 2.38 and assuming no exchange of masses, which yields

$$\Delta T = -\frac{m_3}{M_{123}} \Delta U. \quad (2.42)$$

In the process of the binary increasing its kinetic energy, the binding energy becomes more negative. Since the higher-mass clusters tend to hold on to the binaries longer, this strict minimum kinetic energy for ejection is manifest in the more negative-valued binding energy of the binaries it ejects. It follows from this, that on average, the semi-major axes of the binaries ejected from more massive clusters tend to be smaller. This is confirmed by Figure 2.6, which depicts the distribution of orbital separations as a function of cluster mass.

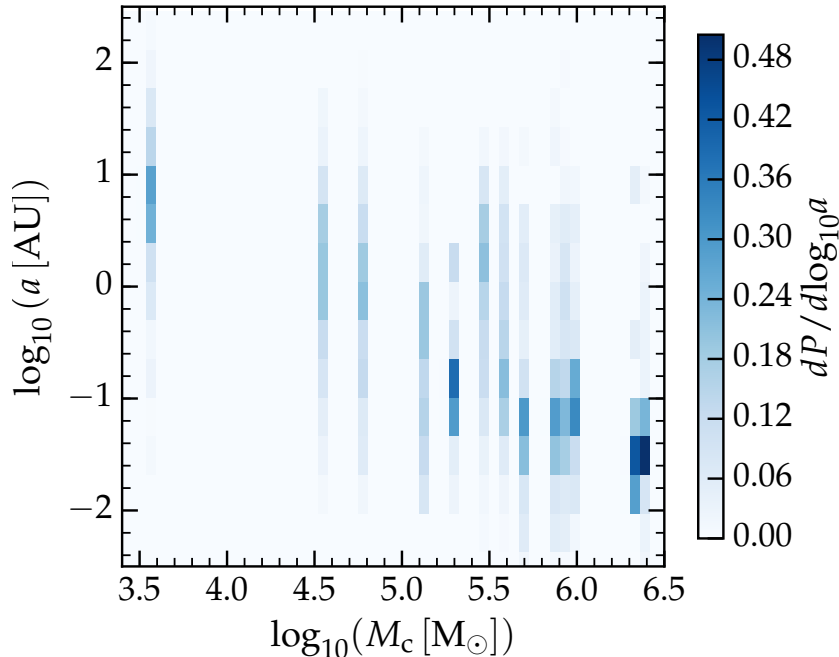


Figure 2.6: The distributions of the semi-major axes at ejection a as a function of the total cluster mass M_c for the ejected binaries. Each vertical bar represents the distribution of a for the corresponding mass M_c and is normalized such that the integral over $\log_{10}a$ in each mass bin yields unity. High mass clusters require a high velocity for escape, which a binary must acquire through three-body interactions in order to be ejected. The energy needed to escape is more easily gained once the orbital separation has decreased sufficiently (see Equation 2.41). As a consequence, the mean value of a at ejection shifts to smaller separation with increasing cluster mass M_c .

In addition to the increase in the expected number of ejected binaries in lower-mass clusters, the total number of expected ejections also increases with an increase in the number of BHs. While the number of ejections is expected to increase with the number of BHs, interestingly, the fraction of ejected binaries composed of a black hole and non-compact object (BH-NC) also grows with the number of BHs (see Figure 2.4 and Table 2.3). This behavior can be attributed to the fact that the BHs are not in energy equipartition with the rest of the cluster. Adding more BHs without affecting the distribution of the luminous cluster members requires that the BHs are spread out farther from the core, where they have traditionally been expected to reside. Accordingly, the mean density of BHs goes down, and they are less likely to interact with each other. However, because they are well mixed with the stars at larger radii, the number of BH-NC binaries that form in three-body exchanges

grows. Additionally, since these binaries form farther from the core, they also have the benefit of a shallower potential to climb out of.

Besides influencing the number of ejected binaries, the number of retained BHs also affects the distribution of the semi-major axes of the ejected binaries. In Figure 2.7, we show the distribution of semi-major axes for the ejected BH-NC binaries in our cluster model for NGC 5694 for the three different choices of BHs retained. We choose this cluster since it is representative of the effect that the number of retained BHs has on the population of ejected BH-NC binaries. Figure 2.7 displays an increase in the width of the distribution of semi-major axes for larger populations of BHs. This is again related to the necessary spreading of the BHs as we increase the number of BHs harboured by the cluster. Therefore, the BH-NC binaries that form outside of the

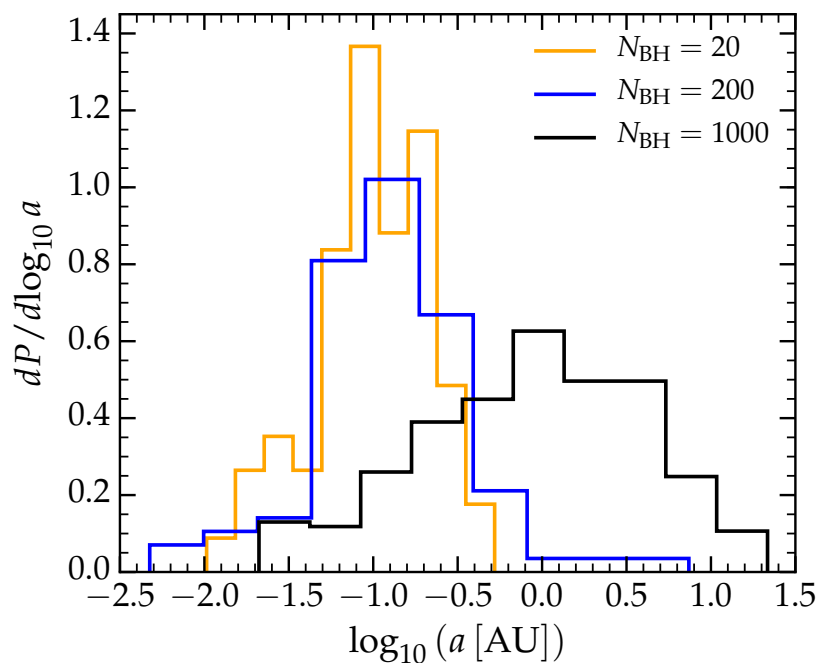


Figure 2.7: The probability distribution for the ejected BH-NC binary semi-major axes from NGC 5694, a representative case, with a population of 20, 200, and 1000 BHs. An increase in the number of BHs requires spreading the BHs outside of the core, where they are more likely to form binaries with NC objects. In the outskirts, the energy necessary to escape is much smaller, allowing the binary to escape before it has had sufficient time to harden. These binaries escape with comparatively low magnitude binding energy and wide orbital separations.

core, where the escape velocity drops rapidly as a function of radius, can be ejected while their binding energies are of comparably lower magnitudes. Although the more widely separated binaries are less likely to become mass-transferring systems,

the simulations with large BH numbers tend to have much higher ejection rates. The higher ejection rates still produce enough tight binaries in the tail of distribution to outnumber those produced with fewer BHs present.

The remaining structural property of GCs that has a clear effect on the population of ejected binaries is the cluster density. In Figure 2.8, we plot the distribution of ejection times as a function of the luminous central density, which is related to the core density as discussed in section 2.3. The distribution establishes that the cluster density has some impact on the time at which binaries are ejected from their host GC. The time between binary-single encounters can be approximated by

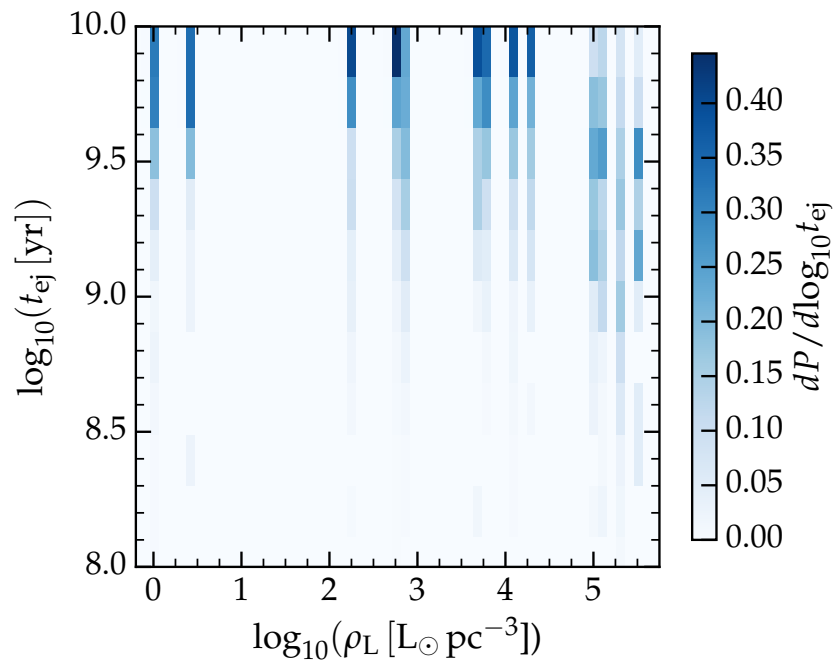


Figure 2.8: The distributions of time of ejection t_{ej} as a function of the luminous central density ρ_L for the ejected binaries. Each vertical bar represents the distribution of t_{ej} for the corresponding core luminosity density ρ_L and is normalized such that the integral over $\log_{10} t_{ej}$ in each density bin yields unity. In higher density clusters, where encounters occur more frequently, many binaries are ejected after only a few Gyr, while in the lower density clusters most ejections occur near the end of the 10 Gyr evolution.

$$t_{enc} = \Gamma^{-1} = \frac{v_m}{2\pi G(m_b + \bar{m})n_o a}, \quad (2.43)$$

where v_m is the mean velocity of stars in the cluster, n_o is its core density, and \bar{m} is the mean mass. Combining this result with Equation 2.40, we can obtain an

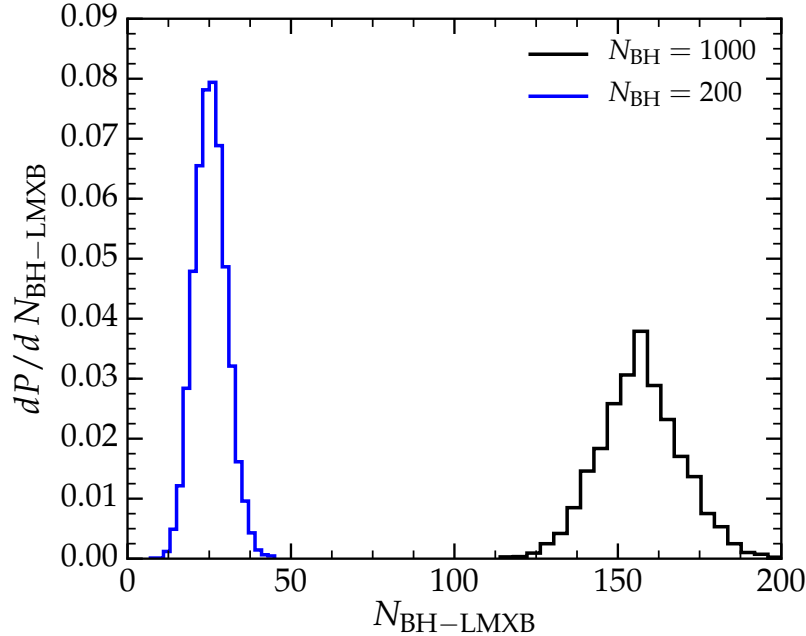


Figure 2.9: The distribution of the number of BH-LMXBs, $N_{\text{BH-LMXB}}$, produced from 10^4 realizations for the $N_{\text{BH}} = 200$ case and 5×10^3 realizations for the $N_{\text{BH}} = 1000$ case. The $N_{\text{BH}} = 20$ case produces a population of zero BH-LMXBs in 10^4 realizations. The expected values for the two producing cases are 25^{+10}_{-6} for $N_{\text{BH}} = 200$ and 156^{+26}_{-24} for $N_{\text{BH}} = 1000$, with the stated uncertainties bounding the 95% confidence interval.

approximation for the rate at which a binary increases its kinetic energy $\Delta T/\Delta t$. As encounters approximately occur in increments of the encounter timescale, letting $\Delta t = t_{\text{enc}}$, we find that the rate at which the binary increases its kinetic energy,

$$\frac{\Delta T}{\Delta t} = \left(\frac{2\pi G^2 m_1 m_2 m_3 \epsilon}{v_m} \right) n_o, \quad (2.44)$$

scales with the cluster core density. Therefore, the time it takes for a binary to acquire a high enough velocity to escape is reduced for higher density clusters. As can be seen in Figure 2.8, in clusters of higher density, where encounters occur more frequently, most BH-NC systems are ejected after only 3 Gyr of evolution whereas in lower density clusters most ejections take place near the end of the 10 Gyr simulation (i.e. the present day),

Black-hole low-mass X-ray binaries

Here we focus strictly on the population of the present-day mass-transferring systems that have successfully become BH-LMXBs. These results reflect the contribution to

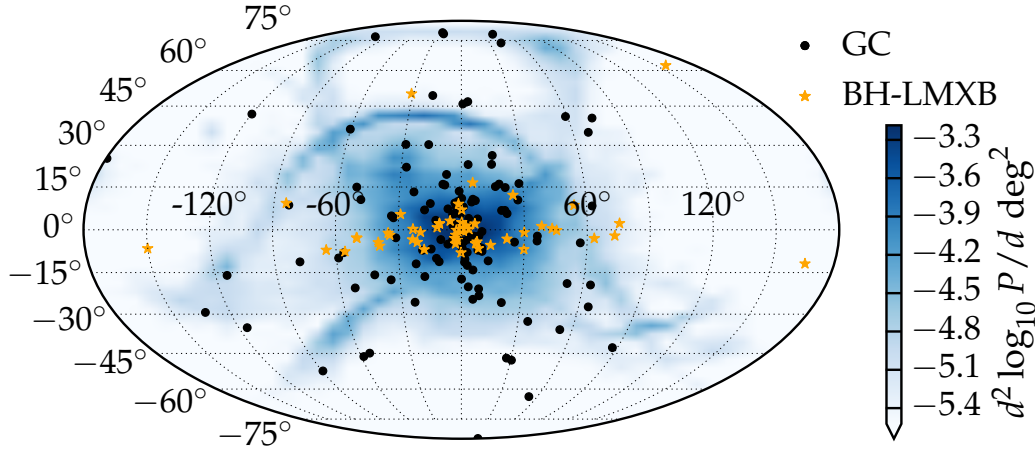


Figure 2.10: The spatial probability distribution of the simulated population of BH-LMXBs from GCs with $N_{\text{BH}} = 1000$. The populations of Milky Way GCs (marked by black circles) and known BH-LMXBs (marked by orange stars) are included for reference. The map is a Mollweide projection of the (l, b) galactic coordinate system. The galactic centre is located near 0° latitude and 0° longitude, where the high density of objects explains the clustering of BH-LMXBs and GCs.

the BH-LMXB population from the entire population of non-core collapsed Milky Way GCs. The production of BH-LMXBs is based on a subset of 15 simulated GCs and the methods detailed in section 2.4. In the following section, we discuss the distribution and the properties of this population of BH-LMXBs from GCs.

As discussed at the end of section 2.4, some clusters require choosing a BH retention fraction of unity, $f_{\text{rBH}} = 1$, in order to obtain the desired quantity of BHs. This occurs in the lowest-mass cluster for each set of N_{BH} , i.e. Pal 13 for $N_{\text{BH}} = 20$, NGC 6838 for $N_{\text{BH}} = 200$, and NGC 6121 for $N_{\text{BH}} = 1000$. These specific parameter sets are not used in determining the population of BH-LMXBs. Although the results from these three sets are included in the previous discussions, they are excluded here due to the unphysical nature of complete BH retention. During BH formation, natal kicks ensure that at least some fraction of the BHs formed from the IMF are ejected from the cluster. This makes complete BH retention essentially unattainable. In consideration of this, we include only those models with $f_{\text{rBH}} < 1$.

Population

The number of mass transferring systems that develop from the BH-NC binaries that are ejected from our model clusters strongly depends on the assumed BH retention

in GCs. We employ the same notation as in section 2.4 for BH retention: MIN refers to $N_{\text{BH}} = 20$, 200 refers to $N_{\text{BH}} = 200$, and MAX refers to $N_{\text{BH}} = 1000$. The populations are generated from 10^4 realizations in the MIN and 200 case and from 5×10^3 realizations for the MAX case, as described in section 2.4. The resulting BH-LMXB population distributions are presented in Figure 2.9. The MIN case produces zero observable BH-LMXB systems. The 200 case produces 25_{-6}^{+10} mass-transferring BH low-mass systems and the MAX case yields an expectation value of 156_{-24}^{+26} ejected BH-LMXBs, with the stated uncertainties bounding the 95% confidence interval.

The clusters that contribute the largest number of BH-LMXBs are those with the highest BH-NC ejection rates (see Table 2.3). As is visible in Figure 2.4, the expected number of ejections can be approximated as a function of the number of retained BHs N_{BH} and the two fundamental parameters describing the cluster: the concentration c and the total cluster mass M_c . While the initial semi-major axis at ejection a , which is sensitive to the cluster mass (Figure 2.6), is an important factor in determining whether a BH-NC will lead to mass transfer, surprisingly, the fraction of BH-NCs that become BH-LMXBs appears nearly constant across clusters. Equivalently stated, $\langle N_{\text{BH-LMXB}} \rangle \sim f_{\text{LMXB}} \langle N_{\text{ej}} \rangle$ appears to hold true for the set of clusters modelled, where $f_{\text{LMXB}} \sim 0.25$ represents the fraction of ejected BH-NC binaries that evolve into BH-LMXBs. Although the distributions of most orbital parameters, which determine whether a system will evolve into a BH-LMXB, vary from cluster to cluster, the thermal eccentricity distribution shared by all clusters ensures that a roughly equal proportion of the ejected binaries will become BH-LMXBs. For clusters that tend to eject wider binaries, it is only the highly eccentric systems that become BH-LMXBs, and vice versa.

For a given BH retention, the number of successfully formed BH-LMXBs from GCs is potentially a function of the ejection time, initial separation, initial eccentricity, primary and companion masses, and the complex internal evolution of the binary. Yet, since we find that the ejection properties are largely determined by the cluster properties, namely the quantities defining the fundamental plane, the size of the BH-LMXB population from GCs is well approximated by the cluster properties alone.

Distribution

As GCs generally have low escape velocities, the ejected BH-LMXBs typically escape with relatively low velocities. Due to this, the distribution of BH-LMXBs closely mimics the distribution of GCs in the Milky Way galaxy. In Figure 2.10, we present the spatial probability distribution of BH-LMXBs from GCs, for the MAX case, on a Mollweide projection of the galactic map in longitudinal and latitudinal galactic coordinates (l, b). Additionally, we include the distribution of galactic GCs and known BH-LMXBs from BlackCAT [14], a catalogue of candidate BH-LMXBs, which we use in all figures including an observed population, unless stated otherwise. Although the 200 case produces fewer BH-LMXBs, the distribution is qualitatively similar to the MAX case. The highest probability density region is near the galactic centre, where the majority of GCs reside. However, as Figure 2.5 illustrates, the distributions of the ejection velocities have widths that span an order of magnitude or more. As a consequence, some fraction of the binaries have ejection velocities that allow them to separate from their parent cluster. Additionally, the binaries that are ejected at an earlier time in the GC's orbit have sufficient time to diverge from the host GC orbit. The higher density streaks in Figure 2.10 can be attributed to these binaries that have drifted from the parent GC.

As GCs primarily follow halo orbits that extend well out of the galactic plane, the GCs are easily able to populate this space with BH-LMXBs. In Figure 2.11, we provide the spatial probability distribution for BH-LMXBs from the MAX case in the $R - z$ plane. Again, we present only the MAX case, as the 200 case is similarly distributed but with a lower overall probability density. The median absolute distance from the galactic plane is $|z| = 1.63$ kpc and the median distance from the galactic centre in the plane is $R = 4.51$ kpc. While it is clear from Figure 2.11 that many of the BH-LMXBs from GCs are located in the galactic disc, the distribution extends well out of the galactic plane into the lower density regions above and below the disc. BH-LMXBs that form in the field will generally reside in the high density galactic plane, unless they receive substantial kicks at birth, which might eject them into the 'high- z ' regions. However, the magnitude of BH-LMXB kicks is still uncertain and the magnitude necessary to reach the highest of BH-LMXBs from GCs is considered unlikely (see, e.g., [21]; [81]). In Figure 2.12, we show the cumulative distribution function of the absolute distance $|z|$ perpendicular to the galactic plane for the MAX case, the 200 case, and the observed population of BH-LMXBs. The observed population terminates at a maximum $|z| \sim 2$ kpc, while the BH-LMXB population

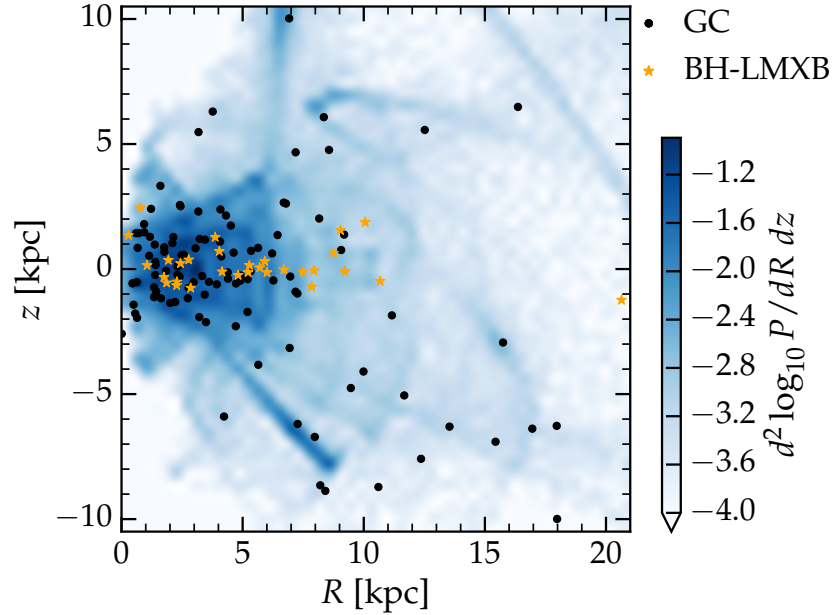


Figure 2.11: The spatial probability distribution of the simulated population of BH-LMXBs from GCs with $N_{\text{BH}} = 1000$ in the $R - z$ plane. The coordinate z specifies the distance perpendicular to the galactic plane and R is the in-plane distance from the galactic centre at the origin. The populations of Milky Way GCs (marked by black circles) and known BH-LMXBs (marked by orange stars) are included for reference. While many of the BH-LMXBs from GCs populate the galactic disc, the distribution extends well out of the galactic plane into the high- $|z|$ region.

from GCs extends well beyond this point. This produces a region of space that is unique to a population of BH-LMXBs from GCs, a population distinct from those forming in the field.

Properties

A typical BH-LMXB with a GC origin has an initial semi-major axis of $5.71 R_{\odot}$, initial BH mass of $8.09 M_{\odot}$, and an initial companion mass of $0.4 M_{\odot}$. The median present-day period is 4.48 h and the median present-day BH mass is $8.25 M_{\odot}$, which has increased above the initial median BH mass due to accretion from the companion. As discussed in section 2.4, the masses used in the Monte Carlo models for the ejected binaries are sampled according to the EMF from the mass bin corresponding to the mass in the ejected BH-NC. This is done for both the primary BH mass M_{BH} and the companion mass m_2 to obtain the mass distributions, which we discuss below.

In Figure 2.13, we show the distribution of the BH mass in the population of

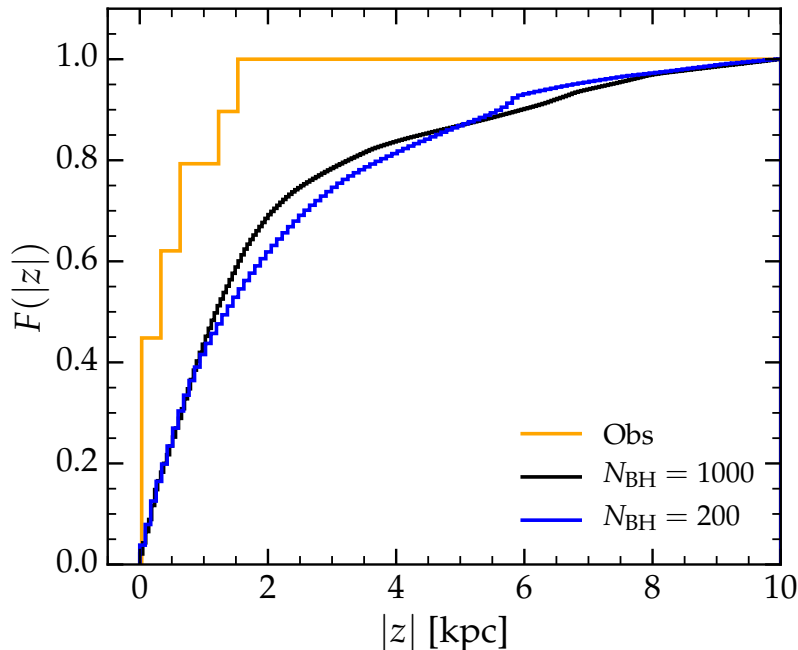


Figure 2.12: The normalized cumulative distribution function of the absolute distance perpendicular to the galactic plane $|z|$. The included distributions are the BH-LMXBs produced in our GC simulations for the cases of $N_{\text{BH}} = 200$, $N_{\text{BH}} = 1000$, and the observed population. Note that in the case that GCs have minimal BH retention ($N_{\text{BH}} = 20$), no mass-transferring systems are produced.

BH-LMXBs from GCs for both cases that produce mass transferring systems. Along with the BH mass distributions for the 200 and MAX cases, we include the inferred BH mass distribution from observations [82]. Although the observed mass distribution reaches down to $\sim 5 M_{\odot}$, our EMF does not produce BH masses in the range $M_{\text{BH}} < 7 M_{\odot}$. The BH primary mass is peaked at $7.4 M_{\odot}$ and displays a preference for the lower-mass BHs. The lack of systems at high BH mass can be attributed to two contributing factors. The leading contribution is the distribution of BH masses in the ejected BH-NCs, which is dominated by the two lowest BH mass bins (i.e. $8.87 M_{\odot}$ and $20.48 M_{\odot}$). Although these are produced in nearly equal numbers, the preference for the lowest mass bin that arises in the BH-LMXBs is due to a secondary effect introduced during the binary stellar evolution. High mass ratio systems are prone to disrupting the companion star, ending the possibility of evolving into a stable BH-LMXB. Despite these barriers to forming BH-LMXBs with high mass BHs, there remains a small population of high mass present-day BH-LMXBs, with $M_{\text{BH}} > 40 M_{\odot}$, which accounts for $\sim 1\%$ of the population.

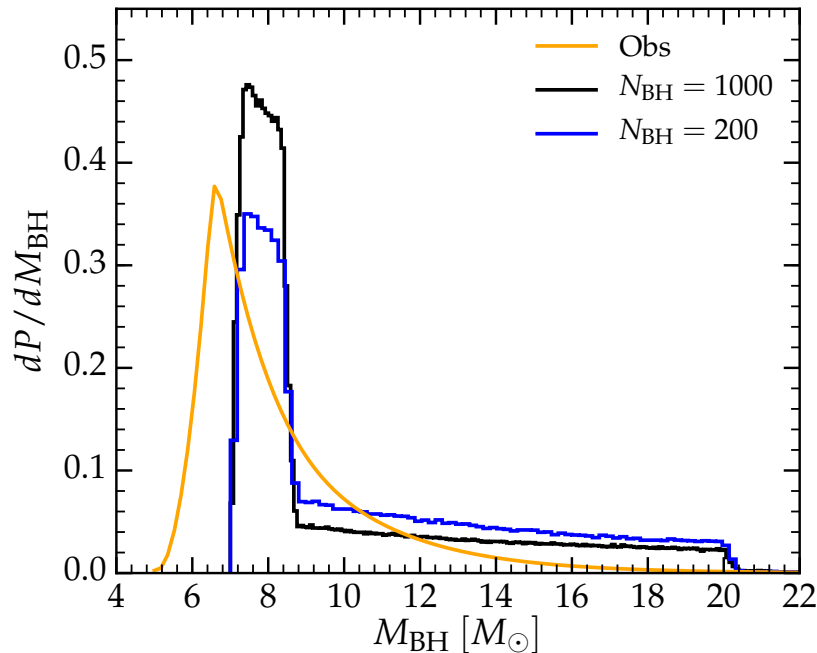


Figure 2.13: The probability distributions of BH masses in BH-LMXBs for the observed population [82] and for the BH-LMXBs produced in our GC simulations for the cases of $N_{\text{BH}} = 200, 1000$. Note that in the case that GCs have minimal BH retention ($N_{\text{BH}} = 20$), no mass-transferring systems are produced. The discontinuous jumps in the distribution correspond to the mass bin minimum and maximum, with a power law distribution in-between determined by the evolved mass function. The lowest BH mass bin was truncated at $7M_{\odot}$.

The low-mass companions are restricted to the range $m_2 < 0.85 M_{\odot}$, where the maximum mass is constrained by the MS turnoff-mass, $m_{\text{to}} = 0.85 M_{\odot}$. The present-day companion mass is a function of the mass-transfer rate and the time since the onset of mass transfer. The majority of the companion masses are MS stars, however there exists a subpopulation of WD companion masses which account for $\sim 10\%$ of the companions in the MAX case and $\sim 20\%$ in the 200 case. In Figure 2.14, we display the companion mass distribution for the MAX case, 200 case, and the observed population of BH-LMXBs. The lack of lower-mass companions in the 200 case relative to the MAX case is due to the higher fraction of WDs, which have masses $m_{\text{WD}} \gtrsim 0.4 M_{\odot}$. In the MAX case there is a larger number of BHs in the outskirts where the lowest masses reside, whereas the 200 case is more centrally concentrated where there is an increase in the probability of picking up a higher mass companion and which includes a larger population of WDs. The observed population in Figure 2.14 is generated from the observational data in the candidate BH-LMXB

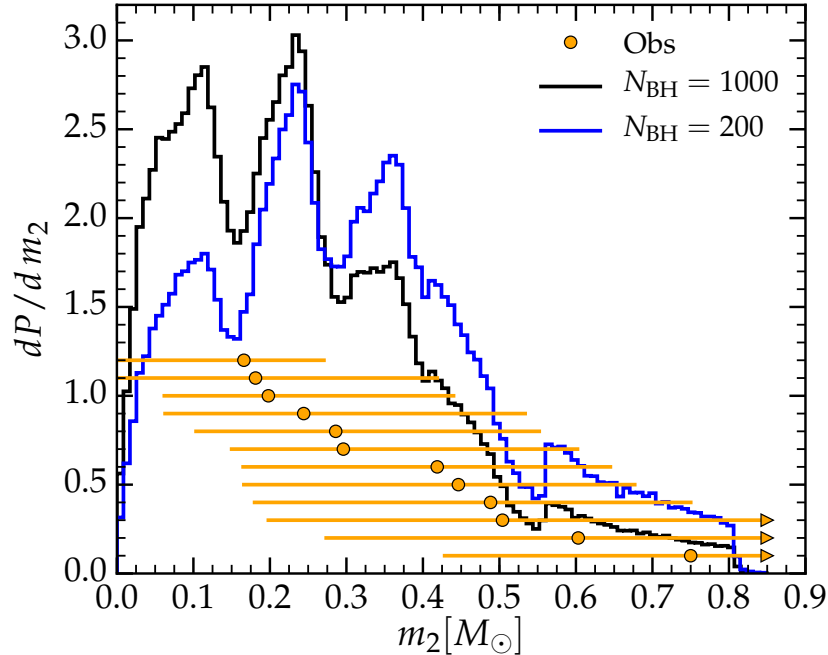


Figure 2.14: The probability distributions of the companion masses in BH-LMXBs for the cases $N_{\text{BH}} = 1000$ and $N_{\text{BH}} = 200$. The observed population includes 12 of the 18 confirmed BH-LMXBs in BlackCAT [14] that have the necessary observational quantities (see section 2.5 for a description of the observed population) and are included for reference; the circles indicate the mean value, the line represents the uncertainty in the observations, and the inclusion of an arrow indicates that the uncertainty is only bounded on one side. The remaining 6 confirmed BH-LMXBs have companion masses above the range considered here, where the axis has been truncated to focus on the range of masses less than the MS turnoff-mass $m_{\text{to}} = 0.85 M_{\odot}$. The peaks in the simulated distributions are due to the sampling of companion masses from the evolved mass function (EMF) within each mass bin.

catalogue BlackCAT. There are 18 confirmed BH-LMXBs in the catalogue that have a measurement of the BH mass M_{BH} and the mass ratio q , which we use to estimate the companion mass $m_2 = q M_{\text{BH}}$. The companion masses in the observed population have large error bars due to the uncertainty in the measurements of the BH mass and the mass ratio.

The initial eccentricity of the binaries follows a thermal distribution, while the initial semi-major axis, as discussed in 2.5, is typically $(a/\text{AU}) \ll 1$, due to their GC origin. The small initial separation of the BH-NCs leads to a distribution of periods p where $\sim 99\%$ of the BH-LMXBs have $p \lesssim 6.2$ h for the MAX case and $p \lesssim 6.8$ h in the 200 case. The subpopulation of BH-LMXBs with a WD companion have a qualitatively

similar distribution but with a reduced period such that $\sim 99\%$ of the population have $p \lesssim 3$ h for both cases, MAX and 200. The reduced period for the WD companions is due to the smaller separations necessary to induce mass transfer for these compact objects. In Figure 2.15, we display the bi-modal distribution of the orbital period for our population of BH-LMXBs along with a subset of the observed population with periods less than $\sim 1/2$ day.

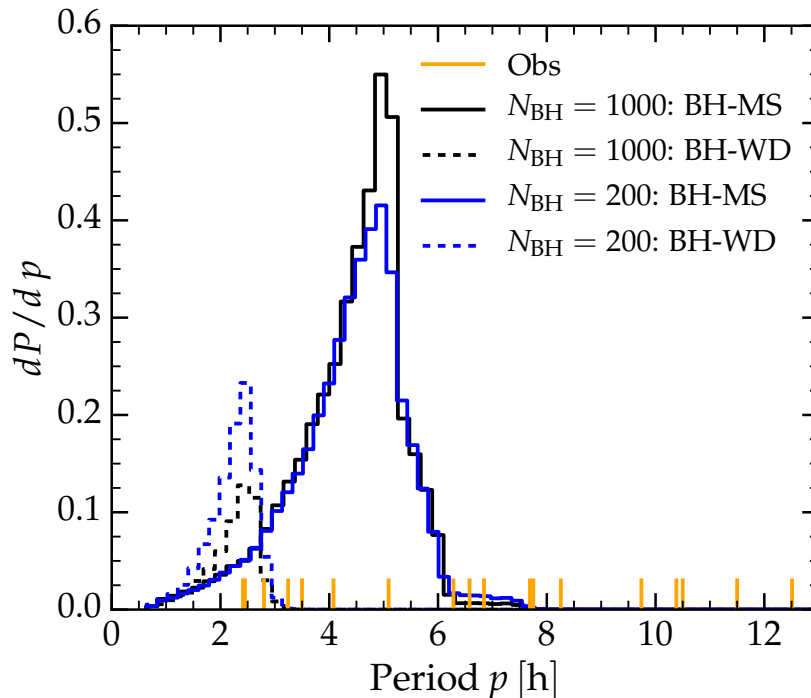


Figure 2.15: The probability distribution of orbital periods in the simulated BH-LMXBs from GCs for the two stellar companion sub-populations: WD and MS. The periods for the observed population of BH-LMXBs that are less than 13 h are included for reference and are identified by orange tick marks (18 of the 28 candidate BH-LMXBs from BlackCAT). To preserve the relative size of the MS and WD companion populations, each distribution is independently normalized and then multiplied by the factors $N_{\text{BH-MS}}/N$ and $N_{\text{BH-WD}}/N$, respectively, with $N = N_{\text{BH-MS}} + N_{\text{BH-WD}}$. This normalization is applied to each N_{BH} case independently.

The mass transfer in these systems is primarily driven by angular momentum loss due to tidal circularization. As the companion star passes the BH at periastron, the tidal forces from the BH deform the star and dissipate energy. This tidal torque efficiently removes eccentricity from the system and eventually leads to circularization of the orbit with a reduced period. Once the period reaches some critical separation, the

companion star overfills its Roche lobe and transitions to a state of mass transfer. This is the same mechanism operating on the BH-LMXBs with a WD companion, however due to the compact nature of WDs, the critical separation which leads to Roche lobe overflow occurs at smaller separations, hence the shorter orbital periods. The binary evolution for the BH-LMXBs from GCs is significantly different from the evolution of field binaries. In the standard binary evolution picture, the companion evolves to overfill its Roche lobe, which can lead to mass transfer at relatively large separations. The MS stars in BH-LMXBs from GCs have not evolved significantly within the cluster, but evolve on much longer timescales, preventing them from achieving mass transfer at wide separations.

In Figure 2.16, we provide a temperature-luminosity diagram for the mass-transferring MS companions. We exclude the WD systems from the diagram, since they are likely too faint for observation. The MS companions have temperatures $\sim 1500 - 6300$ K and luminosities $\sim 6 \times 10^{-4} - 5 \times 10^{-1} L_{\odot}$, making these identifiable as K/M late-type MS stars below the MS turnoff.

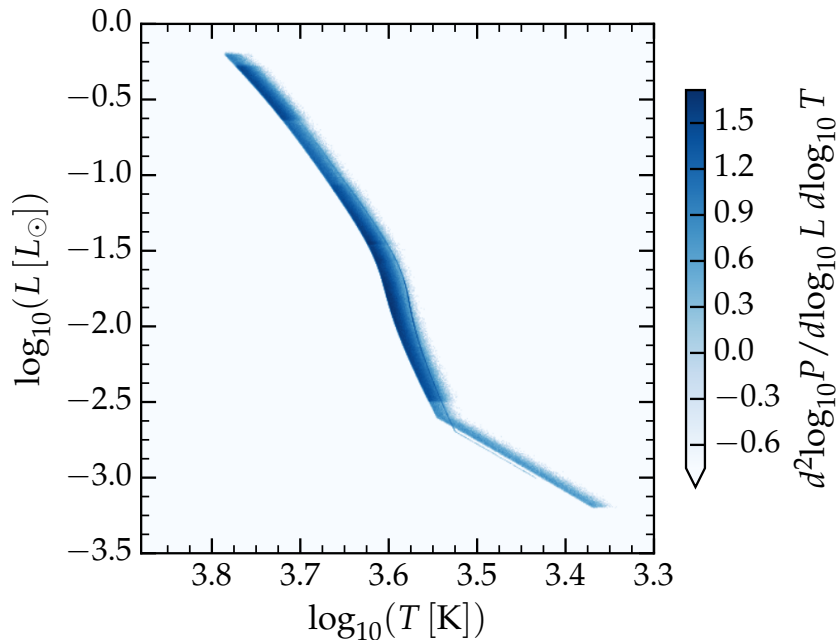


Figure 2.16: Temperature-luminosity diagram for the BH-LMXB companion mass in the simulated population of BH-LMXBs from GCs with $N_{\text{BH}} = 1000$. The low-luminosity WD companions are excluded from the figure, leaving only the mass-transferring MS companions. Since the MS companions from GCs are unevolved stars, the companion temperature-luminosity diagram is essentially the portion of the Hertzsprung-Russell MS branch with $m_2 < m_{10}$.

Name	NBH	3-body mergers				GW mergers		
		BH-NC	BH-WD	BH-NS	BH-BH	BH-WD	BH-NS	BH-BH
NGC 13	19.64	2.53×10^{-1}	1.81×10^{-2}	0.00	0.00	1.42×10^{-2}	0.00	7.74×10^{-3}
NGC 6838	20.61	8.27	1.02	8.98×10^{-3}	1.68×10^{-3}	9.27×10^{-1}	6.85×10^{-2}	2.99×10^{-1}
	174.55	4.40×10^1	4.76	1.71×10^{-2}	4.27×10^{-3}	4.15	2.22×10^{-1}	1.54
NGC 6535	19.89	5.32	5.96×10^{-1}	1.28×10^{-2}	2.77×10^{-4}	5.15×10^{-1}	4.55×10^{-2}	1.97×10^{-1}
	198.95	3.29×10^1	3.30	1.19×10^{-2}	0.00	2.88	1.90×10^{-1}	1.19
NGC 6362	20.22	4.77	4.81×10^{-1}	4.97×10^{-3}	1.24×10^{-3}	5.33×10^{-1}	2.55×10^{-2}	1.83×10^{-1}
	199.33	3.40×10^1	3.82	2.95×10^{-2}	2.95×10^{-3}	3.49	1.59×10^{-1}	1.11
NGC 5053	21.71	5.63×10^{-1}	2.51×10^{-2}	3.14×10^{-4}	3.14×10^{-4}	3.21×10^{-2}	3.14×10^{-4}	1.79×10^{-2}
	199.65	3.89	1.71×10^{-1}	0.00	0.00	2.33×10^{-1}	0.00	1.22×10^{-1}
NGC 6121	20.70	1.51×10^1	2.31	4.30×10^{-2}	5.02×10^{-3}	2.19	6.99×10^{-1}	9.91×10^{-1}
	200.53	1.22×10^2	1.71×10^1	3.25×10^{-1}	2.80×10^{-2}	1.74×10^1	3.45	6.74
NGC 5694	1039.16	3.85×10^2	4.32×10^1	5.90×10^{-1}	8.43×10^{-2}	5.50×10^1	4.80	1.70×10^1
	20.49	2.21×10^1	4.62	9.93×10^{-2}	2.19×10^{-3}	4.36	2.34	2.34
NGC 6093	200.39	1.98×10^2	3.83×10^1	8.39×10^{-1}	4.49×10^{-2}	3.53×10^1	1.57×10^1	1.69×10^1
	1001.94	6.90×10^2	1.10×10^2	2.87	2.87×10^{-2}	1.14×10^2	2.75×10^1	5.06×10^1
NGC 5286	19.85	3.70×10^1	9.09	1.23×10^{-1}	1.33×10^{-3}	6.19	4.46	5.21
	198.31	3.96×10^2	9.52×10^1	1.33	2.83×10^{-2}	6.85×10^1	3.67×10^1	4.64×10^1
NGC 6656	1004.51	2.01×10^3	4.60×10^2	3.68	1.08×10^{-1}	3.81×10^2	1.42×10^2	2.03×10^2
	12.29	1.10×10^1	1.50	3.09×10^{-2}	1.82×10^{-3}	1.45	6.40×10^{-1}	1.06
NGC 1851	198.28	2.07×10^2	3.19×10^1	3.95×10^{-1}	3.95×10^{-2}	3.38×10^1	5.97	1.45×10^1
	787.45	7.43×10^2	1.14×10^2	1.06	9.61×10^{-2}	1.23×10^2	1.20×10^1	3.96×10^1
NGC 6205	19.80	1.53×10^1	2.18	4.90×10^{-2}	7.90×10^{-4}	2.37	4.74×10^{-1}	1.13
	205.86	1.52×10^2	2.32×10^1	2.94×10^{-1}	1.96×10^{-2}	2.46×10^1	3.55	9.43
NGC 6441	1000.35	5.92×10^2	7.79×10^1	1.01	0.00	9.36×10^1	8.09	2.90×10^1
	20.76	2.40×10^1	4.28	9.53×10^{-2}	0.00	2.74	2.69	3.41
NGC 104	203.71	2.77×10^2	4.80×10^1	8.21×10^{-1}	4.40×10^{-2}	3.62×10^1	2.41×10^1	2.85×10^1
	1039.94	1.42×10^3	2.45×10^2	5.24	2.28×10^{-1}	2.30×10^2	8.11×10^1	1.17×10^2
NGC 5139	20.10	1.42×10^1	2.06	4.34×10^{-2}	1.50×10^{-3}	2.28	5.73×10^{-1}	1.17
	199.58	1.35×10^2	1.94×10^1	3.69×10^{-1}	1.20×10^{-2}	2.23×10^1	3.60	8.74
NGC 104	998.62	5.12×10^2	6.68×10^1	7.62×10^{-1}	0.00	7.95×10^1	7.66	2.49×10^1
	20.98	2.57×10^1	3.95	7.91×10^{-2}	1.32×10^{-2}	2.26	2.76	5.12
NGC 5139	212.57	3.54×10^2	6.14×10^1	1.57	4.36×10^{-2}	4.98×10^1	2.65×10^1	5.08×10^1
	1010.37	2.07×10^3	3.32×10^2	7.38	0.00	3.06×10^2	1.06×10^2	1.99×10^2
NGC 5139	22.49	2.51×10^1	4.83	1.88×10^{-1}	4.71×10^{-3}	3.36	4.29	4.34
	222.95	2.92×10^2	5.64×10^1	1.90	1.07×10^{-2}	4.70×10^1	4.08×10^1	3.80×10^1
NGC 5139	979.55	1.30×10^3	2.33×10^2	7.90	5.72×10^{-2}	2.21×10^2	1.29×10^2	1.33×10^2
	20.84	7.15	8.37×10^{-1}	1.89×10^{-2}	7.90×10^{-4}	1.16	1.52×10^{-1}	4.63×10^{-1}
NGC 5139	207.50	7.02×10^1	6.80	1.07×10^{-1}	1.78×10^{-2}	1.15×10^1	9.86×10^{-1}	3.45
	1009.04	2.91×10^2	2.84×10^1	5.15×10^{-1}	2.15×10^{-2}	4.55×10^1	4.29	1.14×10^1

Table 2.4: Expected number of mergers. For each cluster and number of retained BHs, we list the exact number of BHs in the cluster along with the expected number of mergers over the cluster lifetime. The number of expected mergers within a cluster are Poisson distributed. Denoting each expectation value λ , the standard deviation, σ , associated with each value in the table follows from Poisson statistics and is given by $\sigma = \sqrt{\lambda}$.

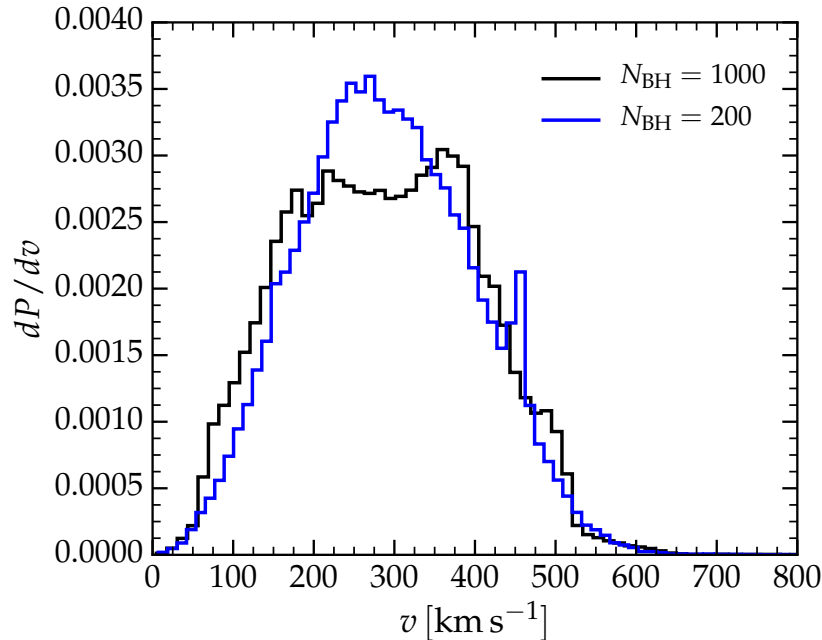


Figure 2.17: The probability distributions for the space velocity v of the simulated BH-LMXB population for the two BHs retention values $N_{\text{BH}} = 1000$ and $N_{\text{BH}} = 200$. The BH-LMXB space velocity is $v = v_{\text{ej}} + v_{\text{GC}}$, where v_{ej} is the ejection velocity and v_{GC} is the velocity of the host GC. Since v_{ej} is approximately the GC escape velocity, the magnitude v is dominated by the relatively large contribution from v_{GC} . As such, the velocity distribution of BH-LMXBs is consistent with the velocity distribution of GCs, which is reflected in the high mean velocities.

A distinct characteristic of these systems are their kinematic properties. In Figure 2.17, we show the distribution of the magnitude of the velocity v of the BH-LMXBs from GCs. The velocity v is computed from the components of the space velocity in the heliocentric galactic coordinate system (U, V, W) , a right-handed coordinate system with U in the direction of the galactic centre, V along the direction of rotation, and W pointing toward the galactic north pole. The median values of the velocity components for the MAX case are $(U, V, W) = (-24.47, -211.31, -22.23)$ km s⁻¹. The large negative velocity in the V component is indicative of this population not participating in galactic rotation. The peculiar velocity — the velocity of a source relative to a local standard of rest, obtained by removing the contribution of galactic rotation at the source distance in the galactic plane R — is sometimes used to infer a ‘natal kick’ for BH-LMXBs. Although it is possible to convert the Galactic space velocity to a peculiar velocity, this inferred ‘kick velocity’ is only justified in assuming the source was born in the galactic disc, where it participates in galactic

rotation. For BH-LMXBs formed in the field, which is most likely to occur in the disc, this is a reasonable assumption. However, the V component of the BH-LMXBs from GCs indicate low rotational velocities, which is consistent with the parent GC halo orbits, which are typically non-circular and extend well out of the galactic plane. As the BH-LMXBs with GC origins are ejected at relatively low velocities along the GC's orbit in the galaxy, this population of BH-LMXBs has a velocity distribution consistent with the high-velocity halo orbits of GCs. As these systems have high apparent peculiar velocities, due to their halo orbits and the lack of participation in galactic rotation, attempting to infer a 'natal kick' from the peculiar velocity in such a case is ill-posed and leads to the conclusion of a large required 'natal kick.'

Merger events

GW-driven mergers

As briefly discussed in section 2.3, we allow for gravitational radiation driven mergers between compact objects. Since all of our 'test binaries' contain at least one BH, the allowable set of GW merger pairs is limited to BH-NS, BH-WD, and BH-BH. In addition to those binaries that merge during their evolution within the cluster, binaries of these types can also be ejected from the cluster. In the case of the ejection of a compact pair, we calculate the expected merger time t_d using the ejected binary parameters and refer to these as post-ejection mergers if $t_{ej} + t_d < t_H$, where $t_H = 10^{10}$ yr is approximately the Hubble time. The total merger rate includes these post-ejection mergers in addition to the in-cluster mergers. Here we present an estimate of the merger rates averaged over the 10^{10} yr simulations for different BH retention values.

For notational convenience, we refer to a parameter set as x_i , where the index i runs over the 39 parameter sets which make up each row of Table 2.2 and corresponds to a specific GC and value of N_{BH} . We compute the expected number of mergers for each parameter set by considering the probability of a BH being involved in a merger, defined simply by $P_m(x_i) = \frac{N_{\text{mergers}}(x_i)}{N_{\text{runs}}(x_i)}$, multiplied by the BH population

$$\langle N_m \rangle_i = P_m(x_i) N_{BH}(x_i) . \quad (2.45)$$

In the case of a merger involving two BHs, the expectation value is calculated using $N_{BH}(x_i)/2$ in order to avoid double counting. The rightmost three columns of Table 2.4 list the expected number of GW-driven compact object mergers over the lifetime of each cluster for a given BH population. The number of BH-BH mergers is strongly correlated with the GC core density n_0 . Each population of BHs has a

merger expectation value that follows a power-law in the core density with exponent ~ 0.58 . Since we do not include primordial binaries, exchange encounters are the only means to forming BH-BH binaries that can later merge. The average rate of encounters is directly proportional to the density, with the highest density clusters providing the largest number of opportunities to successfully form BH-BH binaries. There are additional correlated variables, such as the concentration c and velocity dispersion σ , however these are secondary to the density n_0 and likely due to their own correlation with n_0 .

Given the expected number of mergers for each cluster, we determine a weighted average using the GC mass function, since the total cluster mass of GCs is not uniformly distributed [83]. We do this individually for each group of simulations belonging to the sets $N_{\text{BH}} = \{20, 200, 1000\}$, utilizing the GC mass spectrum $dN(M_c)/dM_c$ of [83]. For each simulated cluster, we assign a weight $w_i = N(M_c(x_i))$ and compute the expected number of mergers per cluster in the Milky Way from

$$\langle N_m(N_{\text{BH}}) \rangle = \frac{\sum_i w_i \langle N_m \rangle_i}{\sum_i w_i} . \quad (2.46)$$

For clarity, to obtain the expected number of mergers for $N_{\text{BH}} = 20$, we sum over all parameter sets in Table 2.2 with $N_{\text{BH}} = 20$. The resulting expected number of BH-BH mergers over the life of a cluster for each choice of N_{BH} are $\langle N_m(20) \rangle = 0.513$, $\langle N_m(200) \rangle = 5.08$, and $\langle N_m(1000) \rangle = 62.5$.

We convert the expected number of mergers to a merger rate density by assuming that our simulations of Milky Way GCs are a fair representation of GCs in other galaxies, that the GCs are all approximately $t_{\text{GC}} = 10^{10}$ yrs old, and that the spatial density of GCs in the universe is $\rho_{\text{GC}} = 0.77 \text{ Mpc}^{-3}$ (see supplemental materials of [84]). Using the weighted averages computed above as our ‘typical’ cluster merger values and assigning this value to each GC in the volume, we obtain the merger rate density due to all GCs in the universe,

$$\langle R(N_{\text{BH}}) \rangle = \frac{\langle N_m(N_{\text{BH}}) \rangle}{t_{\text{GC}}} \rho_{\text{GC}} . \quad (2.47)$$

In Table 2.5, we provide the computed estimated merger rate densities for compact object mergers due to GCs for the three populations of N_{BH} we consider. Although there is an increased interest in the BH-mass spectrum for BH-BH mergers in GCs, stimulated by the larger than expected BH masses recently detected by aLIGO [85], the use of just three discrete BH masses precludes the possibility of such an analysis.

$\langle R(N_{\text{BH}}) \rangle$	BH-BH	BH-NS	BH-WD
$\langle R(20) \rangle$	3.95×10^{-2}	2.71×10^{-2}	7.15×10^{-2}
$\langle R(200) \rangle$	3.91×10^{-1}	2.51×10^{-1}	7.73×10^{-1}
$\langle R(1000) \rangle$	4.81	2.83	10.59

Table 2.5: The contribution to the compact merger rate density from all GCs in the universe, stated in $\text{Gpc}^{-3} \text{yr}^{-1}$. Each row corresponds to the merger rate contribution from GCs with the simulated BH population specified by N_{BH} in $\langle R(N_{\text{BH}}) \rangle$. The merger rate densities are averaged over the life of the cluster, weighted by the GC mass function to account for the non-uniform mass distribution of GCs, and assumes a GC spatial density of $\rho_{\text{GC}} = 0.77 \text{Mpc}^{-3}$.

Since BH-BH mergers from GCs only partially contribute to the total merger rate, with the remaining mergers coming from the field, the rates due to GCs should not exceed the upper bound of the total estimated merger rate. The most recent observational evidence constrains the BH-BH merger rate density to lie in the range $12 - 213 \text{Gpc}^{-3} \text{yr}^{-1}$ [86]. The GC BH-BH merger rate densities given in Table 2.5 for the three different BH retention scenarios are well below the upper bound, presenting no conflict with the observed rate. It is tempting to rule out the lower BH retention cases based on their relatively low merger rate densities compared to the observed lower bound. However, we emphasize that the rates presented in Table 2.5 are the expected rates due to GCs alone, while the observed rate provides bounds on the total BH-BH merger rate that includes the contribution from the field. We could attempt to convert the cluster merger rate to a total rate, but this relies on a well constrained value of the GC fractional contribution. Given the large uncertainty in this fractional contribution, any attempt to approximate the total rate will be dominated by the error in the fractional estimate. Therefore, we presently refrain from ruling out certain BH populations based on their BH-BH merger rate densities alone.

The bounds of our merger rates, which span a wide range of uncertainty in BH retention, are consistent with previous studies that provide estimates of the BH-BH merger rate from GCs ([87]; [88]; [89]; [62], [90]). However, we find that only $\sim 10\%$ of the BH-BH mergers occur outside of the cluster boundaries, which differs from a subset of these previous studies. In [89] no mergers occur in-cluster, while in [62], $\sim 85\%$ of BH-BH mergers occur post-ejection, and [90] find that $\sim 90\%$ merge outside the cluster. In contrast to the small number of BH-BH binaries these studies find merging in cluster, [87] finds that only $\sim 24 - 72\%$ of the BH-BH mergers are post-ejection. Finally, [88] is most closely aligned with our results, with $\sim 10\%$ of mergers occurring out of the cluster.

This discrepancy in merger location can be attributed to the distribution of the BHs in the cluster and their interactions with the lower-mass components. In models with centrally clustered BHs, the BHs are segregated from the remainder of the cluster, forming an isolated and decoupled system. These self-interacting BHs efficiently form BH binaries. Strong binary-binary interactions can eject these binary BHs from the cluster, where they might later merge in isolation. In addition to the efficient removal of BH binaries from the core, binary-single interactions are equally efficient at ejecting single BHs from the cluster. Furthermore, these strong encounters are likely to interrupt potential mergers of eccentric BH binaries which would merge in-cluster if uninterrupted. This channel leads to a majority of BH-BH mergers outside of the cluster and eventually depletes the GC of BHs (e.g., [87]; [91]; [89]). We assume that in order for GCs to retain significant BH populations, the BHs must avoid segregating in the core, which we accomplish through a modified velocity dispersion for the BHs, as discussed in section 2.3. This modified velocity dispersion spreads the BHs throughout the cluster, where they can interact with the lower-mass stars. This supposition is similar to the assumptions made in [88] and produces qualitatively similar results.

In our simulations, a key channel for producing BH-BH binaries is through the formation of a binary composed of a BH and a non-BH outside of the core, which eventually drift to the centre where there is a high density of BHs. The non-BH will be preferentially exchanged with one of the more massive BHs in the core, producing a BH-BH binary that will realize one of three outcomes: (1) the BH-BH binary will be dismantled in the high density region, (2) given a sufficiently large eccentricity (hence a shorter orbital decay time), will eventually merge in the core, or (3) will harden and be ejected from the cluster. This formation channel is similar to that described in [88]. As discussed in section 2.3, we allow for single BHs to exchange into existing binaries. The majority of binaries that a single BH encounters are binaries composed of two low-mass stars. Successful exchanges of a more massive BH for one of the lower-mass stars tend to produce high-eccentricity BH–non-BH binaries following the relation

$$\langle e \rangle \approx 1 - 1.3 \left(\frac{m_{\text{non-BH}}}{m_{\text{BH}}} \right), \quad (2.48)$$

which is independent of the initial eccentricity and applicable when $m_{\text{non-BH}} \ll m_{\text{BH}}$ [69]. For the three BH masses considered, $M_{\text{BH}} = \{8.87, 20.48, 57.18\} M_{\odot}$, and a cluster non-BH star with an average mass of $\langle m_{\text{non-BH}} \rangle \approx 0.3 M_{\odot}$, this leads to mean initial eccentricities of $\langle e \rangle \approx \{0.956, 0.981, 0.993\}$. Once the binary makes it to

the core, the non-BH is easily exchanged for one of the many massive BHs, yielding a highly eccentric BH-BH binary according to Equation 2.48. In Figure 2.18, we display the eccentricity distributions for the BH-BH binaries at formation and at merger or ejection for those binaries that have end states (2) and (3), as described above, respectively. Some fraction of the eccentric binaries that form through this

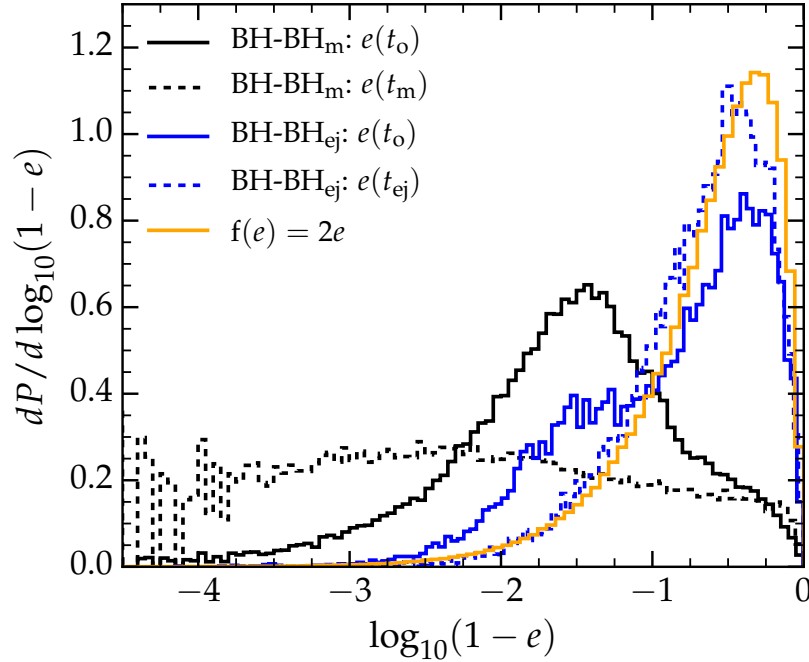


Figure 2.18: The probability distributions of eccentricity for two populations of BH-BH binaries in GCs: BH-BH binaries which form and merge in cluster (BH-BH_m, black lines) and the BH-BH binaries which form and are ejected from the cluster (BH-BH_{ej}, blue lines). For each population, we show the eccentricity distribution at the time the binary forms, $e(t_0)$ (solid lines), and the distribution of eccentricities at the binary’s final state (dashed lines). The final state of the in-cluster mergers is at a time t_m , the time at which the computed merger time is less than the cluster timestep. The final state for the ejected binaries is the time of ejection t_{ej} . A thermal eccentricity distribution, with probability density $f(e) = 2e$, is included for reference.

channel are driven to high enough eccentricities that they can merge in-cluster in-between encounters. The remainder are subject to further encounters that drive their eccentricities toward a thermalized distribution, are hardened in the process, and are eventually ejected.

The eccentricity distribution of merging BH-BH binaries is important for the detection of the resulting gravitational waves. The eccentricity tends to zero as the orbit shrinks,

however modern detectors are sensitive to the GW signal at frequencies when the binary is still in the inspiral phase and the eccentricity is finite. The aLIGO [92] detectors are sensitive to ~ 10 Hz, at design sensitivity, while the future space-based detector LISA [93] will be sensitive to much lower frequencies ~ 1 mHz. We determine the eccentricity at a specific frequency by evolving a_o and e_o , according to $\langle de/da \rangle$ [65], up until some target value a associated with the frequency in consideration. In Figure 2.19, we display the residual eccentricity of the inspiralling

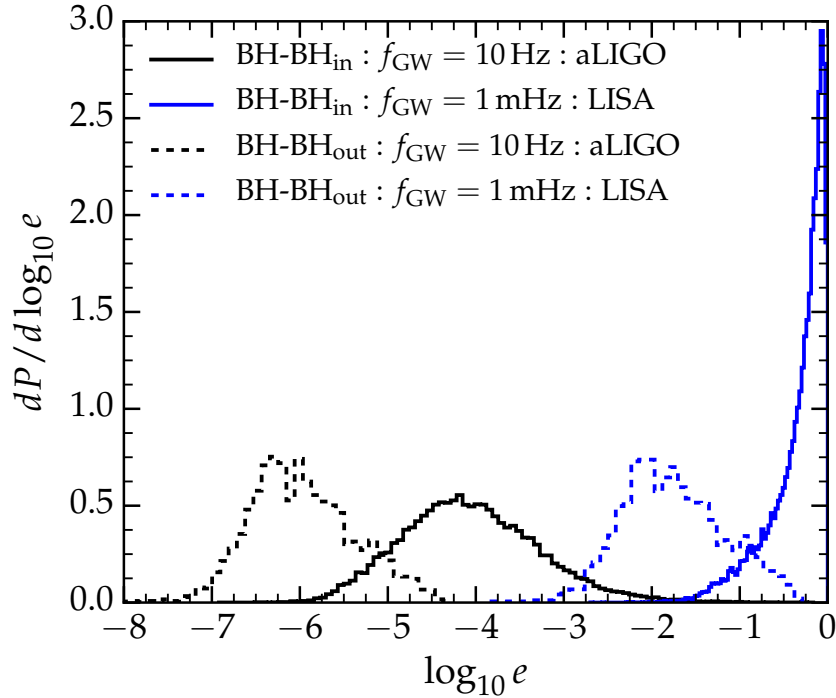


Figure 2.19: The eccentricity probability distributions for two populations of BH-BH mergers from GCs for the two detectors aLIGO and LISA. The two populations correspond to the BH-BH mergers occurring in-cluster (solid lines) and those that merge outside of the cluster, post-ejection (dashed lines). The black lines correspond to the eccentricity of each population when it reaches a corresponding gravitational wave frequency of $f_{\text{GW}} = 10$ Hz, the lower bound frequency of the aLIGO band at design sensitivity. The blue lines represent the eccentricity distribution at $f_{\text{GW}} = 1$ mHz, the proposed lower frequency bound for LISA.

BH-BH binaries as they first enter the design-sensitivity frequency bands for aLIGO and LISA. It is apparent that for aLIGO, both the ejected mergers and the initially high-eccentricity in-cluster mergers have residual eccentricity distributions below 10^{-1} , which has a negligible effect on detections using circularized templates. However, in the case of LISA, while the ejected mergers result in a small eccentricity at 1 mHz, the

initially highly eccentric in-cluster merger population remains significantly eccentric at this frequency.

Utilizing $\langle de/da \rangle$ to determine the evolved eccentricity assumes that the binary evolves in isolation. For the in-cluster mergers, we classify a BH-BH binary as merged once the orbital decay time has fallen below the cluster timestep. However, this could leave significant time for further dynamics to modify the eccentricity such that the binary will not in fact merge in cluster [91]. To account for this possibility, the in-cluster mergers in Figure 2.19 only include those mergers which satisfy the additional constraint $t_{\text{dec}} < \langle t_{\text{enc}} \rangle$, which is satisfied for $\sim 70\%$ of in-cluster mergers. Here, the average encounter time is approximated by $\langle t_{\text{enc}} \rangle = t_{\text{bin}}/N_{\text{enc}}$ with t_{bin} corresponding to the time since the binary's formation and N_{enc} is the number of three-body encounters the binary has been subject to during the time t_{bin} . The remaining $\sim 30\%$ of mergers are uncertain and are not further evolved; they may be broken up, ejected, or merge after subsequent interactions.

Three-body mergers

In addition to the GW-driven mergers, we also calculate the rate of tidally driven mergers or ‘collisions’ that occur during three-body encounters. The merger criteria are based on a minimum separation between bodies, as discussed in section 2.3. We compute the expected number of three-body merger events only for those that involve a BH. Although we track the number of three-body mergers for all object types, including NS-NS, MS-WD, etc., we are missing a significant fraction of these mergers by only tracking single BHs or binaries with at least one BH. We compute the expected number of mergers in a manner similar to the computation of GW mergers above.

The left columns of Table 2.4 list the expected number of mergers involving a BH that occur during three-body encounters over the lifetime of each cluster for a given BH population. These three-body mergers are computed using Equation 2.45 to obtain an expected value for each cluster in the set. As the majority of these events will only be observationally relevant locally, we provide these rates solely for the Milky Way galaxy. Using the computed values from Table 2.4 we construct a cluster weighted average with Equation 2.46. From this we use a modified version of Equation 2.47, with $N_{\text{GC}} \approx 150$, for the approximate number of GCs in our galaxy, in place of ρ_{GC} to obtain the final approximate rate for each event: $\langle R(N_{\text{BH}}) \rangle = \frac{\langle N_{\text{m}}(N_{\text{BH}}) \rangle}{t_{\text{GC}}} N_{\text{GC}}$. These computed rates for BH-BH, BH-NS, BH-WD and BH-NC are shown in Table 2.6,

$\langle R(N_{\text{BH}}) \rangle$	BH-NC	BH-WD	BH-NS	BH-BH
$\langle R(20) \rangle$	1.02×10^{-1}	1.60×10^{-2}	2.65×10^{-4}	1.64×10^{-5}
$\langle R(200) \rangle$	1.08	1.72×10^{-1}	2.53×10^{-3}	1.40×10^{-4}
$\langle R(1000) \rangle$	12.27	2.14	3.03×10^{-2}	1.11×10^{-3}

Table 2.6: The rate of three-body mergers in GCs computed for the Milky Way galaxy and stated in $\text{MWEG}^{-1}\text{Myr}^{-1}$. Each row corresponds to the three-body merger rate in Milky Way GCs with the simulated BH population specified by N_{BH} in $\langle R(N_{\text{BH}}) \rangle$. The merger rates are averaged over the life of the cluster, weighted by the GC mass function to account for the non-uniform mass distribution of GCs, and assumes $N_{\text{GC}} \approx 150$ for the number of GCs in the galaxy.

stated in terms of the number of expected events per Milky Way equivalent galaxy (MWEG) per Myr. The BH-NC merger rate includes the three-body mergers of both BH-RG and BH-MS.

These rates are included to ensure that a large population of retained BHs in GCs does not lead to a conflict with observations. Even in the case of maximal BH retention, the occurrence of these events is relatively infrequent. The most commonly occurring three-body collision is that between a BH and a NC star. The interaction of a NC object with a BH, commonly referred to as a tidal disruption event (TDE), is often studied in the context of supermassive BHs rather than stellar-mass BHs. However, there is some interest in GC-relevant NC collisions with stellar-mass BHs, which are referred to as micro-TDEs [94]. These events lead to full or partial tidal disruption of the NC star and are accompanied by long-duration energetic flares. There is large uncertainty in the signals associated with these events as the strength and duration of the signal depends heavily on the details of the encounter (see, e.g., [94]).

The signals associated with the compact mergers are likely to appear as head-on mergers due to the criteria associated with categorizing mergers during three-body encounters; the exclusion of higher order corrections to Newtonian gravity in our three-body calculations requires extremely close-encounters due to the relatively small size of the compact objects involved. Despite the uncertainty in the observables produced in three-body collisions, the rate of occurrence is low enough that our model does not generate a conflict with present observations.

Comparison with observations and previous results

In our simulations, GCs produce a population of BH-LMXBs with a unique set of characteristic properties. These properties provide some constraints on the likelihood

of a BH-LMXB having a GC origin. In this section, we identify the key characteristics of BH-LMXBs from GCs and determine which of the currently known BH-LMXBs are consistent with this population.

As discussed in section 2.5 and visible in Figure 2.13, the spectrum of BH masses in BH-LMXBs from GCs in our simulations is roughly consistent with the observed population of BH masses. This makes the BH mass a poor candidate for differentiating between field-formed BH-LMXBs and those with a GC origin. As a consequence of the age of GCs, the companions are typically unevolved MS stars, with masses necessarily below the turnoff-mass $m_{\text{to}} = 0.85 M_{\odot}$. Additionally, they reside on a tightly confined branch of a temperature-luminosity diagram (see Figure 2.16). This provides the first distinctive characteristic of BH-LMXBs formed in GCs: a companion mass of $m_2 \lesssim 0.85 M_{\odot}$ and a spectral class consistent with late-type K/M stars. BlackCAT [14] currently contains 18 observed BH-LMXB systems with the proper information to compute an estimate of the companion mass. Of the 18 systems, six BH-LMXBs have companion masses exceeding the maximum companion mass in our population of BH-LMXBs from GCs. Two of these six are near the edge of the distribution with $m_2 \gtrsim 0.9 M_{\odot}$, while the other four have $m_2 \geq 2.52 M_{\odot}$, suggesting these are more consistent with a field-formation scenario.

A second property of a BH-LMXB with a GC origin is a characteristically short period. As shown in Figure 2.15, there is a sharp limit in the distribution confining GC-origin BH-LMXBs to periods shorter than $p \sim 6.5$ h. Of the 27 confirmed BH-LMXBs with measured periods in BlackCAT, 18 have periods with $p > 7$ h, indicating an unlikely GC origin for an additional set of systems. Note, however, that these systems are not necessarily distinct from those ruled unlikely on the basis of companion mass.

Although the GC-origin BH-LMXBs are more likely to reside at larger values of $|z|$ perpendicular to the galactic plane (see Figure 2.12), the overall distribution of the BH-LMXBs from GCs does not provide a strict criterion for discerning between GC origin and field origin. Figure 2.11 illustrates that while the simulated population extends much farther out of the galactic plane than the observed distribution, there is still a significant population of GC-origin BH-LMXBs that reside in the plane, overlapping the region where field-formed binaries are expected to have the highest density. This makes discerning a potential origin for BH-LMXBs in this region difficult. Additionally, for the many systems clustered near the galactic centre or those that reside in the plane, the high density of objects and dust make these systems

Name	$M_{\text{BH}} [M_{\odot}]$	$m_2 [M_{\odot}]$	p [h]	$ z $ [kpc]	References
MAXI J1659-152	5.8 ± 2.2	0.19 ± 0.05	$2.414 \pm 5 \times 10^{-3}$	2.45 ± 1.05	[0,1]
SWIFT J1357.2-0933	> 8.3	> 0.33	$2.8 \pm 3 \times 10^{-1}$	> 1.75	[2,3]
SWIFT J1753.5-0127	$> 7.4 \pm 1.2$	$\geq 0.30 \pm 0.03$	$3.244 \pm 1 \times 10^{-3}$	1.3 ± 0.4	[4-7]
XTE J1118+480	7.55 ± 0.65	0.187 ± 0.083	$4.07841 \pm 1 \times 10^{-5}$	1.52 ± 0.09	[8-11]
GRO J0422+32	8.5 ± 6.5	0.46 ± 0.31	$5.09185 \pm 5 \times 10^{-6}$	0.51 ± 0.06	[12-15]

Table 2.7: Properties of the five observed systems that are consistent with the properties of our simulated population of BH-LMXBs with GC origins. The columns refer to the primary BH mass M_{BH} , the companion mass m_2 , the orbital period p , and the absolute distance perpendicular to the galactic plane $|z|$. [0] Yamaoka et al. [95], [1] Kuulkers et al. [96], [2] Mata Sánchez et al. [97], [3] Corral-Santana et al. [98], [4] Shaw et al. [99], [5] Neustroev et al. [100], [6] Zurita et al. [101], [7] Cadolle Bel et al. [102], [8] Khargharia et al. [103], [9] Calvelo et al. [104], [10] Torres et al. [105], [11] Gelino et al. [106], [12] Casares et al. [107], [13] Beekman et al. [108], [14] Webb et al. [109], [15] Gelino and Harrison [110]

equally difficult to observe optically. Although a number of BH-LMXB candidates are detectable in these regions through X-ray, the detailed properties of these systems remain unknown due to current optical limitations. The spatial distribution of BH-LMXBs from GCs, in general, makes observations of the population difficult, even for those out of the plane. Observation and confirmation of BH-LMXBs rely on a dynamical measurement of the BH mass through optical spectroscopy, introducing a bias toward sources at distances $D < 10$ kpc from the Sun [21]. For the population of BH-LMXBs from our model GCs, the MAX and 200 cases both produce a median distance of $D = 9.7$ kpc, placing roughly half of the systems beyond the observable range.

Although this model population has characteristics that make observations of the binary properties difficult, there are some observed systems that provide a resemblance to those with GC origins. There are 18 observed and confirmed BH-LMXBs in BlackCAT with measured quantities that allow for comparison with our simulated population. Five of the 18 systems have a BH mass, companion mass, and period consistent with the characteristics of our population of BH-LMXBs from GCs. These systems are MAXI J1659-152, SWIFT J1357.2-0933, SWIFT J1753.5-0127, XTE J1118+480, and GRO J0422+32. In Table 2.7, we list the five consistent systems and the known properties that are compatible with the range of values belonging to our population of BH-LMXBs from GCs. While we cannot make any strong claims in regards to the specific origin of these systems, it is worthwhile to note the similarities

of these systems with respect to the population produced in this study.

The BH-LMXB system XTE J1118+480 is well studied, which provides some additional parameters worth comparing with our modelled population of BH-LMXBs from GCs. In addition to the consistent mass of the companion star in XTE J1118+480, the spectral type is also aligned with the band of GC-origin companions in Figure 2.16. Although space-velocity measurements of BH-LMXBs are rare, fortunately there exists a velocity measurement of XTE J1118+480. In the same heliocentric galactic coordinate system (U, V, W) introduced in section 2.5, [111] found a space-velocity for this system of $(U = -105 \pm 16, V = -98 \pm 16, W = -21 \pm 10)$ km s⁻¹. The large magnitude $v \sim 145$ km s⁻¹ and the large negative V component are consistent with a high-velocity halo orbit and a lower than average rotational velocity about the galactic centre. This description is consistent with the velocity distribution of our population of BH-LMXBs from GCs, which inherit the high-velocity halo-orbits when they are ejected from the GC. As a consequence of the high-velocity halo orbit, which manifests itself as a high computed peculiar velocity, this system is commonly invoked to support large natal kicks ([18]; [19]; [20]; [21]). Confidently identifying an origin for this system could help to shed some light on the issue. The relatively low-metallicity environments of GCs provides an additional constraint on properly categorizing BH-LMXBs as originating in GCs versus in the field. Although all of the previous characteristics point to a GC origin, perhaps one of the strongest arguments against a GC origin for this system is the supersolar abundance of elements in the secondary star found by [30], which is consistent with a metal-rich progenitor and makes a GC origin highly unlikely. However, there exist a conflicting claim presented by [29], where through broad-band X-ray spectroscopy, it was concluded that the companion has a metallicity of $Z \sim 10^{-3}$, consistent with the low metallicities expected of systems at large $|z|$ or those with a GC origin. Given that metallicity provides a strong constraint on the origin of a BH-LMXB, additional observations appear necessary to reduce the uncertainty of this case.

To our knowledge, there are no known velocity measurements or metallicity measurements for the four other BH-LMXBs with possible GC origins. Although an increasing number of BH-LMXB candidates are being discovered in X-rays, only a few have been confirmed and characterized with detailed optical follow-up observations. Over time, more data will become available, better constraining the properties of the galactic BH-LMXB population. If even a single BH-LMXB could be confidently attributed to a GC origin this would provide a strong argument in

favor of BH retention in GCs.

2.6 Discussion and conclusions

There is growing observational evidence and theoretical support for a sizable BH population in present-day galactic GCs. These BHs can acquire low-mass companions through dynamical interactions within the GC. Those binaries that are ejected from the GC can evolve into BH-LMXBs and can populate a large region of space above and below the galactic plane. These binaries could potentially explain observed BH-LMXBs at large distances from the plane without a need for large BH birth kicks.

In this study, we have presented a population of Milky Way BH-LMXBs formed through dynamical interactions in GCs. To explore the BH-LMXB population dependence on BH retention in GCs, we performed simulations for retained BH populations of 20, 200, and 1000 BHs. The simulated GCs broadly cover the parameter space and represent a realistic subset of Milky Way GCs. We generated a large number of binary evolution realizations for each set of initial GC parameters and number of retained BHs. This allowed us to derive statistical distributions for the number of ejected binaries and their relevant properties. Using the statistics from the GC simulations, we performed Monte Carlo simulations to obtain a present day population of BH-LMXBs ejected from GCs.

We find that in the case of minimal BH retention ($N_{\text{BH}} = 20$) no observable BH-LMXBs are produced, while the $N_{\text{BH}} = 200$ and $N_{\text{BH}} = 1000$ cases yield 25^{+10}_{-6} and 156^{+26}_{-24} BH-LMXBs, respectively. Here, the uncertainties represent the bounds of the 95% confidence interval. As there is no observable population for minimal BH retention, this suggests that finding any BH-LMXB of GC origin would imply that GCs retain sizable BH populations of more than a few tens of BHs.

Aside from the difference in the size of the population, the properties and distributions of BH-LMXBs are qualitatively similar for the two cases that produce BH-LMXBs, 200 and MAX. We find that BH-LMXBs from GCs have velocity distributions inherited from their host clusters that are consistent with stars on high-velocity halo orbits. Additionally, the ejected BH-LMXBs have a spatial distribution that is also similarly aligned with the GC galactic distribution. This shared distribution is described by a high density in the galactic plane and near the galactic centre, with a significant fraction distributed well above and below the galactic plane. The typical binary is located at an absolute distance of $R = 4.5$ kpc from the galactic core when projected on to the galactic plane, an absolute distance of $|z| = 1.6$ kpc perpendicular

to the galactic plane, and at a distance of $D = 9.74$ kpc from the Sun. The presence of a large population of BH-LMXBs at large distances from the plane is characteristic of BH-LMXBs from GCs, as field formed BH-LMXBs must be subject to large kicks in order to access this region. The average present-day BH-LMXB ejected from a GC is composed of a $8.25 M_{\odot}$ BH and a $0.22 M_{\odot}$ K/M late-type MS star below the turnoff-mass, with a characteristically short orbital period of $p = 0.186$ h. These properties and their associated distributions are key observable characteristics of this predicted population of BH-LMXBs formed in GCs.

Comparing our BH-LMXB systems with the ensemble of observed BH-LMXBs, we find that five of these are candidates for having a GC origin. There are a total of 27 confirmed BH-LMXBs, but just 18 of these have sufficient observations for comparing measured properties against our results. The five systems that are compatible with our simulated population of BH-LMXBs from GCs are MAXI J1659-152, SWIFT J1357.2-0933, SWIFT J1753.5-0127, XTE J1118+480, and GRO J0422+32. XTE J1118+480 is one of the rare systems with a measured space velocity and it is atypically large for a system formed in the galactic disc, with $v \sim 145 \text{ km s}^{-1}$. This system is commonly discussed in the context of formation kicks, since a high-velocity kick is required to explain the large distance from the galactic plane, $|z| \sim 1.52$ kpc, under the assumption that it originated in the plane. However, if XTE J1118+480 comes from a GC, which produces BH-LMXBs at a median distance of $|z| \sim 1.6$ kpc from the plane, then its position and velocity are a natural consequence of the GC origin and do not require a large BH birth kick.

Future observations of the remaining four system velocities would provide an important additional piece of evidence in each of these cases. Additionally, the companion stars in BH-LMXBs from GCs should have the same low metallicity as is typical for GCs. This emphasizes the need for reliable metallicity measurements of the companion metallicity, which could help to support or reject a GC origin scenario. The strength in this measurement relies on the distinctly low-metallicity environments of GCs compared to the disc environment. The metallicity of the companion in XTE J1118+480 has been measured by [29] and [30]. However, the two measurements disagree, with the former finding sub and the latter finding super solar metallicity. Additional observations may be necessary to settle the discussion for XTE J1118+480. Future observations will be needed to more reliably determine or rule out the potential GC origin of the candidate BH-LMXBs. On the basis of our GC simulations, we reaffirm that if one or multiple can be shown to come from a

GC, then GCs retain sizable BH populations.

An additional result from our simulations is a prediction for the BH-BH merger rate as function of the GC BH population. The expected rate of mergers due to all GCs for our maximum retention case, $N_{\text{BH}} = 1000$, is $4.81 \text{ Gpc}^{-3} \text{ yr}^{-1}$, while in the case of minimal retention, $N_{\text{BH}} = 20$, the rate is as low as $3.95 \times 10^{-2} \text{ Gpc}^{-3} \text{ yr}^{-1}$. This rate represents an average over the cluster lifetimes and assumes a spatial density of GCs throughout the universe of $\rho_{\text{GC}} = 0.77 \text{ Mpc}^{-3}$. Our maximum retention rate is consistent with previous estimates of the GC merger rate contribution and is compatible with the recent observations by aLIGO. Although our model produces rates in good agreement with previous studies, our simulations result in a larger than average fraction of mergers occurring in-cluster, as opposed to post-ejection. We attribute the discrepancy to the increased interaction between the BHs and the lower mass stars as a consequence of our cluster BH distribution. The BH-BH binaries that merge in-cluster are a consequence of the large eccentricities, acquired through dynamical formation, leading to significantly shortened orbital decay times. The dynamically formed BH-BH binaries that merge in-cluster are formed with an average eccentricity of $e \sim 0.96$. At the time of merger in the aLIGO band, the residual eccentricities are small and in the range $10^{-6} \lesssim e \lesssim 10^{-2}$. However, we find that when passing through the LISA band years before merger, they still have eccentricities in the range $10^{-2} \lesssim e \lesssim 1$. Models in which the BHs are confined to a subcluster at the core of GCs produce mergers with substantially smaller eccentricities. As the merger formation channels are sufficiently different for a BH subcluster model, LISA might be able to help distinguish how a population of retained BHs is distributed in GCs by observing the distribution of eccentricities.

The present study provides new insights into the population and properties of BH-LMXBs of GC origin. However, there are a number of important limitations that should be kept in mind when interpreting our results. While there is mounting evidence to support that present-day GCs are BH retaining, how GCs are able to retain a significant population of BHs and how those BHs are distributed is still uncertain. Our choice of distributing the BHs throughout the cluster is motivated by preserving the observed structural properties of each modelled GC in the presence of a large BH population. However, this spreading leads to an increase in interaction between the BHs and the lower-mass stars, which is typically a rare occurrence if the BHs remain clustered in the core. If GCs are able to retain a significant population of BHs that remain centrally clustered, formation of BH-NC binaries will likely be suppressed.

The reduced formation of BH-NC binaries would significantly reduce the number of ejected BH-NCs, directly diminishing the number of BH-LMXBs from GCs. Future studies regarding the impact of the BH distribution within BH-retaining GCs are necessary to fully understand the consequences of this limitation. Furthermore, the results presented here rely on the outcomes of many independent realizations. Since we perform each simulation independently in a static cluster background, we are neglecting the change in the BH population and its impact on the cluster as single BHs and BH binaries are ejected over the cluster lifetime. Additionally, we do not account for binary-binary interactions, which have the potential to disrupt existing binaries or possibly aid in ejecting them. Models which account for these limitations are necessary to better understand the impact of ignoring these processes. While N -body simulations and Monte Carlo based models can resolve some of these issues, the computational expense remains a limiting factor in performing many realizations. However, as the computational techniques and resources continue to improve, it will soon be possible to produce many high-accuracy GC simulations that address these limitations.

Acknowledgements

The authors thank Sterl Phinney, Steinn Sigurdsson, and Saul Teukolsky for valuable discussions. Additionally, we thank the anonymous referee for helpful comments on this manuscript. This work is partially supported by the Sherman Fairchild Foundation and by NSF under award No. CAREER PHY-1151197. The simulations were carried out on NSF/NCSA Blue Waters under PRAC award no. ACI-1440083 and on the Caltech cluster Zwicky, supported by the Sherman Fairchild Foundation and NSF award No. PHY-0960291.

References

- [1] K. Belczynski et al. “Initial Populations of Black Holes in Star Clusters”. In: *ApJ* 650 (Oct. 2006), pp. 303–325. DOI: [10.1086/506186](https://doi.org/10.1086/506186). eprint: [astro-ph/0508005](https://arxiv.org/abs/astro-ph/0508005).
- [2] S. R. Kulkarni, P. Hut, and S. McMillan. “Stellar black holes in globular clusters”. In: *Nature* 364 (July 1993), pp. 421–423. DOI: [10.1038/364421a0](https://doi.org/10.1038/364421a0).
- [3] S. Sigurdsson and L. Hernquist. “Primordial black holes in globular clusters”. In: *Nature* 364 (July 1993), pp. 423–425. DOI: [10.1038/364423a0](https://doi.org/10.1038/364423a0).
- [4] J. Strader et al. “Two stellar-mass black holes in the globular cluster M22”. In: *Nature* 490 (Oct. 2012), pp. 71–73. DOI: [10.1038/nature11490](https://doi.org/10.1038/nature11490). arXiv: [1210.0901](https://arxiv.org/abs/1210.0901) [[astro-ph](https://arxiv.org/abs/astro-ph).HE].

- [5] N. Ivanova et al. “Formation of Black Hole X-ray Binaries in Globular Clusters”. In: *ApJ* 717, 948-957 (July 2010), pp. 948–957. DOI: [10.1088/0004-637X/717/2/948](https://doi.org/10.1088/0004-637X/717/2/948). arXiv: [1001.1767](https://arxiv.org/abs/1001.1767) [[astro-ph.HE](#)].
- [6] R. Di Stefano et al. “Bright X-Ray Sources in M31 Globular Clusters”. In: *ApJ* 570 (May 2002), pp. 618–636. DOI: [10.1086/339283](https://doi.org/10.1086/339283). eprint: [astro-ph/0106254](https://arxiv.org/abs/astro-ph/0106254).
- [7] R. Barnard et al. “Four New Black Hole Candidates Identified in M31 Globular Clusters with Chandra and XMM-Newton”. In: *ApJ* 734, 79 (June 2011), p. 79. DOI: [10.1088/0004-637X/734/2/79](https://doi.org/10.1088/0004-637X/734/2/79). arXiv: [1104.0860](https://arxiv.org/abs/1104.0860) [[astro-ph.HE](#)].
- [8] S. J. Aarseth. “Mergers and ejections of black holes in globular clusters”. In: *MNRAS* 422 (May 2012), pp. 841–848. DOI: [10.1111/j.1365-2966.2012.20666.x](https://doi.org/10.1111/j.1365-2966.2012.20666.x). arXiv: [1202.4688](https://arxiv.org/abs/1202.4688) [[astro-ph.SR](#)].
- [9] C. Wang, K. Jia, and X.-D. Li. “On the formation of galactic black hole low-mass X-ray binaries”. In: *MNRAS* 457 (Mar. 2016), pp. 1015–1027. DOI: [10.1093/mnras/stw101](https://doi.org/10.1093/mnras/stw101). arXiv: [1601.02721](https://arxiv.org/abs/1601.02721) [[astro-ph.HE](#)].
- [10] P. G. Breen and D. C. Heggie. “Dynamical evolution of black hole subsystems in idealized star clusters”. In: *MNRAS* 432 (July 2013), pp. 2779–2797. DOI: [10.1093/mnras/stt628](https://doi.org/10.1093/mnras/stt628). arXiv: [1304.3401](https://arxiv.org/abs/1304.3401) [[astro-ph.GA](#)].
- [11] M. Morscher et al. “Retention of Stellar-mass Black Holes in Globular Clusters”. In: *ApJ* 763, L15 (Jan. 2013), p. L15. DOI: [10.1088/2041-8205/763/1/L15](https://doi.org/10.1088/2041-8205/763/1/L15). arXiv: [1211.3372](https://arxiv.org/abs/1211.3372) [[astro-ph.GA](#)].
- [12] A. C. Sippel and J. R. Hurley. “Multiple stellar-mass black holes in globular clusters: theoretical confirmation”. In: *MNRAS* 430 (Mar. 2013), pp. L30–L34. DOI: [10.1093/mnrasl/sls044](https://doi.org/10.1093/mnrasl/sls044). arXiv: [1211.6608](https://arxiv.org/abs/1211.6608) [[astro-ph.GA](#)].
- [13] C. L. Rodriguez et al. “Million-body star cluster simulations: comparisons between Monte Carlo and direct N-body”. In: *MNRAS* 463 (Dec. 2016), pp. 2109–2118. DOI: [10.1093/mnras/stw2121](https://doi.org/10.1093/mnras/stw2121). arXiv: [1601.04227](https://arxiv.org/abs/1601.04227) [[astro-ph.IM](#)].
- [14] J. M. Corral-Santana et al. “BlackCAT: A catalogue of stellar-mass black holes in X-ray transients”. In: *A&A* 587, A61 (Mar. 2016), A61. DOI: [10.1051/0004-6361/201527130](https://doi.org/10.1051/0004-6361/201527130). arXiv: [1510.08869](https://arxiv.org/abs/1510.08869) [[astro-ph.HE](#)].
- [15] J. E. McClintock and R. A. Remillard. “Black hole binaries”. In: *Compact stellar X-ray sources*. Ed. by W. H. G. Lewin and M. van der Klis. Apr. 2006, pp. 157–213.
- [16] J. Casares and P. G. Jonker. “Mass Measurements of Stellar and Intermediate-Mass Black Holes”. In: *Space Sci. Rev.* 183 (Sept. 2014), pp. 223–252. DOI: [10.1007/s11214-013-0030-6](https://doi.org/10.1007/s11214-013-0030-6). arXiv: [1311.5118](https://arxiv.org/abs/1311.5118) [[astro-ph.HE](#)].

- [17] P. G. Jonker and G. Nelemans. “The distances to Galactic low-mass X-ray binaries: consequences for black hole luminosities and kicks”. In: *MNRAS* 354 (Oct. 2004), pp. 355–366. doi: [10.1111/j.1365-2966.2004.08193.x](https://doi.org/10.1111/j.1365-2966.2004.08193.x). eprint: [astro-ph/0407168](https://arxiv.org/abs/astro-ph/0407168).
- [18] A. Gualandris et al. “Has the Black Hole in XTE J1118+480 Experienced an Asymmetric Natal Kick?” In: *ApJ* 618 (Jan. 2005), pp. 845–851. doi: [10.1086/426126](https://doi.org/10.1086/426126). eprint: [astro-ph/0407502](https://arxiv.org/abs/astro-ph/0407502).
- [19] T. Fragos et al. “Understanding Compact Object Formation and Natal Kicks. II. The Case of XTE J1118 + 480”. In: *ApJ* 697 (June 2009), pp. 1057–1070. doi: [10.1088/0004-637X/697/2/1057](https://doi.org/10.1088/0004-637X/697/2/1057). arXiv: [0809.1588](https://arxiv.org/abs/0809.1588).
- [20] S. Repetto, M. B. Davies, and S. Sigurdsson. “Investigating stellar-mass black hole kicks”. In: *MNRAS* 425 (Oct. 2012), pp. 2799–2809. doi: [10.1111/j.1365-2966.2012.21549.x](https://doi.org/10.1111/j.1365-2966.2012.21549.x). arXiv: [1203.3077](https://arxiv.org/abs/1203.3077) [[astro-ph.GA](https://arxiv.org/abs/astro-ph.GA)].
- [21] S. Repetto and G. Nelemans. “Constraining the formation of black holes in short-period black hole low-mass X-ray binaries”. In: *MNRAS* 453 (Nov. 2015), pp. 3341–3355. doi: [10.1093/mnras/stv1753](https://doi.org/10.1093/mnras/stv1753). arXiv: [1507.08105](https://arxiv.org/abs/1507.08105) [[astro-ph.HE](https://arxiv.org/abs/astro-ph.HE)].
- [22] A. Blaauw. “On the origin of the O- and B-type stars with high velocities (the “run-away” stars), and some related problems”. In: *Bull. Astron. Inst. Netherlands* 15 (May 1961), p. 265.
- [23] H.-T. Janka. “Natal kicks of stellar mass black holes by asymmetric mass ejection in fallback supernovae”. In: *MNRAS* 434 (Sept. 2013), pp. 1355–1361. doi: [10.1093/mnras/stt1106](https://doi.org/10.1093/mnras/stt1106). arXiv: [1306.0007](https://arxiv.org/abs/1306.0007) [[astro-ph.SR](https://arxiv.org/abs/astro-ph.SR)].
- [24] H.-T. Janka. “Neutron Star Kicks by the Gravitational Tug-boat Mechanism in Asymmetric Supernova Explosions: Progenitor and Explosion Dependence”. In: *ApJ* 837, 84 (Mar. 2017), p. 84. doi: [10.3847/1538-4357/aa618e](https://doi.org/10.3847/1538-4357/aa618e). arXiv: [1611.07562](https://arxiv.org/abs/1611.07562) [[astro-ph.HE](https://arxiv.org/abs/astro-ph.HE)].
- [25] N. Ivanova et al. “Formation of Black Hole X-Ray Binaries with Non-degenerate Donors in Globular Clusters”. In: *ApJ* 843, L30 (July 2017), p. L30. doi: [10.3847/2041-8213/aa7b76](https://doi.org/10.3847/2041-8213/aa7b76). arXiv: [1706.07577](https://arxiv.org/abs/1706.07577) [[astro-ph.HE](https://arxiv.org/abs/astro-ph.HE)].
- [26] B. P. Abbott et al. “Observation of Gravitational Waves from a Binary Black Hole Merger”. In: *Phys. Rev. Lett.* 116 (6 Feb. 2016), p. 061102. doi: [10.1103/PhysRevLett.116.061102](https://doi.org/10.1103/PhysRevLett.116.061102). URL: <http://link.aps.org/doi/10.1103/PhysRevLett.116.061102>.
- [27] B. P. Abbott et al. “GW151226: Observation of Gravitational Waves from a 22-Solar-Mass Binary Black Hole Coalescence”. In: *Phys. Rev. Lett.* 116.24, 241103 (June 2016), p. 241103. doi: [10.1103/PhysRevLett.116.241103](https://doi.org/10.1103/PhysRevLett.116.241103). arXiv: [1606.04855](https://arxiv.org/abs/1606.04855) [[gr-qc](https://arxiv.org/abs/gr-qc)].

- [28] B. P. Abbott et al. “Astrophysical Implications of the Binary Black-hole Merger GW150914”. In: *ApJ* 818, L22 (Feb. 2016), p. L22. doi: [10.3847/2041-8205/818/2/L22](https://doi.org/10.3847/2041-8205/818/2/L22). arXiv: [1602.03846](https://arxiv.org/abs/1602.03846) [astro-ph.HE].
- [29] F. Frontera et al. “A Measurement of the Broadband Spectrum of XTE J1118+480 with BeppoSAX and Its Astrophysical Implications”. In: *ApJ* 561 (Nov. 2001), pp. 1006–1015. doi: [10.1086/323258](https://doi.org/10.1086/323258). eprint: [astro-ph/0107199](https://arxiv.org/abs/astro-ph/0107199).
- [30] J. I. González Hernández et al. “XTE J1118+480: A Metal-rich Black Hole Binary in the Galactic Halo”. In: *ApJ* 644 (June 2006), pp. L49–L52. doi: [10.1086/505391](https://doi.org/10.1086/505391). eprint: [astro-ph/0605107](https://arxiv.org/abs/astro-ph/0605107).
- [31] A. H. Zonoozi et al. “Direct N-body simulations of globular clusters - I. Palomar 14”. In: *MNRAS* 411 (Mar. 2011), pp. 1989–2001. doi: [10.1111/j.1365-2966.2010.17831.x](https://doi.org/10.1111/j.1365-2966.2010.17831.x). arXiv: [1010.2210](https://arxiv.org/abs/1010.2210).
- [32] L. Spitzer. *Dynamical Evolution of Globular Clusters*. Princeton, NJ: Princeton University Press, 1987.
- [33] H. Cohn. “Numerical integration of the Fokker-Planck equation and the evolution of star clusters”. In: *ApJ* 234 (Dec. 1979), pp. 1036–1053. doi: [10.1086/157587](https://doi.org/10.1086/157587).
- [34] D. F. Chernoff and M. D. Weinberg. “Evolution of globular clusters in the Galaxy”. In: *ApJ* 351 (Mar. 1990), pp. 121–156. doi: [10.1086/168451](https://doi.org/10.1086/168451).
- [35] M. H. Hénon. “The Monte Carlo Method (Papers appear in the Proceedings of IAU Colloquium No. 10 Gravitational N-Body Problem (ed. by Myron Lecar), R. Reidel Publ. Co., Dordrecht-Holland.)” In: *Ap&SS* 14 (Nov. 1971), pp. 151–167. doi: [10.1007/BF00649201](https://doi.org/10.1007/BF00649201).
- [36] L. Spitzer Jr. and M. H. Hart. “Random Gravitational Encounters and the Evolution of Spherical Systems. I. Method”. In: *ApJ* 164 (Mar. 1971), p. 399. doi: [10.1086/150855](https://doi.org/10.1086/150855).
- [37] P. Hut, S. McMillan, and R. W. Romani. “The evolution of a primordial binary population in a globular cluster”. In: *ApJ* 389 (Apr. 1992), pp. 527–545. doi: [10.1086/171229](https://doi.org/10.1086/171229).
- [38] M. B. Davies and W. Benz. “A stellar audit: the computation of encounter rates for 47 Tucanae and omega Centauri”. In: *MNRAS* 276 (Oct. 1995), pp. 876–886. doi: [10.1093/mnras/276.3.876](https://doi.org/10.1093/mnras/276.3.876). eprint: [astro-ph/9507025](https://arxiv.org/abs/astro-ph/9507025).
- [39] M. B. Davies. “The binary zoo: the calculation of production rates of binaries through 2+1 encounters in globular clusters”. In: *MNRAS* 276 (Oct. 1995), pp. 887–905. doi: [10.1093/mnras/276.3.887](https://doi.org/10.1093/mnras/276.3.887). eprint: [astro-ph/9507026](https://arxiv.org/abs/astro-ph/9507026).
- [40] S. Sigurdsson and E. S. Phinney. “Dynamics and Interactions of Binaries and Neutron Stars in Globular Clusters”. In: *ApJS* 99 (Aug. 1995), p. 609. doi: [10.1086/192199](https://doi.org/10.1086/192199). eprint: [astro-ph/9412078](https://arxiv.org/abs/astro-ph/9412078).

- [41] M. J. Benacquista and J. M. B. Downing. “Relativistic Binaries in Globular Clusters”. In: *Living Reviews in Relativity* 16, 4 (Mar. 2013), p. 4. DOI: [10.12942/lrr-2013-4](https://doi.org/10.12942/lrr-2013-4). arXiv: [1110.4423](https://arxiv.org/abs/1110.4423) [astro-ph.SR].
- [42] C. J. Peterson and I. R. King. “The structure of star clusters. VI. Observed radii and structural parameters in globular clusters.” In: *AJ* 80 (June 1975), pp. 427–436. DOI: [10.1086/111759](https://doi.org/10.1086/111759).
- [43] N. A. Bahcall and M. A. Hausman. “The structure of eight globular clusters”. In: *ApJ* 213 (Apr. 1977), pp. 93–99. DOI: [10.1086/155132](https://doi.org/10.1086/155132).
- [44] I. R. King. “The structure of star clusters. III. Some simple dynamical models”. In: *AJ* 71 (Feb. 1966), p. 64. DOI: [10.1086/109857](https://doi.org/10.1086/109857).
- [45] J. Binney and S. Tremaine. *Galactic Dynamics: Second Edition*. Princeton University Press, 2008.
- [46] E. E. Salpeter. “The Luminosity Function and Stellar Evolution.” In: *ApJ* 121 (Jan. 1955), p. 161. DOI: [10.1086/145971](https://doi.org/10.1086/145971).
- [47] P. Kroupa. “On the variation of the initial mass function”. In: *MNRAS* 322 (Apr. 2001), pp. 231–246. DOI: [10.1046/j.1365-8711.2001.04022.x](https://doi.org/10.1046/j.1365-8711.2001.04022.x). eprint: [astro-ph/0009005](https://arxiv.org/abs/astro-ph/0009005).
- [48] G. Meylan and D. C. Heggie. “Internal dynamics of globular clusters”. In: *A&A Rev.* 8 (1997), pp. 1–143. DOI: [10.1007/s001590050008](https://doi.org/10.1007/s001590050008). eprint: [astro-ph/9610076](https://arxiv.org/abs/astro-ph/9610076).
- [49] S. Catalán et al. “The initial-final mass relationship of white dwarfs revisited: effect on the luminosity function and mass distribution”. In: *MNRAS* 387 (July 2008), pp. 1693–1706. DOI: [10.1111/j.1365-2966.2008.13356.x](https://doi.org/10.1111/j.1365-2966.2008.13356.x). arXiv: [0804.3034](https://arxiv.org/abs/0804.3034).
- [50] H. Sana et al. “Binary Interaction Dominates the Evolution of Massive Stars”. In: *Science* 337 (July 2012), pp. 444–. DOI: [10.1126/science.1223344](https://doi.org/10.1126/science.1223344). arXiv: [1207.6397](https://arxiv.org/abs/1207.6397) [astro-ph.SR].
- [51] S. E. de Mink et al. “The Incidence of Stellar Mergers and Mass Gainers among Massive Stars”. In: *ApJ* 782, 7 (Feb. 2014), p. 7. DOI: [10.1088/0004-637X/782/1/7](https://doi.org/10.1088/0004-637X/782/1/7). arXiv: [1312.3650](https://arxiv.org/abs/1312.3650) [astro-ph.SR].
- [52] B. Paxton et al. “Modules for Experiments in Stellar Astrophysics (MESA)”. In: *ApJS* 192, 3 (Jan. 2011), p. 3. DOI: [10.1088/0067-0049/192/1/3](https://doi.org/10.1088/0067-0049/192/1/3). arXiv: [1009.1622](https://arxiv.org/abs/1009.1622) [astro-ph.SR].
- [53] V. Morozova et al. “Light Curves of Core-collapse Supernovae with Substantial Mass Loss Using the New Open-source SuperNova Explosion Code (SNEC)”. In: *ApJ* 814, 63 (Nov. 2015), p. 63. DOI: [10.1088/0004-637X/814/1/63](https://doi.org/10.1088/0004-637X/814/1/63). arXiv: [1505.06746](https://arxiv.org/abs/1505.06746) [astro-ph.HE].
- [54] W. E. Harris. “A Catalog of Parameters for Globular Clusters in the Milky Way”. In: *AJ* 112 (Oct. 1996), p. 1487. DOI: [10.1086/118116](https://doi.org/10.1086/118116).

- [55] A. G. Lyne and D. R. Lorimer. “High birth velocities of radio pulsars”. In: *Nature* 369 (May 1994), pp. 127–129. DOI: [10.1038/369127a0](https://doi.org/10.1038/369127a0).
- [56] E. Pfahl, S. Rappaport, and P. Podsiadlowski. “A Comprehensive Study of Neutron Star Retention in Globular Clusters”. In: *ApJ* 573 (July 2002), pp. 283–305. DOI: [10.1086/340494](https://doi.org/10.1086/340494). eprint: [astro-ph/0106141](https://arxiv.org/abs/astro-ph/0106141).
- [57] N. Ivanova et al. “Formation and evolution of compact binaries in globular clusters - II. Binaries with neutron stars”. In: *MNRAS* 386 (May 2008), pp. 553–576. DOI: [10.1111/j.1365-2966.2008.13064.x](https://doi.org/10.1111/j.1365-2966.2008.13064.x). arXiv: [0706.4096](https://arxiv.org/abs/0706.4096).
- [58] N. Duric. *Advanced astrophysics*. 2004.
- [59] J. M. Fregeau, N. Ivanova, and F. A. Rasio. “Evolution of the Binary Fraction in Dense Stellar Systems”. In: *ApJ* 707 (Dec. 2009), pp. 1533–1540. DOI: [10.1088/0004-637X/707/2/1533](https://doi.org/10.1088/0004-637X/707/2/1533). arXiv: [0907.4196](https://arxiv.org/abs/0907.4196).
- [60] N. Ivanova et al. “The evolution of binary fractions in globular clusters”. In: *MNRAS* 358 (Apr. 2005), pp. 572–584. DOI: [10.1111/j.1365-2966.2005.08804.x](https://doi.org/10.1111/j.1365-2966.2005.08804.x). eprint: [astro-ph/0501131](https://arxiv.org/abs/astro-ph/0501131).
- [61] A. P. Milone et al. “The ACS survey of Galactic globular clusters. XII. Photometric binaries along the main sequence”. In: *A&A* 540, A16 (Apr. 2012), A16. DOI: [10.1051/0004-6361/201016384](https://doi.org/10.1051/0004-6361/201016384). arXiv: [1111.0552](https://arxiv.org/abs/1111.0552) [[astro-ph.SR](https://arxiv.org/abs/astro-ph.SR)].
- [62] M. Morscher et al. “The Dynamical Evolution of Stellar Black Holes in Globular Clusters”. In: *ApJ* 800, 9 (Feb. 2015), p. 9. DOI: [10.1088/0004-637X/800/1/9](https://doi.org/10.1088/0004-637X/800/1/9). arXiv: [1409.0866](https://arxiv.org/abs/1409.0866).
- [63] J. H. Jeans. “The origin of binary systems”. In: *MNRAS* 79 (Apr. 1919), p. 408. DOI: [10.1093/mnras/79.6.408](https://doi.org/10.1093/mnras/79.6.408).
- [64] H. M. Lee and J. P. Ostriker. “Cross sections for tidal capture binary formation and stellar merger”. In: *ApJ* 310 (Nov. 1986), pp. 176–188. DOI: [10.1086/164674](https://doi.org/10.1086/164674).
- [65] P. C. Peters. “Gravitational Radiation and the Motion of Two Point Masses”. In: *Physical Review* 136 (Nov. 1964), pp. 1224–1232. DOI: [10.1103/PhysRev.136.B1224](https://doi.org/10.1103/PhysRev.136.B1224).
- [66] M. Campanelli et al. “Large Merger Recoils and Spin Flips from Generic Black Hole Binaries”. In: *ApJ* 659 (Apr. 2007), pp. L5–L8. DOI: [10.1086/516712](https://doi.org/10.1086/516712). eprint: [gr-qc/0701164](https://arxiv.org/abs/gr-qc/0701164).
- [67] D. Clausen, S. Sigurdsson, and D. F. Chernoff. “Black hole-neutron star mergers in globular clusters”. In: *MNRAS* 428 (Feb. 2013), pp. 3618–3629. DOI: [10.1093/mnras/sts295](https://doi.org/10.1093/mnras/sts295). arXiv: [1210.8153](https://arxiv.org/abs/1210.8153) [[astro-ph.HE](https://arxiv.org/abs/astro-ph.HE)].

- [68] P. Hut and J. N. Bahcall. “Binary-single star scattering. I - Numerical experiments for equal masses”. In: *ApJ* 268 (May 1983), pp. 319–341. DOI: [10.1086/160956](https://doi.org/10.1086/160956).
- [69] S. Sigurdsson and E. S. Phinney. “Binary–Single Star Interactions in Globular Clusters”. In: *ApJ* 415 (Oct. 1993), p. 631. DOI: [10.1086/173190](https://doi.org/10.1086/173190).
- [70] W. Benz and J. G. Hills. “Three-dimensional hydrodynamical simulations of colliding stars . III - Collisions and tidal captures of unequal-mass main-sequence stars”. In: *ApJ* 389 (Apr. 1992), pp. 546–557. DOI: [10.1086/171230](https://doi.org/10.1086/171230).
- [71] M. B. Davies, W. Benz, and J. G. Hills. “Close encounters of the third-body kind”. In: *ApJ* 424 (Apr. 1994), pp. 870–886. DOI: [10.1086/173937](https://doi.org/10.1086/173937).
- [72] D. C. Heggie, P. Hut, and S. L. W. McMillan. “Binary–Single-Star Scattering. VII. Hard Binary Exchange Cross Sections for Arbitrary Mass Ratios: Numerical Results and Semianalytic FITS”. In: *ApJ* 467 (Aug. 1996), p. 359. DOI: [10.1086/177611](https://doi.org/10.1086/177611).
- [73] D. E. McLaughlin. “Binding Energy and the Fundamental Plane of Globular Clusters”. In: *ApJ* 539 (Aug. 2000), pp. 618–640. DOI: [10.1086/309247](https://doi.org/10.1086/309247). eprint: [astro-ph/0002086](https://arxiv.org/abs/astro-ph/0002086).
- [74] E. Moreno, B. Pichardo, and H. Velázquez. “Tidal Radii and Destruction Rates of Globular Clusters in the Milky Way due to Bulge-Bar and Disk Shocking”. In: *ApJ* 793, 110 (Oct. 2014), p. 110. DOI: [10.1088/0004-637X/793/2/110](https://doi.org/10.1088/0004-637X/793/2/110). arXiv: [1408.0457](https://arxiv.org/abs/1408.0457).
- [75] N. V. Kharchenko et al. “Global survey of star clusters in the Milky Way. II. The catalogue of basic parameters”. In: *A&A* 558, A53 (Oct. 2013), A53. DOI: [10.1051/0004-6361/201322302](https://doi.org/10.1051/0004-6361/201322302). arXiv: [1308.5822](https://arxiv.org/abs/1308.5822).
- [76] L. M. Krauss and B. Chaboyer. “Age Estimates of Globular Clusters in the Milky Way: Constraints on Cosmology”. In: *Science* 299 (Jan. 2003), pp. 65–70. DOI: [10.1126/science.1075631](https://doi.org/10.1126/science.1075631).
- [77] J. Bovy. “galpy: A python Library for Galactic Dynamics”. In: *ApJS* 216, 29 (Feb. 2015), p. 29. DOI: [10.1088/0067-0049/216/2/29](https://doi.org/10.1088/0067-0049/216/2/29). arXiv: [1412.3451](https://arxiv.org/abs/1412.3451).
- [78] J. R. Hurley, C. A. Tout, and O. R. Pols. “Evolution of binary stars and the effect of tides on binary populations”. In: *MNRAS* 329 (Feb. 2002), pp. 897–928. DOI: [10.1046/j.1365-8711.2002.05038.x](https://doi.org/10.1046/j.1365-8711.2002.05038.x). eprint: [astro-ph/0201220](https://arxiv.org/abs/astro-ph/0201220).
- [79] D. Clausen et al. “Population Synthesis of Hot Subdwarfs: A Parameter Study”. In: *ApJ* 746, 186 (Feb. 2012), p. 186. DOI: [10.1088/0004-637X/746/2/186](https://doi.org/10.1088/0004-637X/746/2/186). arXiv: [1201.0012](https://arxiv.org/abs/1201.0012) [[astro-ph](https://arxiv.org/abs/astro-ph).SR].

- [80] A. Lamberts et al. “When and where did GW150914 form?” In: *MNRAS* 463 (Nov. 2016), pp. L31–L35. DOI: [10.1093/mnrasl/slw152](https://doi.org/10.1093/mnrasl/slw152). arXiv: [1605.08783](https://arxiv.org/abs/1605.08783) [astro-ph.HE].
- [81] I. Mandel. “Estimates of black hole natal kick velocities from observations of low-mass X-ray binaries”. In: *MNRAS* 456 (Feb. 2016), pp. 578–581. DOI: [10.1093/mnras/stv2733](https://doi.org/10.1093/mnras/stv2733). arXiv: [1510.03871](https://arxiv.org/abs/1510.03871) [astro-ph.HE].
- [82] F. Özel et al. “The Black Hole Mass Distribution in the Galaxy”. In: *ApJ* 725 (Dec. 2010), pp. 1918–1927. DOI: [10.1088/0004-637X/725/2/1918](https://doi.org/10.1088/0004-637X/725/2/1918). arXiv: [1006.2834](https://arxiv.org/abs/1006.2834).
- [83] D. E. McLaughlin and R. E. Pudritz. “The Formation of Globular Cluster Systems. I. The Luminosity Function”. In: *ApJ* 457 (Feb. 1996), p. 578. DOI: [10.1086/176754](https://doi.org/10.1086/176754).
- [84] C. L. Rodriguez et al. “Binary Black Hole Mergers from Globular Clusters: Implications for Advanced LIGO”. In: *Phys. Rev. Lett.* 115.5, 051101 (July 2015), p. 051101. DOI: [10.1103/PhysRevLett.115.051101](https://doi.org/10.1103/PhysRevLett.115.051101). arXiv: [1505.00792](https://arxiv.org/abs/1505.00792) [astro-ph.HE].
- [85] B. P. Abbott et al. “Astrophysical Implications of the Binary Black-hole Merger GW150914”. In: *ApJ* 818, L22 (Feb. 2016), p. L22. DOI: [10.3847/2041-8205/818/2/L22](https://doi.org/10.3847/2041-8205/818/2/L22). arXiv: [1602.03846](https://arxiv.org/abs/1602.03846) [astro-ph.HE].
- [86] B. P. Abbott et al. “GW170104: Observation of a 50-Solar-Mass Binary Black Hole Coalescence at Redshift 0.2”. In: *Phys. Rev. Lett.* 118 (22 June 2017), p. 221101. DOI: [10.1103/PhysRevLett.118.221101](https://doi.org/10.1103/PhysRevLett.118.221101). URL: <https://link.aps.org/doi/10.1103/PhysRevLett.118.221101>.
- [87] R. M. O’Leary et al. “Binary Mergers and Growth of Black Holes in Dense Star Clusters”. In: *ApJ* 637 (Feb. 2006), pp. 937–951. DOI: [10.1086/498446](https://doi.org/10.1086/498446). eprint: [astro-ph/0508224](https://arxiv.org/abs/astro-ph/0508224).
- [88] A. Sadowski et al. “The Total Merger Rate of Compact Object Binaries in the Local Universe”. In: *ApJ* 676, 1162–1169 (Apr. 2008), pp. 1162–1169. DOI: [10.1086/528932](https://doi.org/10.1086/528932). arXiv: [0710.0878](https://arxiv.org/abs/0710.0878).
- [89] J. M. B. Downing et al. “Compact binaries in star clusters - II. Escapers and detection rates”. In: *MNRAS* 416 (Sept. 2011), pp. 133–147. DOI: [10.1111/j.1365-2966.2011.19023.x](https://doi.org/10.1111/j.1365-2966.2011.19023.x). arXiv: [1008.5060](https://arxiv.org/abs/1008.5060).
- [90] C. L. Rodriguez, S. Chatterjee, and F. A. Rasio. “Binary black hole mergers from globular clusters: Masses, merger rates, and the impact of stellar evolution”. In: *PRD* 93.8, 084029 (Apr. 2016), p. 084029. DOI: [10.1103/PhysRevD.93.084029](https://doi.org/10.1103/PhysRevD.93.084029). arXiv: [1602.02444](https://arxiv.org/abs/1602.02444) [astro-ph.HE].
- [91] S. Banerjee, H. Baumgardt, and P. Kroupa. “Stellar-mass black holes in star clusters: implications for gravitational wave radiation”. In: *MNRAS* 402 (Feb. 2010), pp. 371–380. DOI: [10.1111/j.1365-2966.2009.15880.x](https://doi.org/10.1111/j.1365-2966.2009.15880.x). arXiv: [0910.3954](https://arxiv.org/abs/0910.3954) [astro-ph.SR].

- [92] LIGO Scientific Collaboration et al. “Advanced LIGO”. In: *Class. Quantum Grav.* 32.7, 074001 (Apr. 2015), p. 074001. DOI: [10.1088/0264-9381/32/7/074001](https://doi.org/10.1088/0264-9381/32/7/074001). arXiv: [1411.4547](https://arxiv.org/abs/1411.4547) [gr-qc].
- [93] P. Amaro-Seoane et al. “eLISA: Astrophysics and cosmology in the millihertz regime”. In: *GW Notes, Vol. 6, p. 4-110* 6 (May 2013), pp. 4–110. arXiv: [1201.3621](https://arxiv.org/abs/1201.3621) [astro-ph.CO].
- [94] H. B. Perets et al. “Micro-tidal Disruption Events by Stellar Compact Objects and the Production of Ultra-long GRBs”. In: *ApJ* 823, 113 (June 2016), p. 113. DOI: [10.3847/0004-637X/823/2/113](https://doi.org/10.3847/0004-637X/823/2/113). arXiv: [1602.07698](https://arxiv.org/abs/1602.07698) [astro-ph.HE].
- [95] K. Yamaoka et al. “Combined Spectral and Timing Analysis of the Black Hole Candidate MAXI J1659-152, Discovered by MAXI and Swift”. In: *PASJ* 64, 32 (Apr. 2012), p. 32. DOI: [10.1093/pasj/64.2.32](https://doi.org/10.1093/pasj/64.2.32). arXiv: [1110.6512](https://arxiv.org/abs/1110.6512) [astro-ph.HE].
- [96] E. Kuulkers et al. “MAXI J1659-152: the shortest orbital period black-hole transient in outburst”. In: *A&A* 552, A32 (Apr. 2013), A32. DOI: [10.1051/0004-6361/201219447](https://doi.org/10.1051/0004-6361/201219447). arXiv: [1204.5840](https://arxiv.org/abs/1204.5840) [astro-ph.HE].
- [97] D. Mata Sánchez et al. “Swift J1357.2-0933: a massive black hole in the Galactic thick disc”. In: *MNRAS* 454 (Dec. 2015), pp. 2199–2204. DOI: [10.1093/mnras/stv2111](https://doi.org/10.1093/mnras/stv2111). arXiv: [1509.05412](https://arxiv.org/abs/1509.05412) [astro-ph.HE].
- [98] J. M. Corral-Santana et al. “A Black Hole Nova Obscured by an Inner Disk Torus”. In: *Science* 339 (Mar. 2013), pp. 1048–1051. DOI: [10.1126/science.1228222](https://doi.org/10.1126/science.1228222). arXiv: [1303.0034](https://arxiv.org/abs/1303.0034) [astro-ph.GA].
- [99] A. W. Shaw et al. “No evidence for a low-mass black hole in Swift J1753.5-0127”. In: *MNRAS* 463 (Dec. 2016), pp. 1314–1322. DOI: [10.1093/mnras/stw2092](https://doi.org/10.1093/mnras/stw2092). arXiv: [1608.04969](https://arxiv.org/abs/1608.04969) [astro-ph.HE].
- [100] V. V. Neustroev et al. “Spectroscopic evidence for a low-mass black hole in SWIFT J1753.5-0127”. In: *MNRAS* 445 (Dec. 2014), pp. 2424–2439. DOI: [10.1093/mnras/stu1924](https://doi.org/10.1093/mnras/stu1924). arXiv: [1409.4423](https://arxiv.org/abs/1409.4423) [astro-ph.HE].
- [101] C. Zurita et al. “Swift J1753.5-0127: The Black Hole Candidate with the Shortest Orbital Period”. In: *ApJ* 681, 1458-1463 (July 2008), pp. 1458–1463. DOI: [10.1086/588721](https://doi.org/10.1086/588721). arXiv: [0803.2524](https://arxiv.org/abs/0803.2524).
- [102] M. Cadolle Bel et al. “Simultaneous Multiwavelength Observations of the Low/Hard State of the X-Ray Transient Source SWIFT J1753.5-0127”. In: *ApJ* 659 (Apr. 2007), pp. 549–560. DOI: [10.1086/512004](https://doi.org/10.1086/512004). eprint: [astro-ph/0612575](https://arxiv.org/abs/astro-ph/0612575).
- [103] J. Khargharia et al. “The Mass of the Black Hole in XTE J1118+480”. In: *AJ* 145, 21 (Jan. 2013), p. 21. DOI: [10.1088/0004-6256/145/1/21](https://doi.org/10.1088/0004-6256/145/1/21). arXiv: [1211.2786](https://arxiv.org/abs/1211.2786) [astro-ph.SR].

- [104] D. E. Calvelo et al. “Doppler and modulation tomography of XTEJ1118+480 in quiescence”. In: *MNRAS* 399 (Oct. 2009), pp. 539–549. doi: [10.1111/j.1365-2966.2009.15304.x](https://doi.org/10.1111/j.1365-2966.2009.15304.x). arXiv: [0905.1491](https://arxiv.org/abs/0905.1491) [astro-ph.SR].
- [105] M. A. P. Torres et al. “MMT Observations of the Black Hole Candidate XTE J1118+480 near and in Quiescence”. In: *ApJ* 612 (Sept. 2004), pp. 1026–1033. doi: [10.1086/422740](https://doi.org/10.1086/422740). eprint: [astro-ph/0405509](https://arxiv.org/abs/astro-ph/0405509).
- [106] D. M. Gelino et al. “The Inclination Angle and Mass of the Black Hole in XTE J1118+480”. In: *ApJ* 642 (May 2006), pp. 438–442. doi: [10.1086/500924](https://doi.org/10.1086/500924). eprint: [astro-ph/0601409](https://arxiv.org/abs/astro-ph/0601409).
- [107] J. Casares et al. “On the mass of the compact object in GRO J0422+32”. In: *MNRAS* 276 (Oct. 1995), pp. L35–L39. doi: [10.1093/mnras/276.1.L35](https://doi.org/10.1093/mnras/276.1.L35).
- [108] G. Beekman et al. “The mass of the black hole in the low-inclination LMXB transient system GRO J0422+32 (=Nova Persei 1992)”. In: *MNRAS* 290 (Sept. 1997), pp. 303–312. doi: [10.1093/mnras/290.2.303](https://doi.org/10.1093/mnras/290.2.303).
- [109] N. A. Webb et al. “A TiO study of the black hole binary GRO J0422+32 in a very low state”. In: *MNRAS* 317 (Sept. 2000), pp. 528–534. doi: [10.1046/j.1365-8711.2000.03608.x](https://doi.org/10.1046/j.1365-8711.2000.03608.x). eprint: [astro-ph/0004235](https://arxiv.org/abs/astro-ph/0004235).
- [110] D. M. Gelino and T. E. Harrison. “GRO J0422+32: The Lowest Mass Black Hole?” In: *ApJ* 599 (Dec. 2003), pp. 1254–1259. doi: [10.1086/379311](https://doi.org/10.1086/379311). eprint: [astro-ph/0308490](https://arxiv.org/abs/astro-ph/0308490).
- [111] I. F. Mirabel et al. “A high-velocity black hole on a Galactic-halo orbit in the solar neighbourhood”. In: *Nature* 413 (Sept. 2001), pp. 139–141. doi: [10.1038/35093060](https://doi.org/10.1038/35093060). eprint: [astro-ph/0109098](https://arxiv.org/abs/astro-ph/0109098).

*Chapter 3*IMPROVED METHODS FOR SIMULATING NEARLY
EXTREMAL BINARY BLACK HOLES

Mark A. Scheel, Matthew Giesler, Daniel A. Hemberger, Geoffrey Lovelace,
Kevin Kuper, Michael Boyle, Béla Szilágyi, and Lawrence E. Kidder

Classical and Quantum Gravity, 32, 105009 (2015)

[arxiv:1412.1803](https://arxiv.org/abs/1412.1803)

3.1 Abstract

Astrophysical black holes could be nearly extremal (that is, rotating nearly as fast as possible); therefore, nearly extremal black holes could be among the binaries that current and future gravitational-wave observatories will detect. Predicting the gravitational waves emitted by merging black holes requires numerical-relativity simulations, but these simulations are especially challenging when one or both holes have mass m and spin S exceeding the Bowen-York limit of $S/m^2 = 0.93$. We present improved methods that enable us to simulate merging, nearly extremal black holes (i.e., black holes with $S/m^2 > 0.93$) more robustly and more efficiently. We use these methods to simulate an unequal-mass, precessing binary black hole coalescence, where the larger black hole has $S/m^2 = 0.99$. We also use these methods to simulate a non-precessing binary black hole coalescence, where both black holes have $S/m^2 = 0.994$, nearly reaching the Novikov-Thorne upper bound for holes spun up by thin accretion disks. We demonstrate numerical convergence and estimate the numerical errors of the waveforms; we compare numerical waveforms from our simulations with post-Newtonian and effective-one-body waveforms; we compare the evolution of the black-hole masses and spins with analytic predictions; and we explore the effect of increasing spin magnitude on the orbital dynamics (the so-called “orbital hangup” effect).

3.2 Introduction

Second-generation interferometers such as Advanced LIGO, Virgo, and KAGRA [1–4] will soon begin searching for gravitational waves. To increase the number of gravitational-wave detections and to maximize what we can learn about the waves’ sources, we require accurate theoretical models of the sources and the emitted

gravitational radiation.

The inspiral, merger, and ringdown of binary black holes (BBHs) are among the most promising astrophysical sources of gravitational waves. As the black holes orbit, they lose energy to gravitational radiation, inspiraling until they collide and merge to form a final black hole (the “remnant”) that eventually settles to a stationary Kerr state.

A BBH is characterized by 7 intrinsic parameters: the spin angular momenta \vec{S} of each hole and the mass ratio q . The spin magnitude of a black hole is often characterized by the dimensionless quantity $\chi \equiv S/m^2$, where $S = |\vec{S}|$, m is the black-hole mass, and we use geometrized units where $c = G = 1$. A black hole with the maximum possible dimensionless spin $\chi = 1$ is called extremal. There is considerable uncertainty in the expected mass ratios and spins of astrophysical BBHs that are likely to be detected by gravitational-wave interferometers; however, there is evidence that nearly extremal black holes exist in nature. For instance, recent measurements of stellar-mass black holes (such as Cygnus X-1 [5–7], GRS 1915+105 [8], and GX 339-4 [9]) and supermassive black holes (such as Swift J0501.9-3239 [10]) suggest that there could be a population of black holes with spins of $\chi \sim 1$. (See, e.g., Refs. [11, 12] for reviews of astrophysical black-hole spin measurements.)

Post-Newtonian (PN) methods accurately model the binary evolution and the emitted gravitational radiation during the early inspiral [13], but numerical simulations solving the full Einstein equations are necessary to model the binary through late inspiral, merger, and ringdown. Following breakthroughs in 2005–2006 [14–16], a number of research groups have made tremendous progress toward simulating merging black holes with different black-hole masses and spins (see, e.g., [17–20] for recent reviews), and several groups are building catalogs of BBH simulations [21–26].

So far, the region of the parameter space with black-hole spins near the theoretical maximum $\chi = 1$ remains almost completely unexplored. Numerical simulations of nearly extremal, merging black holes are especially challenging. One reason for this is that initial data for a BBH must satisfy the Einstein constraint equations, but the simplest method for constructing constraint-satisfying initial data, the Bowen-York method [27–29], cannot yield initial data with nearly extremal black holes. This is because the Bowen-York construction assumes that the initial spatial geometry is conformally flat (i.e., that the initial spatial metric is proportional to the metric of flat space). Conformally flat spacetimes cannot represent black holes that i) are in

equilibrium, and ii) possess linear [30] or angular [31, 32] momentum; therefore, conformally-flat spinning black holes are out of equilibrium and will quickly relax to an equilibrium state. Specifically, Bowen-York puncture initial data can produce BBHs with initial spins as large as $\chi = 0.984$, but when evolved, the spins rapidly relax to about $\chi = 0.93$ or less (the Bowen-York limit) [33–35].

Even given initial data containing black holes with spins exceeding the Bowen-York limit, evolving those data through inspiral, merger, and ringdown is especially challenging for two reasons, as discussed in Refs. [36–38]. First, the portion of the spacetime near the horizons requires very high resolution (and thus high computational cost), since metric gradients are much larger than for lower spins. Second, for evolution methods that excise the singularities inside each black hole and evolve only the exterior region, constructing and maintaining a suitable computational domain that keeps each excision boundary just inside the corresponding apparent horizon becomes more and more challenging as the spin approaches extremality.

In this paper, we use the phrase “nearly extremal” to refer to $\chi > 0.93$, i.e., to a black hole with a spin above the Bowen-York limit. Note that a black hole with $\chi = 0.93$ is significantly less extremal than a black hole with $\chi = 0.998$, the Novikov-Thorne upper bound for black holes spun up by accretion [39, 40]. This is because the effects of spin scale nonlinearly with increasing χ . For instance, if the rotational energy of a Kerr black hole with a fixed mass is denoted $E_{\text{rot}}(\chi)$, then $E_{\text{rot}}(0.93)/E_{\text{rot}}(1)$ is only 59%, while $E_{\text{rot}}(0.998)/E_{\text{rot}}(1)$ is 92.5% (c.f., Fig. 1 of Ref. [36]). Furthermore, the total energy that a BBH emits in gravitational waves also scales nonlinearly with χ . For example, for equal masses and equal spins aligned with the orbital angular momentum, a BBH with $\chi = 1$ radiates 10% more energy than a BBH with $\chi = 0.93$, whereas a BBH with $\chi = 0.07$ radiates only 4% more energy than a BBH with $\chi = 0$ (Eq. (9) of Ref. [41]). Nonlinear scaling with χ is also seen for binaries consisting of a black hole and a neutron star: the amount of neutron-star matter remaining outside the black hole just after tidal disruption increases very rapidly with black-hole spin (Fig. 10 of Ref. [38]).

Several groups have constructed and evolved Bowen-York puncture initial data with spins near (but below) the Bowen-York limit [42–45]. Recently, Ruchlin et al. [46] constructed and evolved puncture initial data for a head-on collision of two black holes with equal mass and spins of magnitude $\chi = 0.99$. Only four previously published simulations [24, 36, 37] out of hundreds published to date contain the quasi-circular coalescence of BBHs with $\chi > 0.93$. These four simulations were evolved using the

Spectral Einstein Code (SpEC) [47] from “superposed-Kerr-Schild” excision initial data [48] and have equal masses and equal spins aligned or anti-aligned with the orbital angular momentum.

In this paper, we present technical improvements that have enabled us to simulate BBHs with black-hole spins up to $\chi = 0.994$ (*i.e.*, $E_{\text{rot}}(0.994)/E_{\text{rot}}(1) = 87.1\%$) and to complete the first nearly extremal BBH simulation that includes precession. We compare the results of these simulations with analytical models describing the remnant properties (e.g. final spin and total radiated energy) as a function of the initial black-hole spins; these models were constructed using lower-spin simulations and then extrapolated to higher spins. We measure the slow increase in mass (“tidal heating”) and decrease in spin (“tidal torquing”) of the individual black holes before merger, and we compare these measurements with perturbative calculations of the same quantities. We also compare gravitational waveforms from these simulations with post-Newtonian and effective-one-body [49] models.

The methods described here allow us to robustly explore the portion of the BBH parameter space where one or both black holes are nearly extremal. Simulations using these methods will enable us to calibrate and validate analytic waveform models, construct improved models of the dependence of remnant properties on the initial masses and spins of the black holes, and explore the dynamics of the strongly warped spacetime during the merger. In a companion paper, we use these methods to explore the extremality of apparent horizons in numerical simulations [50].

The remainder of this paper is organized as follows. We summarize our techniques in Sec. 3.3, focusing on new improvements to our algorithm that enable us to simulate higher black-hole spins more robustly. We present three new simulations in Sec. 3.4, and we present results in Sec. 3.5, including a comparison of the emitted gravitational waveforms with analytical predictions and also a comparison of the evolution of the black-hole masses and spins with analytic predictions. We briefly conclude in Sec. 3.6.

3.3 Techniques

We carry out numerical simulations with the Spectral Einstein Code (SpEC) [47]. We construct [51] quasi-equilibrium [48, 52] constraint-satisfying [53] initial data based on a weighted superposition of two boosted, spinning Kerr-Schild black holes [48]. We use an iterative method to produce initial data with low eccentricity [54–56].

We use a generalized harmonic formulation [57–60] of Einstein’s equations and

damped harmonic gauge [61–63] to evolve the initial data. The adaptively-refined [36, 64] grid extends from pure-outflow excision boundaries just inside the apparent horizons [63, 65–67] to an artificial outer boundary, where we enforce constraint-preserving boundary conditions [60, 68, 69]. The grid has only one excision boundary after the holes merge [65, 66]. We use a pseudospectral fast-flow algorithm [70] to find apparent horizons, and we compute spins on these apparent horizons using the approximate Killing vector formalism of Cook, Whiting, and Owen [71, 72].

In the remainder of this section, we describe new techniques that allow simulations of binaries with large black-hole spins. Large spins are difficult for two reasons. First, the metric gradients near the black-hole horizons become larger with larger spin, making increased numerical resolution necessary in this region. Second, black-hole excision is more difficult: in SpEC, we remove the physical singularity inside each black hole by placing an artificial *excision boundary* just inside each apparent horizon and evolve only the region exterior to all excision boundaries. We find that the maximum required coordinate distance between an excision boundary and the corresponding horizon becomes smaller with larger spin, so that our algorithm for dynamically adjusting the excision boundaries to track the size, shape, and motion of the horizons must be more accurate. We consider both of these difficulties below.

Not all of the improvements discussed here were necessary for all of the simulations described in Sec. 3.4. For example, the simulation discussed in Sec. 3.4 succeeded without some of the grid and control system improvements; however, these improvements became necessary when simulating even larger black-hole spins (Sec. 3.4) or allowing generic spin directions and unequal masses (Sec. 3.4).

Grid improvements

Meeting the need for high resolution near the horizons is accomplished via spectral adaptive mesh refinement [64]. This includes both p -type refinement (changing the number of collocation points in a given spectral subdomain) and h -type refinement (adding, removing, or changing the distribution of subdomains). The simulations described here used the algorithm detailed in [64], with adjustments to default parameters so as to allow for higher resolution. In particular: We increased the number of radial collocation points in a spherical subdomain that forces h -refinement from 20 points to 40, we disabled angular h -refinement in the spherical subdomains that touch the excision boundary so as to retain a single spherical subdomain at this boundary, and we increased the allowed number of spherical-harmonic coefficients

in spherical shells from $L = 40$ to $L = 80$. Note that most of these changes (such as allowing up to $L = 80$) were necessary only for a small portion of the simulation when the horizons are highly distorted, such as during the initial “junk radiation” transients (when spurious gravitational radiation is emitted as the BBH relaxes to equilibrium) and near the moment of merger.

We also reduced the initial distance between the apparent horizons and the excision boundaries. To understand this change, note that when solving elliptic equations for initial data, the excision boundaries are made to coincide exactly with the apparent horizons via boundary conditions imposed on those surfaces. But for the evolution, the excision boundaries must be slightly inside the horizons, so that the horizons are fully contained in the computational domain and therefore can be determined by the apparent horizon finder. To accomplish this, after the initial data have been determined, these data are extrapolated slightly inside the horizons to a new excision boundary, before the evolution begins. For large spins, this extrapolation occurs in the region where metric gradients are growing rapidly as r decreases, so placing the excision boundary at a larger r reduces those gradients. To carry out some of the simulations shown here, we moved the initial excision boundary radius from 94% to 98% of the initial horizon radius.

Control system improvements

Several of the improvements necessary for handling high spins involve control systems used to adjust mappings between coordinate systems. These control systems and the mappings are described in detail in [66]. Here we briefly summarize important points, and we discuss key differences from [66].

Summary of size and shape control systems

In SpEC, we remove the physical singularity inside each black hole by placing an artificial excision boundary just inside each apparent horizon, evolving only the region exterior to all excision boundaries. We use multiple coordinate systems to handle excision of black holes that are moving and changing shape [63, 65, 66, 73–76]. We call “inertial coordinates” \bar{x}^i those asymptotically inertial coordinates in which the black holes orbit each other, have a distorted and dynamical shape, and approach each other as energy is lost to gravitational radiation. We apply spectral methods in a different coordinate system, “grid coordinates” x^i , in which the excision boundaries are spherical and time-independent. We connect these two coordinate

systems with an analytic mapping function $\mathcal{M}: x^i \rightarrow \bar{x}^i$ that depends on a set of time-dependent parameters $\lambda(t)$. These parameters $\lambda(t)$ are adjusted automatically by feedback control systems so that, as the apparent horizons of the black holes move and change shape (in the inertial frame), the excision boundaries are mapped to inertial-coordinate surfaces that follow this motion and remain just inside the apparent horizons.

The control of all parameters $\lambda(t)$ is accomplished in the same way, using a general control system we have developed, as described in [66]. The part of the algorithm that distinguishes one $\lambda(t)$ from another is the specification of the control error $Q(t)$, which is different for each control parameter. For example, the $\lambda_{\text{Scaling}}(t)$ that represents the distance between the excision boundaries has a different $Q(t)$ than the matrix $\lambda_{\text{Rotation}}(t)$ that represents the rotation of the inertial coordinates with respect to the grid coordinates. If there exists a desired value of $\lambda(t)$, call it λ_{target} , which depends on observables A (such as the positions or shapes of the apparent horizons) but does not depend on λ itself, then we define

$$Q(t) = \lambda_{\text{target}}(A) - \lambda(t). \quad (3.1)$$

For more general situations in which λ_{target} depends on λ itself, we generalize the above definition: we require that λ takes on its desired value when $Q = 0$, and we require that

$$\frac{\partial Q}{\partial \lambda} = -1 + \mathcal{O}(Q). \quad (3.2)$$

Given $Q(t)$, our algorithm adjusts the corresponding $\lambda(t)$ so that $Q(t)$ is driven towards zero; this driving occurs on a timescale τ_d that is determined dynamically and that is different for each control system.

The full map from grid to inertial coordinates is $\bar{x}^i = \mathcal{M}x^i$, where

$$\begin{aligned} \mathcal{M} = & \mathcal{M}_{\text{Translation}} \circ \mathcal{M}_{\text{Rotation}} \circ \mathcal{M}_{\text{Scaling}} \\ & \circ \mathcal{M}_{\text{Skew}} \circ \mathcal{M}_{\text{CutX}} \circ \mathcal{M}_{\text{Shape}}. \end{aligned} \quad (3.3)$$

Each of these maps is described in detail in Sec. 4 of [66].

Shape control. Here we are concerned only with the last map, $\mathcal{M}_{\text{Shape}}$, which is defined as:

$$x^i \mapsto x^i \left(1 - \sum_H \frac{f_H(r_H, \theta_H, \phi_H)}{r_H} \sum_{\ell m} Y_{\ell m}(\theta_H, \phi_H) \lambda_{\ell m}^H(t) \right). \quad (3.4)$$

The index H goes over each of the two excised regions A and B , and the map is applied to the grid-frame coordinates. The polar coordinates (r_H, θ_H, ϕ_H) centered

about excised region H are defined in the usual way, the quantities $Y_{\ell m}(\theta_H, \phi_H)$ are spherical harmonics, and $\lambda_{\ell m}^H(t)$ are expansion coefficients that parameterize the map near excision region H ; these $\lambda_{\ell m}^H(t)$ are the coefficients that we adjust using a control system. The function $f_H(r_H, \theta_H, \phi_H)$ is chosen to be unity near excision region H and zero near the other excision region, so that the distortion maps for the two black holes are decoupled; see Eq. 72 and Fig. 4 of [66] for a precise definition of $f_H(r_H, \theta_H, \phi_H)$. In the following, the control systems for each excised region H , while independent, are identical in operation, so we will omit the H labels for simplicity.

We control $\lambda_{\ell m}(t)$ so that each excision boundary is driven to the same shape as the corresponding apparent horizon; this results in conditions on $\lambda_{\ell m}(t)$ for $\ell > 0$, but leaves $\lambda_{00}(t)$ unconstrained [66].

Size control. The size of the excision boundary, as encoded in the remaining coefficient $\lambda_{00}(t)$, must satisfy two conditions.

Horizon tracking. The first is that the excision boundary remains inside the apparent horizon. To satisfy this condition, we first write the shape of each apparent horizon as an expansion in spherical harmonics, parameterized in terms of polar coordinates about the center of the corresponding excision boundary,

$$\hat{r}^{\text{AH}}(\hat{\theta}, \hat{\phi}) = \sum_{\ell m} \hat{S}_{\ell m} Y_{\ell m}(\hat{\theta}, \hat{\phi}), \quad (3.5)$$

where the intermediate frame \hat{x}^i is connected to the grid frame by the map

$$\mathcal{M}_{\text{Distortion}} = \mathcal{M}_{\text{CutX}} \circ \mathcal{M}_{\text{Shape}}. \quad (3.6)$$

By construction, $\mathcal{M}_{\text{Distortion}}$ leaves invariant the centers of the excision boundaries, and the angles with respect to these centers. Then we choose

$$Q = \dot{\hat{S}}_{00}(\Delta r - 1) - \dot{\lambda}_{00} \quad (3.7)$$

where

$$\Delta r = 1 - \frac{\langle \hat{r}_{\text{EB}} \rangle}{\langle \hat{r}_{\text{AH}} \rangle} \quad (3.8)$$

is the relative difference between the average radius of the apparent horizon (in the intermediate frame) and the average radius of the excision boundary. The angle brackets in Eq. (3.8) represent averaging over angles. Choosing $Q(t)$ according to Eq. (3.7) drives $d/dt(\Delta r)$ towards zero, so that the excision boundary remains a fixed (relative) distance inside the apparent horizon.

Characteristic speed tracking. The second condition that must be satisfied by $\lambda_{00}(t)$ involves characteristic speeds of the evolved Einstein equations: well-posedness of our system of equations requires that all of the characteristic speeds be non-negative, i.e. characteristic fields must flow into the black hole. The minimum characteristic speed at each excision boundary is given by

$$v = -\alpha - \bar{\beta}^i \bar{n}_i - \bar{n}_i \frac{\partial \bar{x}^i}{\partial t}, \quad (3.9)$$

where α is the lapse, $\bar{\beta}^i$ is the shift, and \bar{n}_i is the normal to the excision boundary pointing *out of the computational domain*, i.e., toward the center of the hole. It is possible to write [66]

$$v = v_0 + \hat{n}_i \frac{x^i}{r} Y_{00} \dot{\lambda}_{00}, \quad (3.10)$$

where v_0 collects all terms that are independent of $\dot{\lambda}_{00}$. Therefore, a control system that controls $\dot{\lambda}_{00}$ and drives v to some target value v_T can be constructed by defining the control error

$$Q = (\min(v) - v_T) / \langle -\Xi \rangle, \quad (3.11)$$

where

$$\Xi = \hat{n}_i \frac{x^i}{r} Y_{00}, \quad (3.12)$$

and the minimum is over the excision boundary. Note that $\Xi < 0$ because \hat{n}_i and x^i/r point in opposite directions.

Switching between horizon and characteristic speed tracking. Note that Eqs. (3.7) and (3.11) specify two *different* control systems that control the same degree of freedom, λ_{00} : the first control system, which we call “horizon tracking”, adjusts $\dot{\lambda}_{00}$ to control Δr , and the other, which we call “characteristic speed tracking”, adjusts $\dot{\lambda}_{00}$ to control v . Both Δr and v must remain nonnegative for a successful evolution, but we cannot use both Eqs. (3.7) and (3.11) simultaneously. Furthermore, changes in $\dot{\lambda}_{00}$ affect Δr and v in the opposite direction: if $\dot{\lambda}_{00}$ increases, Δr increases, but the characteristic speed v decreases.

In practice (Sec. 3.3), we now alternate between the two control systems, Eqs. (3.7) and (3.11). We monitor both v and Δr as functions of time and predict whether either of these quantities is likely to become negative in the immediate future; if so, we estimate the timescale τ_v or $\tau_{\Delta r}$ on which this will occur. If $\tau_{\Delta r}$ is small enough, i.e. Δr is in imminent danger of becoming negative, we use Eq. (3.7) to control Δr . If τ_v is small enough that v is in danger of becoming negative, we use Eq. (3.11) to

control v . The details of how we make these decisions have been improved since the description in Sec. 5.3 of [66], so we describe the improved algorithm below.

Improved choice of control system timescales

We now describe improvements in the control systems that were necessary for our new high-spin simulations to succeed.

Comoving characteristic speed as a control system diagnostic. We define a new quantity v_c which we call the *comoving characteristic speed*:

$$v_c = -\alpha - \bar{\beta}^i \bar{n}_i - \bar{n}_i \frac{\partial \bar{x}^i}{\partial \hat{t}} + \hat{n}_i \frac{x^i}{r} \left[Y_{00} \hat{S}_{00} (\Delta r - 1) + \sum_{\ell > 0} Y_{\ell m}(\theta, \phi) \dot{\lambda}_{\ell m}(t) \right]. \quad (3.13)$$

The comoving characteristic speed v_c is what the characteristic speed v *would be* if $Q(t)$ in Eq. (3.7) were exactly zero, i.e. if Δr were constant in time. In other words, if we turn on horizon tracking, the control system drives v toward v_c . This tells us (for instance) that if we find $v_c < 0$, we should not use horizon tracking, since horizon tracking would drive v to a negative value. The instantaneous value of v_c is independent of $\dot{\lambda}_{00}$ and roughly independent of λ_{00} ; the only dependence on λ_{00} comes from the smooth spatial variation of the metric functions. Hence, v_c is a useful quantity for separating the effects of the control system for $\dot{\lambda}_{00}$ from the effects of other control systems.

One way we use v_c is in determining whether our control system for $\dot{\lambda}_{00}$ will fail. During a simulation, v_c is usually positive, but it routinely becomes negative for short periods of time, particularly when the shapes of the horizons are changing rapidly, for example near $t = 0$ when the black holes are ringing down from initial “junk radiation” transients. However, if v_c becomes negative and remains so indefinitely, our control system for $\dot{\lambda}_{00}$ must eventually fail. This is because for $v > 0$ and $v_c < 0$, Δr must be decreasing, so if we keep $v > 0$ the excision boundary will eventually intersect the apparent horizon.

Control error damping timescale improvements. For many of the high-spin SpEC simulations that failed before we made the improvements described in this paper, we observed that $v_c < 0$ for an extended period of time. This was caused by inaccurate control systems for the $\lambda(t)$ parameters *other than* λ_{00} ; in particular, the shape parameters $\lambda_{\ell m}$ for $\ell > 0$. In other words, the shape and position of the excision

boundary differed from the shape and position of the horizon by a sufficient amount that it was not possible to make both $v > 0$ and $\Delta r > 0$ everywhere by adjusting only the radial motion of the excision boundary, λ_{00} .

This particular problem was fixed by changing the algorithm for setting the tolerance on the control error $Q(t)$, for all $Q(t)$ except Q_{00} . Associated with each of our control systems is a timescale parameter τ_d which is adjusted dynamically. The control error $Q(t)$ is damped like e^{-t/τ_d} , under the assumption that τ_d is smaller than all other timescales in the problem. Therefore decreasing τ_d results in smaller values of $Q(t)$. The previous method of adjusting τ_d is described in Sec. 3.3 of [66]: at regular time intervals t_i , the timescale is changed according to

$$\tau_d^{i+1} = \beta \tau_d^i, \quad (3.14)$$

where

$$\beta = \begin{cases} 0.99, & \text{if } \dot{Q}/Q > -1/2\tau_d \text{ and } |Q| \text{ or } |\dot{Q}\tau_d| > Q_t^{\text{Max}} \\ 1.01, & \text{if } |Q| < Q_t^{\text{Min}} \text{ and } |\dot{Q}\tau_d| < Q_t^{\text{Min}} \\ 1, & \text{otherwise.} \end{cases} \quad (3.15)$$

Here Q_t^{Min} and Q_t^{Max} are thresholds for the control error Q , set to constant values

$$Q_t^{\text{Max}} = \frac{2 \times 10^{-3}}{m_A/m_B + m_B/m_A}, \quad (3.16)$$

$$Q_t^{\text{Min}} = \frac{1}{4} Q_t^{\text{Max}}, \quad (3.17)$$

where m_A and m_B are the Christodoulou masses of the two black holes.

In the new algorithm, we make three changes. The first is that Q_t^{Max} is no longer a constant: instead, it is chosen to be $Q_t^{\text{Max}} = a\Delta r_{\text{min}}$, where a is a constant (typically chosen to be $0.05(m_A + m_B)$ for those Q values with dimensions of length, and 0.05 for those Q values that are dimensionless) and Δr_{min} is the minimum relative distance between the excision boundary and the apparent horizon:

$$\Delta r_{\text{min}} = \min_{\hat{\theta}, \hat{\phi}} \left(1 - \frac{\hat{r}_{\text{EB}}(\hat{\theta}, \hat{\phi})}{\hat{r}_{\text{AH}}(\hat{\theta}, \hat{\phi})} \right). \quad (3.18)$$

The second change is that we define an estimate of the time that the horizon will cross the excision surface

$$\tau_{\Delta r \text{cross}} = -\Delta r_{\text{min}} \left(\frac{d}{dt} \Delta r_{\text{min}} \right)^{-1}, \quad (3.19)$$

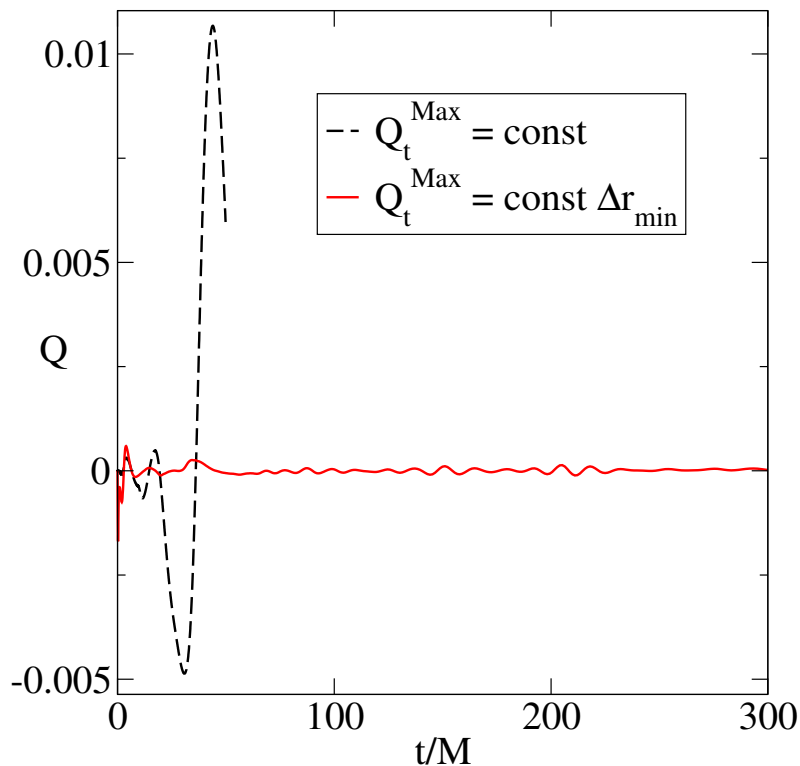


Figure 3.1: The control error $Q(t)$ associated with one particular control system for two different $S_{0.994}^{++}$ simulations which differ only in the treatment of Q_t^{Max} for that control system. The black dashed curve shows the case in which Q_t^{Max} is a constant, given by Eq. (3.16), and the red solid curve shows the case in which Q_t^{Max} is chosen to be $0.05\Delta r_{\text{min}}$, with Δr_{min} given by Eq. (3.18). The former simulation crashes at $t \sim 50M$.

and if $\tau_{\Delta r_{\text{cross}}} > 0$ and $\tau_d^i > \tau_{\Delta r_{\text{cross}}}$, then we set $\tau_d^{i+1} = \tau_{\Delta r_{\text{cross}}}$ instead of using Eq. (3.14).

Both of the above changes force each $Q(t)$ to be closer to zero when the excision boundary approaches the horizon. A third, minor, change we make in the algorithm affects only the behavior of $Q(t)$ at early times: the initial values of each τ_d were decreased so that each $Q(t)$ is smaller at earlier times; these initial values are specified separately from the tolerances Q_t^{Max} that determine when τ_d is modified. The effect of the first change, setting Q_t^{Max} proportional to Δr_{min} , is illustrated in Fig. 3.1 for one particular control system.¹ In Fig. 3.1 and the remainder of the paper, $M \equiv m_A + m_B$

¹ The $Q(t)$ illustrated here is the one for the control system that computes a smooth approximation $\hat{r}_{\text{AH}}^{\text{appx}}(t)$ to the average horizon radius; this approximate value is used to compute \hat{S}_{00} and Δr in Eq. (3.7), in order to reduce the number of calls to the computationally expensive horizon finder (see section 7 and Eq. (108) of [66] for details).

is the sum of the Christodoulou masses of the two black holes at the time t_{relax} when the initial “junk radiation” transients have decayed away.

Size control: switching between Eqs. (3.7) and (3.11).

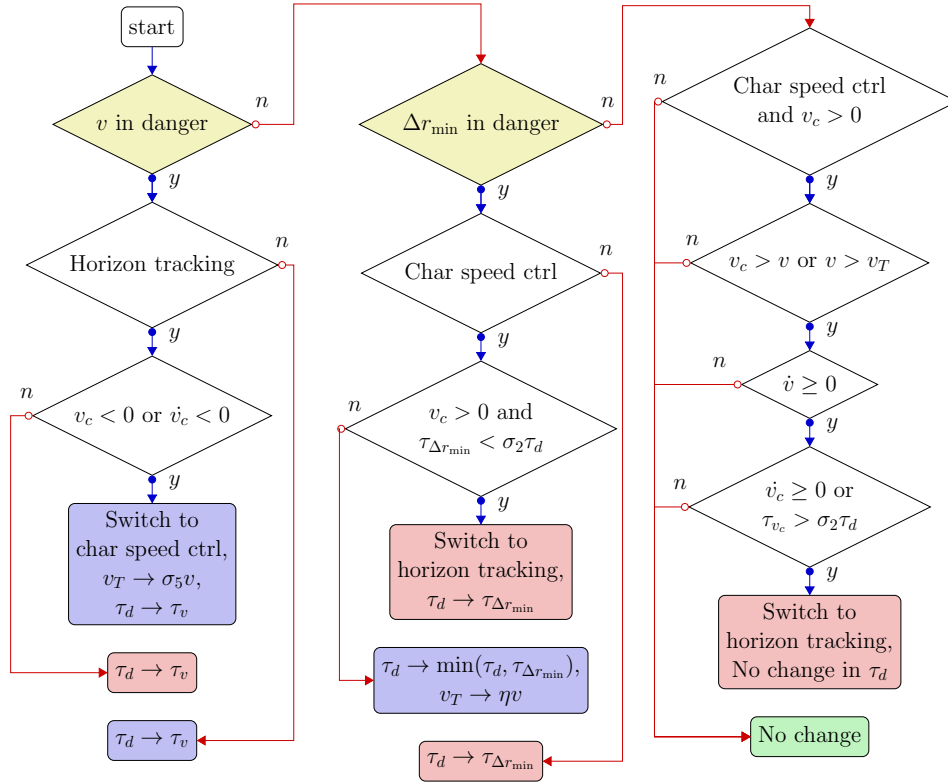


Figure 3.2: Flowchart illustrating how the control system for λ_{00} switches between horizon tracking (Q given by Eq. (3.7)) and characteristic speed control (Q given by Eq. (3.11)), and how the control system changes values of τ_d and v_T . The yellow diamonds labeled “ v in danger” and “ Δr_{\min} in danger” are illustrated in separate flowcharts in Fig. 3.3. Red final states indicate horizon tracking, purple final states indicate characteristic speed control, and the green final state indicates that no change is made. The algorithm is described in detail in § 3.3.

At every time step, the control system for λ_{00} is governed by a Q given by either Eq. (3.7) or Eq. (3.11), with an associated damping timescale τ_d and (if using characteristic speed control) a target speed v_T . At regular intervals (typically every time step), the algorithm has an opportunity to change from using Eq. (3.7) to using Eq. (3.11) or vice versa, and to choose a new value of τ_d and (if using characteristic speed control) v_T . Here we describe how we make these choices. A previous version of this algorithm was described in [66], but many improvements have been made since then. The algorithm is summarized by the flowcharts shown in Figs. 3.2 and 3.3.

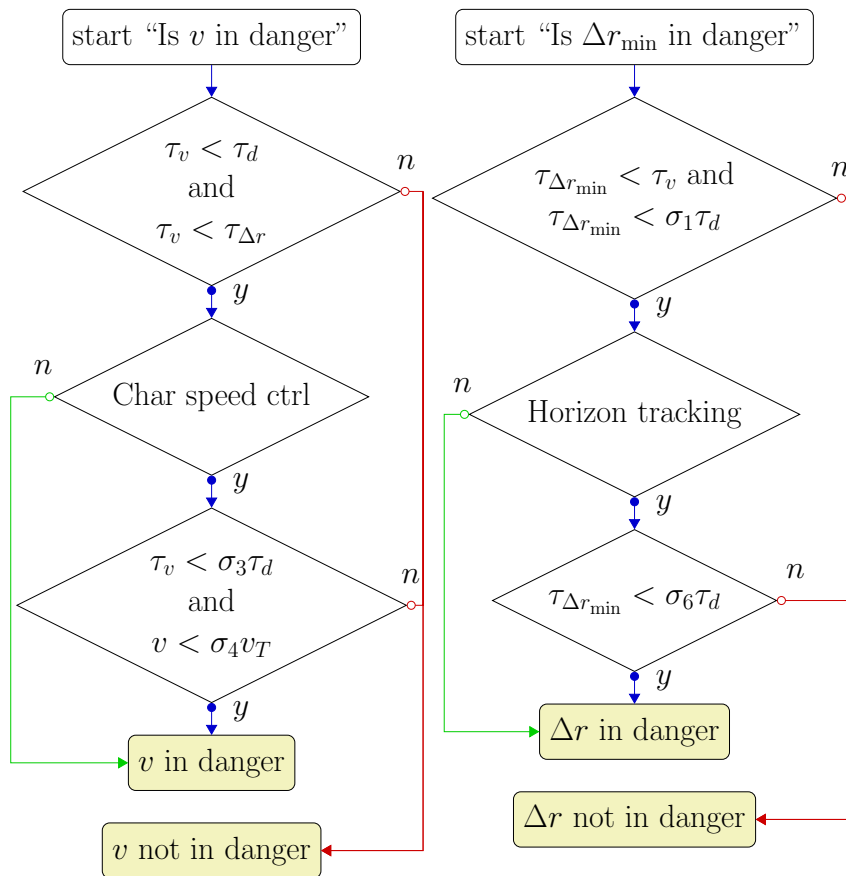


Figure 3.3: Flowcharts illustrating how the characteristic speed v (left) and the minimum distance between the horizon and the excision boundary Δr_{\min} (right) are deemed in danger of becoming negative. Each of these flowcharts is represented as a yellow diamond in Fig. 3.2.

Because the goal of the λ_{00} control system is to keep both v and Δr_{\min} positive, we regularly monitor v and Δr_{\min} as functions of time. We predict whether either of these quantities is likely to become negative in the immediate future, and if so, we estimate the timescale τ_v or $\tau_{\Delta r_{\min}}$ on which this will occur, using the method described in Appendix C of [66]. Because the sign of v_c is important to the success of horizon tracking, we also monitor v_c as a function of time, and if it is positive and decreasing, we predict the timescale τ_{v_c} on which it will become negative. If v , v_c , or Δr_{\min} are increasing instead of decreasing, we define the corresponding timescale τ_v , τ_{v_c} , or $\tau_{\Delta r_{\min}}$ to be infinite.

We begin by determining whether v is in imminent danger of becoming negative, so that some immediate action must be taken to prevent this from occurring. We regard v to be in danger if $\tau_v < \tau_d$ and $\tau_v < \tau_{\Delta r_{\min}}$. Furthermore, if characteristic

speed control is in effect, we additionally require $\tau_v < \sigma_3 \tau_d$ and $v < \sigma_4 v_T$ to deem v in danger; here $\sigma_3 \lesssim 1$ and $\sigma_4 \sim 1$ are constants, typically chosen to be 0.99 and 1.1, respectively². The first requirement, $\tau_v < \sigma_3 \tau_d$, prevents the algorithm from switching back and forth between characteristic speed control and horizon tracking on each time step. The second requirement, $v < \sigma_4 v_T$, prevents the control system from rapidly *decreasing* the characteristic speed to achieve a target v_T that is less than v .

If v is deemed to be in danger, the action taken to prevent v from becoming negative depends on the current state of the control system. If characteristic speed control is in effect, then it remains in effect, and τ_d is set equal to τ_v in order to drive v towards v_T more quickly. If horizon tracking is in effect, and if $v_c < 0$ or v_c is decreasing, then characteristic speed control goes into effect, with $v_T = \sigma_5 v$, and τ_d is left unchanged. The constant σ_5 , typically 1.01, prevents the control system from switching back and forth on each timestep. Finally, if horizon tracking is in effect, and if $v_c > 0$ and v_c is nondecreasing, then horizon tracking remains in effect and we set τ_d equal to τ_v . This change is all that is required because horizon tracking will drive v toward v_c , which is in no danger of becoming negative.

If v is deemed not to be in danger, then we check whether Δr_{\min} is in danger of soon becoming negative. We regard Δr_{\min} to be in danger if $\tau_{\Delta r_{\min}} < \tau_v$ and if $\tau_{\Delta r_{\min}} < \sigma_1 \tau_d$, where σ_1 is a constant typically chosen to be 20. Furthermore, if horizon tracking is in effect, we additionally require $\tau_{\Delta r_{\min}} < \sigma_6 \tau_d$ to deem $\tau_{\Delta r_{\min}}$ in danger, where $\sigma_6 < 1$ is usually chosen to be 0.99; this condition prevents the control system from switching on every time step.

If Δr_{\min} is in danger, the action again depends on the state of the control system and other variables. If horizon tracking is in effect, then it remains in effect, and τ_d is set equal to $\tau_{\Delta r_{\min}}$ in order to drive Δr_{\min} to a constant more quickly. If characteristic speed control is in effect, $v_c > 0$, and $\tau_{\Delta r_{\min}} < \sigma_2 \tau_d$, then horizon tracking goes into effect, and τ_d is set equal to $\tau_{\Delta r_{\min}}$. Here σ_2 is a constant we usually set to 5. We require $v_c > 0$ to activate horizon tracking because horizon tracking drives v towards v_c , and we wish to maintain $v > 0$; if horizon tracking becomes active even if $v_c < 0$, the simulation often fails, as shown in Fig. 3.4. To solve the problem illustrated by Fig. 3.4, when the code finds that Δr_{\min} is in danger while characteristic speed control is in effect and if $v_c < 0$, then the code allows characteristic speed control to remain in effect, but it sets the new τ_d to $\min(\tau_d, \tau_{\Delta r_{\min}})$, and it reduces v_T to ηv ,

²Labels for control system constants like σ_i and η are consistent with the notation in Ref. [66].

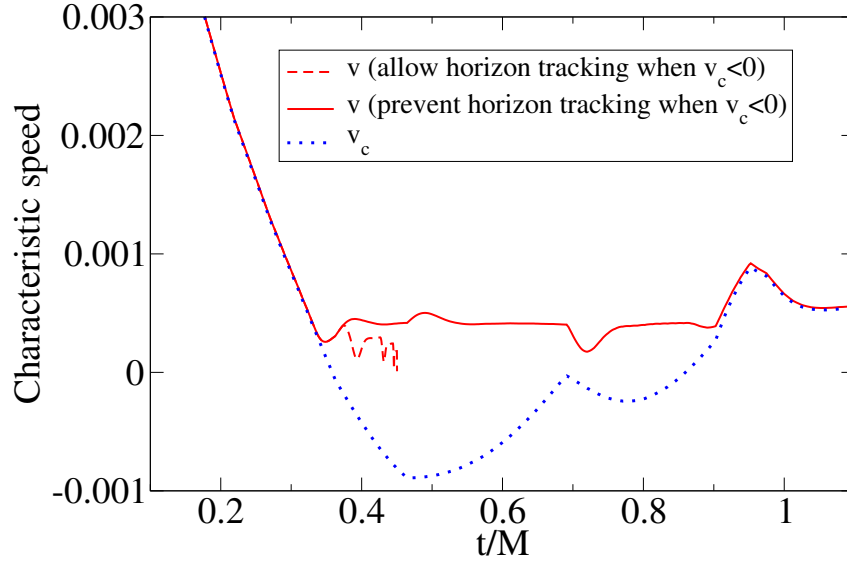


Figure 3.4: Characteristic speed v and comoving characteristic speed v_c for two different $S_{0.994}^{++}$ simulations that differ only in the algorithm for treating the situation in which Δr_{\min} is deemed in danger while characteristic speed control is in effect and $v_c < 0$. The dashed red curve shows v for a simulation in which horizon tracking becomes active in this situation; the code crashes early, at only $t \sim 0.4M$. The solid red curve shows v for a simulation in which for this situation characteristic speed control remains in effect, but the target characteristic speed is reduced as described in the text. The quantity v_c is the same for both simulations.

where $\eta < 1$ is a constant typically chosen to be 0.125. Reducing the target v_T will reduce v but will increase Δr_{\min} . If $v_c < 0$ for an extended period of time, several such reductions of v_T will occur as needed. As mentioned above, if $v_c < 0$ and remains so, this algorithm must eventually fail; the way to prevent such a failure is to adjust the control systems *other than* the one for λ_{00} to attempt to make v_c positive, as discussed in Sec. 3.3.

If neither v nor Δr_{\min} are in imminent danger of becoming negative, then the system attempts to find an equilibrium using horizon tracking. If characteristic speed control is in effect, and if $v_c > 0$, $\dot{v} \geq 0$, either $v > v_T$ or $v_c > v$, and either $\dot{v}_c \geq 0$ or $\tau_{v_c} > \sigma_2 \tau_d$, then horizon tracking goes into effect, using the current τ_d . The purpose of these various conditions on v , v_c , and their derivatives and predicted zero-crossing times is to prevent horizon tracking from going into effect when it is likely that a switch back to characteristic speed control will soon be necessary. For example, if v_c is decreasing fast enough so that $\tau_{v_c} < \sigma_2 \tau_d$, then we anticipate that v_c will soon become negative, in which case horizon tracking is inappropriate because it would

Name	SXS ID	t_{relax}	q^r	m_A^r	m_B^r	$M\omega_{\text{orb}}^r$	χ_A^r	θ_A^r/π	ϕ_A^r/π	χ_B^r	θ_B^r/π	ϕ_B^r/π	$10^4 e$	N_{orb}	M_f	χ_f
$\overline{S}_{0.99}^{++}$	0177	320	1.0	0.5	0.5	0.0154	0.989	0.00	–	0.989	0.00	–	12.6	25.4	0.888	0.949
$S_{0.994}^{++}$	0178	640	1.0	0.5	0.5	0.0157	0.994	0.00	–	0.994	0.00	–	8.6	25.4	0.887	0.950
$S_{0.20}^{0.99}$	0179	380	1.5	0.6	0.4	0.0148	0.991	0.00	0.73	0.200	0.24	0.23	322.4	23.8	0.922	0.897

Table 3.1: Summary of physical simulation parameters. Data are publicly available online [77] indexed by their Catalog ID. Quantities with an r superscript are reported at time $t = t_{\text{relax}}$, the time after the initial “junk radiation” transients have settled down: q is the mass ratio, m_H is the Christodoulou mass of an individual black hole (where H represents black hole A or B), $M\omega_{\text{orb}}$ is the orbital frequency (computed via $d^2\vec{\omega}_{\text{orb}} = \vec{d} \times \dot{\vec{d}}$, where \vec{d} is the coordinate separation between the black holes), χ_H is the dimensionless spin, θ_H is the angle between $\vec{\omega}_{\text{orb}}$ and $\vec{\chi}_H$, and ϕ_H is the angle between the separation vector and the component of $\vec{\chi}_H$ in the orbital plane. The remaining quantities are eccentricity e , number of orbits N_{orb} from $t = 0$ to merger, final Christodoulou mass M_f , and final spin magnitude χ_f .

drive v towards zero.

The behavior of the control system depends on various constants σ_i ($1 < i < 6$) and η described above; these constants govern decisions made by the algorithm. These constants have restricted values (e.g. η should not be greater than unity), but they were chosen without any fine tuning. Changing their values slightly will change details such as the exact value of τ_d at a particular timestep, but we expect that small changes in parameters will not change whether a simulation succeeds or fails, and will change physical results only at the level of truncation error (because the control system changes the grid coordinates).

Occasionally when horizon tracking is in effect, we find that the value of Δr_{min} is excessively large or small. If it is excessively small, then τ_d becomes small, and we are forced to reduce the timestep in the evolution equations to keep the control system stable, resulting in a large computational expense. If it is too large, then the excision boundary lies deep inside the horizon, and excessive computational resources are needed to resolve the large gradients. Therefore, we allow a drift term to sometimes be added to Eq. (3.7), as discussed in [66].

3.4 Simulations

We present three new simulations, summarized in Table 3.1. We will refer to quantities defined in Table 3.1 throughout the remainder of this paper. The techniques described in Sec. 3.3 were essential to the successful completion of these simulations.

Equal-mass, aligned spins $\chi = 0.99$

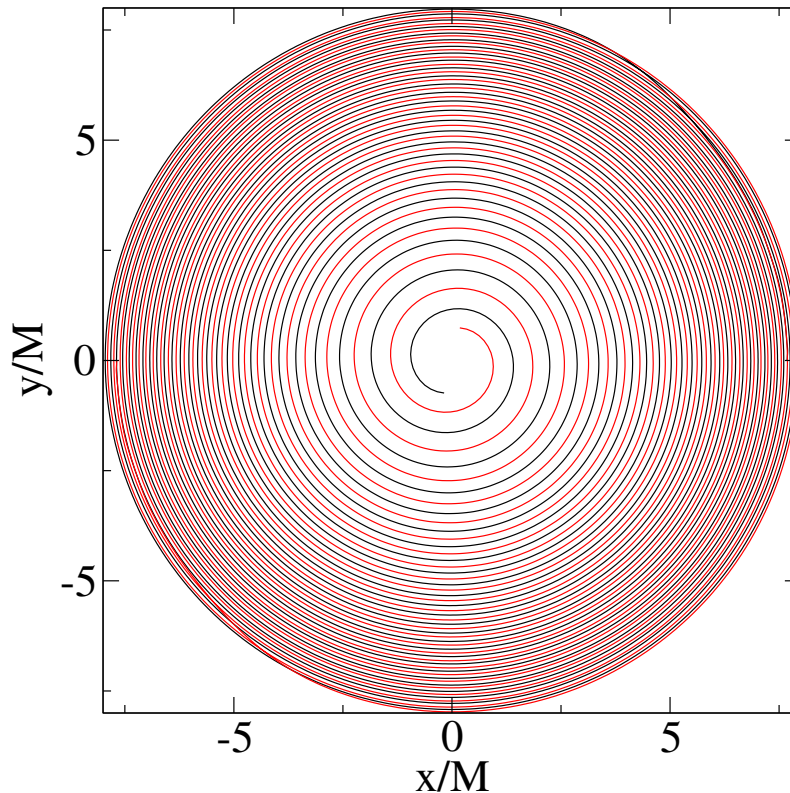


Figure 3.5: The trajectories of the centers of the individual apparent horizons for the highest resolution of $S_{0.99}^{++}$.

The first simulation we present, and refer to as $S_{0.99}^{++}$, is an equal-mass case in which each black hole has a spin of $\chi = 0.99$ aligned with the orbital angular momentum. At $t = t_{\text{relax}}$ the simulation has $M\omega_{\text{orb}} = 0.0154$, where M is the sum of the relaxed Christodoulou masses. The binary then evolves through 25 orbits, merger and ringdown. The coordinate trajectories of the black holes are shown in Fig. 3.5. This simulation took 83 days on 48 cores for the highest resolution.

To assess numerical convergence, we perform several simulations that are identical except for the numerical resolution, which we label by an integer N . Larger N corresponds to finer resolution, but the absolute scale of N is different for different physically distinct simulations. The value of N enters the simulation through the tolerance in adaptive mesh refinement (AMR): the AMR truncation error tolerance is chosen to be proportional to e^{-N} . For each value of N , we compute the complex phase ϕ of the $\ell = 2, m = 2$ component of Ψ_4 . We then take the difference $\Delta\phi$ between ϕ computed using otherwise-identical simulations using different values of

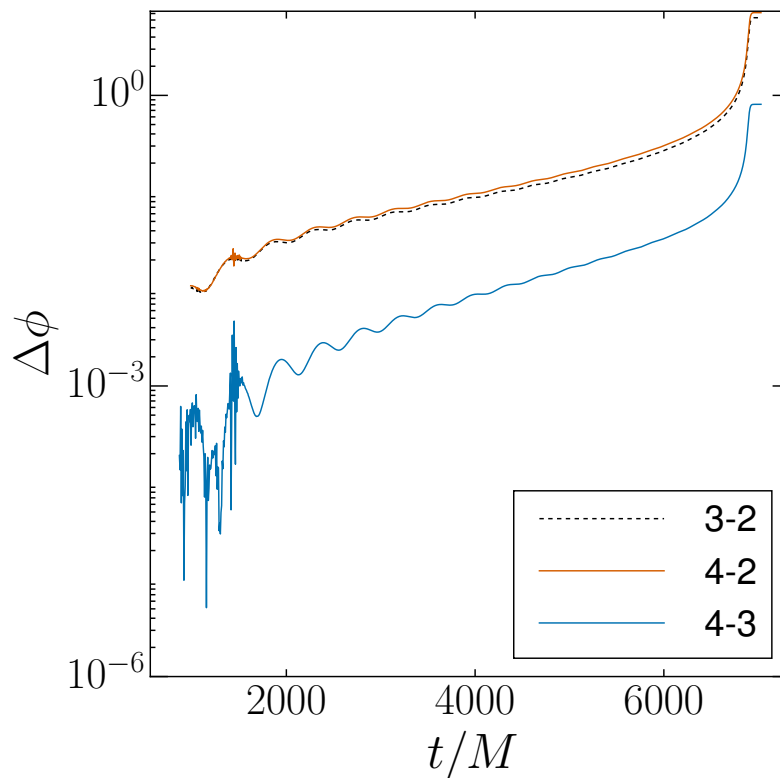


Figure 3.6: Convergence test for $S_{0.99}^{++}$. Shown are gravitational-wave phase differences between Ψ_4 computed using different values of the numerical resolution parameter N . Several differences are shown, and labeled by the values of N that are compared, e.g. “3-2” means $N = 3$ versus $N = 2$. Waveforms are extracted at a finite radius $r = 465M$, and no alignment of waveforms was performed.

N .

Figure 3.6 shows these differences for $S_{0.99}^{++}$. No alignment of the waveforms in time or phase has been performed. Note the rapid convergence: $\Delta\phi$ between $N = 3$ and $N = 4$ (labeled “4-3”) is significantly smaller than $\Delta\phi$ between the two lower resolutions. Also note that the difference “3-2” is nearly the same as “4-2”, indicating that this difference effectively measures the numerical truncation error in the $N = 2$ simulation. Similarly, the difference “4-3” represents the numerical truncation error in the $N = 3$ simulation. Furthermore, one would expect that the truncation error in the $N = 4$ simulation is smaller than the “4-3” curve by another order of magnitude (although it would be necessary to run an $N = 5$ simulation to actually measure this).

In the $S_{0.99}^{++}$ initial data, the spin of each black hole is 0.99. When the system is

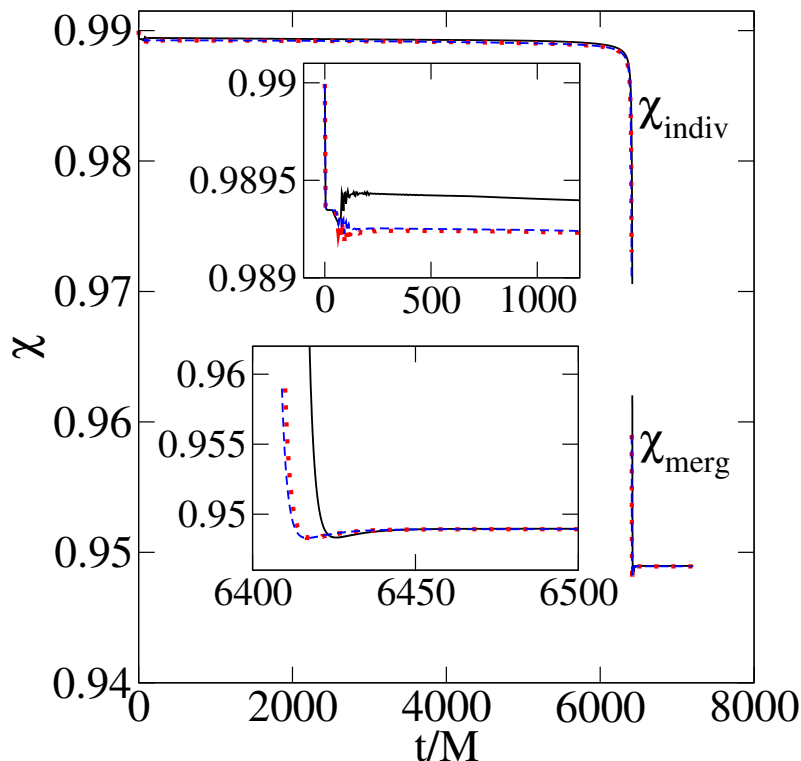


Figure 3.7: Spin magnitude as a function of time for $S_{0.99}^{++}$. At early times, the spin of one of the apparent horizons is shown at resolutions $N = 2$ (black solid), $N = 3$ (red dotted) and $N = 4$ (blue dashed). A closeup of early times is shown in the upper inset. At late times, the spin of the merged apparent horizon is shown as a function of time for the same resolutions, and a closeup of late times is shown in the lower inset.

evolved, the spins decrease very slightly for the first $\sim 10M$ as initial transients propagate away from the horizons, as shown in the upper inset of Fig. 3.7. Then the spins level off and become roughly constant, but with a small negative slope. All values of resolution N agree quite well, and the higher two resolutions are indistinguishable in Fig. 3.7. The spins decrease more rapidly just before merger ($t \sim 6400M$). The common horizon first appears with a spin greater than the final value, and then relaxes as the remnant black hole settles down, as shown in the lower inset of Fig. 3.7. The final spin is $\chi_f = 0.948927(3)$, where the uncertainty is the difference between the two highest resolution simulations.

The radiated energy fraction E_{rad} is the relative change in energy of the binary from $t = -\infty$ to $t = \infty$ and can be computed from

$$E_{\text{rad}} \equiv 1 - \frac{E_{\infty}}{E_{-\infty}} = 1 - \frac{M_f}{M}. \quad (3.20)$$

The final Christodoulou mass M_f is the energy of the system at $t = \infty$, because the remnant is in equilibrium at the end of the simulation; the total Christodoulou mass M at $t = t_{\text{relax}}$ is the energy of the system at $t = -\infty$, because the individual black-hole masses change by less than one part in 10^6 between $t = -\infty$ and $t = t_{\text{relax}}$ (see, e.g. Eq. 14 in Ref. [78]). We find that $E_{\text{rad}} = 11.26593(3)\%$, where the uncertainty is again the difference between the two highest resolutions.

The formulas from Ref. [41] predict $\chi_f = 0.94933(8)$ and a radiated energy fraction $E_{\text{rad}} = 11.24(2)\%$, in good agreement with the simulations. While the fractional differences between the measured and predicted values are small, their uncertainty intervals are disjoint, i.e. our measurements lie outside the uncertainty interval of the formulas. This is because the error estimates in Ref. [41] did not account for the observed correlated trends in the fit residuals (as seen in the lower panels of Figs. 6 and 8 of Ref. [41]). As a result, extrapolating these formulas to initial spins above $\chi = 0.97$ is expected to overestimate the final spin (see Fig. 6 in Ref. [41]) and underestimate the final radiated energy (see Fig. 8 in Ref. [41]), and this is what we find with $S_{0.99}^{++}$.

Equal-mass, aligned spins $\chi = 0.994$

We repeated the equal-mass aligned-spin simulation above, but with a larger spin. We refer to this case as $S_{0.994}^{++}$. The initial data were chosen with $\chi = 0.995$ for each black hole, but the spins drop to $\chi = 0.9942$ after about $t = 10M$ of evolution time, a much smaller timescale than the relaxation time t_{relax} (this rapid initial decrease in spin can also be seen for $S_{0.99}^{++}$ in the upper inset of Fig. 3.7). The simulation $S_{0.994}^{++}$ represents the largest spin ever simulated for a black-hole binary. It has $M\omega_{\text{orb}} = 0.0157$ at $t = t_{\text{relax}}$, and then proceeds through 25 orbits, merger, and ringdown. The highest resolution completed in approximately 71 days on 48 cores. Note that this simulation, $S_{0.994}^{++}$, was computationally cheaper than the lower-spin simulation, $S_{0.99}^{++}$, and achieved a smaller overall phase error (see Figs. 3.6 and 3.8). This is due to parallelization, load-balancing, and AMR improvements [64] that were done between the time that the $S_{0.99}^{++}$ and $S_{0.994}^{++}$ simulations were carried out; for the same version of SpEC, there is actually a steep increase in computational cost as a function of spin.

Obtaining convergence was more difficult for this simulation than for $S_{0.99}^{++}$. The reason is that it is difficult to fully resolve the initial transients, sometimes called “junk radiation”, that result from imperfect initial data. If these transients are unresolved,

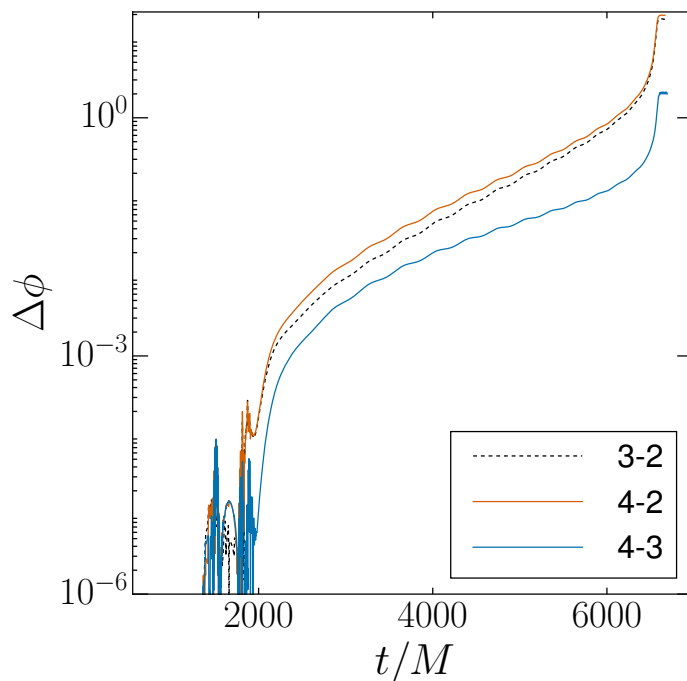


Figure 3.8: Convergence test for $S_{0.994}^{++}$. Labels are the same as for Fig. 3.6. For $N \neq 5$, the simulations were started at $t_{\text{branch}} = 1414M$, using the $N = 5$ solution as initial data.

then the small changes in masses, spins, and trajectories caused by these transients are effectively random, and therefore otherwise-identical simulations run with different values of resolution N will differ by random small amounts that will not converge with increasing N . So to investigate convergence, we remove the initial transients in the following way. We first carry out a simulation with one value of N , call it N_{base} . In the case of $S_{0.994}^{++}$, N_{base} represents the highest resolution. Then we choose some fiducial time $t = t_{\text{branch}} > t_{\text{relax}}$ at which we decide that the transients have decayed away³. We then carry out simulations with $N \neq N_{\text{base}}$ starting at $t = t_{\text{branch}}$, using the $N = N_{\text{base}}$ solution as initial data. This procedure removes the effects of the transients from our convergence tests.

However, this procedure alone was insufficient to achieve convergence. When convergence is rapid enough in a particular subdomain so that adding a single grid point results in a large decrease in truncation error, it is possible for two different AMR truncation error tolerances, e.g. e^N and e^{N-1} , to result in the same number of

³For the simulations presented here, t_{branch} was chosen *ad hoc*. As long as $t_{\text{branch}} > t_{\text{relax}}$, we do not expect the results to depend sensitively on t_{branch} .

grid points for that subdomain. This makes the truncation error in that subdomain identical for two different values of N , which spoils convergence tests for simulations with those values of N . To remedy this problem in such cases, we increase the spacing in truncation error tolerance as a function of level N : the truncation error tolerance is proportional to 10^N instead of e^N . This, combined with the procedure to remove the effect of transients, results in good convergence, as shown in Fig. 3.8.

The spin of the remnant black hole is $\chi_f = 0.949931(5)$ and the radiated energy fraction is $E_{\text{rad}} = 11.351(5)\%$. The formulas in Ref. [41] predict $\chi_f = 0.95021(8)$ and $E_{\text{rad}} = 11.30(2)\%$, in good agreement with the simulations. However, the uncertainty intervals of the measured and predicted values are disjoint for the same reason as explained in Sec. 3.4.

Unequal-mass, precessing

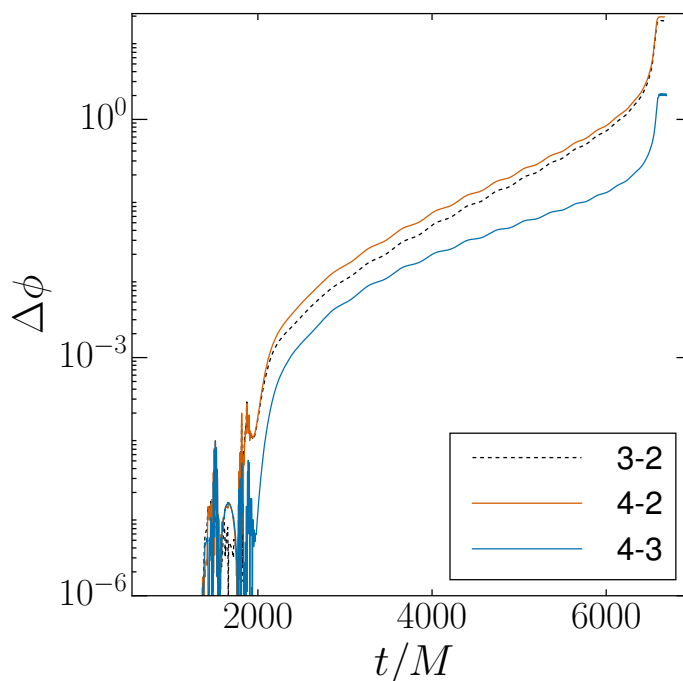


Figure 3.9: Convergence test for $S_{0.20}^{0.99}$. Labels are the same as for Figure 3.6. For $N \neq 4$, the simulations were started at $t_{\text{branch}} = 1362M$, using the $N = 4$ solution as initial data.

The final simulation we present is an unequal-mass case with $q = 1.5$, in which the larger black hole has a spin of $\chi = 0.99$ aligned with the orbital angular momentum, while the smaller black hole has a spin magnitude of $\chi = 0.2$ in an arbitrary

direction misaligned with the orbital angular momentum. We will refer to this case as $S_{0.20}^{0.99}$, using a notation similar to that introduced earlier. The simulation has $M\omega_{\text{orb}} = 0.0148$ at $t = t_{\text{relax}}$, and then proceeds through 23 orbits, merger, and ringdown. This simulation took approximately 26 days on 48 cores for the highest resolution using the same optimized version of SpEC as the $S_{0.994}^{++}$ case described in Sec. 3.4.

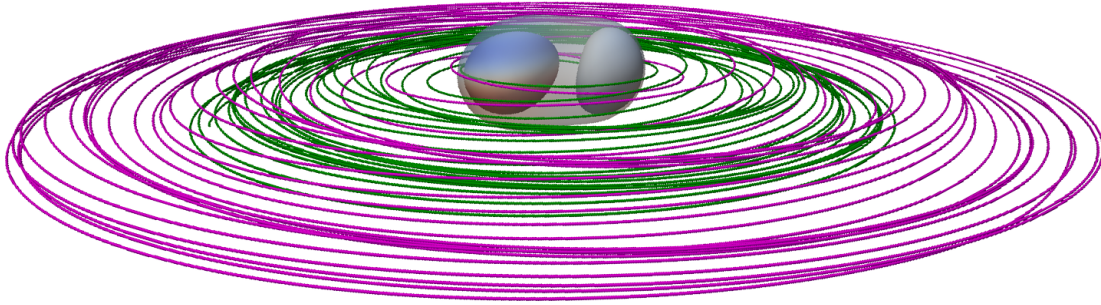


Figure 3.10: Coordinate trajectories (green and purple lines) of the black holes and coordinate shapes of the individual and common apparent horizons (surfaces) at the moment of merger, for $S_{0.20}^{0.99}$. The horizons are colored according to their vorticity [79].

We found that for $S_{0.20}^{0.99}$ we needed to remove the effect of unresolved initial transients and increase the spacing in AMR truncation error tolerance to obtain acceptable convergence results. To do this we followed the same procedure as for $S_{0.994}^{++}$, described in Sec. 3.4. Figure 3.9 shows good convergence of the gravitational-wave phase difference when using this procedure.

Figure 3.10 shows the trajectories of the centers of the apparent horizons for this simulation, as well as the individual apparent horizons and the common apparent horizon at the moment when the common horizon first appears. Trajectories and horizon shapes are shown in the asymptotically inertial coordinate system used in the simulation. Because the spin of the smaller hole $\vec{\chi}_B$ is not aligned with the orbital angular momentum, the system precesses, so the trajectories do not lie in a plane.

Figure 3.11 shows the precession of the spin and orbital frequency vectors in $S_{0.20}^{0.99}$. The spin $\vec{\chi}_A$ and orbital frequency $\vec{\omega}_{\text{orb}}$ initially point along the z -axis. Because the misaligned spin $\vec{\chi}_B$ is on the smaller black hole and is much smaller in magnitude than $\vec{\chi}_A$, it has a minimal effect on the orbital dynamics, so $\vec{\chi}_A$ and $\vec{\omega}_{\text{orb}}$ remain near the z -axis throughout the simulation. Therefore, we consider the precession to be mild. As angular momentum is carried away by gravitational radiation, the opening

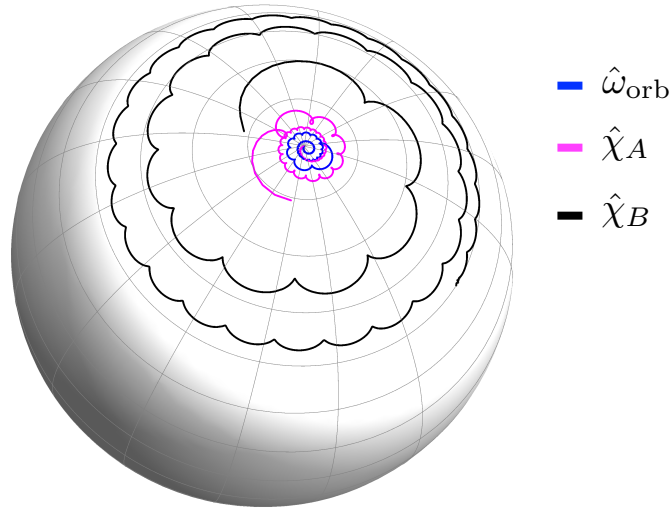


Figure 3.11: Precession of the spins and orbital frequency for the highest-resolution simulation $N = 4$ of $S_{0.20}^{0.99}$. The unit vector spins, $\hat{\chi}_A$ and $\hat{\chi}_B$, and orbital frequency $\hat{\omega}_{\text{orb}}$ trace the precession on the unit sphere. The precession curves for $N = 2$ and $N = 3$ converge to the $N = 4$ curves shown here, and the curves for $N = 3$ and $N = 4$ are nearly indistinguishable.

angles of the precession cones change. The angles of $\vec{\omega}_{\text{orb}}$ and $\vec{\chi}_A$ with respect to the z -axis increase from 0° at $t = 0$ to 6° and 12° , respectively, at the time of merger. In contrast, the angle of $\vec{\chi}_B$ with respect to the z -axis decreases from 45° to 12° . The spins $\vec{\chi}_A$ and $\vec{\chi}_B$ complete 2.1 and 2.5 precession cycles, respectively, and $\vec{\omega}_{\text{orb}}$ completes 2.4 precession cycles.

The spin of the remnant black hole is $\chi_f = 0.89692(5)$, and the radiated energy fraction is $E_{\text{rad}} = 7.8560(8)\%$. The formulas from Healy et al. (2014) [25] predict $\chi_f = 0.89686$ and $E_{\text{rad}} = 7.8365\%$. Even though these predictions lie outside the numerical uncertainty of the measured values, the agreement is quite good.⁴

3.5 Results

Spin evolution during inspiral

During the inspiral, the tidal field of each black hole affects its companion, and this interaction slowly changes the black-hole masses and spins as a function of time.

⁴ To evaluate the quantities $S_{||}$ and $\Delta_{||}$ in Ref. [25], we used the z -component of \vec{S} and $\vec{\Delta}$ at t_{relax} , which should be strictly valid only for non-precessing binaries. Also, the formula for χ_f in Ref. [25] requires evaluating certain quantities at the innermost stable circular orbit (ISCO) of a Kerr black hole with a spin of χ_f , so that χ_f is not given in closed form; for simplicity we evaluate the ISCO quantities using the measured χ_f from the simulation.

For aligned spins, Alvi [78] has derived perturbative expressions for the time rate of change of the mass and spin of a black hole in a binary. Chatziioannou, Poisson, and Yunes (hereafter CPY) [80], have recently extended these expressions to higher order in perturbation theory. Although CPY's expressions in Ref. [80] are computed to 1.5PN beyond leading order (i.e. terms in dS/dt proportional to v^{15} and terms in dm/dt proportional to v^{18} , where $v^2 = M/r$ is the PN expansion parameter), their 1.5PN terms are incorrect and will be corrected soon [81]; so here we will truncate CPY's expressions to 1PN order. Note that the time derivatives in Ref. [80] are taken with respect to the time \bar{t} of an observer comoving with one of the black holes; we instead compute time derivatives with respect to the PN barycentric time t . A relation between \bar{t} and t can be found in Ref. [82].

In our simulations we track the apparent horizons as a function of time, and at frequent time intervals we measure both the surface area and the spin of the horizons. The spin computation is carried out using the approximate Killing vector formalism of Cook, Whiting, and Owen [71, 72]. The mass of the black hole is then computed using Christodoulou's formula. We compare our numerical results to the analytic results of Alvi and CPY.

To compare a black-hole mass or spin from a numerical simulation to that of a perturbative expression, the two quantities must be compared at the same event along the black hole trajectory. Although *waveform* quantities at future null infinity computed by numerical simulations are routinely compared with waveforms computed by PN expansions, it is not straightforward to compare near-zone quantities like black-hole masses and spins because of gauge ambiguities. A further complication is that spin is defined differently for PN and NR; but note that the two definitions appear to agree well in practice [83]. Here we make two comparisons. The first compares quantities at the same numerical and perturbative t coordinate. The second assumes that the orbital angular velocity $\omega_{\text{orb}} = d\phi/dt$ of the black hole in the numerical simulation can be equated with that of the perturbative expression. Note that in both the numerical and perturbative cases, the t coordinate becomes the Minkowski t at infinity, and the ϕ coordinate is periodic. Because of the approximate helical Killing vector $d/dt + \omega_{\text{orb}}d/d\phi$, ω_{orb} is approximately an angular velocity at infinity. Therefore, one might hope that equating the perturbative and numerical ω_{orb} yields better agreement than, e.g., equating the radial coordinate r of the simulation with that of perturbation theory.

Figure 3.12 compares the magnitude of dS/dt of one of the black holes for $S_{0.994}^{++}$

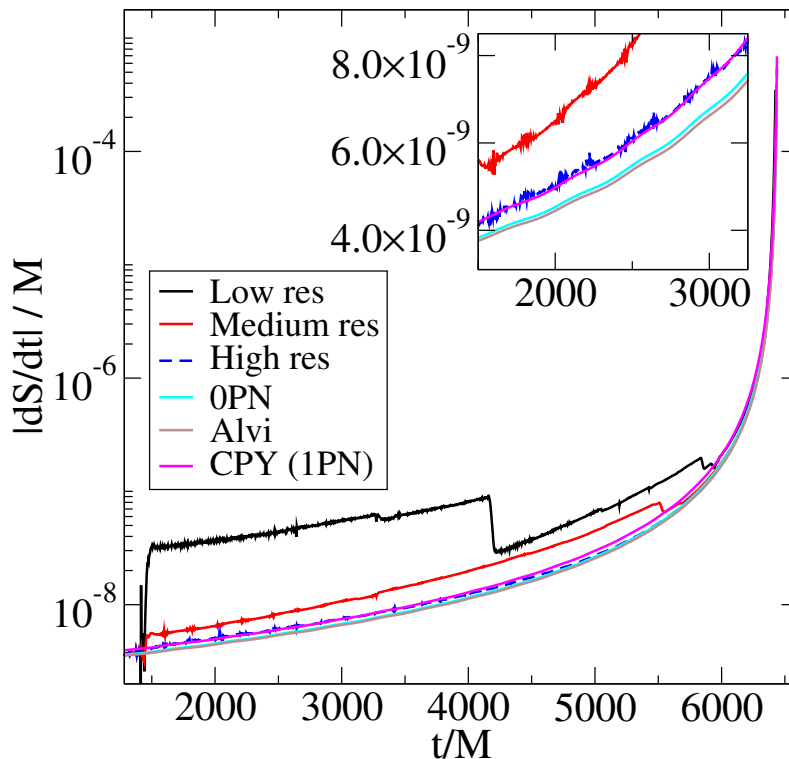


Figure 3.12: Magnitude of dS/dt of one of the black holes from $S_{0.994}^{++}$. Shown are three numerical resolutions, Alvi’s expression (Eq. (11) of [78]), the 0PN expression, and the CPY expression [80, 81] to 1PN order. The inset zooms closer to the high-resolution numerical curve.

with the expressions of both CPY and Alvi⁵ We include numerical results for three resolutions in Fig. 3.12 because the magnitude of dS/dt is extremely small and difficult to resolve. Indeed, the lowest resolution fails to resolve dS/dt until around $t = 6000M$, when dS/dt grows to about $10^{-7}M$, and the medium resolution fails to resolve dS/dt only slightly earlier. Note that Alvi’s expression includes some 1.5PN terms, but ignores 1PN effects such as magnetic-type tidal perturbations and the difference between the global PN time coordinate and the local time coordinate of a frame moving along with one of the black holes. Therefore, we plot both Alvi’s expression in its entirety, and Alvi’s expression truncated to lowest (0PN) order. The CPY expression includes 0PN and 1PN terms. The CPY and Alvi expressions agree to 0PN order.

Figure 3.12 shows overall excellent agreement between the PN and numerical

⁵ Figures 3.12– 3.15 do not change qualitatively if we use $S_{0.99}^{++}$ instead of $S_{0.994}^{++}$, so we do not show plots for $S_{0.99}^{++}$ here.

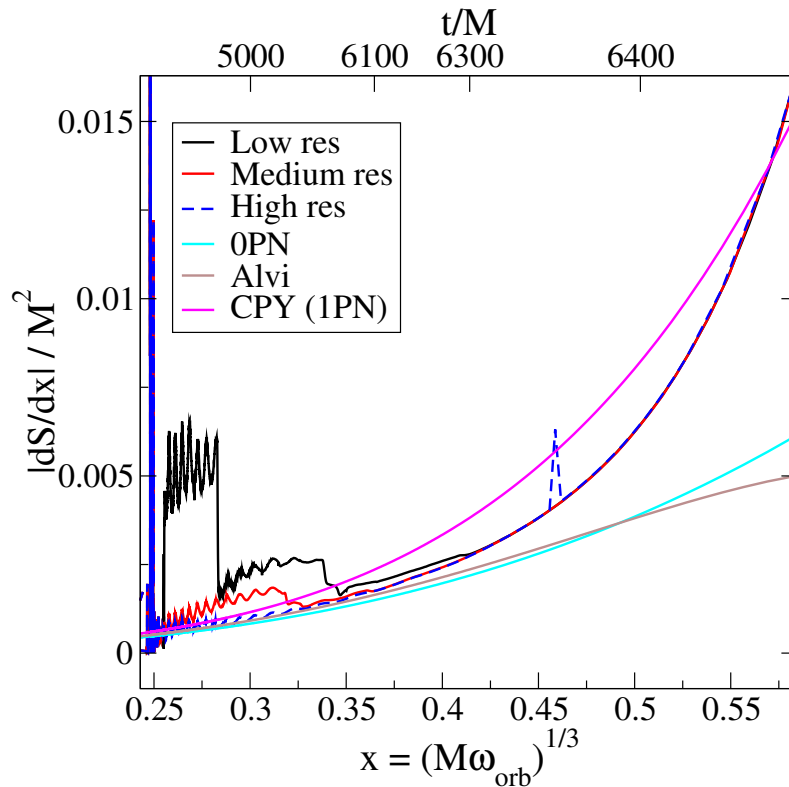


Figure 3.13: Magnitude of dS/dx , where $x \equiv (M\omega_{\text{orb}})^{1/3}$, of one of the black holes from $S_{0,994}^{++}$. The top horizontal axis shows t/M of the highest-resolution numerical simulation, for comparison with values of x .

simulation results. For $t \lesssim 5500M$, all the perturbative curves agree within our numerical error, and for $t \lesssim 3500M$ the CPY 1PN curve agrees remarkably well with our highest-resolution result. However, by the time the medium resolution simulation starts to resolve dS/dt at $t \gtrsim 5500M$, none of the perturbative approximations agree with the numerical result within numerical error, with the largest disagreement for the CPY result. This disagreement at late times is not surprising since all the perturbative expressions should lose accuracy shortly before merger.

We can eliminate the time coordinate, a possible source of gauge dependence, by instead plotting dS/dx versus x , where $x \equiv (M\omega_{\text{orb}})^{1/3}$. This is shown in Fig. 3.13. To obtain dS/dx from dS/dt and to obtain x from t , it is necessary to have some function $x(t)$. For the numerical curves, this function is obtained from the numerical time coordinate and the numerical orbital frequency. For the perturbative curves, this function is the PN expression for $x(t)$ derived from Eq. (4.14) of Ref. [84].⁶ Thus,

⁶Although $x(t)$ contains terms up to 2PN order, we truncate the perturbative expressions for dS/dx (and for dS/dt , dm/dt , and dm/dx) at a consistent PN order, i.e. at 0PN for the OPN curve,

all the numerical curves in Figs. 3.12 and 3.13 are independent of any perturbative assumptions, and all the perturbative curves in Figs. 3.12 and 3.13 are independent of the numerical data, except that the perturbative and numerical t coordinates are both represented by the same horizontal axis of Fig. 3.12, and the perturbative and numerical ω_{orb} are both represented by the same horizontal axis of Fig. 3.13.

In Fig. 3.13, the perturbative and numerical expressions agree early in the inspiral, but not at late times; this is expected because perturbative expressions become inaccurate for large x . Alvi’s full expression appears to agree with the numerical simulations slightly better than the others for small x , but that expression diverges from the numerical result at larger x earlier than the others. Note that Fig. 3.13 emphasizes late times because the frequency increases very rapidly with time. The small spike in the numerical curve at $x \sim 0.45$ in Fig. 3.13 is caused by a discontinuous change in the number of spherical-harmonic $Y_{\ell m}$ modes retained by the apparent horizon finder (the number of modes is chosen adaptively). The resulting discontinuous change in S is very small (below numerical error), but its effect on $dS/dx = (dS/dt)(dx/dt)^{-1}$ is magnified because dS/dt and dx/dt are computed using finite differencing with a fine spacing in t . This change also causes a similar spike at the same value of x in Fig. 3.15.

Figures 3.14 and 3.15 are similar to Figs. 3.12 and 3.13 except that they show the change in Christodoulou mass instead of the change in dimensionful spin. Both the Alvi and CPY formulas agree well with each other and with the numerical result early in the inspiral, but do not agree at late times. Note that since the derivative of the mass is smaller (by a factor of v^3 in PN) than the derivative of the spin, dm/dt is more difficult to resolve numerically than dS/dt , as seen by the larger numerical errors in Figs. 3.14 and 3.15 compared with the numerical errors in Figs. 3.12 and 3.13.

Orbital hangup

During a BBH inspiral, the orbital frequency ω_{orb} secularly evolves along with the black-hole masses and spins. For equal-mass binaries with equal spins aligned (or antialigned) with the orbital angular momentum, the number of orbits until merger increases as a function of $\vec{S} \cdot \vec{L}$. Damour [85] observed this effect, today commonly called “orbital hangup”, in an effective-one-body model of the holes’ motion; the effect is a consequence of post-Newtonian spin-orbit coupling [86]. Campanelli, Lousto, and Zlochower [87] first demonstrated orbital hangup in numerical simulations of

1PN for the CPY curve, and 1.5PN for the Alvi curve.

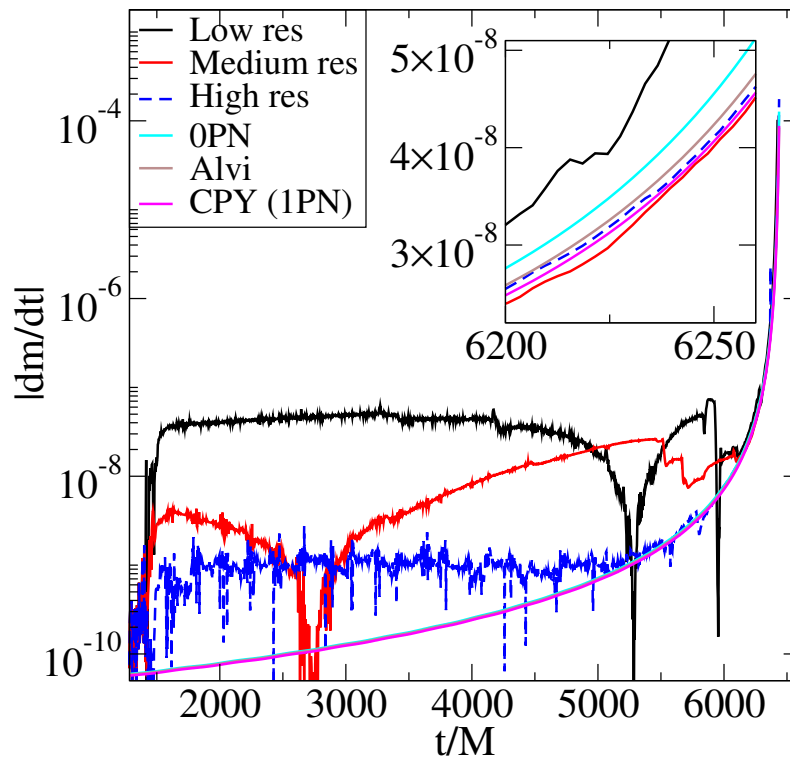


Figure 3.14: Magnitude of dm/dt of one of the black holes from $S_{0.994}^{++}$. Shown are three numerical resolutions, Alvi’s expression (Eq. (11) of [78]), the 0PN expression, and the CPY expression [80, 81] truncated to 1PN order. The inset zooms closer to the high-resolution numerical curve.

merging BBHs.

Instead of examining the number of orbits from the trajectories, we infer the number of orbits from the dominant $\ell = m = 2$ mode of the emitted gravitational waves⁷. We do this because it is easier to define a gauge-invariant time of merger from the waveforms than from the trajectories; specifically, we define the time of merger as the time when the waveform amplitude is at a maximum.

Let $h_{22}(t)$ be the ${}_{-2}Y_{22}$ spin-weighted spherical harmonic mode of the gravitational wave strain $h(t)$, and let ω_{22} be the frequency of $h_{22}(t)$. Figure 3.16 shows the time evolution of $d\omega_{22}/dt$ for simulations $S_{0.99}^{++}$ and $S_{0.994}^{++}$. For comparison, we also show results for other simulations with equal masses and equal spins aligned with the orbital angular momentum [24, 37, 41]. Note that $d\omega_{22}/dt$ is positive and steadily increasing: the frequency does not slow down or momentarily remain constant, as a

⁷Specifically, we extrapolate the gravitational waves measured on a series of concentric shells to $r \rightarrow \infty$, as discussed in detail in Sec. 3.5.

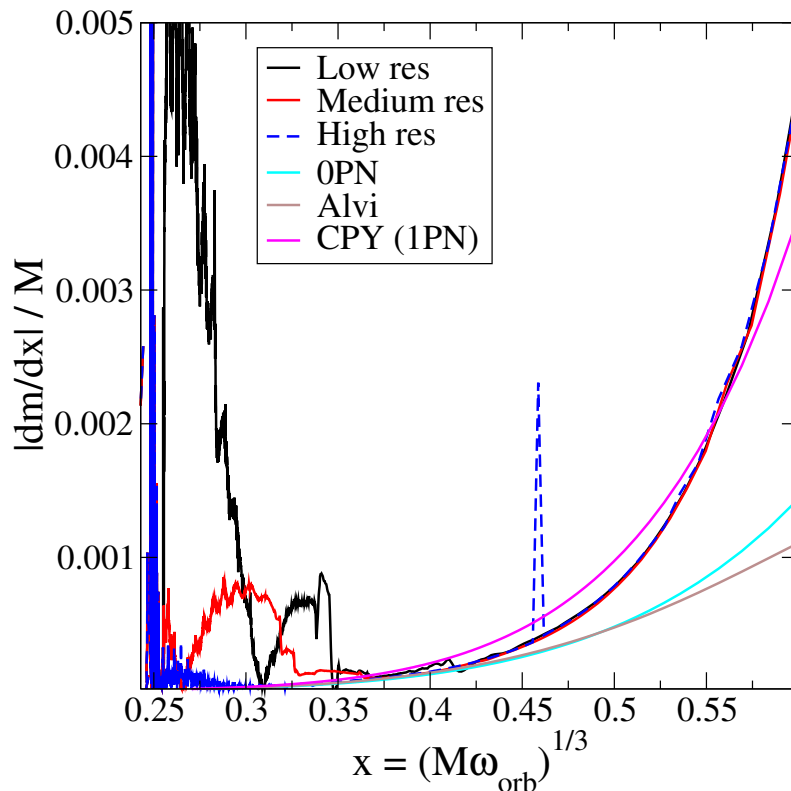


Figure 3.15: Magnitude of dm/dx , where $x \equiv (M\omega_{\text{orb}})^{1/3}$, of one of the black holes from $S_{0.994}^{++}$.

literal interpretation of the term “orbital hangup” might suggest.

Figure 3.17 shows the gravitational-wave cycles accumulated between an initial gravitational-wave frequency of $M\omega_{22} = 0.036$ (i.e., an initial orbital frequency of $M\omega_{\text{orb}} = 0.018$) and merger (when the amplitude of h_{22} peaks). Simulations $S_{0.99}^{++}$ and $S_{0.994}^{++}$ reveal that the orbital hangup depends approximately linearly on the initial spin χ , even at spins that are nearly extremal; however, most of our simulations only agree with the linear fit to $O(0.1\%)$, which is often larger than our estimated numerical uncertainties. This linearity implies that even near extremality, the orbital hangup effect is dominated by spin-orbit coupling; resolving nonlinear features in Fig. 3.17 would require more simulations with higher accuracy.

Comparison with analytic approximants

We compare the gravitational waveforms from our simulations to several analytic waveform approximants. The numerical waveforms were computed by performing Regge-Wheeler-Zerilli extraction [88, 89] at a sequence of radii r_{extr} between $100M$ and

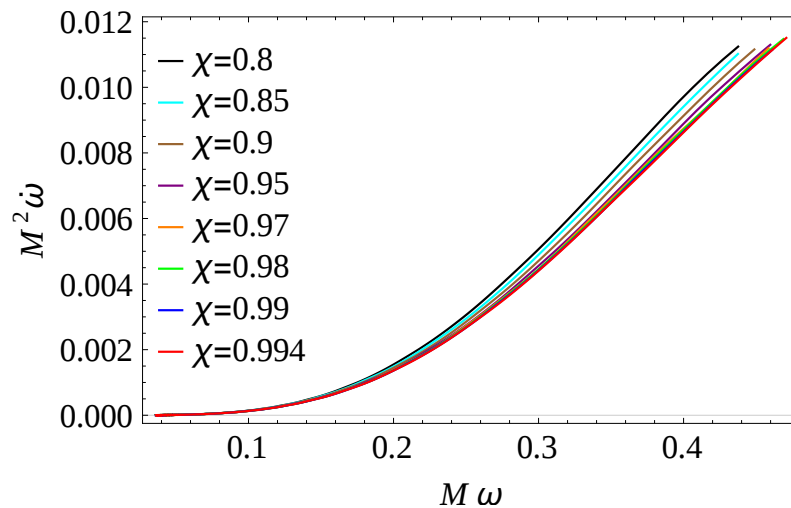


Figure 3.16: The evolution of the derivative of the gravitational-wave frequency $\dot{\omega}_{22} = d\omega_{22}/dt$, for simulations $S_{0.99}^{++}$ and $S_{0.994}^{++}$ and (for comparison) simulations $S_{0.8}^{++}$ [41], $S_{0.85}^{++}$ [41], $S_{0.9}^{++}$ [41], $S_{0.95}^{++}$ [41], $S_{0.97}^{++}$ [37], and $S_{0.98}^{++}$ [24].

$465M$, and then extrapolating to \mathcal{S}^+ with a second-order polynomial in $1/r_{\text{extr}}$ using the open-source GWFrames software package [83, 90, 91]. The TaylorT1, TaylorT4, and TaylorT5 approximants were constructed using the PostNewtonian module in GWFrames.⁸ The EOB approximants were constructed using SEOBNRv2 [49] from the LIGO Algorithm Library, with the function `SimIMRSpinAlignedEOBWaveform` modified to return $h_{22}(t)$. Physical parameters (i.e. initial masses, spin vectors, and orbital frequency vector) for the approximants were taken from the highest resolution from each simulation at the relaxation time. Eccentricity in the NR simulation is not taken into account when constructing the approximants.

Because SEOBNRv2 is strictly valid only for non-precessing systems, and therefore accepts only scalar values of the spins as input, it is not obvious what to input for the case of $S_{0.20}^{0.99}$. We pass the z -component of the spins into the model. If instead we pass the spin magnitudes, we see larger disagreements between the EOB and numerical waveforms for $S_{0.20}^{0.99}$, likely due to a change in the strength of spin-orbit coupling. We will see below that non-precessing EOB agrees remarkably well with

⁸To our knowledge, the PostNewtonian module includes all terms currently found in the literature. Non-spin terms are given up to 4.0 PN order for the binding energy [13, 92]; 3.5 PN [13] with incomplete 4.0 PN information [93] for the flux; and 3.5 PN for the waveform modes [94–96]. The spin-orbit terms are given to 4.0 PN in the binding energy [97]; 4.0 PN in flux [98]; and 2.0 PN in the waveform modes [91, 99]. Terms quadratic in spin are given to 2.0 PN order in the binding energy and flux [100, 101], and waveform modes [91, 99, 100].

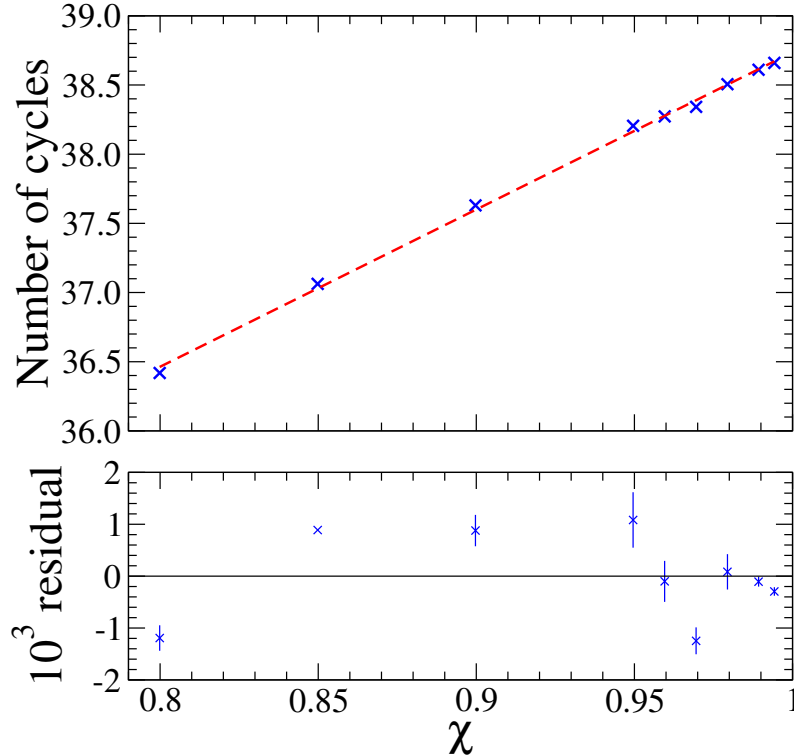


Figure 3.17: The number of gravitational-wave cycles as a function of the initial spin χ , measured after the initial relaxation, for simulations $S_{0.99}^{++}$ and $S_{0.994}^{++}$ and (for comparison) simulations $S_{0.8}^{++}$ [41], $S_{0.85}^{++}$ [41], $S_{0.9}^{++}$ [41], $S_{0.95}^{++}$ [41], $S_{0.96}^{++}$ [50], $S_{0.97}^{++}$ [37], and $S_{0.98}^{++}$ [24]. *Upper panel:* The number of gravitational-wave cycles of h_{22} accumulated between a gravitational-wave frequency $M\omega_{22} = 0.036$ and merger (i.e., the time when the amplitude of h_{22} peaks). The dashed line is a linear fit to the data. *Lower panel:* Fractional difference (“residual”) between our results and the linear fit, with uncertainties for simulations except $S_{0.85}^{++}$ (which we ran at only one resolution) estimated as differences between medium and high numerical resolutions.

$S_{0.20}^{0.99}$ despite the mild precession of this simulation.

In Figs. 3.18, 3.19, and 3.20, we show for $S_{0.99}^{++}$, $S_{0.994}^{++}$, and $S_{0.20}^{0.99}$ (respectively) the phase difference $\Delta\phi$ of h_{22} between the highest numerical resolution and the PN and EOB approximants. We also include $\Delta\phi$ between the highest numerical resolution and other numerical resolutions for comparison. To compute $\Delta\phi$, we first align each waveform with the highest resolution numerical-relativity (NR) waveform using the procedure prescribed in Ref. [102]: we find the time offset δt and phase offset $\delta\phi$ that minimize $\Phi(\delta t, \delta\phi)$, a measure of the phase difference in h_{22} , given by

$$\Phi(\delta t, \delta\phi) \equiv \int_{t_1}^{t_2} [\phi_a(t) - \phi_b(t + \delta t) - \delta\phi]^2 dt. \quad (3.21)$$

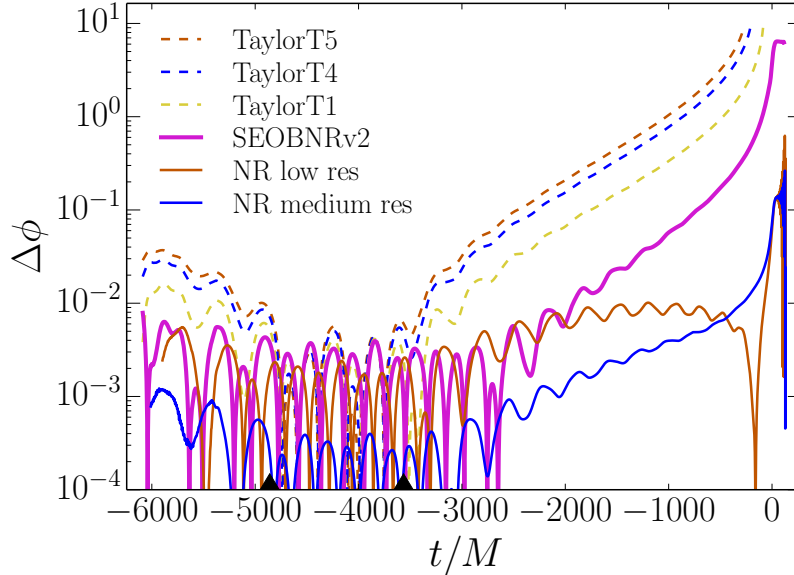


Figure 3.18: Phase differences $\Delta\phi$ of h_{22} as a function of retarded time before merger for $S_{0.99}^{++}$. Shown are differences between the highest numerical resolution and several analytic approximants. Differences between the highest numerical resolution and other numerical resolutions are shown for comparison. The waveforms are aligned in the time interval delimited by the black triangles.

This can be reduced to a one-dimensional minimization problem by computing the optimal $\delta\phi$ analytically, given any value of δt : differentiating Eq. (3.21) with respect to $\delta\phi$, setting the result to zero, and solving for $\delta\phi$ yields

$$\delta\phi(\delta t) = \frac{1}{t_2 - t_1} \int_{t_1}^{t_2} [\phi_a(t) - \phi_b(t + \delta t)] dt. \quad (3.22)$$

The alignment interval $t \in [t_1, t_2]$ is the same for all comparisons with a particular simulation. The lower bound t_1 is chosen such that the junk radiation has left the computational domain for all numerical resolutions, specifically $t_1 = \max[t_0 + 3(t_{\text{relax}} - t_0)]$, where t_0 is the time at the beginning of the waveform. The upper bound t_2 is chosen such that the gravitational-wave frequency changes by at least 10% during the interval $[t_1, t_2]$, as suggested in Ref. [103].

We have also computed $\Delta\phi$ with a few other alignment methods, including the three-dimensional minimization of complex h_{22} differences in Ajith et al. 2008 (Eq. 4.9 in Ref. [104]) and the four-dimensional minimization over time and frame-rotation degrees of freedom in Boyle 2013 (Eq. 22 in Ref. [90]). We have found that our results are qualitatively independent of alignment method.

The TaylorT family of PN approximants shows the largest discrepancy with our

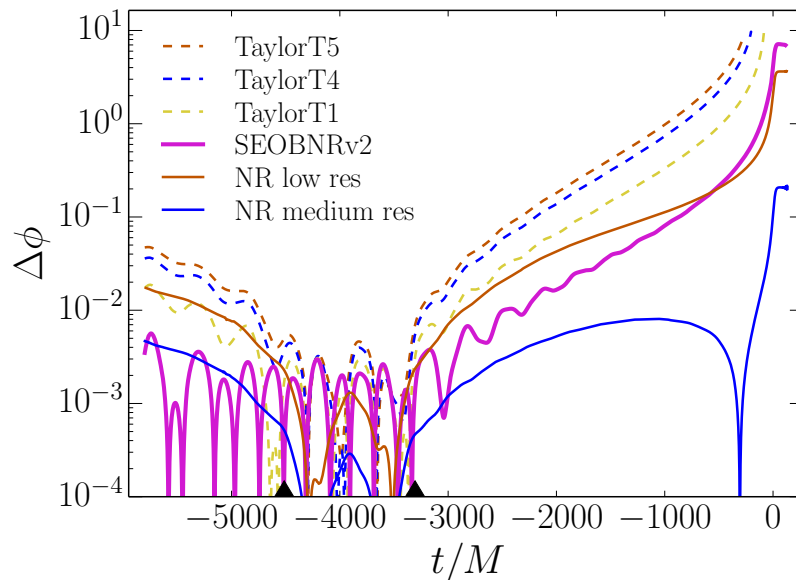


Figure 3.19: Phase differences $\Delta\phi$ of h_{22} between numerical and approximant data for $S_{0.994}^{++}$. Labels are the same as for Fig. 3.18.

highest numerical resolution. Phase errors between PN and NR waveforms grow to several radians before the merger in every case. The smallest phase errors outside the alignment interval occur for $S_{0.20}^{0.99}$, which is likely a consequence of the smaller black hole having a moderate spin. We find the best agreement with TaylorT1, in contrast to PN comparisons for other nearly extremal systems [37], which found the best agreement with TaylorT4 for spins aligned with the orbital angular momentum; note that the PN waveforms considered in Ref. [37] include fewer higher-order PN terms than we do here. This is further evidence that agreement with a particular PN approximant in the TaylorT family depends sensitively on the PN order. Agreement with a particular PN approximant also depends on the parameters of the simulation (e.g., Ref. [37]).

The EOB approximant performs significantly better than the PN approximants for $S_{0.99}^{++}$ and $S_{0.994}^{++}$, which is impressive considering that the parameters of these waveforms are outside the range in which SEOBNRv2 was calibrated to NR. Only about 5 radians of phase error is accumulated in $S_{0.99}^{++}$ and $S_{0.994}^{++}$.⁹ Phase error increases to a little over 10 radians in $S_{0.20}^{0.99}$, but this case is precessing, and SEOBNRv2 is only valid for non-precessing systems. However, the precession is mild (cf. Figs. 3.10 and 3.11), which could account for the relatively good agreement.

⁹Note that SEOBNRv2 was calibrated by minimizing unfaithfulness rather than phase error; it is possible to have relatively large phase errors even when the unfaithfulness is small [49].

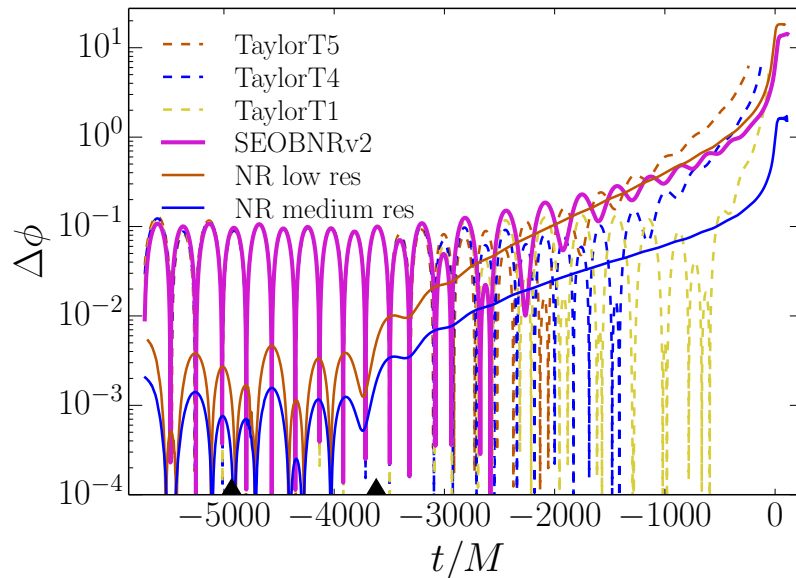


Figure 3.20: Phase differences $\Delta\phi$ of h_{22} between numerical and approximant data for $S_{0.20}^{0.99}$. Labels are the same as for Fig. 3.18. Note that the Taylor models include precession but SEOBNRv2 does not. However, the precession of $S_{0.20}^{0.99}$ is mild so the numerical waveform still agrees reasonably well with SEOBNRv2.

The analytic approximants show much larger $\Delta\phi$ at early times for $S_{0.20}^{0.99}$ (see Fig. 3.20) than for $S_{0.99}^{++}$ and $S_{0.994}^{++}$. We conjecture that this is due to the relatively large eccentricity of $S_{0.20}^{0.99}$ (see Table 3.1), whereas the PN and EOB models used here are non-eccentric. Note that we use precessing PN models for comparing to $S_{0.20}^{0.99}$.

The phase errors between numerical waveforms computed at different resolutions are convergent. Because of the rapid convergence, the difference between the two highest numerical resolutions represents the numerical error in the *second highest* resolution; to determine the numerical error of the highest resolution waveform, we would need to perform a simulation at an even higher resolution. As a conservative estimate of the numerical error of the highest resolution waveform, we use the difference between the two highest-resolution waveforms as an upper bound. The upper bound of the numerical phase error of the highest resolution simulation, computed in this way, is thus about 0.2 radians for $S_{0.99}^{++}$ and $S_{0.994}^{++}$ and about 1 radian for $S_{0.20}^{0.99}$.

In Figs. 3.18, 3.19, and 3.20, the larger numerical phase errors in the *lower* resolutions of $S_{0.994}^{++}$ and $S_{0.20}^{0.99}$ are expected, because these simulations use a larger spacing in AMR truncation error tolerance as described in Sec. 3.4. The larger spacing increases relative phase errors between successive numerical resolutions. Nevertheless, our

comparisons show that numerical errors are much smaller than the errors in the PN and EOB waveforms for systems with nearly extremal black holes, indicating that these numerical waveforms will be useful for calibrating and extending the regime of validity for approximate waveforms.

3.6 Conclusion

We have presented improved methods for simulating the binary evolution of nearly extremal black holes, i.e., black holes with spins above the Bowen-York limit of $\chi = 0.93$. These techniques enable robust simulations in the portion of BBH parameter space where the black holes have very large spins. Because nearly extremal black holes might exist in astrophysical binaries, these simulations will be important for helping to maximize what we can learn from gravitational-wave experiments.

We have applied our new methods to carry out the first unequal-mass, mildly-precessing BBH simulation containing a nearly extremal black hole, and to extend aligned-spin BBH simulations to spin magnitudes that begin to approach the Novikov-Thorne limit of $\chi = 0.998$. From these new simulations, we have learned that perturbative predictions for tidal heating and tidal torquing agree well with the numerics at low frequency, even for nearly extremal spins. However, we find that our numerical errors are still large enough that we cannot reliably distinguish between 0PN and 1PN predictions. Doing so would require further investigation with more accurate simulations.

While many physical quantities depend on χ in an extremely nonlinear fashion, we find that the number of orbits starting from a chosen orbital frequency (i.e., the orbital hangup) scales approximately linearly with χ . Finally, after demonstrating numerical convergence, we have found that our numerical waveforms agree with SEOBNRv2 much better than with TaylorT PN approximants, even though the parameters for these simulations are outside the range in which SEOBNRv2 was calibrated. However, even the SEOBNRv2 waveforms disagree with our numerical waveforms by more than our numerical truncation error. This indicates that these simulations are sufficiently accurate to validate and further improve analytical waveform approximants for future gravitational-wave observations. How significant these improvements will be for Advanced LIGO is the subject of future work.

Acknowledgments

We are grateful to Eric Poisson, Nicolas Yunes, and Katerina Chatziioannou for detailed discussions about perturbative expressions for tidal torquing and about the problems inherent in comparing numerical and post-Newtonian expressions for near-field quantities. We thank Alessandra Buonanno and Sebastiano Bernuzzi for helpful discussions. Simulations used in this work were computed with SpEC [47]. This work was supported in part by the Sherman Fairchild Foundation; NSF grants PHY-1440083 and AST-1333520 at Caltech, NSF grants PHY-1306125 and AST-1333129 at Cornell, and NSF grant PHY-1307489 at California State University Fullerton; a 2013–2014 California State University Fullerton Junior Faculty Research Grant. Computations were performed on the Zwicky cluster at Caltech, which is supported by the Sherman Fairchild Foundation and by NSF award PHY-0960291; on the NSF XSEDE network under grant TG-PHY990007N; on the Orca cluster supported by NSF award NSF-1429873, the Research Corporation for Science Advancement, and by California State University Fullerton; and on the GPC supercomputer at the SciNet HPC Consortium [105]. SciNet is funded by: the Canada Foundation for Innovation under the auspices of Compute Canada; the Government of Ontario; Ontario Research Fund–Research Excellence; and the University of Toronto.

References

- [1] Gregory M. Harry. “Advanced LIGO: The next generation of gravitational wave detectors”. In: *Class. Quantum Grav.* 27 (2010), p. 084006. DOI: [10.1088/0264-9381/27/8/084006](https://doi.org/10.1088/0264-9381/27/8/084006).
- [2] The Virgo Collaboration. *Advanced Virgo Baseline Design*. [VIR-0027A-09]. 2009. URL: <https://tds.ego-gw.it/ql/?c=6589>.
- [3] The Virgo Collaboration. *Advanced Virgo Technical Design Report*. [VIR-0128A-12]. 2012. URL: <https://tds.ego-gw.it/ql/?c=6940>.
- [4] K. Somiya and the KAGRA Collaboration. “Detector configuration of KAGRA—the Japanese cryogenic gravitational-wave detector”. In: *Class. Quantum Grav.* 29.12 (2012), p. 124007. DOI: [10.1088/0264-9381/29/12/124007](https://doi.org/10.1088/0264-9381/29/12/124007).
- [5] Lijun Gou et al. “The Extreme Spin of the Black Hole in Cygnus X-1”. In: *Astrophys. J.* 742 (2011), p. 85. DOI: [10.1088/0004-637X/742/2/85](https://doi.org/10.1088/0004-637X/742/2/85). arXiv: [1106.3690](https://arxiv.org/abs/1106.3690) [astro-ph.HE].
- [6] A.C. Fabian et al. “On the determination of the spin of the black hole in Cyg X-1 from X-ray reflection spectra”. In: *Mon. Not. Roy. Astr. Soc.* 424 (2012), p. 217. arXiv: [1204.5854](https://arxiv.org/abs/1204.5854) [astro-ph.HE].

- [7] Lijun Gou et al. “CONFIRMATION VIA THE CONTINUUM-FITTING METHOD THAT THE SPIN OF THE BLACK HOLE IN CYGNUS X-1 IS EXTREME”. In: *Astrophys.J.* 790 (2014), p. 29. DOI: [10.1088/0004-637X/790/1/29](https://doi.org/10.1088/0004-637X/790/1/29).
- [8] Jeffrey E McClintock et al. “The Spin of the Near-Extreme Kerr Black Hole GRS 1915+105”. In: *Astrophys. J.* 652 (2006), p. 518.
- [9] J.M. Miller et al. “Stellar-mass Black Hole Spin Constraints from Disk Reflection and Continuum Modeling”. In: *Astrophys.J.* 697 (2009), pp. 900–912. DOI: [10.1088/0004-637X/697/1/900](https://doi.org/10.1088/0004-637X/697/1/900). arXiv: [0902.2840](https://arxiv.org/abs/0902.2840) [[astro-ph.HE](#)].
- [10] D.J. Walton et al. “Suzaku observations of ‘bare’ active galactic nuclei”. In: *MNRAS* 428 (2013), p. 2901. arXiv: [1210.4593](https://arxiv.org/abs/1210.4593) [[astro-ph.HE](#)].
- [11] Jeffrey E. McClintock, Ramesh Narayan, and James F. Steiner. “Black Hole Spin via Continuum Fitting and the Role of Spin in Powering Transient Jets”. In: *Space Sci.Rev.* 183.1-4 (2014), pp. 295–322. DOI: [10.1007/s11214-013-0003-9](https://doi.org/10.1007/s11214-013-0003-9). arXiv: [1303.1583](https://arxiv.org/abs/1303.1583) [[astro-ph.HE](#)].
- [12] Christopher S. Reynolds. “Measuring Black Hole Spin using X-ray Reflection Spectroscopy”. In: *Space Science Reviews* 183 (2014), p. 277. arXiv: [1302.3260](https://arxiv.org/abs/1302.3260) [[astro-ph.HE](#)].
- [13] Luc Blanchet. “Gravitational radiation from post-Newtonian sources and inspiralling compact binaries”. In: *Living Rev. Rel.* 17 (2014), p. 2. URL: <http://www.livingreviews.org/lrr-2014-2>.
- [14] Frans Pretorius. “Evolution of binary black hole spacetimes”. In: *Phys. Rev. Lett.* 95 (2005), p. 121101. DOI: [10.1103/PhysRevLett.95.121101](https://doi.org/10.1103/PhysRevLett.95.121101). arXiv: [gr-qc/0507014](https://arxiv.org/abs/gr-qc/0507014) [[gr-qc](#)].
- [15] Manuela Campanelli et al. “Accurate evolutions of orbiting black-hole binaries without excision”. In: *Phys. Rev. Lett.* 96 (2006), p. 111101. DOI: [10.1103/PhysRevLett.96.111101](https://doi.org/10.1103/PhysRevLett.96.111101). arXiv: [gr-qc/0511048](https://arxiv.org/abs/gr-qc/0511048) [[gr-qc](#)].
- [16] John G. Baker et al. “Gravitational wave extraction from an inspiraling configuration of merging black holes”. In: *Phys. Rev. Lett.* 96 (2006), p. 111102. DOI: [10.1103/PhysRevLett.96.111102](https://doi.org/10.1103/PhysRevLett.96.111102). arXiv: [gr-qc/0511103](https://arxiv.org/abs/gr-qc/0511103) [[gr-qc](#)].
- [17] Joan Centrella et al. “Black-hole binaries, gravitational waves, and numerical relativity”. In: *Rev. Mod. Phys.* 82.4 (Nov. 2010), p. 3069. DOI: [10.1103/RevModPhys.82.3069](https://doi.org/10.1103/RevModPhys.82.3069).
- [18] Harald P. Pfeiffer. “Numerical simulations of compact object binaries”. In: *Class. Quantum Grav.* 29 (2012), p. 124004. DOI: [10.1088/0264-9381/29/12/124004](https://doi.org/10.1088/0264-9381/29/12/124004). arXiv: [1203.5166](https://arxiv.org/abs/1203.5166) [[gr-qc](#)].
- [19] Mark Hannam. “Modelling gravitational waves from precessing black-hole binaries: Progress, challenges and prospects”. In: *Gen. Rel. Grav.* 46 (2014), p. 1767. arXiv: [1312.3641](https://arxiv.org/abs/1312.3641) [[gr-qc](#)].

- [20] Alexandre Le Tiec. “The Overlap of Numerical Relativity, Perturbation Theory and Post-Newtonian Theory in the Binary Black Hole Problem”. In: *Int. J. Mod. Phys. D* 23.10 (2014), p. 1430022. DOI: [10.1142/S0218271814300225](https://doi.org/10.1142/S0218271814300225). arXiv: [1408.5505](https://arxiv.org/abs/1408.5505) [gr-qc].
- [21] P. Ajith et al. “The NINJA-2 catalog of hybrid post-Newtonian/numerical-relativity waveforms for non-precessing black-hole binaries”. In: *Class. Quantum Grav.* 29.12 (2012), p. 124001.
- [22] Ian Hinder et al. “Error-analysis and comparison to analytical models of numerical waveforms produced by the NRAR Collaboration”. In: *Class. Quantum Grav.* 31.2 (2014), p. 025012. arXiv: [1307.5307](https://arxiv.org/abs/1307.5307) [gr-qc].
- [23] Larne Pekowsky et al. “Comparing gravitational waves from nonprecessing and precessing black hole binaries in the corotating frame”. In: *Phys. Rev. D* 88 (2013), p. 024040. arXiv: [1304.3176](https://arxiv.org/abs/1304.3176) [gr-qc].
- [24] Abdul H. Mroue et al. “A Catalog of 174 Binary Black Hole Simulations for Gravitational Wave Astronomy”. In: *Phys. Rev. Lett.* 111 (2013), p. 241104. DOI: [10.1103/PhysRevLett.111.241104](https://doi.org/10.1103/PhysRevLett.111.241104). arXiv: [1304.6077](https://arxiv.org/abs/1304.6077) [gr-qc].
- [25] James Healy, Carlos O. Lousto, and Yosef Zlochower. “Remnant mass, spin, and recoil from spin aligned black-hole binaries”. In: *Phys. Rev. D* 89 (2014), p. 104052. arXiv: [1406.7295](https://arxiv.org/abs/1406.7295) [gr-qc].
- [26] J. Clark et al. “Investigating Binary Black Hole Mergers with Principal Component Analysis”. In: *Gravitational Wave Astrophysics*. Ed. by Carlos F. Sopuerta. Vol. 40. Astrophysics and Space Science Proceedings. Cham, Switzerland: Springer International Publishing, 2015, pp. 281–287. ISBN: 978-3-319-10487-4. DOI: [10.1007/978-3-319-10488-1_24](https://doi.org/10.1007/978-3-319-10488-1_24). arXiv: [1406.5426](https://arxiv.org/abs/1406.5426) [gr-qc]. URL: http://dx.doi.org/10.1007/978-3-319-10488-1_24.
- [27] Jeffrey M. Bowen. “General form for the longitudinal momentum of a spherically symmetric source”. In: *Gen. Relativ. Gravit.* 11.3 (1979), pp. 227–231.
- [28] Jeffrey M. Bowen and James W. York, Jr. “Time-asymmetric initial data for black holes and black-hole collisions”. In: *Phys. Rev. D* 21.8 (1980), pp. 2047–2056.
- [29] Steve Brandt and Bernd Brügmann. “A Simple Construction of Initial Data for Multiple Black Holes”. In: *Phys. Rev. Lett.* 78.19 (1997), pp. 3606–3609.
- [30] James W. York, Jr. “Energy and Momentum of the Gravitational Field”. In: *Essays in General Relativity*. Ed. by F. J. Tipler. New York: Academic, 1980, pp. 39–58.
- [31] Alcides Garat and Richard H Price. “Nonexistence of conformally flat slices of the Kerr spacetime”. In: *Phys. Rev. D* 61 (2000), p. 124011.

- [32] Juan Antonio Valiente Kroon. “Nonexistence of Conformally Flat Slices in Kerr and Other Stationary Spacetimes”. In: *Phys. Rev. Lett.* 92 (2004), p. 041101.
- [33] Gregory B. Cook and James W. York, Jr. “Apparent horizons for boosted or spinning black holes”. In: *Phys. Rev. D* 41.4 (1990), pp. 1077–1085.
- [34] Sergio Dain, Carlos O. Lousto, and Ryoji Takahashi. “New conformally flat initial data for spinning black holes”. In: *Phys. Rev. D* 65 (2002), p. 104038. DOI: [10.1103/PhysRevD.65.104038](https://doi.org/10.1103/PhysRevD.65.104038).
- [35] Mark Hannam, Sacha Husa, and Niall Ó Murchadha. “Bowen-York trumpet data and black-hole simulations”. In: *Phys. Rev. D* 80 (2009), p. 124007. DOI: [10.1103/PhysRevD.80.124007](https://doi.org/10.1103/PhysRevD.80.124007).
- [36] Geoffrey Lovelace, Mark. A. Scheel, and Béla Szilágyi. “Simulating merging binary black holes with nearly extremal spins”. In: *Phys. Rev. D* 83 (2011), p. 024010. DOI: [10.1103/PhysRevD.83.024010](https://doi.org/10.1103/PhysRevD.83.024010). arXiv: [1010.2777 \[gr-qc\]](https://arxiv.org/abs/1010.2777).
- [37] Geoffrey Lovelace et al. “High-accuracy gravitational waveforms for binary-black-hole mergers with nearly extremal spins”. In: *Class. Quantum Grav.* 29 (2012), p. 045003. DOI: [10.1088/0264-9381/29/4/045003](https://doi.org/10.1088/0264-9381/29/4/045003). eprint: [arXiv:1110.2229\[gr-qc\]](https://arxiv.org/abs/1110.2229).
- [38] G. Lovelace et al. “Massive disc formation in the tidal disruption of a neutron star by a nearly extremal black hole”. In: *Class. Quantum Grav.* 30.13, 135004 (July 2013), p. 135004. DOI: [10.1088/0264-9381/30/13/135004](https://doi.org/10.1088/0264-9381/30/13/135004). arXiv: [1302.6297 \[gr-qc\]](https://arxiv.org/abs/1302.6297).
- [39] I. D. Novikov and K. S. Thorne. “Black Holes”. In: ed. by C. DeWitt and B.S. DeWitt. New York: Gordon and Breach, 1973, p. 343.
- [40] Kip S. Thorne. “Disk-accretion onto a black hole. II. Evolution of the hole.” In: *Astrophys. J.* 191 (1974), p. 507. DOI: [10.1086/152991](https://doi.org/10.1086/152991).
- [41] Daniel A. Hemberger et al. “Final spin and radiated energy in numerical simulations of binary black holes with equal masses and equal, aligned or antialigned spins”. In: *Phys. Rev. D* 88 (6 Sept. 2013), p. 064014. DOI: [10.1103/PhysRevD.88.064014](https://doi.org/10.1103/PhysRevD.88.064014). arXiv: [1305.5991 \[gr-qc\]](https://arxiv.org/abs/1305.5991). URL: <http://link.aps.org/doi/10.1103/PhysRevD.88.064014>.
- [42] Luciano Rezzolla et al. “Spin Diagrams for Equal-Mass Black-Hole Binaries with Aligned Spins”. In: *Astrophys. J.* 679 (2008), pp. 1422–1426. arXiv: [0708.3999 \[gr-qc\]](https://arxiv.org/abs/0708.3999).
- [43] Mark Hannam et al. “Simulations of black-hole binaries with unequal masses or nonprecessing spins: Accuracy, physical properties, and comparison with post-Newtonian results”. In: *Phys. Rev. D* 82 (2010), p. 124008. eprint: [arXiv:1007.4789](https://arxiv.org/abs/1007.4789).

- [44] Pedro Marronetti et al. “High-spin binary black hole mergers”. In: *Phys. Rev. D* 77 (2008), p. 064010. DOI: [10.1103/PhysRevD.77.064010](https://doi.org/10.1103/PhysRevD.77.064010). arXiv: [0709.2160](https://arxiv.org/abs/0709.2160) [gr-qc].
- [45] Sergio Dain, Carlos O Lousto, and Yosef Zlochower. “Extra-Large Remnant Recoil Velocities and Spins from Near-Extremal-Bowen–York-Spin Black-Hole Binaries”. In: *Phys. Rev. D* 78 (2008), p. 024039. arXiv: [0803.0351v2](https://arxiv.org/abs/0803.0351v2) [gr-qc].
- [46] Ian Ruchlin et al. “New Puncture Initial Data for Black-Hole Binaries: High Spins and High Boosts”. In: (2014). arXiv: [1410.8607](https://arxiv.org/abs/1410.8607) [gr-qc].
- [47] <http://www.black-holes.org/SpEC.html>.
- [48] Geoffrey Lovelace et al. “Binary-black-hole initial data with nearly-extremal spins”. In: *Phys. Rev. D* 78 (2008), p. 084017. DOI: [10.1103/PhysRevD.78.084017](https://doi.org/10.1103/PhysRevD.78.084017).
- [49] Andrea Taracchini et al. “Effective-one-body model for black-hole binaries with generic mass ratios and spins”. In: *Phys. Rev. D* 89.6 (2014), 061502(R). DOI: [10.1103/PhysRevD.89.061502](https://doi.org/10.1103/PhysRevD.89.061502). arXiv: [1311.2544](https://arxiv.org/abs/1311.2544) [gr-qc].
- [50] Geoffrey Lovelace, Mark A. Scheel, Robert Owen, Matthew Giesler, Reza Katebi, Bela Szilagyi, Tony Chu, Nicholas Demos, Daniel A. Hemberger, and Lawrence E. Kidder. “Nearly extremal apparent horizons in simulations of merging black holes”. In: *Class. Quant. Grav.* 32.6 (2015), p. 065007. DOI: [10.1088/0264-9381/32/6/065007](https://doi.org/10.1088/0264-9381/32/6/065007). arXiv: [1411.7297](https://arxiv.org/abs/1411.7297) [gr-qc].
- [51] H. P. Pfeiffer et al. “A multidomain spectral method for solving elliptic equations”. In: *Comput. Phys. Commun.* 152 (May 2003), pp. 253–273. DOI: [10.1016/S0010-4655\(02\)00847-0](https://doi.org/10.1016/S0010-4655(02)00847-0). eprint: [gr-qc/0202096](https://arxiv.org/abs/gr-qc/0202096).
- [52] Matthew Caudill et al. “Circular orbits and spin in black-hole initial data”. In: *Phys. Rev. D* 74.6 (2006), p. 064011. eprint: [gr-qc/0605053](https://arxiv.org/abs/gr-qc/0605053).
- [53] James W. York. “Conformal “Thin-Sandwich” Data for the Initial-Value Problem of General Relativity”. In: *Phys. Rev. Lett.* 82.7 (Feb. 1999), pp. 1350–1353. DOI: [10.1103/PhysRevLett.82.1350](https://doi.org/10.1103/PhysRevLett.82.1350).
- [54] Harald P. Pfeiffer et al. “Reducing orbital eccentricity in binary black hole simulations”. In: *Class. Quantum Grav.* 24.12 (2007), S59–S81. eprint: [gr-qc/0702106](https://arxiv.org/abs/gr-qc/0702106).
- [55] Alessandra Buonanno et al. “Reducing orbital eccentricity of precessing black-hole binaries”. In: *Phys. Rev. D* 83 (2011), p. 104034. DOI: [10.1103/PhysRevD.83.104034](https://doi.org/10.1103/PhysRevD.83.104034). arXiv: [1012.1549](https://arxiv.org/abs/1012.1549) [gr-qc].
- [56] Abdul H. Mroué and Harald P. Pfeiffer. “Precessing Binary Black Holes Simulations: Quasicircular Initial Data”. In: (2012). arXiv: [1210.2958](https://arxiv.org/abs/1210.2958) [gr-qc].

- [57] Helmut Friedrich. “On the hyperbolicity of Einstein’s and other gauge field equations”. In: *Commun. Math. Phys.* 100.4 (1985), pp. 525–543. DOI: [10.1007/BF01217728](https://doi.org/10.1007/BF01217728). URL: <http://www.springerlink.com/content/w602g633428x8365>.
- [58] David Garfinkle. “Harmonic coordinate method for simulating generic singularities”. In: *Phys. Rev. D* 65.4 (2002), p. 044029.
- [59] F. Pretorius. “Numerical relativity using a generalized harmonic decomposition”. In: *Class. Quantum Grav.* 22 (Jan. 2005), p. 425. DOI: [10.1088/0264-9381/22/2/014](https://doi.org/10.1088/0264-9381/22/2/014). eprint: [gr-qc/0407110](https://arxiv.org/abs/gr-qc/0407110).
- [60] Lee Lindblom et al. “A new generalized harmonic evolution system”. In: *Class. Quantum Grav.* 23 (Aug. 2006), S447. DOI: [10.1088/0264-9381/23/16/S09](https://doi.org/10.1088/0264-9381/23/16/S09). eprint: [gr-qc/0512093](https://arxiv.org/abs/gr-qc/0512093).
- [61] Lee Lindblom and Béla Szilágyi. “An Improved Gauge Driver for the GH Einstein System”. In: *Phys. Rev. D* 80 (2009), p. 084019. eprint: [arXiv:0904.4873](https://arxiv.org/abs/0904.4873).
- [62] Matthew W. Choptuik and Frans Pretorius. “Ultra Relativistic Particle Collisions”. In: *Phys. Rev. Lett.* 104 (2010), p. 111101. DOI: [10.1103/PhysRevLett.104.111101](https://doi.org/10.1103/PhysRevLett.104.111101). arXiv: [0908.1780](https://arxiv.org/abs/0908.1780) [gr-qc].
- [63] Béla Szilágyi, Lee Lindblom, and Mark A. Scheel. “Simulations of Binary Black Hole Mergers Using Spectral Methods”. In: *Phys. Rev. D* 80 (2009), p. 124010. arXiv: [0909.3557](https://arxiv.org/abs/0909.3557) [gr-qc].
- [64] Béla Szilágyi. “Key Elements of Robustness in Binary Black Hole Evolutions using Spectral Methods”. In: *Int. J. Mod. Phys. D* 23.7 (2014), p. 1430014. DOI: [10.1142/S0218271814300146](https://doi.org/10.1142/S0218271814300146). arXiv: [1405.3693](https://arxiv.org/abs/1405.3693) [gr-qc].
- [65] M. A. Scheel, M. Boyle, T. Chu, L. E. Kidder, K. D. Matthews and H. P. Pfeiffer. “High-accuracy waveforms for binary black hole inspiral, merger, and ringdown”. In: *Phys. Rev. D* 79 (2009), p. 024003. eprint: [arXiv:gr-qc/0810.1767](https://arxiv.org/abs/gr-qc/0810.1767).
- [66] Daniel A. Hemberger et al. “Dynamical Excision Boundaries in Spectral Evolutions of Binary Black Hole Spacetimes”. In: *Class. Quantum Grav.* 30.11 (2013), p. 115001. DOI: [10.1088/0264-9381/30/11/115001](https://doi.org/10.1088/0264-9381/30/11/115001). arXiv: [1211.6079](https://arxiv.org/abs/1211.6079) [gr-qc]. URL: <http://stacks.iop.org/0264-9381/30/i=11/a=115001>.
- [67] Serguei Ossokine, Lawrence E. Kidder, and Harald P. Pfeiffer. “Precession-tracking coordinates for simulations of compact-object-binaries”. In: *Phys. Rev. D* 88 (2013), p. 084031. DOI: [10.1103/PhysRevD.88.084031](https://doi.org/10.1103/PhysRevD.88.084031). arXiv: [1304.3067](https://arxiv.org/abs/1304.3067) [gr-qc].

- [68] Oliver Rinne. “Stable radiation-controlling boundary conditions for the generalized harmonic Einstein equations”. In: *Class. Quantum Grav.* 23 (2006), pp. 6275–6300. URL: <http://stacks.iop.org/0264-9381/23/6275>.
- [69] Oliver Rinne, Lee Lindblom, and Mark A. Scheel. “Testing outer boundary treatments for the Einstein equations”. In: *Class. Quantum Grav.* 24 (2007), pp. 4053–4078. URL: <http://stacks.iop.org/0264-9381/24/4053>.
- [70] Carsten Gundlach. “Pseudospectral apparent horizon finders: An efficient new algorithm”. In: *Phys. Rev. D* 57.2 (Jan. 1998), pp. 863–875. DOI: [10.1103/PhysRevD.57.863](https://doi.org/10.1103/PhysRevD.57.863). URL: <http://link.aps.org/abstract/PRD/v57/p863>.
- [71] Gregory B. Cook and Bernard F. Whiting. “Approximate Killing Vectors on S^2 ”. In: *Phys. Rev. D* 76.4, 041501(R) (2007), 041501(R). DOI: [10.1103/PhysRevD.76.041501](https://doi.org/10.1103/PhysRevD.76.041501).
- [72] Robert Owen. “Topics in Numerical Relativity: The periodic standing-wave approximation, the stability of constraints in free evolution, and the spin of dynamical black holes”. PhD thesis. California Institute of Technology, 2007. URL: <http://resolver.caltech.edu/CaltechETD:etd-05252007-143511>.
- [73] Mark A. Scheel et al. “Solving Einstein’s Equations With Dual Coordinate Frames”. In: *Phys. Rev. D* 74 (2006), p. 104006. DOI: [10.1103/PhysRevD.74.104006](https://doi.org/10.1103/PhysRevD.74.104006).
- [74] Michael Boyle et al. “High-accuracy comparison of numerical relativity simulations with post-Newtonian expansions”. In: *Phys. Rev. D* 76.12 (2007), p. 124038. arXiv: [0710.0158 \[gr-qc\]](https://arxiv.org/abs/0710.0158).
- [75] Luisa T. Buchman et al. “Simulations of unequal mass binary black holes with spectral methods”. In: *Phys. Rev. D* 86 (2012), p. 084033. arXiv: [1206.3015 \[gr-qc\]](https://arxiv.org/abs/1206.3015).
- [76] Tony Chu, Harald P. Pfeiffer, and Mark A. Scheel. “High accuracy simulations of black hole binaries: Spins anti-aligned with the orbital angular momentum”. In: *Phys. Rev. D* 80 (2009), p. 124051. DOI: [10.1103/PhysRevD.80.124051](https://doi.org/10.1103/PhysRevD.80.124051). arXiv: [0909.1313 \[gr-qc\]](https://arxiv.org/abs/0909.1313).
- [77] <http://www.black-holes.org/waveforms>.
- [78] Kashif Alvi. “Energy and angular momentum flow into a black hole in a binary”. In: *Phys. Rev. D* 64.10 (Oct. 2001), p. 104020. URL: <http://link.aps.org/doi/10.1103/PhysRevD.64.104020>.
- [79] Robert Owen et al. “Frame-Dragging Vortexes and Tidal Tendexes Attached to Colliding Black Holes: Visualizing the Curvature of Spacetime”. In: *Phys. Rev. Lett.* 106 (2011), p. 151101.

- [80] K. Chatziioannou, E. Poisson, and N. Yunes. “Tidal heating and torquing of a Kerr black hole to next-to-leading order in the tidal coupling”. In: *Phys. Rev. D* 87.4, 044022 (Feb. 2013), p. 044022. DOI: [10.1103/PhysRevD.87.044022](https://doi.org/10.1103/PhysRevD.87.044022). arXiv: [1211.1686](https://arxiv.org/abs/1211.1686) [gr-qc].
- [81] K. Chatziioannou, E. Poisson, and N. Yunes. In: (). In preparation.
- [82] Stephanie Taylor and Eric Poisson. “Nonrotating black hole in a post-Newtonian tidal environment”. In: *Phys. Rev. D* 77 (2008), p. 044012.
- [83] Serguei Ossokine et al. “Comparing Post-Newtonian and Numerical-Relativity Precession Dynamics”. In: *Phys. Rev. D* 92.10 (2015), p. 104028. DOI: [10.1103/PhysRevD.92.104028](https://doi.org/10.1103/PhysRevD.92.104028). eprint: [arXiv:1502.01747](https://arxiv.org/abs/1502.01747)[gr-qc].
- [84] Lawrence E. Kidder. “Coalescing binary systems of compact objects to (post)^{5/2}-Newtonian order. V. Spin effects”. In: *Phys. Rev. D* 52.2 (July 1995), pp. 821–847. DOI: [10.1103/PhysRevD.52.821](https://doi.org/10.1103/PhysRevD.52.821).
- [85] Thibault Damour. “Coalescence of two spinning black holes: an effective one-body approach”. In: *Phys. Rev. D* 64 (2001), p. 124013. DOI: [10.1103/PhysRevD.64.124013](https://doi.org/10.1103/PhysRevD.64.124013). arXiv: [gr-qc/0103018](https://arxiv.org/abs/gr-qc/0103018) [gr-qc].
- [86] Lawrence E. Kidder. “Coalescing binary systems of compact objects to postNewtonian 5/2 order. 5. Spin effects”. In: *Phys. Rev. D* 52 (1995), pp. 821–847. DOI: [10.1103/PhysRevD.52.821](https://doi.org/10.1103/PhysRevD.52.821). arXiv: [gr-qc/9506022](https://arxiv.org/abs/gr-qc/9506022).
- [87] Manuela Campanelli, Carlos O. Lousto, and Yosef Zlochower. “Gravitational radiation from spinning-black-hole binaries: The orbital hang up”. In: *Phys. Rev. D* 74 (2006), 041501(R). eprint: [gr-qc/0604012](https://arxiv.org/abs/gr-qc/0604012).
- [88] Olivier Sarbach and Manuel Tiglio. “Gauge-invariant perturbations of Schwarzschild black holes in horizon-penetrating coordinates”. In: *Phys. Rev. D* 64 (Sept. 2001), p. 084016. DOI: [10.1103/PhysRevD.64.084016](https://doi.org/10.1103/PhysRevD.64.084016). URL: <http://link.aps.org/abstract/PRD/v64/e084016>.
- [89] Oliver Rinne et al. “Implementation of higher-order absorbing boundary conditions for the Einstein equations”. In: *Class. Quantum Grav.* 26 (2009), p. 075009.
- [90] Michael Boyle. “Angular velocity of gravitational radiation from precessing binaries and the corotating frame”. In: *Phys. Rev. D* 87.10 (May 2013), p. 104006. DOI: [10.1103/PhysRevD.87.104006](https://doi.org/10.1103/PhysRevD.87.104006). URL: <http://link.aps.org/doi/10.1103/PhysRevD.87.104006> (visited on 05/09/2013).
- [91] M. Boyle et al. “Gravitational-wave modes from precessing black-hole binaries”. In: (2014). arXiv:1409.4431. arXiv: [1409.4431](https://arxiv.org/abs/1409.4431).
- [92] Donato Bini and Thibault Damour. “Analytical determination of the two-body gravitational interaction potential at the 4th post-Newtonian approximation”. In: *Phys. Rev. D* 87 (12 June 2013), p. 121501. DOI: [10.1103/PhysRevD.87.121501](https://doi.org/10.1103/PhysRevD.87.121501). arXiv: [1305.4884](https://arxiv.org/abs/1305.4884) [gr-qc]. URL: <http://link.aps.org/doi/10.1103/PhysRevD.87.121501>.

- [93] Ryuichi Fujita. “Gravitational radiation for extreme mass ratio inspirals to the 14th post-Newtonian order”. In: *Progress of Theoretical Physics* 127.3 (2012), pp. 583–590. arXiv: 1104.5615 [gr-qc]. URL: <http://ptp.oxfordjournals.org/content/127/3/583.abstract>.
- [94] Luc Blanchet et al. “The Third post-Newtonian gravitational wave polarisations and associated spherical harmonic modes for inspiralling compact binaries in quasi-circular orbits”. In: *Class. Quantum Grav.* 25 (2008), p. 165003. DOI: 10.1088/0264-9381/25/16/165003. arXiv: 0802.1249 [gr-qc].
- [95] Guillaume Faye et al. “The third and a half post-Newtonian gravitational wave quadrupole mode for quasi-circular inspiralling compact binaries”. In: *cqg* 29.17 (Sept. 2012), p. 175004. URL: <http://arxiv.org/abs/1204.1043>.
- [96] Guillaume Faye, Luc Blanchet, and Bala R. Iyer. “Non-linear multipole interactions and gravitational-wave octupole modes for inspiralling compact binaries to third-and-a-half post-Newtonian order”. In: *Class. Quantum Grav.* 32.4 (2015), p. 045016. arXiv: 1409.3546 [gr-qc]. URL: <http://stacks.iop.org/0264-9381/32/i=4/a=045016>.
- [97] Alejandro Bohé et al. “Next-to-next-to-leading order spin-orbit effects in the near-zone metric and precession equations of compact binaries”. In: *cqg* 30.7 (Apr. 2013), p. 075017. URL: <http://iopscience.iop.org/0264-9381/30/7/075017>.
- [98] Sylvain Marsat et al. “Next-to-leading tail-induced spin-orbit effects in the gravitational radiation flux of compact binaries”. In: *Class. Quantum Grav.* 31.2 (2014), p. 025023. URL: <http://stacks.iop.org/0264-9381/31/i=2/a=025023>.
- [99] Alessandra Buonanno, Guillaume Faye, and Tanja Hinderer. “Spin effects on gravitational waves from inspiraling compact binaries at second post-Newtonian order”. In: *Phys. Rev. D* 87.4 (Feb. 2013), p. 044009. DOI: 10.1103/PhysRevD.87.044009. URL: <http://link.aps.org/doi/10.1103/PhysRevD.87.044009> (visited on 04/09/2013).
- [100] Clifford M. Will and Alan G. Wiseman. “Gravitational radiation from compact binary systems: Gravitational waveforms and energy loss to second post-Newtonian order”. In: *Phys. Rev. D* 54.8 (Oct. 1996), pp. 4813–4848. DOI: 10.1103/PhysRevD.54.4813. URL: <http://link.aps.org/abstract/PRD/v54/p4813>.
- [101] K.G. Arun et al. “Higher-order spin effects in the amplitude and phase of gravitational waveforms emitted by inspiraling compact binaries: Ready-to-use gravitational waveforms”. In: *Phys. Rev. D* 79 (2009), p. 104023. DOI: 10.1103/PhysRevD.79.104023, 10.1103/PhysRevD.84.049901, 10.1103/PhysRevD.79.104023, 10.1103/PhysRevD.84.049901. arXiv: 0810.5336 [gr-qc].

- [102] Michael Boyle et al. “High-accuracy numerical simulation of black-hole binaries: Computation of the gravitational-wave energy flux and comparisons with post-Newtonian approximants”. In: *Phys. Rev. D* 78 (2008), p. 104020. DOI: [10.1103/PhysRevD.78.104020](https://doi.org/10.1103/PhysRevD.78.104020). arXiv: [0804.4184](https://arxiv.org/abs/0804.4184) [gr-qc].
- [103] Ilana MacDonald, Samaya Nissanke, and Harald P. Pfeiffer. “Suitability of post-Newtonian/numerical-relativity hybrid waveforms for gravitational wave detectors”. In: *Class. Quantum Grav.* 28.13 (July 2011), p. 134002. ISSN: 0264-9381. DOI: [10.1088/0264-9381/28/13/134002](https://doi.org/10.1088/0264-9381/28/13/134002). arXiv: [1102.5128](https://arxiv.org/abs/1102.5128) [gr-qc]. URL: <http://iopscience.iop.org/0264-9381/28/13/134002/>.
- [104] P. Ajith et al. “A Template bank for gravitational waveforms from coalescing binary black holes. I. Non-spinning binaries”. In: *Phys. Rev. D* 77 (2008), p. 104017. DOI: [10.1103/PhysRevD.77.104017](https://doi.org/10.1103/PhysRevD.77.104017), [10.1103/PhysRevD.79.129901](https://doi.org/10.1103/PhysRevD.79.129901), [10.1103/PhysRevD.77.104017](https://doi.org/10.1103/PhysRevD.77.104017), [10.1103/PhysRevD.79.129901](https://doi.org/10.1103/PhysRevD.79.129901). arXiv: [0710.2335](https://arxiv.org/abs/0710.2335) [gr-qc].
- [105] Chris Loken et al. “SciNet: Lessons Learned from Building a Power-efficient Top-20 System and Data Centre”. In: *J. Phys.: Conf. Ser.* 256 (2010), p. 012026. DOI: [10.1088/1742-6596/256/1/012026](https://doi.org/10.1088/1742-6596/256/1/012026).

*Chapter 4***BLACK HOLE RINGDOWN: THE IMPORTANCE OF OVERTONES**

Matthew Giesler, Maximiliano Isi, Mark A. Scheel, and Saul A. Teukolsky

Physical Review X, 9, 041060 (2019)

[arxiv:1903.08284](https://arxiv.org/abs/1903.08284)**4.1 Abstract**

It is possible to infer the mass and spin of the remnant black hole from binary black hole mergers by comparing the ringdown gravitational wave signal to results from studies of perturbed Kerr spacetimes. Typically these studies are based on the fundamental quasinormal mode of the dominant $\ell = m = 2$ harmonic. By modeling the ringdown of accurate numerical relativity simulations, we find, in agreement with previous findings, that the fundamental mode alone is insufficient to recover the true underlying mass and spin, unless the analysis is started very late in the ringdown. Including higher overtones associated with this $\ell = m = 2$ harmonic resolves this issue, and provides an unbiased estimate of the true remnant parameters. Further, including overtones allows for the modeling of the ringdown signal for all times beyond the peak strain amplitude, indicating that the linear quasinormal regime starts much sooner than previously expected. This implies that the spacetime is well described as a linearly perturbed black hole with a fixed mass and spin as early as the peak. A model for the ringdown beginning at the peak strain amplitude can exploit the higher signal-to-noise ratio in detectors, reducing uncertainties in the extracted remnant quantities. These results should be taken into consideration when testing the no-hair theorem.

4.2 Introduction

The end state of astrophysical binary black hole (BBH) mergers is a perturbed single black hole (BH) characterized by two parameters: the final remnant mass M_f and spin angular momentum S_f [1–3]. The perturbed BH radiates gravitational waves at a specific set of frequencies over characteristic timescales completely determined by the mass and spin. The segment of the gravitational wave signal associated with the single BH's oscillations is known as the ‘ringdown’ phase, as the perturbed BH rings

down analogous to a struck bell. The set of frequencies and damping times associated with a given BH are known as quasinormal modes (QNMs), the damped oscillations connected to the underlying BH geometry. The modes can be decomposed into spin-weighted spheroidal harmonics with angular indices (ℓ, m) [4–6]. For each (ℓ, m) , there exists a discrete set of complex frequencies denoted $\omega_{\ell mn}$, where n is the ‘overtone’ index. The oscillatory behavior is described by $\Re(\omega_{\ell mn})$, while $\Im(\omega_{\ell mn})$ is related to the damping timescale by $\tau_{\ell mn} = -\Im(\omega_{\ell mn})^{-1}$. For a given (ℓ, m) , the overtone index sorts the QNMs in order of decreasing damping timescales, so that $n = 0$ corresponds to the least-damped mode (i.e. the longest-lived mode), which is often referred to as the fundamental mode.

The recent detections of merging BBHs [7–13] by Advanced LIGO [14] and Virgo [15], including the ringdown phase, have stimulated significant interest in measuring the QNMs from the observations [16–22]. Accurately determining the QNMs allows for precise tests of general relativity (GR) [23–29]. In [16], the frequency and damping time of the fundamental mode were inferred from the ringdown data of the first event (GW150914). The analysis was performed at several time offsets with respect to the time of peak strain amplitude. For sufficiently late values of this start time, the frequency and damping time were found to be in agreement with the prediction from GR for a remnant consistent with the full waveform. The multiple start times used in the analysis reflect an uncertainty about when the fundamental mode becomes a valid description for the ringdown, as there is noticeable disagreement between the measured mode and the GR prediction at early times. This raises the question: *at what point in the ringdown does perturbation theory become relevant?*

In this paper, we consider the contribution of QNM overtones to the ringdown. Including overtones allows for an excellent description of the waveform well before the fundamental mode becomes dominant and extends the regime over which perturbation theory is applicable to times even before the peak strain amplitude of the waveform. Moreover, an improved model for the ringdown through the inclusion of overtones can provide more accurate estimates of the remnant mass and spin [30, 31]. Furthermore, the inclusion of higher overtones provides a means to test GR at a more stringent level, because the QNM frequencies of all included overtones are independently constrained by GR for any given M_f and S_f .

We begin by demonstrating the benefits of including overtones, in agreement with [30, 31], by analyzing a numerical relativity (NR) waveform. We then show how overtones can improve the extraction of information from noisy LIGO or Virgo data. We show

that the overtones are not subdominant as is often assumed, but are instead critically necessary to properly model the linear ringdown regime. The inclusion of QNM overtones provides a high accuracy description of the ringdown as early as the time of peak strain amplitude, where the high signal-to-noise ratio (SNR) can be exploited to significantly reduce uncertainty in the extracted remnant properties.

4.3 Previous studies

There have been numerous attempts to identify the start time of ringdown, that is, the point in time where a transition has occurred from the non-linear regime into one where the signal can be described by a linear superposition of damped sinusoids [19, 21, 31–34]. To highlight the existing disagreement in the literature, the following studies, each using NR waveforms as a testbed, come to different conclusions regarding this transition time. In [32], the start of the ringdown phase is inferred to be $10M$ (where M is the total binary mass, and $G = c = 1$) after the peak luminosity of the $\ell = m = 2$ component of the strain h ; this is the time at which the frequency of the $\ell = m = 2$ mode roughly agrees with that of the fundamental QNM. In [33], the ringdown portion of the waveform is considered to be $10M$ after the peak luminosity of the Newman-Penrose scalar Ψ_4 (related to two time-derivatives of h). A ringdown model with the fundamental and the first two overtones was built under this assumed start time and employed in [21], which concluded that a start time of $16M$ after the peak strain amplitude is optimal. The peak of Ψ_4 is implicitly used as the start time for the ringdown in [31], where a superposition of the fundamental mode plus the first two overtones provides an accurate representation of the remnant properties and the fundamental frequency expected from perturbation theory. Interestingly, in one of the earliest analyses of BBH waveforms using NR simulations, despite the limited numerical accuracy available for simulations at that time, Buonanno, Cook, and Pretorius [30] were able to fit 3 overtones to the NR ringdown waveform by extending their analysis to times *before* the peak amplitude of Ψ_4 . A superposition of QNMs, including overtones and pseudo QNMs, became an integral part of modeling the merger-ringdown regime in earlier EOB models [35–37].¹

A likely cause of confusion is that start times are defined with respect to the peak of

¹A recent extension of EOB, referred to as pEOBNR [20], was designed for future tests of the no-hair theorem by measuring the frequencies of the $\ell = m = 2$ and $\ell = m = 3$ fundamental modes. Restricted to non-spinning binaries, pEOBNR models the full inspiral and merger with an attached ringdown model (including overtones), in order to avoid deciding at what time the QNMs alone provide an accurate description of the waveform.

some waveform quantity, and different authors choose different waveform quantities for this purpose. To illuminate the implicit time offsets incurred by differences in this choice, consider as a specific example the GW150914-like NR waveform SXS:BBH:0305 in the Simulating eXtreme Spacetimes (SXS) catalog [38, 39]. For this waveform, the peak of h occurs first, followed by the peak luminosity of h , then the peak of Ψ_4 , and finally the peak luminosity of Ψ_4 . These last 3 times are $\sim 7M, 10M, 11M$ after the peak of h . As we will show, overtones beyond $n \sim 2$ are expected to have significantly decayed by the peak of Ψ_4 , so that relying on the peak of Ψ_4 to begin a ringdown analysis may be problematic.

The miscellany of start times above can be reconciled, to some extent, by considering the contribution of overtones to the ringdown. Relying solely on the fundamental mode as a description for the ringdown should result in only late time agreement. Additional consideration of overtones at late times should result in finding significantly reduced amplitudes in any overtones that remain. As we demonstrate below, this is because overtones decay more quickly for larger n ; each additional included overtone leads to a superposition of QNMs that provides a description of the ringdown at earlier times. Ignoring the contribution of overtones, by considering them negligible as in [19] indirectly leads to the conclusion that remnant properties remain unconstrainable even in the infinite SNR limit—which we find to be untrue.

4.4 Model

We use the fundamental QNM and a varying number of overtones to determine when the linear QNM solution best describes the (ℓ, m) mode extracted from NR simulations. Throughout, we focus on the aforementioned astrophysically relevant NR waveform SXS:BBH:0305 in the SXS catalog, which is modeled after the GW150914 event. The waveform represents a simulated system with a mass ratio of 1.22, where the larger BH has a dimensionless spin $\vec{\chi} = 0.33 \hat{z}$ and the smaller companion BH has dimensionless spin $\vec{\chi} = -0.44 \hat{z}$. The resulting remnant in this simulation has a final mass $M_f = 0.9520 M$ and dimensionless spin $\chi_f = S_f/M_f^2 = 0.6921$. We explore at what time the linear QNM description provides not only an optimal fit for the resulting ringdown waveform, but also an optimal estimate of the remnant mass and spin.

We model the ringdown radiation as a sum of damped sinusoids [40–43] by writing

each angular mode of the complex strain, $h = h_+ - ih_\times$, as

$$h_{\ell m}^N(t) = \sum_{n=0}^N C_{\ell mn} e^{-i\omega_{\ell mn}(t-t_0)} \quad t \geq t_0, \quad (4.1)$$

with complex frequencies $\omega_{\ell mn} = \omega_{\ell mn}(M_f, \chi_f)$ as determined by perturbation theory [44, 45]. Here, t_0 corresponds to a specifiable ‘start time’ for the model and times before t_0 are not included in the model. The complex coefficients $C_{\ell mn}$, which are not known a priori as they depend on the binary configuration and dynamics near merger, are determined using unweighted linear least squares in the time domain. The complex-valued amplitudes can be factored into a real-valued amplitude and phase, $C_{\ell mn} = |A_{\ell mn}|e^{-i\phi_{\ell mn}}$, of which we make direct use in Sec. 4.5.

Throughout, we focus on describing the dominant *spherical* harmonic mode in the NR simulation, the $\ell = m = 2$ mode.² The natural angular basis in perturbation theory is spin-weighted *spheroidal* harmonics [4–6], which can be written as an expansion in spin-weighted spherical harmonics [6, 46–48]. Decomposing the ringdown into spherical harmonics results in mixing of the spheroidal and spherical bases between the angular functions with the same m , but different ℓ ’s, and this mixing increases with χ_f [6, 49]. For the SXS:BBH:0305 waveform, the $\ell = m = 2$ spherical harmonic remains a good approximation for the $\ell = m = 2$ spheroidal harmonic. The amplitudes of the spheroidal and spherical $\ell = m = 2$ modes differ by a maximum of only 0.4%, which occurs roughly $15M$ after the peak of h . This difference is significantly smaller at the peak. The mixing is small because higher (ℓ, m) harmonics are subdominant for this waveform, but in a more general case, these higher harmonics may play a more important role.

4.5 Results

QNM overtone fits

The linear superposition of the fundamental QNM and N overtones is an excellent description of the waveform around and before the peak strain. To demonstrate this, we begin by fixing the remnant properties to the final values provided by the NR simulation. With the mass M_f and dimensionless spin χ_f fixed, the set of frequencies $\omega_{22n}(M_f, \chi_f)$ is fully specified by perturbation theory. The only remaining free parameters in Eq. (4.1) are the complex coefficients C_{22n} and the model start time t_0 . For N included overtones, and a given choice of t_0 , we determine the $(N + 1)$ complex

²We have verified the presence and early dominance of overtones in other resolvable (ℓ, m) ’s in the NR waveform.

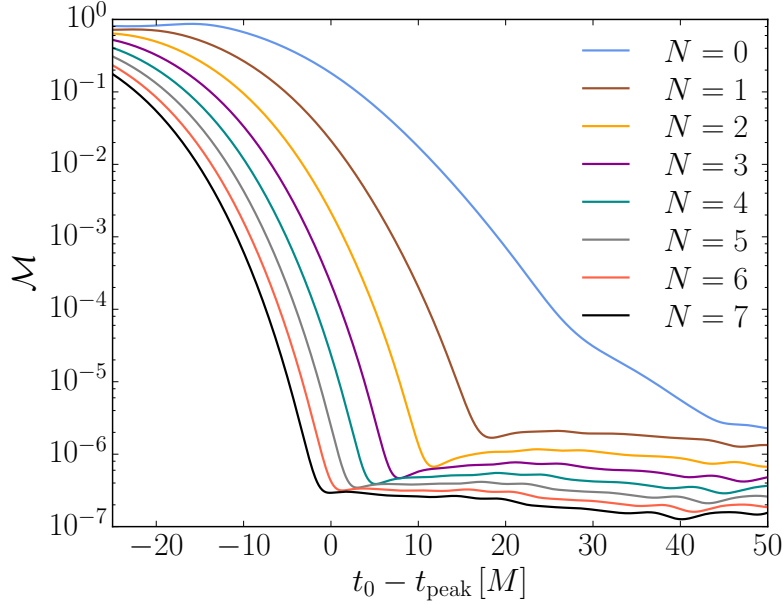


Figure 4.1: Mismatches as a function of time for the eight models, each including up to N QNM overtones. The mismatch associated with each model at a given t_0 corresponds to the mismatch computed using Eq. (4.2), between the model and the NR waveform for $t \geq t_0$, where t_0 specifies the lower limit used in Eq. (4.3). Each additional overtone decreases the minimum achievable mismatch, with the minimum consistently shifting to earlier times.

C_{22n} 's using unweighted linear least squares, thus obtaining a model waveform given by Eq. (4.1). We construct such a model waveform for $t \geq t_0$ at many start times beginning at $t_0 = t_{\text{peak}} - 25M$ and extending to times $t_0 = t_{\text{peak}} + 60M$, where t_{peak} is the peak amplitude of the complex strain. For each start time t_0 , we compute the mismatch \mathcal{M} between our model waveform, h_{22}^N , and the NR waveform, h_{22}^{NR} , through

$$\mathcal{M} = 1 - \frac{\langle h_{22}^{\text{NR}}, h_{22}^N \rangle}{\sqrt{\langle h_{22}^{\text{NR}}, h_{22}^{\text{NR}} \rangle \langle h_{22}^N, h_{22}^N \rangle}} . \quad (4.2)$$

In the above, the inner product between two complex waveforms, say $x(t)$ and $y(t)$, is defined by

$$\langle x(t), y(t) \rangle = \int_{t_0}^T x(t) \overline{y(t)} dt , \quad (4.3)$$

where the bar denotes the complex conjugate, the lower limit of the integral is the start time parameter t_0 in Eq. (4.1), and the upper limit of the integral T is chosen to be a time before the NR waveform has decayed to numerical noise. For the aforementioned NR simulation, we set $T = t_{\text{peak}} + 90M$.

This procedure results in mismatches as a function of t_0 for each set of overtones; these are presented in Fig. 4.1. The figure shows that $N = 7$ overtones provides the minimum mismatch and at the earliest of times, as compared to the other overtone models. The waveform corresponding to the $N = 7$ overtone model and $t_0 = t_{\text{peak}}$ is

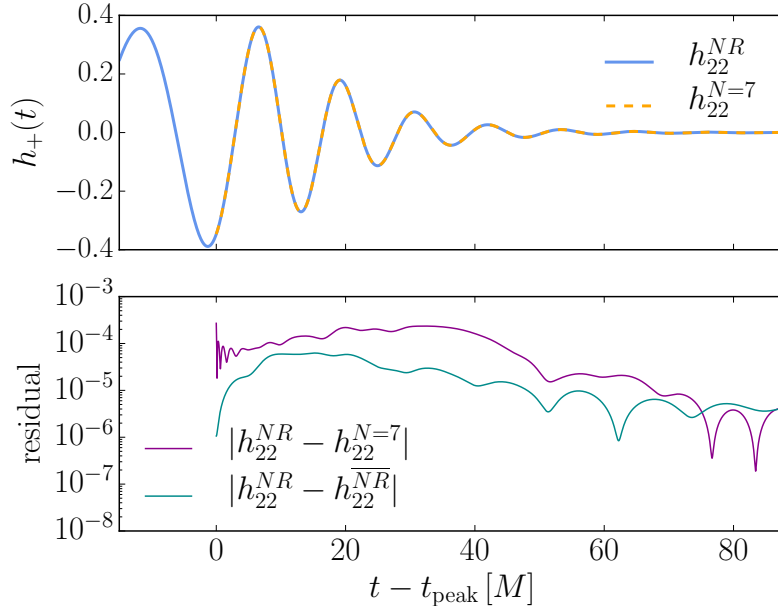


Figure 4.2: Comparison between the plus polarization of the $\ell = m = 2$ mode of the NR waveform and the $N = 7$ linear QNM model. The QNM model begins at $t_0 = t_{\text{peak}}$. The upper panel shows both waveforms, and the lower panel shows the residual for $t \geq t_{\text{peak}}$. For reference, the lower panel also shows an estimate of the error in the NR waveform, $|h_{22}^{NR} - h_{22}^{NR}|$, where h_{22}^{NR} refers to the highest resolution waveform of SXS:BBH:0305 and h_{22}^{NR} refers to the next highest resolution waveform for this same system. The two NR waveforms are aligned at $t_0 = t_{\text{peak}}$, in both time and phase.

visualized in Fig. 4.2, where the model waveform is compared to the NR waveform along with the fit residual.

At face value, Fig. 4.1 provides us with a guide for determining the times where a linear ringdown model with N QNM overtones is applicable. However, relying on the mismatch alone can be deceiving. The $n = 7$ overtone decays away very quickly, yet Fig. 4.1 shows that retaining this overtone still produces small mismatches at times beyond when this mode should no longer be numerically resolvable. This is due to overfitting to numerical noise after the higher overtones in each model have sufficiently decayed. We find that the turnover subsequent to the first mismatch

minimum in Fig. 4.1 is a good approximation for when each overtone has a negligible amplitude.

It is important then that the model not only minimizes the residual in the waveform quantity, but also that it provides faithful estimates of the underlying system parameters. In particular, we may demand that the inferred mass and spin agree with the true values known from the NR simulation. To check that the model does indeed faithfully represent the NR waveform with the correct final mass and spin, we repeat the fits but we allow M_f and χ_f to vary, and we set the frequencies of each overtone to their GR-consistent values through the perturbation-theory formula for $\omega_{22n}(M_f, \chi_f)$. As a measure of error, we use

$$\epsilon = \sqrt{(\delta M_f/M)^2 + (\delta \chi_f)^2}, \quad (4.4)$$

where δM_f and $\delta \chi_f$ are the differences between the best fit estimates for M_f and χ_f as compared to the remnant values from the NR simulation. Using a model with $N = 7$ overtones and $t_0 = t_{\text{peak}}$, the best fit estimates for M_f and χ_f yield a value of $\epsilon \sim 2 \times 10^{-4}$. For reference, by comparing the two highest resolutions of this simulation, we estimate the error in the NR measured remnant mass and spin to be $\delta M_f \sim 1.3 \times 10^{-5} M$ and $\delta \chi_f \sim 2.1 \times 10^{-5}$, which corresponds to a value of $\epsilon \sim 2 \times 10^{-5}$. Furthermore, the difference in the recovered M_f and χ_f as compared to the NR values increases as we drop overtones from the model. This behavior appears to be robust. Repeating the above analysis on roughly 80 additional waveforms in the SXS catalog with aligned spins and mass ratios up to 8 [38, 50] yields similar results, with median value of $\epsilon \sim 10^{-3}$. The full distribution of ϵ for this part of parameter space, with $N = 7$ overtones at $t_0 = t_{\text{peak}}$ is shown in Fig. 4.3.

Returning to our analysis of SXS:BBH:0305, to highlight the worst-fit and best-fit cases and to visualize the mismatch as a function of mass and spin, we compute the mismatch between NR and the model Eq. (4.1) with $t_0 = t_{\text{peak}}$ and the C_{22n} 's determined by a least-squares fit for a grid of M_f and χ_f values. In Fig. 4.4, we see that with $N = 7$ overtones, the mismatch has a deep minimum associated with the true remnant quantities. However, using solely the fundamental mode, $N = 0$, with $t_0 = t_{\text{peak}}$ provides largely biased estimates for the remnant M_f and χ_f , as is visible in Fig. 4.5. This is not surprising in light of Fig. 4.1, where at this time the $N = 0$ model provides the poorest mismatch; this is a consequence of the higher overtones dominating the waveform at this time. The bias can be overcome by waiting a sufficiently long time, which allows the overtones to decay away and the fundamental

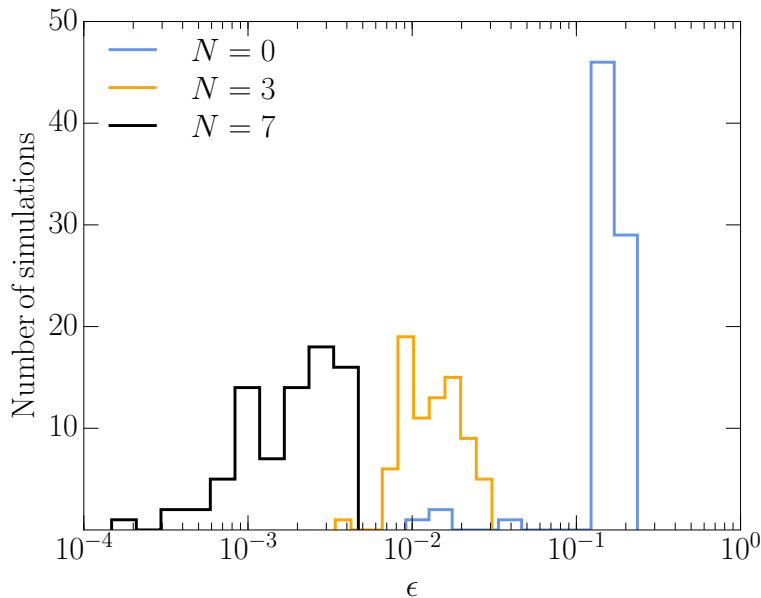


Figure 4.3: The distribution of ϵ , Eq. (4.4), for a range of simulations in the SXS catalog. The distribution includes systems with mass ratios up to 8 and orbit-aligned component spins with $|\vec{\chi}| \leq 0.8$. The distributions shown are for $N = \{0, 3, 7\}$ overtones at the peak of the strain amplitude. For the best performing model, $N = 7$, the median value is 2×10^{-3} and the maximum error in estimating the mass and spin is $\sim 5 \times 10^{-3}$.

mode to become dominant. This can be seen in Fig. 4.6, where we repeat the same procedure with $N = 0$ and $t_0 = t_{\text{peak}} + 47M$. Here the resulting distribution of mismatches in the $M_f - \chi_f$ plane is on par with the distribution associated with including $N = 7$ overtones and $t_0 = t_{\text{peak}}$, with the $N = 7$ case producing a smaller absolute mismatch than the $N = 0$ case. The key point is that we can recover similar information about the underlying remnant at the peak, through the inclusion of overtones, as we can by analyzing the waveform at late times. As discussed in more detail in Sec. 4.5, extending the ringdown model to earlier times allows us to access higher signal-to-noise ratios and can significantly reduce uncertainties in parameter estimation.

One might be concerned that the additional free parameters in the fit, introduced by including the overtones, simply allow for fitting away any non-linearities that may be present, making the fundamental mode more easily resolvable, and therefore better determining the underlying remnant mass and spin. A simple test of this idea is to repeat the fit while still setting the fundamental frequencies $\omega_{220}(M_f, \chi_f)$ according to perturbation theory, but to intentionally set the frequencies of the overtones to

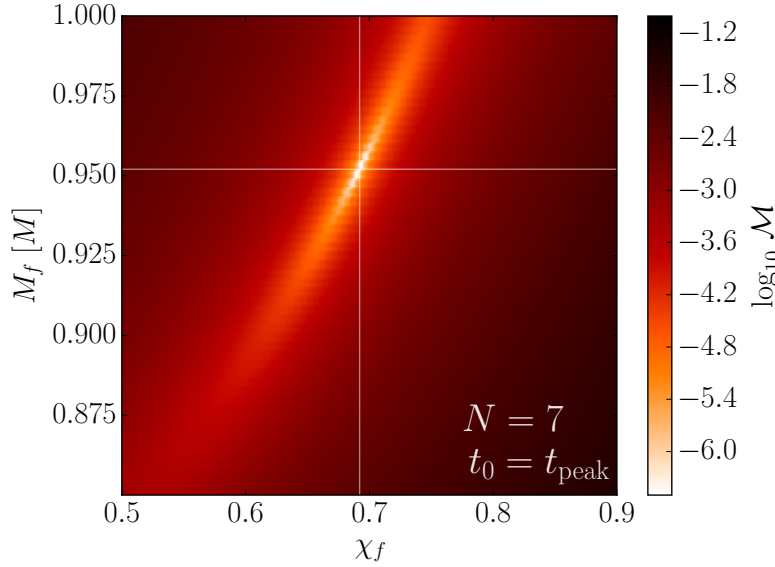


Figure 4.4: Mismatches for the $\ell = m = 2$ mode between NR and Eq. (4.1) for a grid of M_f and χ_f with $N = 7$ and $t_0 = t_{\text{peak}}$. The white horizontal and vertical lines correspond to the NR values and are in good agreement with the M_f and χ_f mismatch distribution using the maximum number of overtones considered.

incorrect values. The fit will then have the same number of degrees of freedom as previously, but without the correct physics. Let $\omega_{22n}(M_f, \chi_f)$ be the set of frequencies determined by perturbation theory and take $\tilde{\omega}_{22n}(M_f, \chi_f)$ to be the set of frequencies with the fundamental unmodified, but with $\tilde{\omega}_{22n}(M_f, \chi_f) = \omega_{22n}(M_f, \chi_f)(1 + \delta)$, for $n > 0$. As a measure of error, we rely on ϵ , Eq. (4.4), the root-mean-squared error in the estimated mass and spin as compared to the known NR values.

For demonstration purposes, we let δ take on values from the set $\pm\{0.01, 0.05, 0.2\}$ and fit to the spherical $\ell = m = 2$ mode with $t_0 = t_{\text{peak}}$ for different numbers of included overtones N . A comparison between the unmodified and modified models with the same number of degrees of freedom is presented in Fig. 4.7. From Fig. 4.7, it is evident that the unmodified set of QNMs, $\omega_{22n}(M_f, \chi_f)$, remains true to the underlying mass and spin and converges to smaller errors as the number of included overtones is increased. In the case where the overtones are given slightly incorrect frequencies by the δ parameter introduced above, including higher overtones yield fits that remain biased away from the true values, leading to larger values of ϵ .

Furthermore, in an additional test we have allowed for different values of δ for each n , each independently sampled from a normal distribution with mean $\mu = 0$ and standard deviation $\sigma = 0.2$. In this test, each overtone frequency is randomly modified to a

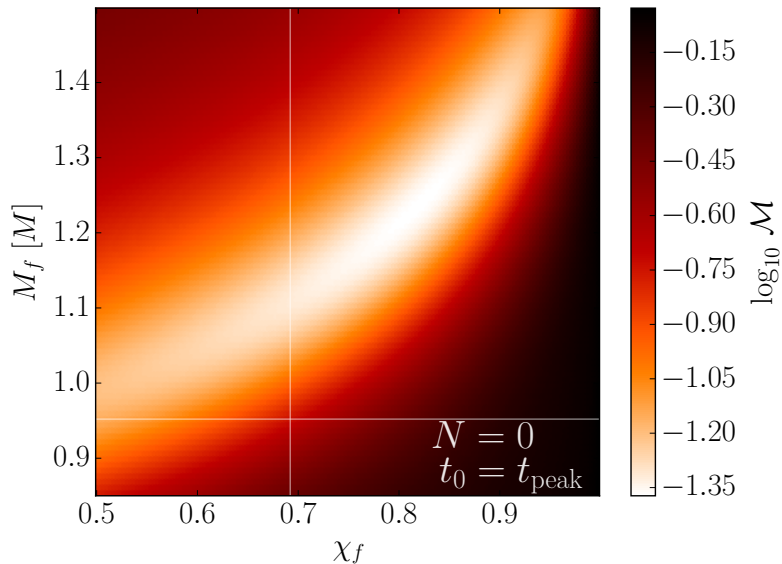


Figure 4.5: The mismatches for the $\ell = m = 2$ mode between NR and Eq. (4.1) over a grid of χ_f and M_f with $N = 0$, the fundamental mode only, and $t_0 = t_{\text{peak}}$. The white horizontal and vertical lines correspond to the remnant values from NR. As the fundamental mode is subdominant at this time, this single-mode model is a poor probe of the underlying remnant mass and spin. Note that the mass and mismatch scales used in this figure are significantly different than Fig. 4.4, due to the discrepant single-mode fit at early times.

different extent about $\omega_{22n}(M_f, \chi_f)$. In all 100 cases randomly generated from the above distribution, the ϵ 's associated with the modified frequencies always remain bounded from below by the ϵ associated with the GR frequencies of the asymptotic remnant. A random, representative, subset of these 100 cases is shown as faint grey traces in Fig. 4.7. This suggests that the overtones associated with the asymptotic remnant provide a sufficiently good linear description of the perturbations for all times beyond the peak of this mode, while a similar set of overtones that are inconsistent with the asymptotic remnant do not.

Characterizing the overtones

The behavior in the previous section can be explained by carefully understanding how the overtones contribute to the ringdown. As briefly touched on in Sec. 4.2, the overtones are those modes with $n > 0$, where n orders the modes based on decreasing damping time. While these modes are the least important in a time-weighted sense, describing them as ‘overtones’ is somewhat of a misnomer. In a classical description of harmonics, overtones are at higher frequencies than the fundamental, typically

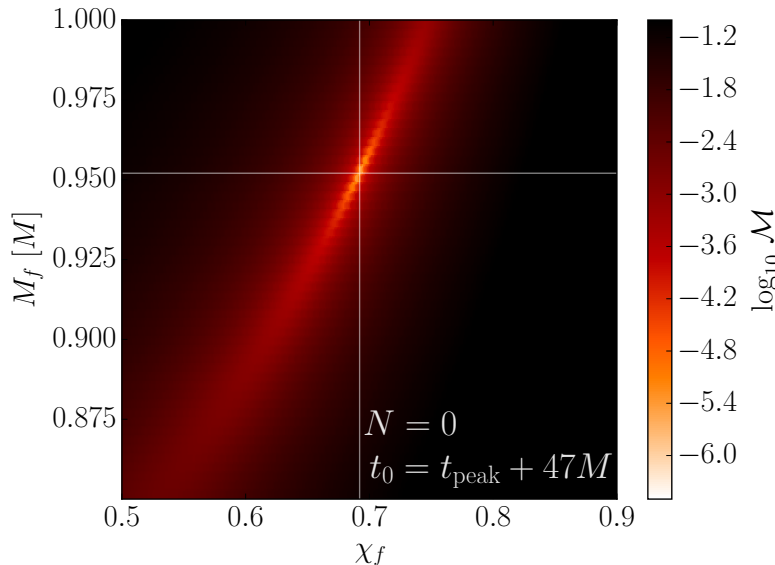


Figure 4.6: Mismatches for the $\ell = m = 2$ mode between NR and Eq. (4.1) for a grid of M_f and χ_f with $N = 0$, the fundamental mode, at a late time $t_0 = t_{\text{peak}} + 47M$. Here the fundamental mode is dominant, since the overtones have decayed away by this time. Again, the white horizontal and vertical lines correspond to the remnant values from NR and now, at this late time, we find good agreement between the true values and those recovered by using only the fundamental mode as a probe for M_f and χ_f .

multiples of the first harmonic, and are usually subdominant. However, for QNMs, the overtones decrease in frequency and are not necessarily subdominant. As briefly mentioned in Sec. 4.4, the amplitude of each QNM overtone in the ringdown depends on the binary configuration and the dynamics leading up to merger. This dynamics specifies the ‘initial data’ for the ringdown, determining which QNMs are excited and to what extent. As such, the overtone amplitudes for waveform SXS:BBH:0305 will differ from those with different ‘initial data’, i.e., binary configurations with different mass ratios or different spin vectors.

To provide a qualitative understanding of the relative amplitudes of different overtones, we decompose the ringdown waveform of SXS:BBH:0305 into its constituent overtones. Using $t_0 = t_{\text{peak}}$ and $N = 7$ overtones, we determine the C_{22n} ’s as in Sec. 4.5 with M_f and χ_f fixed to the NR simulation values. The corresponding values $A_n = |C_{22n}(t = t_0 = t_{\text{peak}})|$ form the entries in the bottom row of Table 4.1. For $N = 6$ we keep $t_0 = t_{\text{peak}}$, so that the amplitudes are measured with respect to the peak, but we include in our fit only data for $t \geq t_{\text{fit}}$, where t_{fit} corresponds to

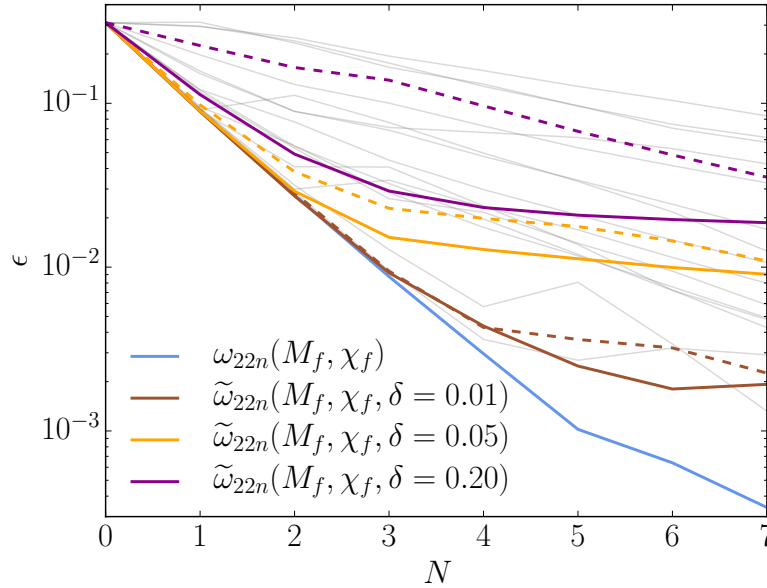


Figure 4.7: The root-mean-squared error, ϵ , defined in Eq. (4.4), for different sets of frequencies, as a function of number of included overtones N . The fits are performed on the spherical $\ell = m = 2$ mode at $t = t_0 = t_{\text{peak}}$. The label $\omega_{22n}(M_f, \chi_f)$ represents the set of frequencies consistent with perturbation theory, while $\tilde{\omega}_{22n}(M_f, \chi_f)$ represents the set of frequencies with the fundamental mode, $n = 0$, unmodified but with a slight modification to the overtone frequencies by a factor of $(1 + \delta)$. For each δ , there is an associated dashed line of the same color that corresponds to $\delta \rightarrow -\delta$. The faint grey lines correspond to frequencies with a random δ for each n , as explained in the last paragraph of Sec. 4.5. The results suggest there is information present in the overtones that contribute to extracting the remnant properties at the peak, as these outperform a similar set of functions, with the same degrees of freedom for each N , but with frequencies inconsistent with the asymptotic remnant.

the earliest minimum in Fig 4.1 for this N . These amplitudes correspond to the penultimate row of Table 4.1 and the fit time t_{fit} is stated, with respect to t_{peak} , in the last column. The result of this procedure for the remaining N is Table 4.1, where we provide our best estimate of the amplitudes at $t = t_0 = t_{\text{peak}}$ associated with each overtone. The values in Table 4.1 are computed for the highest numerical resolution of the NR waveform SXS:BBH:0305, but are truncated at a level such that the estimates agree with the next highest resolution.

The initial amplitude of the fundamental mode A_0 is consistently recovered for all models, each model having a different N and a different fit time that is optimal for that N . The first few overtones show similar behavior, while the higher overtones display

larger uncertainties in the recovered amplitudes and are increasingly sensitive to the fit time and the number of included overtones. This sensitivity is a consequence of the strong exponential time dependence in the overtones and is recognized as the *time-shift problem* [51]. But, perhaps the most important thing to notice is that the overtones can have significantly higher amplitudes than the fundamental mode. As discussed above, the initial amplitudes of the overtones depend on the details of the nonlinear binary coalescence, which ultimately depend on the binary parameters. Consequently, the amplitudes of the overtones relative to the fundamental mode will vary across parameter space. The complex amplitudes $C_{\ell mn}$, also known as the QNM excitation coefficients, can be written as $C_{\ell mn} = B_{\ell mn} I_{\ell mn}$, where $B_{\ell mn}$ is a purely geometric piece determined by the remnant BH, referred to as the QNM excitation factor, and $I_{\ell mn}$ is the source term that depends on the binary dynamics [52–54]. Excitation factors have been computed for the first three overtones for Kerr BHs in [54, 55]; these QNM excitation factors can provide some insight into how the relative amplitudes might behave for different remnant spins.

The NR waveform SXS:BBH:0305 has a dimensionless remnant spin $\chi_f \sim 0.7$, for which the relative excitation factors, $|B_{22n}|/|B_{220}|$, of the fundamental and the first three $\ell = m = 2$ QNM overtones are roughly 1.0, 3.53, 5.23, 5.32. However, for a remnant of $\chi_f = 0$, the excitation factors $|B_{22n}/B_{220}|$ of these same QNMs are 1.0, 1.28, 1.06, 0.62, which indicates that the overtones may be relatively less important for lower remnant spins. Using [55], we have computed the excitation factors for the next two highest overtones of the remnant of SXS:BBH:0305 and we find that $|B_{224}|/|B_{220}| \sim 15.21$ and $|B_{225}|/|B_{220}| \sim 29.31$. Additional excitation factors are difficult to compute, but the trend is not expected to continue as it is conjectured that for Kerr BHs $B_{\ell mn} \sim 1/n$ for large n [54].

The overtone amplitudes in Table 4.1 increase with overtone number, peak around $n = 4$, and then decrease. Therefore we expect that the rapidly decaying overtones beyond about $n = 7$ are subdominant; this justifies truncating the expansion in the vicinity of $n = 7$. Preliminary studies indicate that $n = 8$ does not improve the fit at $t_0 = t_{\text{peak}}$. An additional caveat is that the amplitudes in Table 4.1 are those recovered from the $\ell = m = 2$ spherical harmonic as opposed to the $\ell = m = 2$ spheroidal harmonic. However, the spherical-spheroidal mixing is small (c.f. Sec. 4.4), and should not significantly change the qualitative behavior of the relative amplitudes in Table 4.1.

Using our results from the last row of Table 4.1, and using the analytic decay rates

N	A_0	A_1	A_2	A_3	A_4	A_5	A_6	A_7	$t_{\text{fit}} - t_{\text{peak}}$
0	0.971	-	-	-	-	-	-	-	47.00
1	0.974	3.89	-	-	-	-	-	-	18.48
2	0.973	4.14	8.1	-	-	-	-	-	11.85
3	0.972	4.19	9.9	11.4	-	-	-	-	8.05
4	0.972	4.20	10.6	16.6	11.6	-	-	-	5.04
5	0.972	4.21	11.0	19.8	21.4	10.1	-	-	3.01
6	0.971	4.22	11.2	21.8	28	21	6.6	-	1.50
7	0.971	4.22	11.3	23.0	33	29	14	2.9	0.00

Table 4.1: Best-fit estimates of the amplitudes A_n of the fundamental mode and overtones in the ringdown of NR simulation SXS:BBH:0305, with $t_0 = t_{\text{peak}}$. Amplitudes are computed for various values of N , the total number of overtones included in the fit. Also shown is the time t_{fit} where the fit is performed for each N , stated with respect to t_{peak} . A_n are always the amplitudes at $t = t_0 = t_{\text{peak}}$, even if the fit is performed at a later time. The amplitude values are truncated such that the last significant figure agrees with the the two highest resolutions for the NR simulation.

corresponding to the true M_f and χ_f , we can reconstruct the expected individual contributions of each overtone to the total $\ell = m = 2$ ringdown signal at any given t ; in other words, we can compute the time-dependent amplitudes $A_{22n}(t)$ of each overtone. These are related to the A_n in Table 4.1 by $A_{22n}(t) = A_n e^{-(t-t_0)/\tau_{22n}}$. These amplitudes are shown in Fig. 4.8. This establishes why one has to wait until 10–20 M after the peak before the fundamental becomes the dominant contribution.

Note that Fig. 4.8 uses a single fit over the range $t \geq t_{\text{peak}}$, and assumes the expected analytic time dependence of each overtone amplitude for $t \geq t_{\text{peak}}$. Alternatively, we can attempt to reconstruct each $A_{22n}(t)$ numerically by performing a different fit for the amplitudes at each time t . For each time t we choose $t_0 = t_{\text{fit}} = t$ and we fit data only for times $\geq t_0$. The numerically extracted time dependence of the overtone amplitudes, $A_{22n}(t)$, are shown in Fig. 4.9. Obtaining an accurate fit in this way is difficult because of various numerical complications, such as the small differences in frequencies and amplitudes between neighboring overtones, the poor resolution of overtones with small amplitudes, and the risk of overfitting at late times after some overtones have decayed away. At later times, there is significantly less power in the highest overtones—making them more difficult to resolve. To mitigate some of these difficulties, when performing the fit at each time t , we exclude overtones whose fitted amplitude has increased relative to that at the previous time. This is motivated by the fact that the model is one of exponentially damped sinusoids. Therefore, if at any time an overtone has a larger amplitude than the amplitude recovered at a

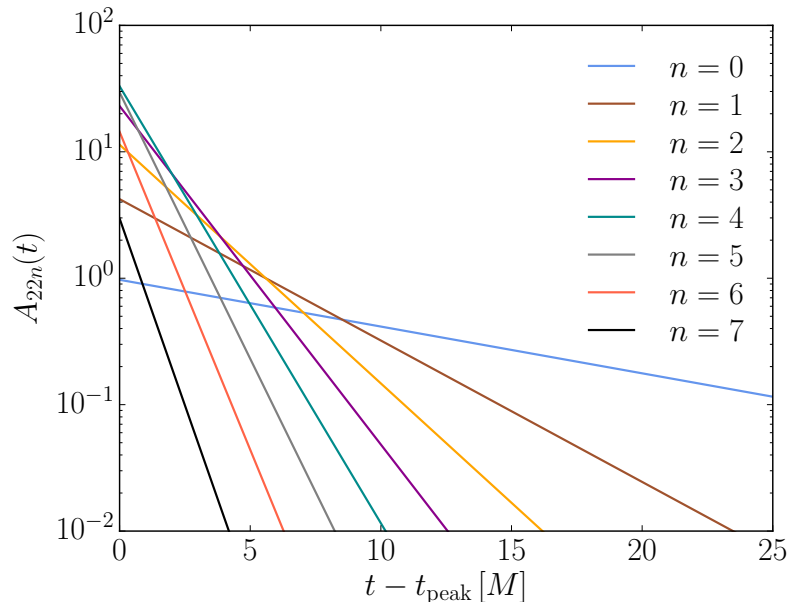


Figure 4.8: A decomposition of the ringdown in terms of the overtones for $N = 7$. The evolution of the overtones is computed from the analytic decay rates with initial amplitudes at $t = t_0 = t_{\text{peak}}$ specified by the bottom row of Table 4.1. Notice that the fundamental mode does not dominate the ringdown of SXS:BBH:0305 until roughly $10M$ after t_{peak} .

previous time, we consider that overtone to no longer be of physical relevance and we permanently remove it from the allowed set of modes for future fit times. It is always the highest overtone available in the remaining set of modes that gets dropped, as this mode decays more quickly than the other ones. Although we only show up to $N = 4$ in Fig. 4.9 because numerically extracting amplitudes is difficult at late times, the benefit of using overtones up to $N = 7$ in estimating the remnant mass and spin is apparent in Fig. 4.7. Consequently, more advanced fitting methods should allow for an improvement in numerically recovering higher-order overtones as a function of time, which will be explored further in future work.

Finally, it is worth pointing out that there is good agreement between the model and NR even at times before t_{peak} , as indicated by the mismatches in Fig. 4.1, as well as by the early agreement between the numerically extracted amplitude of the fundamental mode and the expected analytic behavior visible in Fig. 4.9. Since the QNMs are solutions to perturbed single BH spacetimes, the agreement could be interpreted as an indication that the region of the pre-peak waveform already begins to behave as a perturbed single BH to observers at infinity. This observed behavior

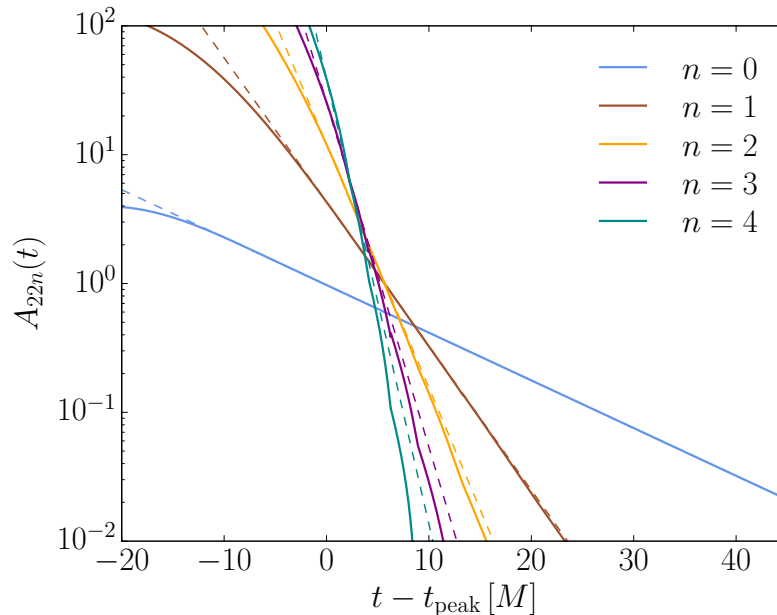


Figure 4.9: The numerically recovered amplitudes for the fundamental QNM and the first few overtones at each fit time, t (solid curves). Dashed lines are the same as the lines in Fig. 4.8. The numerically extracted amplitudes across t agree very well with the expected decay for the longest-lived modes, while modes that decay more quickly are more susceptible to fitting issues. Interestingly, the fundamental mode is in excellent agreement with the expected decay rate at times preceding the peak amplitude of the strain.

will be explored further in future work.

Observing overtones with GW detectors

Overtones can enhance the power of gravitational wave detectors to probe the ringdown regime. We illustrate this by studying the simulated output of a LIGO-like detector in response to the same GW considered above, the NR simulation SXS:BBH:0305. For simplicity, we assume the orbital plane of the source faces the instrument head-on (no inclination). We choose a sky location for which the detector has optimal response to the plus polarization but none to cross, with polarizations defined in the same frame implicitly assumed in Eq. (4.1). To mimic GW150914, we rescale the NR template to correspond to a total initial binary mass of $72M_{\odot}$, in the detector frame, and a source distance of 400 Mpc. We inject the $\ell = m = 2$ mode of the signal into simulated Gaussian noise corresponding to the sensitivity of Advanced LIGO in its design configuration [56]. This yields a post-peak optimal

SNR of ~ 42 .³

To extract information from the noisy data, we carry out a Bayesian analysis similar to that in [16, 57] but based on the overtone ringdown model of Eq. (4.1), with $\ell = m = 2$ and varying N . For any given start time t_0 , we obtain a posterior probability density over the space of remnant mass and spin, as well as the amplitudes and phases of the set of QNMs included in the template. We parametrize start times via $\Delta t_0 = t_0 - t_{h\text{-peak}}$, where $t_{h\text{-peak}}$ refers to the signal peak at the detector ($t_{h\text{-peak}} \approx t_{\text{peak}} - 0.48 \text{ ms} \approx t_{\text{peak}} - 1.3 M$). Unlike [16], we sample over the amplitudes and phases directly, instead of marginalizing over them analytically, and we place uniform priors on all parameters. In particular, we consider masses and orbit-aligned spins within $[10, 100] M_\odot$ and $[0, 1]$ respectively. We allow the QNM phases to cover their full range, $[0, 2\pi]$, but restrict the amplitudes (measured at $t = t_{h\text{-peak}}$) to $[0.01, 250] h_{\text{peak}}$, where $h_{\text{peak}} = 2 \times 10^{-21}$ is the total signal peak. This arbitrary amplitude interval fully supports the posterior in all cases we consider. We assume all extrinsic parameters, like sky location and inclination, are perfectly known. We sample posteriors using the Markov chain Monte Carlo (MCMC) implementations in `kombine` [58] and, for verification, `emcee` [59].

The highest N we consider in our inference model is $N = 3$, as that is the most we can hope to resolve given the SNR of our simulation. A guiding principle for two waveforms to be indistinguishable is $\mathcal{M} < \text{SNR}^{-2}/2$, in terms of the mismatch \mathcal{M} defined in Eq. (4.2) but with a noise-weighted inner product [60–62]. For the system at hand, this implies that post-merger templates with mismatches $\mathcal{M} \lesssim 3 \times 10^{-4}$ are effectively identical. If fitting from the peak on, Fig. 4.1 then implies that differences between $N \geq 3$ templates are unmeasurable. We confirmed this empirically by checking that $N = 4$ does not lead to inference improvements with respect to $N = 3$ and only seems to introduce degenerate parameters. By the same token, we have also verified that, at this SNR, our results are largely unaffected by the presence or absence of the next dominant angular mode (3, 2) in the injected NR waveform, as its amplitude is an order of magnitude weaker than that of the dominant (2, 2) mode for the chosen system. At higher SNRs, additional (2, 2) overtones and/or angular modes (potentially, with their respective overtones) are necessary to keep the modeling error below the statistical error.

Our findings are summarized in Figs. 4.10 and 4.11. In Fig. 4.10 we show the

³Defined as the SNR in frequencies above 154.68 Hz, the instantaneous frequency at the peak of the time-domain signal.

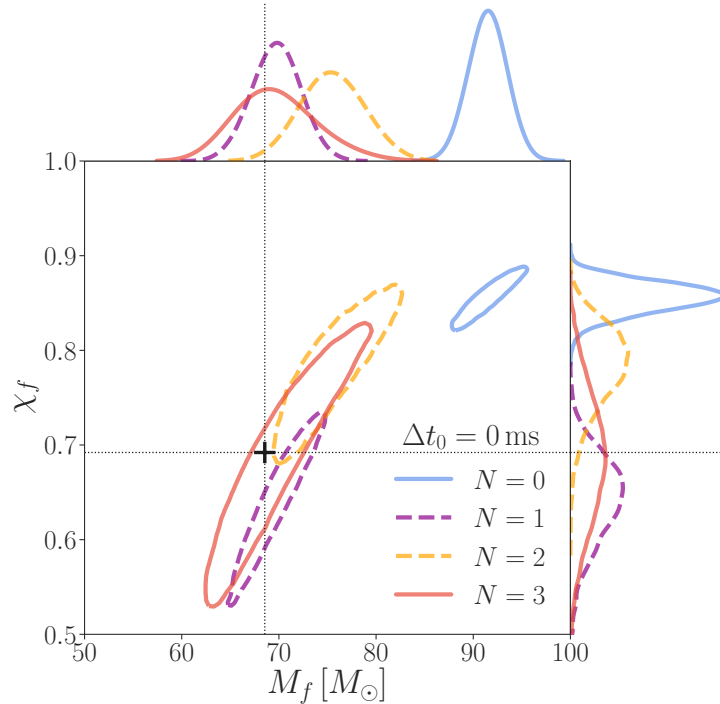


Figure 4.10: Remnant parameters inferred with different number of overtones, using data starting at the peak amplitude of the injected strain. Contours represent 90%-credible regions on the remnant mass (M_f) and dimensionless spin (χ_f), obtained from the Bayesian analysis of a GW150914-like NR signal injected into simulated noise for a single Advanced LIGO detector at design sensitivity. The inference model was as in Eq. (4.1), with ($\ell = m = 2$) and different number of overtones N : 0 (solid blue), 1 (dashed purple), 2 (dashed yellow), 3 (solid red). In all cases, the analysis uses data starting at peak strain ($\Delta t_0 = t_0 - t_{h\text{-peak}} = 0$). The top and right panels show 1D posteriors for M_f and χ_f respectively. Amplitudes and phases are marginalized over. The intersection of the dotted lines marks the true value ($M_f = 68.5M_\odot$, $\chi_f = 0.69$).

posteriors recovered for the remnant mass and spin under the assumption that the ringdown begins at the peak of the signal strain and for models with different numbers of overtones. For each case, the main panel displays contours enclosing 90% of the posterior probability, while the curves on the top and right represent the corresponding marginalized distributions for the mass and spin. As expected, the fundamental mode ($N = 0$) is insufficient to describe the signal near the peak, yielding an estimate of the remnant properties that is far from the true values determined from the NR simulation (dotted lines). As the number of overtones is increased, the inferred mass and spin become increasingly more accurate, with $N = 3$ producing the best results

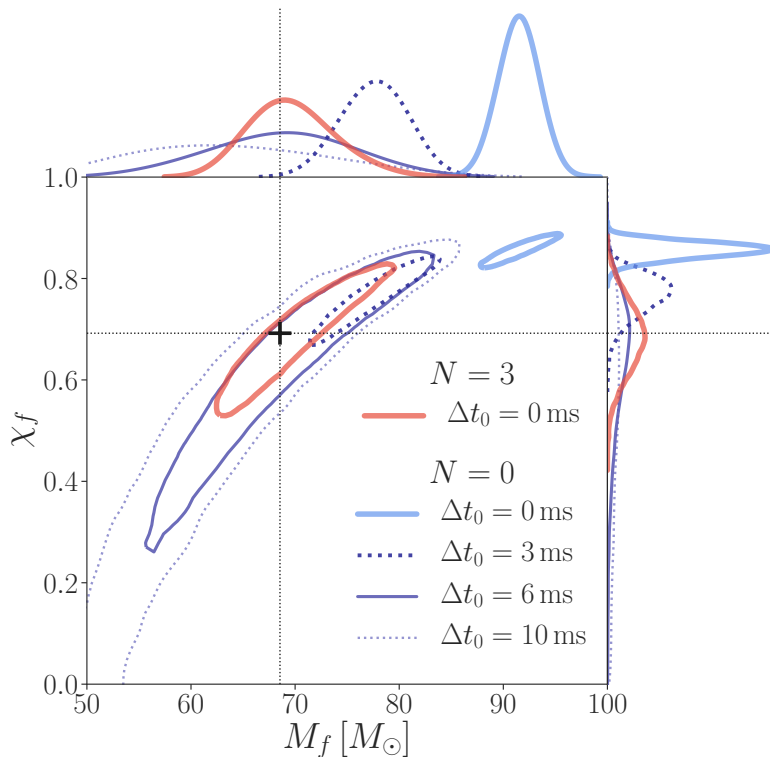


Figure 4.11: Remnant parameters inferred using only the fundamental mode, using data starting at different times relative to the peak amplitude of the injected strain. Contours represent 90%-credible regions on the remnant mass (M_f) and dimensionless spin (χ_f), obtained from the Bayesian analysis of a GW150914-like NR signal injected into simulated noise for a single Advanced LIGO detector at design sensitivity. For the blue contours, the inference model included no overtones ($N = 0$) and used data starting at different times after the peak: $\Delta t_0 = t_0 - t_{h\text{-peak}} \in [0, 3, 6, 10]$ ms (blue contours). For the red contour, the analysis was conducted with three overtones ($N = 3$) starting at the peak ($\Delta t_0 = 0$), as in Fig. 4.10. The top and right panels show 1D posteriors for M_f and χ_f respectively. Amplitudes and phases are marginalized over. The intersection of the dotted lines marks the true value ($M_f = 68.5M_\odot$, $\chi_f = 0.69$).

(true value within top 40%-credible region). This result illustrates how the overtones can provide an independent measurement of the remnant properties by studying the signal near the peak.

We find that the estimate of the mass and spin obtained with overtones at the peak is more accurate than the one obtained with only the fundamental mode at later times. We illustrate this in Fig. 4.11, which shows the 90%-credible regions on M_f and χ_f inferred using only the fundamental mode ($N = 0$) at different times after the peak

strain (blue contours), as well as the $N = 3$ result from Fig. 4.10 for comparison (red contour). As anticipated in [16], the fundamental mode is a faithful representation of the signal only at later times, which in our case means that the true values are enclosed in the 90%-credible region only for $\Delta t_0 \geq 5$ ms. The penalty for analyzing the signal at later times is a reduction in SNR that results in increased uncertainty, as evidenced by the large area of the blue contours in Fig. 4.11. We obtain a more precise estimate by taking advantage of the overtones at the peak. We suspect that the observed agreement at 3 ms in [16] is a consequence of the lower SNR of GW150914. At lower SNRs, the statistical errors outweigh the systematic errors associated with including only the fundamental mode.

4.6 Discussion and conclusions

For a given mass M_f and spin χ_f , perturbation theory precisely predicts the spectrum of QNMs associated with a ringing single BH, including the characteristic frequencies for these QNMs. The QNM frequencies are denoted $\omega_{\ell mn}(M_f, \chi_f)$, where ℓ and m describe the angular dependence of a mode and n , the often-ignored integer overtone index, sorts QNMs with the same angular dependence by how quickly they decay. The slowest decaying fundamental mode, $n = 0$, is often considered to be of primary importance, while the more quickly decaying overtones are often disregarded. However, we find that the overtones are not necessarily subdominant as is often assumed, but instead, can dominate the early part of the ringdown.

Using a superposition of QNMs, we model the ringdown portion of the $\ell = m = 2$ mode of the numerical relativity waveform SXS:BBH:0305, which is consistent with GW150914. We find that with enough included overtones, the QNMs provide an excellent description for the GW strain for all times beyond the peak amplitude of the complex strain h . For the GW150914-like NR waveform we analyzed, the overtones dominate the early part of the perturbations but decay away much more quickly than the fundamental mode, which eventually becomes dominant roughly $10M$ after the peak amplitude (Fig. 4.8). This later time where the fundamental dominates is sometimes referred to in the literature as the start of the ringdown, the time of a transition to the linear regime, or the beginning of the domain of applicability of perturbation theory. However, this time is merely the time at which one may ignore the contribution of overtones, which play a key role in the early ringdown. Including the QNM overtones extends the reach of perturbation theory back to the time of the peak strain amplitude, indicating that the linear ringdown regime begins much earlier than one would conclude by ignoring these additional modes. As mentioned

in Sec. 4.5, we have verified, on a sizeable set of aligned-spin waveforms in the SXS catalog, that the inclusion of overtones provides an accurate model for the post-peak strain. Not only do the overtones provide excellent mismatches, but the best fit mass and spin are accurately recovered with median absolute errors in M_f/M and χ_f of $\sim 10^{-3}$. We therefore expect the early dominance of overtones to be a generic feature of the ringdown.

The QNM overtones can enhance the power of GW detectors to probe the ringdown regime. They can be used to extract information about QNMs at the peak of the signal, where the SNR is high. In contrast, the usual approach relies solely on the later portion of the signal that is dominated by the (initially weaker) fundamental mode, paying the price of larger statistical errors and uncertainty in the appropriate time where this mode dominates [16–22, 25–29]. This effect is visible in Fig. 4.11, where a model with $N = 3$ overtones remains faithful to the true remnant mass and spin with less uncertainty than one with $N = 0$ at later times. The resolvability of these overtones provides a set of independent modes, each with unique frequencies, that can potentially be used to constrain deviations from GR.

Studies of the ringdown GW spectrum can provide a direct way to experimentally determine whether compact binary coalescences result in the Kerr BHs predicted by GR [23, 24]. This includes tests of the no-hair theorem and the area law, as well as searches for BH mimickers. The program, sometimes known as “black-hole spectroscopy,” generally requires independent measurement of at least two modes, which are conventionally taken to be the fundamentals of two different angular harmonics (e.g. [25, 29]). However, such choice is only available for systems that present a sufficiently strong secondary angular mode, which only tends to occur under some specific conditions (e.g. for high mass ratios) [63–67]. Further, as we have observed, these fundamental modes should dominate only at late times, being subject to significantly more noise than modes that can be extracted near the peak of the waveform. The extraction of an overtone, in addition to the fundamental mode, could potentially serve as an alternative two-mode test of the no-hair theorem.

The impact of overtones on ringdown tests of GR can already be glimpsed from Fig. 4.11: by studying the QNMs at early and late times we may obtain two independent measurements of the remnant parameters, enabling powerful consistency checks. Unlike tests that rely on a multiplicity of angular modes, studies of overtones should be feasible at SNRs achievable with existing detectors, as we demonstrate by our study of a GW150914-like signal seen at design sensitivity by Advanced LIGO

(Sec. 4.5). For signals in which they are measurable, higher angular modes and their overtones could make these tests even more powerful. Overtone can therefore enable a whole new set of precision studies of the ringdown and make black-hole spectroscopy realizable with current detectors.

4.7 Acknowledgments

The authors thank Vijay Varma for many valuable discussions. We also thank Katerina Chatziioannou and Leo Stein for useful comments. M.G. and M.S. are supported by the Sherman Fairchild Foundation and NSF grants PHY-1708212 and PHY-1708213 at Caltech. M.I. is a member of the LIGO Laboratory. LIGO was constructed by the California Institute of Technology and Massachusetts Institute of Technology with funding from the National Science Foundation and operates under cooperative agreement PHY-0757058. M.I. is supported by NASA through the NASA Hubble Fellowship grant No. HST-HF2-51410.001-A awarded by the Space Telescope Science Institute, which is operated by the Association of Universities for Research in Astronomy, Inc., for NASA, under contract NAS5-26555. S.T. is supported in part by the Sherman Fairchild Foundation and by NSF Grants PHY-1606654 and ACI-1713678 at Cornell. Computations were performed on the Wheeler cluster at Caltech, which is supported by the Sherman Fairchild Foundation and by Caltech. Computation were also performed on the Nemo computing cluster at the University of Wisconsin-Milwaukee, supported by NSF Grant PHY-1626190.

References

- [1] Werner Israel. “Event Horizons in Static Vacuum Space-Times”. In: *Phys. Rev.* 164 (5 Dec. 1967), pp. 1776–1779. DOI: [10.1103/PhysRev.164.1776](https://doi.org/10.1103/PhysRev.164.1776). URL: <https://link.aps.org/doi/10.1103/PhysRev.164.1776>.
- [2] B. Carter. “Axisymmetric Black Hole Has Only Two Degrees of Freedom”. In: *Phys. Rev. Lett.* 26 (6 Feb. 1971), pp. 331–333. DOI: [10.1103/PhysRevLett.26.331](https://doi.org/10.1103/PhysRevLett.26.331). URL: <https://link.aps.org/doi/10.1103/PhysRevLett.26.331>.
- [3] S. W. Hawking. “Black holes in general relativity”. In: *Commun. Math. Phys.* 25 (1972), pp. 152–166. DOI: [10.1007/BF01877517](https://doi.org/10.1007/BF01877517).
- [4] S. A. Teukolsky. “Rotating black holes - separable wave equations for gravitational and electromagnetic perturbations”. In: *Phys. Rev. Lett.* 29 (1972), pp. 1114–1118. DOI: [10.1103/PhysRevLett.29.1114](https://doi.org/10.1103/PhysRevLett.29.1114).

- [5] S. A. Teukolsky. “Perturbations of a Rotating Black Hole. I. Fundamental Equations for Gravitational, Electromagnetic, and Neutrino-Field Perturbations”. In: *ApJ* 185 (Oct. 1973), pp. 635–648. DOI: [10.1086/152444](https://doi.org/10.1086/152444).
- [6] W. H. Press and S. A. Teukolsky. “Perturbations of a Rotating Black Hole. II. Dynamical Stability of the Kerr Metric”. In: *ApJ* 185 (Oct. 1973), pp. 649–674. DOI: [10.1086/152445](https://doi.org/10.1086/152445).
- [7] B. P. Abbott et al. “Observation of Gravitational Waves from a Binary Black Hole Merger”. In: *Phys. Rev. Lett.* 116.6 (Feb. 2016), p. 061102. ISSN: 0031-9007. DOI: [10.1103/PhysRevLett.116.061102](https://doi.org/10.1103/PhysRevLett.116.061102). URL: <http://link.aps.org/doi/10.1103/PhysRevLett.116.061102>.
- [8] B. P. Abbott et al. “GW151226: Observation of Gravitational Waves from a 22-Solar-Mass Binary Black Hole Coalescence”. In: *Phys. Rev. Lett.* 116.24 (June 2016), p. 241103. ISSN: 0031-9007. DOI: [10.1103/PhysRevLett.116.241103](https://doi.org/10.1103/PhysRevLett.116.241103). URL: <http://link.aps.org/doi/10.1103/PhysRevLett.116.241103>.
- [9] B. P. Abbott et al. “Binary Black Hole Mergers in the First Advanced LIGO Observing Run”. In: *Phys. Rev. X* 6.4 (Oct. 2016), p. 041015. ISSN: 2160-3308. DOI: [10.1103/PhysRevX.6.041015](https://doi.org/10.1103/PhysRevX.6.041015). URL: <http://arxiv.org/abs/1606.04856> <https://dcc.ligo.org/LIGO-%20P1600088/public%20https://link.aps.org/doi/10.1103/%20PhysRevX.6.041015>.
- [10] B. P. Abbott et al. “GW170104: Observation of a 50-Solar-Mass Binary Black Hole Coalescence at Redshift 0.2”. In: *Phys. Rev. Lett.* 118.22 (June 2017), p. 221101. ISSN: 0031-9007. DOI: [10.1103/PhysRevLett.118.221101](https://doi.org/10.1103/PhysRevLett.118.221101). URL: <https://journals.aps.org/prl/abstract/10.1103/%20PhysRevLett.118.221101%20https://dcc.ligo.org/LIGO-P170104/%20public%20https://arxiv.org/abs/1706.01812>.
- [11] B. P. Abbott et al. “GW170608: Observation of a 19-solar-mass Binary Black Hole Coalescence”. In: *Astrophys. J.* 851.2 (2017), p. L35. DOI: [10.3847/2041-8213/aa9f0c](https://doi.org/10.3847/2041-8213/aa9f0c). arXiv: [1711.05578](https://arxiv.org/abs/1711.05578) [astro-ph.HE].
- [12] B. P. Abbott et al. “GW170814: A Three-Detector Observation of Gravitational Waves from a Binary Black Hole Coalescence”. In: *Phys. Rev. Lett.* 119.14 (2017), p. 141101. DOI: [10.1103/PhysRevLett.119.141101](https://doi.org/10.1103/PhysRevLett.119.141101). arXiv: [1709.09660](https://arxiv.org/abs/1709.09660) [gr-qc].
- [13] B. P. Abbott et al. “GWTC-1: A Gravitational-Wave Transient Catalog of Compact Binary Mergers Observed by LIGO and Virgo during the First and Second Observing Runs”. In: *Phys. Rev. X* 9.3 (2019), p. 031040. DOI: [10.1103/PhysRevX.9.031040](https://doi.org/10.1103/PhysRevX.9.031040). arXiv: [1811.12907](https://arxiv.org/abs/1811.12907) [astro-ph.HE].
- [14] J. Aasi et al. “Advanced LIGO”. In: *Class. Quant. Grav.* 32 (2015), p. 074001. DOI: [10.1088/0264-9381/32/7/074001](https://doi.org/10.1088/0264-9381/32/7/074001). arXiv: [1411.4547](https://arxiv.org/abs/1411.4547) [gr-qc].

- [15] F. Acernese et al. “Advanced Virgo: a second-generation interferometric gravitational wave detector”. In: *Class. Quant. Grav.* 32.2 (2015), p. 024001. DOI: [10.1088/0264-9381/32/2/024001](https://doi.org/10.1088/0264-9381/32/2/024001).
- [16] B. P. Abbott et al. “Tests of General Relativity with GW150914”. In: *Phys. Rev. Lett.* 116.22 (May 2016), p. 221101. ISSN: 0031-9007. DOI: [10.1103/PhysRevLett.116.221101](https://doi.org/10.1103/PhysRevLett.116.221101). URL: <http://link.aps.org/doi/10.1103/PhysRevLett.116.221101> <https://arxiv.org/abs/1602.03841>.
- [17] Walter Del Pozzo and Alessandro Nagar. “Analytic family of post-merger template waveforms”. In: *Phys. Rev.* D95.12 (2017), p. 124034. DOI: [10.1103/PhysRevD.95.124034](https://doi.org/10.1103/PhysRevD.95.124034). arXiv: [1606.03952](https://arxiv.org/abs/1606.03952) [gr-qc].
- [18] Miriam Cabero et al. “Observational tests of the black hole area increase law”. In: *Phys. Rev.* D97.12 (2018), p. 124069. DOI: [10.1103/PhysRevD.97.124069](https://doi.org/10.1103/PhysRevD.97.124069). arXiv: [1711.09073](https://arxiv.org/abs/1711.09073) [gr-qc].
- [19] Eric Thrane, Paul D. Lasky, and Yuri Levin. “Challenges testing the no-hair theorem with gravitational waves”. In: *Phys. Rev.* D96.10 (2017), p. 102004. DOI: [10.1103/PhysRevD.96.102004](https://doi.org/10.1103/PhysRevD.96.102004). arXiv: [1706.05152](https://arxiv.org/abs/1706.05152) [gr-qc].
- [20] Richard Brito, Alessandra Buonanno, and Vivien Raymond. “Black-hole Spectroscopy by Making Full Use of Gravitational-Wave Modeling”. In: *Phys. Rev.* D98.8 (2018), p. 084038. DOI: [10.1103/PhysRevD.98.084038](https://doi.org/10.1103/PhysRevD.98.084038). arXiv: [1805.00293](https://arxiv.org/abs/1805.00293) [gr-qc].
- [21] Gregorio Carullo et al. “Empirical tests of the black hole no-hair conjecture using gravitational-wave observations”. In: *Phys. Rev.* D98.10 (2018), p. 104020. DOI: [10.1103/PhysRevD.98.104020](https://doi.org/10.1103/PhysRevD.98.104020). arXiv: [1805.04760](https://arxiv.org/abs/1805.04760) [gr-qc].
- [22] Gregorio Carullo, Walter Del Pozzo, and John Veitch. “Observational Black Hole Spectroscopy: A time-domain multimode analysis of GW150914”. In: *Phys. Rev.* D99.12 (2019), p. 123029. DOI: [10.1103/PhysRevD.99.123029](https://doi.org/10.1103/PhysRevD.99.123029). arXiv: [1902.07527](https://arxiv.org/abs/1902.07527) [gr-qc].
- [23] Olaf Dreyer et al. “Black hole spectroscopy: Testing general relativity through gravitational wave observations”. In: *Class. Quant. Grav.* 21 (2004), pp. 787–804. DOI: [10.1088/0264-9381/21/4/003](https://doi.org/10.1088/0264-9381/21/4/003). arXiv: [gr-qc/0309007](https://arxiv.org/abs/gr-qc/0309007) [gr-qc].
- [24] Emanuele Berti, Vitor Cardoso, and Clifford M. Will. “On gravitational-wave spectroscopy of massive black holes with the space interferometer LISA”. In: *Phys. Rev.* D73 (2006), p. 064030. DOI: [10.1103/PhysRevD.73.064030](https://doi.org/10.1103/PhysRevD.73.064030). arXiv: [gr-qc/0512160](https://arxiv.org/abs/gr-qc/0512160) [gr-qc].
- [25] S. Gossan, J. Veitch, and B. S. Sathyaprakash. “Bayesian model selection for testing the no-hair theorem with black hole ringdowns”. In: *Phys. Rev.* D85 (2012), p. 124056. DOI: [10.1103/PhysRevD.85.124056](https://doi.org/10.1103/PhysRevD.85.124056). arXiv: [1111.5819](https://arxiv.org/abs/1111.5819) [gr-qc].

- [26] J. Meidam et al. “Testing the no-hair theorem with black hole ringdowns using TIGER”. In: *Phys. Rev. D* 90.6 (2014), p. 064009. DOI: [10.1103/PhysRevD.90.064009](https://doi.org/10.1103/PhysRevD.90.064009). arXiv: [1406.3201](https://arxiv.org/abs/1406.3201) [gr-qc].
- [27] Emanuele Berti et al. “Testing General Relativity with Present and Future Astrophysical Observations”. In: *Class. Quant. Grav.* 32 (2015), p. 243001. DOI: [10.1088/0264-9381/32/24/243001](https://doi.org/10.1088/0264-9381/32/24/243001). arXiv: [1501.07274](https://arxiv.org/abs/1501.07274) [gr-qc].
- [28] Emanuele Berti et al. “Spectroscopy of Kerr black holes with Earth- and space-based interferometers”. In: *Phys. Rev. Lett.* 117.10 (2016), p. 101102. DOI: [10.1103/PhysRevLett.117.101102](https://doi.org/10.1103/PhysRevLett.117.101102). arXiv: [1605.09286](https://arxiv.org/abs/1605.09286) [gr-qc].
- [29] Vishal Baibhav and Emanuele Berti. “Multimode black hole spectroscopy”. In: *Phys. Rev. D* 99.2 (2019), p. 024005. DOI: [10.1103/PhysRevD.99.024005](https://doi.org/10.1103/PhysRevD.99.024005). arXiv: [1809.03500](https://arxiv.org/abs/1809.03500) [gr-qc].
- [30] Alessandra Buonanno, Gregory B. Cook, and Frans Pretorius. “Inspirals, merger and ring-down of equal-mass black-hole binaries”. In: *Phys. Rev. D* 75 (2007), p. 124018. DOI: [10.1103/PhysRevD.75.124018](https://doi.org/10.1103/PhysRevD.75.124018). arXiv: [gr-qc/0610122](https://arxiv.org/abs/gr-qc/0610122) [gr-qc].
- [31] Vishal Baibhav et al. “Black Hole Spectroscopy: Systematic Errors and Ringdown Energy Estimates”. In: *Phys. Rev. D* 97.4 (2018), p. 044048. DOI: [10.1103/PhysRevD.97.044048](https://doi.org/10.1103/PhysRevD.97.044048). arXiv: [1710.02156](https://arxiv.org/abs/1710.02156) [gr-qc].
- [32] Ioannis Kamaretzos et al. “Black-hole hair loss: learning about binary progenitors from ringdown signals”. In: *Phys. Rev. D* 85 (2012), p. 024018. DOI: [10.1103/PhysRevD.85.024018](https://doi.org/10.1103/PhysRevD.85.024018). arXiv: [1107.0854](https://arxiv.org/abs/1107.0854) [gr-qc].
- [33] Lionel London, Deirdre Shoemaker, and James Healy. “Modeling ringdown: Beyond the fundamental quasinormal modes”. In: *Phys. Rev. D* 90.12 (2014). [Erratum: *Phys. Rev. D* 94, no. 6, 069902 (2016)], p. 124032. DOI: [10.1103/PhysRevD.90.124032](https://doi.org/10.1103/PhysRevD.90.124032). arXiv: [1404.3197](https://arxiv.org/abs/1404.3197) [gr-qc].
- [34] Swetha Bhagwat, Maria Okounkova, Stefan W. Ballmer, Duncan A. Brown, Matthew Giesler, Mark A. Scheel, and Saul A. Teukolsky. “On choosing the start time of binary black hole ringdowns”. In: *Phys. Rev. D* 97.10 (2018), p. 104065. DOI: [10.1103/PhysRevD.97.104065](https://doi.org/10.1103/PhysRevD.97.104065). arXiv: [1711.00926](https://arxiv.org/abs/1711.00926) [gr-qc].
- [35] Yi Pan et al. “Inspirals-merger-ringdown waveforms of spinning, precessing black-hole binaries in the effective-one-body formalism”. In: *Phys. Rev. D* 89.8 (2014), p. 084006. DOI: [10.1103/PhysRevD.89.084006](https://doi.org/10.1103/PhysRevD.89.084006). arXiv: [1307.6232](https://arxiv.org/abs/1307.6232) [gr-qc].
- [36] Andrea Taracchini et al. “Effective-one-body model for black-hole binaries with generic mass ratios and spins”. In: *Phys. Rev. D* 89.6 (2014), 061502(R). DOI: [10.1103/PhysRevD.89.061502](https://doi.org/10.1103/PhysRevD.89.061502). arXiv: [1311.2544](https://arxiv.org/abs/1311.2544) [gr-qc].

- [37] Stanislav Babak, Andrea Taracchini, and Alessandra Buonanno. “Validating the effective-one-body model of spinning, precessing binary black holes against numerical relativity”. In: *Phys. Rev. D* 95.2 (2017), p. 024010. DOI: [10.1103/PhysRevD.95.024010](https://doi.org/10.1103/PhysRevD.95.024010). arXiv: [1607.05661](https://arxiv.org/abs/1607.05661) [gr-qc].
- [38] <http://www.black-holes.org/waveforms>.
- [39] Abdul H. Mroue et al. “A Catalog of 174 Binary Black Hole Simulations for Gravitational Wave Astronomy”. In: *Phys. Rev. Lett.* 111 (2013), p. 241104. DOI: [10.1103/PhysRevLett.111.241104](https://doi.org/10.1103/PhysRevLett.111.241104). arXiv: [1304.6077](https://arxiv.org/abs/1304.6077) [gr-qc].
- [40] C. V. Vishveshwara. “Stability of the Schwarzschild Metric”. In: *Phys. Rev. D* 1 (10 May 1970), pp. 2870–2879. DOI: [10.1103/PhysRevD.1.2870](https://doi.org/10.1103/PhysRevD.1.2870). URL: <https://link.aps.org/doi/10.1103/PhysRevD.1.2870>.
- [41] William H. Press. “Long Wave Trains of Gravitational Waves from a Vibrating Black Hole”. In: *Astrophys. J.* 170 (1971), pp. L105–L108. DOI: [10.1086/180849](https://doi.org/10.1086/180849).
- [42] S. A. Teukolsky. “Perturbations of a rotating black hole. 1. Fundamental equations for gravitational electromagnetic and neutrino field perturbations”. In: *Astrophys. J.* 185 (1973), pp. 635–647. DOI: [10.1086/152444](https://doi.org/10.1086/152444).
- [43] S. Chandrasekhar and S. Detweiler. “The Quasi-Normal Modes of the Schwarzschild Black Hole”. In: *Proc. R. Soc. A* 344.1639 (1975), pp. 441–452. ISSN: 00804630. URL: <http://www.jstor.org/stable/78902>.
- [44] E. Berti, V. Cardoso, and A. O. Starinets. “TOPICAL REVIEW: Quasinormal modes of black holes and black branes”. In: *Class. Quantum Grav.* 26.16 (Aug. 2009), p. 163001. DOI: [10.1088/0264-9381/26/16/163001](https://doi.org/10.1088/0264-9381/26/16/163001). arXiv: [0905.2975](https://arxiv.org/abs/0905.2975) [gr-qc].
- [45] <http://pages.jh.edu/~eberti2/ringdown>.
- [46] E. T. Newman and R. Penrose. “Note on the Bondi–Metzner–Sachs Group”. In: *J. Math. Phys.* 7 (1966), pp. 863–870. DOI: [10.1063/1.1931221](https://doi.org/10.1063/1.1931221). URL: <http://link.aip.org/link/?JMP/7/863/1>.
- [47] J. N. Goldberg et al. “Spin- s Spherical Harmonics and δ ”. In: *Journal of Mathematical Physics* 8.11 (1967), pp. 2155–2161. DOI: [10.1063/1.1705135](https://doi.org/10.1063/1.1705135). URL: <http://link.aip.org/link/?JMP/8/2155/1>.
- [48] Kip S. Thorne. “Multipole expansions of gravitational radiation”. In: *Rev. Mod. Phys.* 52.2 (Apr. 1980), pp. 299–339. DOI: [10.1103/RevModPhys.52.299](https://doi.org/10.1103/RevModPhys.52.299).
- [49] Emanuele Berti and Antoine Klein. “Mixing of spherical and spheroidal modes in perturbed Kerr black holes”. In: *Phys. Rev. D* 90.6 (2014), p. 064012. DOI: [10.1103/PhysRevD.90.064012](https://doi.org/10.1103/PhysRevD.90.064012). arXiv: [1408.1860](https://arxiv.org/abs/1408.1860) [gr-qc].

- [50] Vijay Varma et al. “Surrogate model of hybridized numerical relativity binary black hole waveforms”. In: *Phys. Rev. D* 99.6 (2019), p. 064045. DOI: [10.1103/PhysRevD.99.064045](https://doi.org/10.1103/PhysRevD.99.064045). arXiv: [1812.07865](https://arxiv.org/abs/1812.07865) [gr-qc].
- [51] Ernst Nils Dorband et al. “A Numerical study of the quasinormal mode excitation of Kerr black holes”. In: *Phys. Rev. D* 74 (2006), p. 084028. DOI: [10.1103/PhysRevD.74.084028](https://doi.org/10.1103/PhysRevD.74.084028). arXiv: [gr-qc/0608091](https://arxiv.org/abs/gr-qc/0608091) [gr-qc].
- [52] E. W. Leaver. “An Analytic representation for the quasi normal modes of Kerr black holes”. In: *Proc. Roy. Soc. Lond.* A402 (1985), pp. 285–298. DOI: [10.1098/rspa.1985.0119](https://doi.org/10.1098/rspa.1985.0119).
- [53] Edward W. Leaver. “Spectral decomposition of the perturbation response of the Schwarzschild geometry”. In: *Phys. Rev. D* 34 (1986), pp. 384–408. DOI: [10.1103/PhysRevD.34.384](https://doi.org/10.1103/PhysRevD.34.384).
- [54] Emanuele Berti and Vitor Cardoso. “Quasinormal ringing of Kerr black holes. I. The Excitation factors”. In: *Phys. Rev. D* 74 (2006), p. 104020. DOI: [10.1103/PhysRevD.74.104020](https://doi.org/10.1103/PhysRevD.74.104020). arXiv: [gr-qc/0605118](https://arxiv.org/abs/gr-qc/0605118) [gr-qc].
- [55] Zhongyang Zhang, Emanuele Berti, and Vitor Cardoso. “Quasinormal ringing of Kerr black holes. II. Excitation by particles falling radially with arbitrary energy”. In: *Phys. Rev. D* 88 (2013), p. 044018. DOI: [10.1103/PhysRevD.88.044018](https://doi.org/10.1103/PhysRevD.88.044018). arXiv: [1305.4306](https://arxiv.org/abs/1305.4306) [gr-qc].
- [56] David H. Shoemaker et al. *Advanced LIGO anticipated sensitivity curves*. Tech. rep. LIGO-T0900288. LIGO Laboratory, 2009. URL: <https://dcc.ligo.org/LIGO-T0900288/public>.
- [57] Reinhard Prix. *Bayesian QNM search on GW150914*. Tech. rep. LIGO-T1500618. LIGO Scientific Collaboration, 2016. URL: <https://dcc.ligo.org/LIGO-T1500618/public>.
- [58] B. Farr and W. M. Farr. “kombine: a kernel-density-based, embarrassingly parallel ensemble sampler”. in prep. 2015. URL: <https://github.com/bfarr/kombine>.
- [59] D. Foreman-Mackey et al. “emcee: The MCMC Hammer”. In: *PASP* 125 (Mar. 2013), p. 306. DOI: [10.1086/670067](https://doi.org/10.1086/670067). arXiv: [1202.3665](https://arxiv.org/abs/1202.3665) [astro-ph.IM].
- [60] Eanna E. Flanagan and Scott A. Hughes. “Measuring gravitational waves from binary black hole coalescences: 2. The Waves’ information and its extraction, with and without templates”. In: *Phys. Rev. D* 57 (1998), pp. 4566–4587. DOI: [10.1103/PhysRevD.57.4566](https://doi.org/10.1103/PhysRevD.57.4566). arXiv: [gr-qc/9710129](https://arxiv.org/abs/gr-qc/9710129) [gr-qc].
- [61] Lee Lindblom, Benjamin J. Owen, and Duncan A. Brown. “Model Waveform Accuracy Standards for Gravitational Wave Data Analysis”. In: *Phys. Rev. D* 78 (2008), p. 124020. DOI: [10.1103/PhysRevD.78.124020](https://doi.org/10.1103/PhysRevD.78.124020). arXiv: [0809.3844](https://arxiv.org/abs/0809.3844) [gr-qc].

- [62] Sean T. McWilliams, Bernard J. Kelly, and John G. Baker. “Observing mergers of non-spinning black-hole binaries”. In: *Phys. Rev. D* 82 (2010), p. 024014. DOI: [10.1103/PhysRevD.82.024014](https://doi.org/10.1103/PhysRevD.82.024014). arXiv: [1004.0961](https://arxiv.org/abs/1004.0961) [gr-qc].
- [63] Vijay Varma and Parameswaran Ajith. “Effects of nonquadrupole modes in the detection and parameter estimation of black hole binaries with nonprecessing spins”. In: *Phys. Rev. D* 96.12 (2017), p. 124024. DOI: [10.1103/PhysRevD.96.124024](https://doi.org/10.1103/PhysRevD.96.124024). arXiv: [1612.05608](https://arxiv.org/abs/1612.05608) [gr-qc].
- [64] Collin Capano, Yi Pan, and Alessandra Buonanno. “Impact of higher harmonics in searching for gravitational waves from nonspinning binary black holes”. In: *Phys. Rev. D* 89.10 (2014), p. 102003. DOI: [10.1103/PhysRevD.89.102003](https://doi.org/10.1103/PhysRevD.89.102003). arXiv: [1311.1286](https://arxiv.org/abs/1311.1286) [gr-qc].
- [65] Tyson B. Littenberg et al. “Systematic biases in parameter estimation of binary black-hole mergers”. In: *Phys. Rev. D* 87 (2013), p. 104003. DOI: [10.1103/PhysRevD.87.104003](https://doi.org/10.1103/PhysRevD.87.104003). arXiv: [1210.0893](https://arxiv.org/abs/1210.0893) [gr-qc].
- [66] J. Calderón Bustillo, P. Laguna, and D. Shoemaker. “Detectability of gravitational waves from binary black holes: Impact of precession and higher modes”. In: *PRD* 95.10, 104038 (May 2017), p. 104038. DOI: [10.1103/PhysRevD.95.104038](https://doi.org/10.1103/PhysRevD.95.104038). arXiv: [1612.02340](https://arxiv.org/abs/1612.02340) [gr-qc].
- [67] Vijay Varma et al. “Gravitational-wave observations of binary black holes: Effect of nonquadrupole modes”. In: *Phys. Rev. D* 90.12 (2014), p. 124004. DOI: [10.1103/PhysRevD.90.124004](https://doi.org/10.1103/PhysRevD.90.124004). arXiv: [1409.2349](https://arxiv.org/abs/1409.2349) [gr-qc].

Chapter 5

TESTING THE NO-HAIR THEOREM WITH GW150914

Maximiliano Isi, Matthew Giesler, Will M. Farr, Mark A. Scheel, and Saul A.
Teukolsky
Physical Review Letters, 123, 111102 (2019)
[arxiv:1905.00869](https://arxiv.org/abs/1905.00869)

5.1 Abstract

We analyze gravitational-wave data from the first LIGO detection of a binary black-hole merger (GW150914) in search of the ringdown of the remnant black hole. Using observations beginning at the peak of the signal, we find evidence of the fundamental quasinormal mode and at least one overtone, both associated with the dominant angular mode ($\ell = m = 2$), with 3.6σ confidence. A ringdown model including overtones allows us to measure the final mass and spin magnitude of the remnant exclusively from postinspiral data, obtaining an estimate in agreement with the values inferred from the full signal. The mass and spin values we measure from the ringdown agree with those obtained using solely the fundamental mode at a later time, but have smaller uncertainties. Agreement between the postinspiral measurements of mass and spin and those using the full waveform supports the hypothesis that the GW150914 merger produced a Kerr black hole, as predicted by general relativity, and provides a test of the no-hair theorem at the $\sim 10\%$ level. An independent measurement of the frequency of the first overtone yields agreement with the no-hair hypothesis at the $\sim 20\%$ level. As the detector sensitivity improves and the detected population of black hole mergers grows, we can expect that using overtones will provide even stronger tests.

5.2 Introduction

The coalescence of two astrophysical black holes consists of a long inspiral followed by a violent plunge, during which the full richness of spacetime dynamics comes into play. The two objects merge, forming a single distorted black hole that rings down as it settles to a final stationary state. Gravitational waves are emitted throughout the entire process, at each moment carrying information about the evolving source. In general relativity, radiation from the ringdown stage takes the form of superposed

damped sinusoids, corresponding to the quasinormal-mode oscillations of the final Kerr black hole [1–4]. The frequencies and decay rates of these damped sinusoids are uniquely determined by the final hole’s mass M_f and dimensionless spin magnitude χ_f . This is a consequence of the *no-hair theorem*—the statement that mass and spin are the only two properties of astrophysical black holes in general relativity.¹ The ringdown spectrum is thus a fingerprint that identifies a Kerr black hole: measuring the quasinormal modes from gravitational-wave observations would provide us with a unique laboratory to test general relativity and probe the true nature of remnants from compact-binary mergers, including testing the no-hair theorem [5–13]. This program has been called *black-hole spectroscopy*, in analogy to the spectroscopic study of atomic elements [6].

Although LIGO [14] and Virgo [15] have already confidently detected gravitational waves from multiple binary-black-hole coalescences [16–22], black hole spectroscopy has remained elusive [23–29]. This is because past analyses looked for the ringdown in data at late times after the signal peak, where the quasinormal modes are too weak to confidently characterize with current instruments. The choice to focus on the late, weak-signal regime stemmed from concerns about nonlinearities surrounding the black hole merger, which were traditionally expected to contaminate the ringdown measurement at earlier times [8, 25, 26, 28–31].

Concerns about nonlinearities are, however, unfounded: the linear description can be extended to the full waveform following the peak of the gravitational wave strain [32]. Rather than nonlinearities, times around the peak are dominated by ringdown *overtones*—the quasinormal modes with the fastest decay rates, but also the highest amplitudes near the waveform peak [32, 33]. Indications of this can be found in the waveform modeling literature, with overtones an integral part of earlier equivalent one-body models [34–36] (although later abandoned, c.f. [37]). Yet, with a few exceptions [12, 27], previous ringdown analyses have neglected overtones, under the assumption that their contribution to the signal should always be marginal [8, 23–26, 28, 29, 38]. As a consequence, these studies ignored important signal content and were unable to extract multiple ringdown modes.

The inclusion of overtones enables us to perform a multimodal spectroscopic analysis of a black-hole ringdown, which we apply to LIGO data from the GW150914 event [16] (Fig. 5.1). We rely on overtones of the $\ell = m = 2$ angular mode to

¹In general, black holes may also possess electric charge, but this is expected to be negligible for astrophysical objects.

measure the remnant mass and spin from data starting at the peak of the signal, assuming first that quasinormal modes are as predicted for a Kerr black hole within general relativity. We find the least-damped (‘fundamental’) mode and at least one overtone with 3.6σ confidence (Fig. 5.2). At least one overtone, in addition to the fundamental, is needed to describe the waveform near the peak amplitude. This agrees with our expectations from [32] given the signal-to-noise ratio of GW150914.

Assuming the remnant is a Kerr black hole, frequencies and damping rates of the fundamental mode and one overtone imply a detector-frame mass of $(68 \pm 7) M_{\odot}$ and a dimensionless spin magnitude of 0.63 ± 0.16 , with 68% credibility. This is the best constraint on the remnant mass and spin obtained in this work. This measurement agrees with the one obtained from the fundamental mode alone beginning 3 ms after the waveform peak amplitude (Figures 5.1 and 5.3) [39]. It also agrees with the mass and spin inferred from the full waveform using fits to numerical relativity. The fractional difference between the best-measured combination of mass and spin² at the peak with one overtone and the same combination solely with the fundamental 3 ms after the peak is $(0 \pm 10)\%$. This is evidence at the $\sim 10\%$ level that GW150914 did result in a Kerr black hole as predicted by general relativity, and that the postmerger signal is in agreement with the no-hair theorem. Similarly, the fractional difference between the best-measured combination of mass and spin at the peak with one overtone and the same combination using the full waveform is $(7 \pm 7)\%$.

Traditional proposals for black-hole spectroscopy require frequency measurements for two or more quasinormal modes [6]. In that spirit, we also consider a single-overtone model that allows the overtone frequency and damping time to deviate from the Kerr prediction for any given mass and spin. This enables us to evaluate agreement of the observed ringdown spectrum with the prediction for a perturbed Kerr black hole, regardless of the specific properties of the remnant. From analysis of data starting at peak strain, we find the spectrum to be in agreement with the no-hair hypothesis to within $\sim 20\%$, with 68% credibility (Fig. 5.4). This is a test of the no-hair theorem based purely on the postinspiral regime.

5.3 Method

Each quasinormal mode has a frequency $\omega_{\ell mn}$ and a damping time $\tau_{\ell mn}$, where n is the ‘overtone’ index and (ℓ, m) are indices of spin-weighted angular harmonics that describe the angular dependence of the mode. We focus on the fundamental

²That is, the measurement of the linear combination of M_f and χ_f corresponding to the principal component of the posterior distribution with the smallest associated eigenvalue.

and overtones of the dominant $\ell = m = 2$ spin-weighted spherical harmonic of the strain.³ This is the only angular harmonic expected to be relevant for GW150914 [43, 44].⁴ For ease of notation, we generally drop the ℓ and m indices, retaining only the overtone index n . The $\ell = m = 2$ mode of the parametrized ringdown strain ($h = h_+ - ih_\times$) can be written as a sum of damped sinusoids [1–4],

$$h_{22}^N(t) = \sum_{n=0}^N A_n \exp[-i(\omega_n t + \phi_n) - t/\tau_n], \quad (5.1)$$

for times t greater than some start time t_0 , where $\Delta t = t - t_0$. The overtone index n orders the different modes by decreasing damping time τ_n , so that $n = 0$ denotes the longest-lived mode. N is the index of the highest overtone included in the model, which in this work will be $N \leq 2$. Importantly, higher n does not imply a higher frequency ω_n ; rather, the opposite is generally true. All frequencies and damping times are implicit functions of the remnant mass and spin magnitude (M_f, χ_f), and can be computed from perturbation theory [45–47]. The amplitudes A_n and phases ϕ_n encode the degree to which each overtone is excited as the remnant is formed and cannot be computed within perturbation theory, so we treat them as free parameters in our fit.

We use the model in Eq. (5.1) to carry out a Bayesian analysis of LIGO Hanford and LIGO Livingston data for GW150914 [16, 22, 48]. For any given start time t_0 , we produce a posterior probability density over the space of remnant mass and spin magnitude, as well as the amplitudes and phases of the included overtones. We parametrize start times via $\Delta t_0 = t_0 - t_{\text{peak}}$, where $t_{\text{peak}} = 1126259462.423$ GPS refers to the inferred signal peak at the LIGO Hanford detector [23, 49]. We define the likelihood in the time domain in order to explicitly exclude all data before t_0 . We place uniform priors on $(M_f, \chi_f, A_n, \phi_n)$, with a restriction to corotating modes ($\omega_n > 0$). All overtones we consider share the same $\ell = m = 2$ angular dependence, allowing us to simplify the handling of antenna patterns and other subtleties. Details specific to our implementation are provided in the supplementary material.

³The spin-weighted *spheroidal* harmonics form the natural basis that arises in perturbation theory [3, 40, 41]. These functions are equivalent to the spin-weighted spherical harmonics in the limit of zero spin. For $\chi_f > 0$, the spin-weighted spheroidal harmonics can be written as superpositions of the spin-weighted spherical harmonics of the same m , but different ℓ [41, 42]. The effect of this mixing on the dominant $\ell = m = 2$ spin-weighted spherical mode is negligible for a GW150914-like system [32].

⁴Dedicated studies have found no evidence of higher angular harmonics in the late ringdown of GW150914 [29].

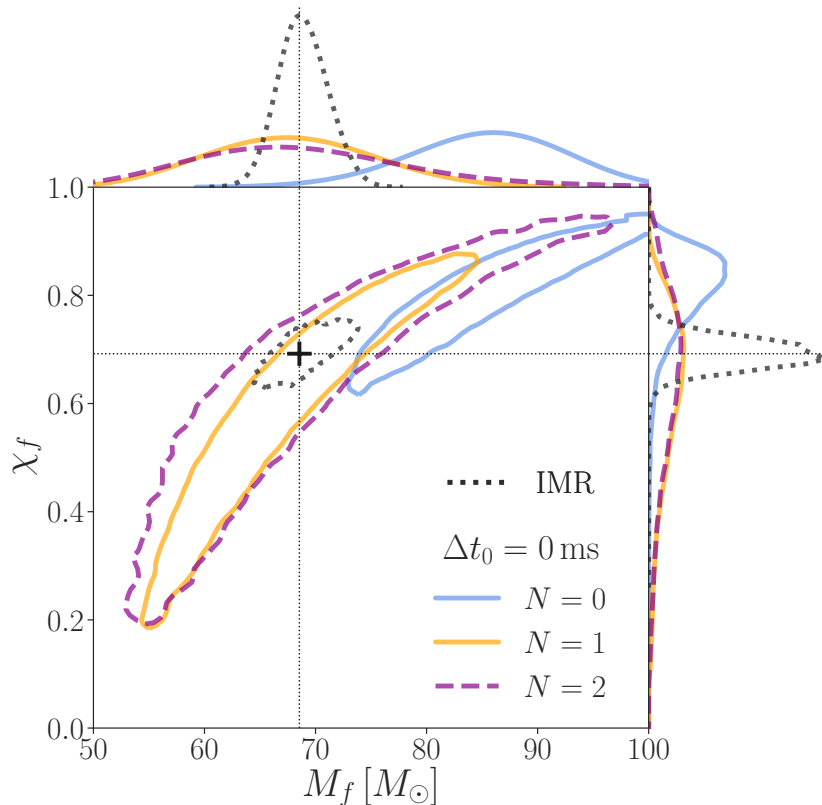


Figure 5.1: Remnant parameters inferred with different number of overtones, using data starting at peak strain amplitude. Contours represent 90%-credible regions on the remnant mass (M_f) and dimensionless spin magnitude (χ_f), obtained from the Bayesian analysis of GW150914. The inference model is that of Eq. (5.1), with different number of overtones N : 0 (solid blue), 1 (solid yellow), 2 (dashed purple). In all cases, the analysis uses data starting at peak strain ($\Delta t_0 = t_0 - t_{\text{peak}} = 0$). Amplitudes and phases are marginalized over. The black contour is the 90%-credible region obtained from the full IMR waveform, as described in the text. The intersection of the dotted lines marks the peak of this distribution ($M_f = 68.5 M_\odot$, $\chi_f = 0.69$). The top and right panels show 1D posteriors for M_f and χ_f respectively. The linear quasinormal mode models with $N > 0$ provide measurements of the mass and spin consistent with the full IMR waveform, in agreement with general relativity.

We compare our ringdown-only measurements of the remnant mass and spin magnitude to those obtained from the analysis of the full inspiral-merger-ringdown (IMR) signal. To do so, we rely on fitting formulas based on numerical relativity to translate measured values of the binary mass ratio q and component spins ($\vec{\chi}_1, \vec{\chi}_2$) into expected remnant parameters [50, 51]. We use posterior samples on the binary parameters made available by the LIGO and Virgo collaborations [22, 48],

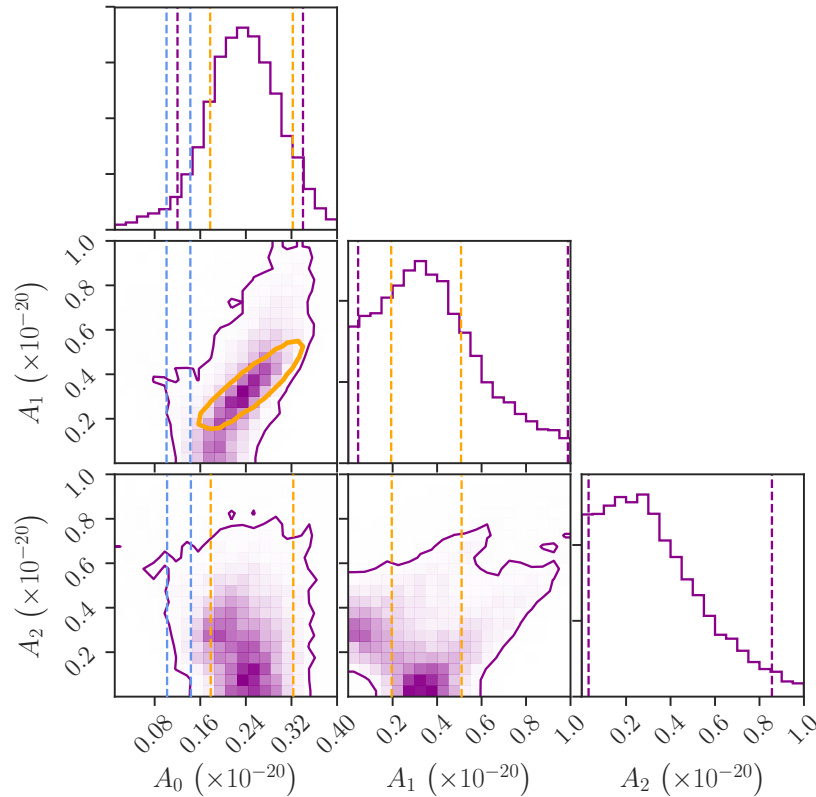


Figure 5.2: Measured quasinormal-mode amplitudes for a model with the fundamental mode and two overtones ($N = 2$). The purple colormap represents the joint posterior distribution for the three amplitudes in the $N = 2$ model: A_0 , A_1 , A_2 , as defined in Eq. (5.1). The solid curves enclose 90% of the probability mass. A yellow curve in the A_0 – A_1 plane, as well as corresponding yellow dashed lines, represents the 90%-credible measurement of the amplitudes assuming $N = 1$. Similarly, blue dashed lines give the 90%-credible measurement of A_0 assuming $N = 0$. All amplitudes are defined at $t = t_{\text{peak}}$, where all fits here are carried out ($\Delta t_0 = 0$). Values have been rescaled by a constant to correspond to the strain measured by the LIGO Hanford detector. Assuming $N = 1$, the mean of the A_1 marginalized posterior lies 3.6 standard deviations away from zero, i.e. $A_1 = 0$ is disfavored at 3.6σ . Assuming $N = 2$, $A_1 = A_2 = 0$ is disfavored with 90% credibility.

marginalizing over unavailable component-spin angles.

We consider explicit deviations from the Kerr spectrum by allowing the frequency and damping time of the first overtone to differ from the no-hair values. Under this modified $N = 1$ model, the overtone angular frequency becomes $\omega_1 = 2\pi f_1^{(\text{GR})} (1 + \delta f_1)$, with δf_1 a fractional deviation away from the Kerr frequency $f_1^{(\text{GR})}$ for any given M_f and χ_f . Similarly, the damping time is allowed to vary by letting $\tau_1 = \tau_1^{(\text{GR})} (1 + \delta\tau_1)$.

Fixing $\delta f_1 = \delta \tau_1 = 0$ recovers the regular $N = 1$ analysis. We may then compute the relative likelihood of the no-hair hypothesis by means of the Savage-Dickey density ratio [52].

5.4 Results

Fig. 5.1 shows the 90%-credible regions for the remnant mass (abscissa) and spin magnitude (ordinate) obtained by analyzing data starting at t_{peak} with different numbers of overtones ($N = 0, 1, 2$) in the ringdown template of Eq. (5.1). The quasinormal-mode amplitudes and phases have been marginalized over. For comparison, we also show the 90%-credible region inferred from the full IMR signal, as explained above. If the remnant is sufficiently well described as a perturbed Kerr black hole, and if general relativity is correct, we expect the ringdown and IMR measurements to agree. As expected, this is not the case if we assume the ringdown is composed solely of the longest-lived mode ($N = 0$), in which case we obtain a biased estimate of the remnant properties. In contrast, the ringdown and IMR measurements begin to agree with the addition of one overtone ($N = 1$). This is expected from previous work suggesting that, given the network signal-to-noise ratio of GW150914 (~ 14 in the post-peak region, for frequencies > 154.7 Hz), we should be able to resolve only one mode besides the fundamental [32].

Indeed, a ringdown model with two overtones ($N = 2$) does not lead to further improvement in the mass and spin measurement. On the contrary, the 90%-credible region obtained with $N = 2$ is slightly broader than the one with $N = 1$, as might be expected from the two additional free parameters (A_2, ϕ_2). This is because the analysis is unable to unequivocally identify the second overtone in the data, as shown by the amplitude posteriors in Fig. 5.2. The $N = 2$ posterior supports a range of values for A_1 and A_2 , but excludes $A_1 = A_2 = 0$ with 90% credibility (center panel in bottom row of Fig. 5.2). The joint posterior distribution on A_1 and A_2 tends to favor the first overtone at the expense of the second: the maximum a posteriori waveform scarcely includes any contribution from $n = 2$, and favors a value of A_1 in agreement with the $N = 1$ posterior (yellow traces in Fig. 5.2).

We next compare measurements carried out with overtones at the peak with measurements without overtones after the peak. Fig. 5.3 shows 90%-credible regions for the remnant mass and spin magnitude obtained with the fundamental mode ($N = 0$) at different times after t_{peak} ($\Delta t_0 \in [1, 3, 5]$ ms). As the overtones die out, the fundamental mode becomes a better model for the signal. We find that

the $N = 0$ contour coincides with the IMR measurement ~ 3 ms after the peak, in agreement with [23]. However, the uncertainty in this measurement is larger than for the $N = 1$ contour at the peak (also shown for reference). This can be attributed to the exponential decrease in signal-to-noise ratio for times after the peak.

Finally, we allow the first-overtone frequency and damping time to float around the no-hair values in an $N = 1$ model. As in Fig. 5.1, we analyze data starting at the inferred peak of the strain. Fig. 5.4 shows the resulting marginalized posterior over the fractional frequency and damping time deviations (δf_1 and $\delta \tau_1$ respectively). With 68% credibility, we measure $\delta f_1 = -0.05 \pm 0.2$. To that level of credibility, this establishes agreement with the no-hair hypothesis ($\delta f_1 = 0$) at the 20% level. The damping time is largely unconstrained in the $-0.06 \lesssim \delta \tau_1 \lesssim 1$ range. This has little impact on the frequency measurement, which is unaffected by setting $\delta \tau_1 = 0$. We find that the ratio of marginal likelihoods (the Bayes factor) between the no-hair model ($\delta f_1 = \delta \tau_1 = 0$) and our floating frequency and damping time model is 1.75.

5.5 Discussion and prospects

A linearly perturbed Kerr black hole radiates gravitational waves in the form of damped sinusoids, with specific frequencies and decay rates determined exclusively by the hole’s mass and spin. For any given angular harmonic, the quasinormal modes can be ordered by decreasing damping time through an overtone index n , with $n = 0$ denoting the longest-lived mode (also known as the ‘fundamental’). Although modes of all n contribute to the linear description, the fundamental has long been the only one taken into account in observational studies of the ringdown, with overtones virtually ignored [23–26, 28, 29]. Yet, these short-lived modes can dominate the gravitational wave signal for times around the peak and are an essential part of the ringdown [32, 33]. We demonstrate this with a multimode analysis of the GW150914 ringdown.

Making use of overtones, we extract information about the GW150914 remnant using only postinspiral data, starting at the peak of the signal (Fig. 5.1). We find evidence of the fundamental mode plus at least one overtone (Fig. 5.2), and obtain a 90%-credible measurement of the remnant mass and spin magnitude in agreement with that inferred from the full waveform. This measurement is also consistent with the one obtained using solely the fundamental mode at a later time, but has reduced uncertainties (Fig. 5.3).

The agreement between all measurements is evidence that, beginning as early as

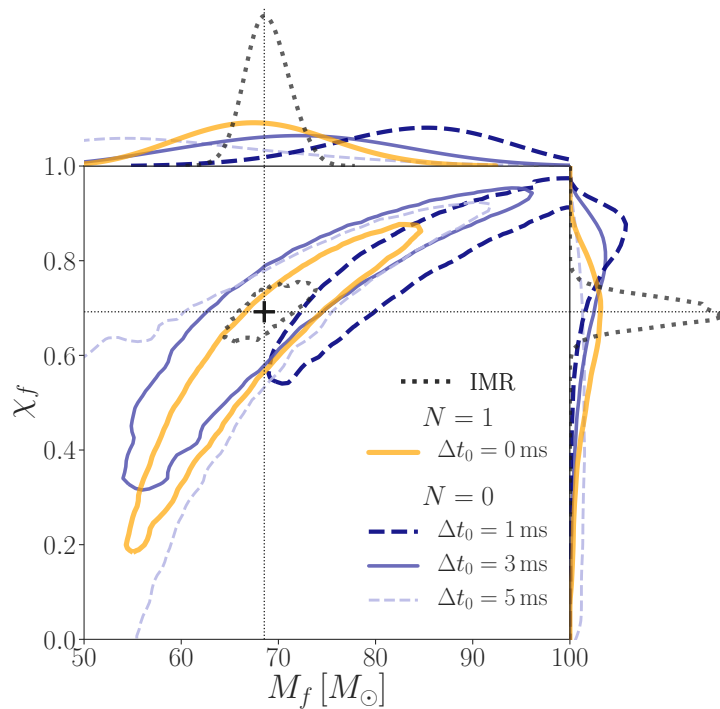


Figure 5.3: Remnant parameters inferred only from the fundamental mode, using data starting at different times after the peak. Contours represent 90%-credible regions on the remnant mass (M_f) and dimensionless spin magnitude (χ_f), obtained from the Bayesian analysis of GW150914. For the blue contours, the inference model included no overtones ($N = 0$) and used data starting at different times after the peak: $\Delta t_0 = t_0 - t_{\text{peak}} \in [1, 3, 5]$ ms. For the yellow contour, the analysis was conducted with one overtone ($N = 1$) starting at the peak ($\Delta t_0 = 0$), as in Fig. 5.1. Amplitudes and phases are marginalized over. The black contour is the 90%-credible region obtained from the full IMR waveform, as described in the text. The intersection of the dotted lines marks the peak of this distribution ($M_f = 68.5 M_\odot$, $\chi_f = 0.69$). The top and right panels show 1D posteriors for M_f and χ_f respectively. Around $\Delta t_0 = 3$ ms, the overtones have become unmeasurable and only the fundamental mode remains; consequently, at that time $N = 0$ returns a measurement of the final mass and spin consistent with both the full IMR waveform and the $N > 0$ models at the peak, in agreement with general relativity.

the signal peak, a far-away observer cannot distinguish the source from a linearly perturbed Kerr background with a fixed mass and spin, i.e., we do not observe nonlinearities in this regime. The agreement between the IMR and postmerger estimates implies that the data agree with the full prediction of general relativity. This is similar to the consistency test between inspiral and merger-ringdown [53, 54], but relies on a manifestly linear description of the postinspiral signal. More specifically, it validates the prediction for the final state of a collision between two black holes.

With the identification of multiple ringdown modes, this is also a step toward the goal of black hole spectroscopy. The agreement between postinspiral measurements with two different sets of modes (Fig. 5.3) supports the hypothesis that GW150914 produced a Kerr black hole as described by general relativity. Moreover, we constrain deviations away from the no-hair spectrum by allowing the overtone frequency and damping time to vary freely (Fig. 5.4). This is equivalent to independently measuring the frequencies of the fundamental and first overtone, and establishing their consistency with the Kerr hypothesis.

Future studies of black-hole ringdowns relying on overtones could potentially allow us to identify black-hole mimickers and probe the applicability of the no-hair theorem with high precision, even with existing detectors. Such advances will be facilitated by improvements in our understanding of how the overtones are sourced, so that we can predict the amplitudes and phases from the binary properties. This would reduce the dimensionality of the problem and lead to more specific predictions from general relativity.

5.6 Acknowledgments

We thank Aaron Zimmerman for valuable feedback. We thank Gregorio Carullo, Walter del Pozzo, and John Veitch for discussions of their paper on and methods for time-domain analysis [29]. We thank Alessandra Buonanno for clarifications on past use of quasinormal and pseudo-quasinormal ringdown modes in waveform modeling. M.I. is supported by NASA through the NASA Hubble Fellowship grant No. HST-HF2-51410.001-A awarded by the Space Telescope Science Institute, which is operated by the Association of Universities for Research in Astronomy, Inc., for NASA, under contract NAS5-26555. M.I. is a member of the LIGO Laboratory. LIGO was constructed by the California Institute of Technology and Massachusetts Institute of Technology with funding from the National Science Foundation and

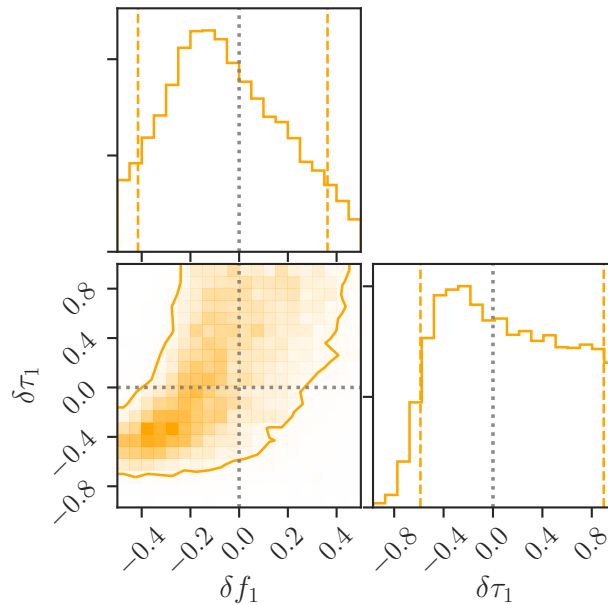


Figure 5.4: Measurement of the frequency and damping time of the first overtone, using data starting at the peak. The colormap represents the posterior distribution of the fractional deviations δf_1 and $\delta \tau_1$ away from the no-hair value $\delta f_1 = \delta \tau_1 = 0$ (gray dotted lines). The solid contour and dashed vertical lines enclose 90% of the posterior probability. All other parameters, including M_f and χ_f have been marginalized away. Fixing $\delta f_1 = \delta \tau_1 = 0$ recovers the $N = 1$ analysis in Figs. 5.1 and 5.3.

operates under cooperative agreement PHY-0757058. M.G. and M.S. are supported by the Sherman Fairchild Foundation and NSF grants PHY-1708212 and PHY-1708213 at Caltech. S.T. is supported in part by the Sherman Fairchild Foundation and by NSF Grants PHY-1606654 and ACI-1713678 at Cornell. The Flatiron Institute is supported by the Simons Foundation. This research has made use of data, software and/or web tools obtained from the Gravitational Wave Open Science Center [48, 55], a service of the LIGO Laboratory, the LIGO Scientific Collaboration and the Virgo Collaboration. This paper carries LIGO document number LIGO-P1900135.

5.7 Appendix: Technical Details

Time-domain likelihood

The signal model used in this analysis has a sharp transition in the time domain. We do not wish to incorporate any data from the detectors before our model begins so that we avoid bias; equivalently, we want to assume that we are infinitely uncertain about the gravitational wave signal before the start point of our signal model. This requires

special treatment compared to the standard LIGO data analysis [39, 56]. Other approaches to quasi-normal mode extraction treat the data similarly [29] except for the assumption of periodicity, enforced by tapering, which is absent in our treatment (see below).

As in previous analyses of GW150914, we assume that the detector measures a discrete data stream \mathbf{d} that contains our signal \mathbf{s} contaminated by additive, Gaussian noise \mathbf{n} . At time t_i ,

$$d_i = h(t_i) + n_i, \quad (5.2)$$

with the noise time series \mathbf{n} having a multivariate normal distribution,

$$\mathbf{n} \sim \mathcal{N}(\boldsymbol{\mu}, \boldsymbol{\Sigma}), \quad (5.3)$$

with mean $\boldsymbol{\mu}$ and covariance matrix $\boldsymbol{\Sigma}$. The actual noise in the detector has very large low-frequency components, while our signal lives primarily at high ($\gtrsim 100$ Hz) frequencies [46, 47]. To reduce the low-frequency components of the noise, we first apply a fourth-order, high-pass Butterworth filter with a roll-on frequency of 20 Hz. After the filter, the data are very close to zero mean, so we assume $\boldsymbol{\mu} = \mathbf{0}$.

The distribution of the noise implies that the log-likelihood function (i.e., the distribution of data \mathbf{d} conditioned on a signal \mathbf{h}) is

$$\begin{aligned} \log p(\mathbf{d} | \mathbf{h}) = & -\frac{1}{2} (\mathbf{d} - \mathbf{h})^T \boldsymbol{\Sigma}^{-1} (\mathbf{d} - \mathbf{h}) \\ & -\frac{1}{2} \log \det \boldsymbol{\Sigma} - \frac{K}{2} \log 2\pi, \end{aligned} \quad (5.4)$$

where K is the total number of samples.

We assume that the noise in the detector is stationary, so that the covariance matrix takes a special (Toeplitz) form where the ij component depends only on the time separation between samples i and j :

$$\Sigma_{ij} = \langle n_i n_j \rangle = \rho(|i - j|), \quad (5.5)$$

where ρ is the autocovariance function,

$$\rho(k) = \langle n_i n_{i+k} \rangle. \quad (5.6)$$

(The expectation above runs over all times, i .) The assumptions of stationary Gaussian noise have been checked for GW150914 specifically [39, 56–58] and the LIGO events in general [22, 59].

The standard LIGO data analysis imposes an additional assumption that

$$\rho(k) = \rho(K - k) \quad (5.7)$$

for $0 \leq k < K$. This “circularity” assumption is appropriate for data that are periodic with period K ; periodicity is typically enforced by tapering the data segment at the beginning and end [56, 60]. The benefit of this assumption is that a circular Toeplitz matrix is diagonal in the Fourier basis (i.e. stationary periodic noise has statistically-independent Fourier components), and therefore the matrix-inversion step in the log-likelihood reduces to a sum over independent frequency components. Such a likelihood can also be computed directly in the time domain [29].

A taper is not appropriate for our data analysis since we wish to ignore data from times before the peak of the waveform, where our signal model begins. We do not have data before the peak in which to implement a taper; and tapering past the peak would significantly reduce our signal. Happily, fast and stable algorithms exist for solving linear equations with a Toeplitz structure [61–63], so a direct implementation of our likelihood in Eq. (5.4) is not too costly.

We estimate the autocovariance function by the empirical autocovariance of 64 s of off-source data, after high-pass filtering as above. This is analogous to the Welch method for estimating power spectral densities in the frequency domain [64] used by the standard LIGO analyses [56, 60]. Our analysis is based on data at a sample rate of 2048 Hz, beginning at the peak signal amplitude at 1126259462.423 GPS and running for 0.5 s. The autocovariance estimate is truncated to that same duration.

Other details

We handle polarizations by projecting the complex-valued strain in Eq. (5.1) of the main text onto each LIGO detector by means of the corresponding antenna patterns. To do so, we assume the source of GW150914 had right ascension $\alpha = 1.95$ rad and declination $\delta = -1.27$ rad, with polarization angle $\psi = 0.82$ rad and inclination $\iota = \pi$ rad. These parameters are consistent with the maximum a posteriori estimates inferred for GW150914 [16, 48, 49]. We also time-shift the LIGO Livingston data by the corresponding arrival-time delay of 7 ms [16, 49], so as to align the signal at the two detectors. As noted in the main text, we may make these simplifications because all ringdown modes we consider are subject to the same angular dependence ($\ell = m = 2$). A version of this analysis with the more simplified approach of [23, 65] yields compatible results.

Our priors are such that quasinormal-mode amplitudes A_n are allowed to vary in the range $[0, 2.5 \times 10^{-19}]$, an arbitrary range found to offer full support to the posterior in all cases. The corresponding phases ϕ_n are unrestricted in the full range $[0, 2\pi]$. For computational efficiency, we internally parameterize the amplitude and phase of each mode using the two quadratures $c_n = A_n \cos \phi_n$ and $s_n = A_n \sin \phi_n$, but set priors uniform in A_n and ϕ_n . The remnant mass M_f is allowed to vary within $[50, 100] M_\odot$, while the dimensionless spin magnitude χ_f varies within $[0, 1]$. When considering explicit deviations from the no-hair theorem, we set uniform priors such that $-0.5 < \delta f_1 < 0.5$ and $-1 < \delta \tau_1 < 1$. In all cases, samples are drawn from the posterior using `kombine` [66].

References

- [1] C. V. Vishveshwara. “Stability of the Schwarzschild Metric”. In: *Phys. Rev. D* 1 (10 May 1970), pp. 2870–2879. DOI: [10.1103/PhysRevD.1.2870](https://doi.org/10.1103/PhysRevD.1.2870). URL: <https://link.aps.org/doi/10.1103/PhysRevD.1.2870>.
- [2] William H. Press. “Long Wave Trains of Gravitational Waves from a Vibrating Black Hole”. In: *Astrophys. J.* 170 (1971), pp. L105–L108. DOI: [10.1086/180849](https://doi.org/10.1086/180849).
- [3] S. A. Teukolsky. “Perturbations of a rotating black hole. 1. Fundamental equations for gravitational electromagnetic and neutrino field perturbations”. In: *Astrophys. J.* 185 (1973), pp. 635–647. DOI: [10.1086/152444](https://doi.org/10.1086/152444).
- [4] S. Chandrasekhar and S. Detweiler. “The Quasi-Normal Modes of the Schwarzschild Black Hole”. In: *Proc. R. Soc. A* 344.1639 (1975), pp. 441–452. ISSN: 00804630. URL: <http://www.jstor.org/stable/78902>.
- [5] F. Echeverria. “Gravitational Wave Measurements of the Mass and Angular Momentum of a Black Hole”. In: *Phys. Rev. D* 40 (1989), pp. 3194–3203. DOI: [10.1103/PhysRevD.40.3194](https://doi.org/10.1103/PhysRevD.40.3194).
- [6] Olaf Dreyer et al. “Black hole spectroscopy: Testing general relativity through gravitational wave observations”. In: *Class. Quant. Grav.* 21 (2004), pp. 787–804. DOI: [10.1088/0264-9381/21/4/003](https://doi.org/10.1088/0264-9381/21/4/003). arXiv: [gr-qc/0309007](https://arxiv.org/abs/gr-qc/0309007) [gr-qc].
- [7] Emanuele Berti, Vitor Cardoso, and Clifford M. Will. “On gravitational-wave spectroscopy of massive black holes with the space interferometer LISA”. In: *Phys. Rev. D* 73 (2006), p. 064030. DOI: [10.1103/PhysRevD.73.064030](https://doi.org/10.1103/PhysRevD.73.064030). arXiv: [gr-qc/0512160](https://arxiv.org/abs/gr-qc/0512160) [gr-qc].
- [8] S. Gossan, J. Veitch, and B. S. Sathyaprakash. “Bayesian model selection for testing the no-hair theorem with black hole ringdowns”. In: *Phys. Rev. D* 85 (2012), p. 124056. DOI: [10.1103/PhysRevD.85.124056](https://doi.org/10.1103/PhysRevD.85.124056). arXiv: [1111.5819](https://arxiv.org/abs/1111.5819) [gr-qc].

- [9] J. Meidam et al. “Testing the no-hair theorem with black hole ringdowns using TIGER”. In: *Phys. Rev. D* 90.6 (2014), p. 064009. DOI: [10.1103/PhysRevD.90.064009](https://doi.org/10.1103/PhysRevD.90.064009). arXiv: [1406.3201](https://arxiv.org/abs/1406.3201) [gr-qc].
- [10] Emanuele Berti et al. “Testing General Relativity with Present and Future Astrophysical Observations”. In: *Class. Quant. Grav.* 32 (2015), p. 243001. DOI: [10.1088/0264-9381/32/24/243001](https://doi.org/10.1088/0264-9381/32/24/243001). arXiv: [1501.07274](https://arxiv.org/abs/1501.07274) [gr-qc].
- [11] Emanuele Berti et al. “Spectroscopy of Kerr black holes with Earth- and space-based interferometers”. In: *Phys. Rev. Lett.* 117.10 (2016), p. 101102. DOI: [10.1103/PhysRevLett.117.101102](https://doi.org/10.1103/PhysRevLett.117.101102). arXiv: [1605.09286](https://arxiv.org/abs/1605.09286) [gr-qc].
- [12] Vishal Baibhav et al. “Black Hole Spectroscopy: Systematic Errors and Ringdown Energy Estimates”. In: *Phys. Rev. D* 97.4 (2018), p. 044048. DOI: [10.1103/PhysRevD.97.044048](https://doi.org/10.1103/PhysRevD.97.044048). arXiv: [1710.02156](https://arxiv.org/abs/1710.02156) [gr-qc].
- [13] Vishal Baibhav and Emanuele Berti. “Multimode black hole spectroscopy”. In: *Phys. Rev. D* 99.2 (2019), p. 024005. DOI: [10.1103/PhysRevD.99.024005](https://doi.org/10.1103/PhysRevD.99.024005). arXiv: [1809.03500](https://arxiv.org/abs/1809.03500) [gr-qc].
- [14] J. Aasi et al. “Advanced LIGO”. In: *Class. Quant. Grav.* 32 (2015), p. 074001. DOI: [10.1088/0264-9381/32/7/074001](https://doi.org/10.1088/0264-9381/32/7/074001). arXiv: [1411.4547](https://arxiv.org/abs/1411.4547) [gr-qc].
- [15] F. Acernese et al. “Advanced Virgo: a second-generation interferometric gravitational wave detector”. In: *Class. Quant. Grav.* 32.2 (2015), p. 024001. DOI: [10.1088/0264-9381/32/2/024001](https://doi.org/10.1088/0264-9381/32/2/024001).
- [16] B. P. Abbott et al. “Observation of Gravitational Waves from a Binary Black Hole Merger”. In: *Phys. Rev. Lett.* 116.6 (Feb. 2016), p. 061102. ISSN: 0031-9007. DOI: [10.1103/PhysRevLett.116.061102](https://doi.org/10.1103/PhysRevLett.116.061102). URL: <http://link.aps.org/doi/10.1103/PhysRevLett.116.061102>.
- [17] B. P. Abbott et al. “GW151226: Observation of Gravitational Waves from a 22-Solar-Mass Binary Black Hole Coalescence”. In: *Phys. Rev. Lett.* 116.24 (June 2016), p. 241103. ISSN: 0031-9007. DOI: [10.1103/PhysRevLett.116.241103](https://doi.org/10.1103/PhysRevLett.116.241103). URL: <http://link.aps.org/doi/10.1103/PhysRevLett.116.241103>.
- [18] B. P. Abbott et al. “Binary Black Hole Mergers in the First Advanced LIGO Observing Run”. In: *Phys. Rev. X* 6.4 (Oct. 2016), p. 041015. ISSN: 2160-3308. DOI: [10.1103/PhysRevX.6.041015](https://doi.org/10.1103/PhysRevX.6.041015). URL: <http://arxiv.org/abs/1606.04856><https://dcc.ligo.org/LIGO-%20P1600088/public%20https://link.aps.org/doi/10.1103/%20PhysRevX.6.041015>.
- [19] B. P. Abbott et al. “GW170104: Observation of a 50-Solar-Mass Binary Black Hole Coalescence at Redshift 0.2”. In: *Phys. Rev. Lett.* 118.22 (June 2017), p. 221101. ISSN: 0031-9007. DOI: [10.1103/PhysRevLett.118.221101](https://doi.org/10.1103/PhysRevLett.118.221101). URL: <https://journals.aps.org/prl/abstract/10.1103/%20PhysRevLett.118.221101%20https://dcc.ligo.org/LIGO-P170104/%20public%20https://arxiv.org/abs/1706.01812>.

- [20] B.. P. Abbott et al. “GW170608: Observation of a 19-solar-mass Binary Black Hole Coalescence”. In: *Astrophys. J.* 851.2 (2017), p. L35. DOI: [10.3847/2041-8213/aa9f0c](https://doi.org/10.3847/2041-8213/aa9f0c). arXiv: [1711.05578](https://arxiv.org/abs/1711.05578) [astro-ph.HE].
- [21] B. P. Abbott et al. “GW170814: A Three-Detector Observation of Gravitational Waves from a Binary Black Hole Coalescence”. In: *Phys. Rev. Lett.* 119.14 (2017), p. 141101. DOI: [10.1103/PhysRevLett.119.141101](https://doi.org/10.1103/PhysRevLett.119.141101). arXiv: [1709.09660](https://arxiv.org/abs/1709.09660) [gr-qc].
- [22] B. P. Abbott et al. “GWTC-1: A Gravitational-Wave Transient Catalog of Compact Binary Mergers Observed by LIGO and Virgo during the First and Second Observing Runs”. In: *Phys. Rev. X* 9.3 (2019), p. 031040. DOI: [10.1103/PhysRevX.9.031040](https://doi.org/10.1103/PhysRevX.9.031040). arXiv: [1811.12907](https://arxiv.org/abs/1811.12907) [astro-ph.HE].
- [23] B. P. Abbott et al. “Tests of General Relativity with GW150914”. In: *Phys. Rev. Lett.* 116.22 (May 2016), p. 221101. ISSN: 0031-9007. DOI: [10.1103/PhysRevLett.116.221101](https://doi.org/10.1103/PhysRevLett.116.221101). URL: <http://link.aps.org/doi/10.1103/PhysRevLett.116.221101> <https://arxiv.org/abs/1602.03841>.
- [24] Walter Del Pozzo and Alessandro Nagar. “Analytic family of post-merger template waveforms”. In: *Phys. Rev. D* 95.12 (2017), p. 124034. DOI: [10.1103/PhysRevD.95.124034](https://doi.org/10.1103/PhysRevD.95.124034). arXiv: [1606.03952](https://arxiv.org/abs/1606.03952) [gr-qc].
- [25] Miriam Cabero et al. “Observational tests of the black hole area increase law”. In: *Phys. Rev. D* 97.12 (2018), p. 124069. DOI: [10.1103/PhysRevD.97.124069](https://doi.org/10.1103/PhysRevD.97.124069). arXiv: [1711.09073](https://arxiv.org/abs/1711.09073) [gr-qc].
- [26] Eric Thrane, Paul D. Lasky, and Yuri Levin. “Challenges testing the no-hair theorem with gravitational waves”. In: *Phys. Rev. D* 96.10 (2017), p. 102004. DOI: [10.1103/PhysRevD.96.102004](https://doi.org/10.1103/PhysRevD.96.102004). arXiv: [1706.05152](https://arxiv.org/abs/1706.05152) [gr-qc].
- [27] Richard Brito, Alessandra Buonanno, and Vivien Raymond. “Black-hole Spectroscopy by Making Full Use of Gravitational-Wave Modeling”. In: *Phys. Rev. D* 98.8 (2018), p. 084038. DOI: [10.1103/PhysRevD.98.084038](https://doi.org/10.1103/PhysRevD.98.084038). arXiv: [1805.00293](https://arxiv.org/abs/1805.00293) [gr-qc].
- [28] Gregorio Carullo et al. “Empirical tests of the black hole no-hair conjecture using gravitational-wave observations”. In: *Phys. Rev. D* 98.10 (2018), p. 104020. DOI: [10.1103/PhysRevD.98.104020](https://doi.org/10.1103/PhysRevD.98.104020). arXiv: [1805.04760](https://arxiv.org/abs/1805.04760) [gr-qc].
- [29] Gregorio Carullo, Walter Del Pozzo, and John Veitch. “Observational Black Hole Spectroscopy: A time-domain multimode analysis of GW150914”. In: *Phys. Rev. D* 99.12 (2019), p. 123029. DOI: [10.1103/PhysRevD.99.123029](https://doi.org/10.1103/PhysRevD.99.123029). arXiv: [1902.07527](https://arxiv.org/abs/1902.07527) [gr-qc].
- [30] Ioannis Kamaretsos et al. “Black-hole hair loss: learning about binary progenitors from ringdown signals”. In: *Phys. Rev. D* 85 (2012), p. 024018. DOI: [10.1103/PhysRevD.85.024018](https://doi.org/10.1103/PhysRevD.85.024018). arXiv: [1107.0854](https://arxiv.org/abs/1107.0854) [gr-qc].

- [31] Lionel London, Deirdre Shoemaker, and James Healy. “Modeling ringdown: Beyond the fundamental quasinormal modes”. In: *Phys. Rev. D* 90.12 (2014). [Erratum: *Phys. Rev. D* 94, no. 6, 069902 (2016)], p. 124032. DOI: [10.1103/PhysRevD.90.124032](https://doi.org/10.1103/PhysRevD.90.124032). arXiv: [1404.3197](https://arxiv.org/abs/1404.3197) [gr-qc].
- [32] Matthew Giesler, Maximiliano Isi, Mark Scheel, and Saul Teukolsky. “Black hole ringdown: the importance of overtones”. In: *Phys. Rev. X* 9.4 (2019), p. 041060. DOI: [10.1103/PhysRevX.9.041060](https://doi.org/10.1103/PhysRevX.9.041060). arXiv: [1903.08284](https://arxiv.org/abs/1903.08284) [gr-qc].
- [33] Alessandra Buonanno, Gregory B. Cook, and Frans Pretorius. “Inspirational merger and ring-down of equal-mass black-hole binaries”. In: *Phys. Rev. D* 75 (2007), p. 124018. DOI: [10.1103/PhysRevD.75.124018](https://doi.org/10.1103/PhysRevD.75.124018). arXiv: [gr-qc/0610122](https://arxiv.org/abs/gr-qc/0610122) [gr-qc].
- [34] Yi Pan et al. “Inspirational-merger-ringdown waveforms of spinning, precessing black-hole binaries in the effective-one-body formalism”. In: *Phys. Rev. D* 89.8 (2014), p. 084006. DOI: [10.1103/PhysRevD.89.084006](https://doi.org/10.1103/PhysRevD.89.084006). arXiv: [1307.6232](https://arxiv.org/abs/1307.6232) [gr-qc].
- [35] Andrea Taracchini et al. “Effective-one-body model for black-hole binaries with generic mass ratios and spins”. In: *Phys. Rev. D* 89.6 (2014), 061502(R). DOI: [10.1103/PhysRevD.89.061502](https://doi.org/10.1103/PhysRevD.89.061502). arXiv: [1311.2544](https://arxiv.org/abs/1311.2544) [gr-qc].
- [36] Stanislav Babak, Andrea Taracchini, and Alessandra Buonanno. “Validating the effective-one-body model of spinning, precessing binary black holes against numerical relativity”. In: *Phys. Rev. D* 95.2 (2017), p. 024010. DOI: [10.1103/PhysRevD.95.024010](https://doi.org/10.1103/PhysRevD.95.024010). arXiv: [1607.05661](https://arxiv.org/abs/1607.05661) [gr-qc].
- [37] Alejandro Bohe et al. “Improved effective-one-body model of spinning, nonprecessing binary black holes for the era of gravitational-wave astrophysics with advanced detectors”. In: *Phys. Rev. D* 95.4 (2017), p. 044028. DOI: [10.1103/PhysRevD.95.044028](https://doi.org/10.1103/PhysRevD.95.044028). arXiv: [1611.03703](https://arxiv.org/abs/1611.03703) [gr-qc].
- [38] Swetha Bhagwat, Duncan A. Brown, and Stefan W. Ballmer. “Spectroscopic analysis of stellar mass black-hole mergers in our local universe with ground-based gravitational wave detectors”. In: *Phys. Rev. D* 94.8 (2016). [Erratum: *Phys. Rev. D* 95, no. 6, 069906 (2017)], p. 084024. DOI: [10.1103/PhysRevD.94.084024](https://doi.org/10.1103/PhysRevD.94.084024), [10.1103/PhysRevD.95.069906](https://doi.org/10.1103/PhysRevD.95.069906). arXiv: [1607.07845](https://arxiv.org/abs/1607.07845) [gr-qc].
- [39] B. P. Abbott et al. “Tests of general relativity with GW150914”. In: *Phys. Rev. Lett.* 116 (2016), p. 221101. arXiv: [1602.03841](https://arxiv.org/abs/1602.03841) [gr-qc].
- [40] S. A. Teukolsky. “Rotating black holes - separable wave equations for gravitational and electromagnetic perturbations”. In: *Phys. Rev. Lett.* 29 (1972), pp. 1114–1118. DOI: [10.1103/PhysRevLett.29.1114](https://doi.org/10.1103/PhysRevLett.29.1114).
- [41] W. H. Press and S. A. Teukolsky. “Perturbations of a Rotating Black Hole. II. Dynamical Stability of the Kerr Metric”. In: *ApJ* 185 (Oct. 1973), pp. 649–674. DOI: [10.1086/152445](https://doi.org/10.1086/152445).

- [42] Emanuele Berti and Antoine Klein. “Mixing of spherical and spheroidal modes in perturbed Kerr black holes”. In: *Phys. Rev. D* 90.6 (2014), p. 064012. doi: [10.1103/PhysRevD.90.064012](https://doi.org/10.1103/PhysRevD.90.064012). arXiv: [1408.1860](https://arxiv.org/abs/1408.1860) [gr-qc].
- [43] B. P. Abbott et al. “Directly comparing GW150914 with numerical solutions of Einstein’s equations for binary black hole coalescence”. In: *Phys. Rev. D* 94 (2016), p. 064035. arXiv: [1606.01262](https://arxiv.org/abs/1606.01262) [gr-qc].
- [44] Benjamin P. Abbott et al. “Effects of waveform model systematics on the interpretation of GW150914”. In: *Class. Quant. Grav.* 34.10 (2017), p. 104002. doi: [10.1088/1361-6382/aa6854](https://doi.org/10.1088/1361-6382/aa6854). arXiv: [1611.07531](https://arxiv.org/abs/1611.07531) [gr-qc].
- [45] E. W. Leaver. “An Analytic representation for the quasi normal modes of Kerr black holes”. In: *Proc. Roy. Soc. Lond.* A402 (1985), pp. 285–298. doi: [10.1098/rspa.1985.0119](https://doi.org/10.1098/rspa.1985.0119).
- [46] E. Berti, V. Cardoso, and A. O. Starinets. “TOPICAL REVIEW: Quasinormal modes of black holes and black branes”. In: *Class. Quantum Grav.* 26.16 (Aug. 2009), p. 163001. doi: [10.1088/0264-9381/26/16/163001](https://doi.org/10.1088/0264-9381/26/16/163001). arXiv: [0905.2975](https://arxiv.org/abs/0905.2975) [gr-qc].
- [47] <http://pages.jh.edu/~eberti2/ringdown>.
- [48] <https://www.gw-openscience.org>.
- [49] B. P. Abbott et al. “Properties of the Binary Black Hole Merger GW150914”. In: *Phys. Rev. Lett.* 116.24 (June 2016), p. 241102. ISSN: 0031-9007. doi: [10.1103/PhysRevLett.116.241102](https://doi.org/10.1103/PhysRevLett.116.241102). arXiv: [1602.03840](https://arxiv.org/abs/1602.03840) [gr-qc]. URL: <http://link.aps.org/doi/10.1103/PhysRevLett.116.241102>.
- [50] Vijay Varma et al. “High-accuracy mass, spin, and recoil predictions of generic black-hole merger remnants”. In: *Phys. Rev. Lett.* 122.1 (2019), p. 011101. doi: [10.1103/PhysRevLett.122.011101](https://doi.org/10.1103/PhysRevLett.122.011101). arXiv: [1809.09125](https://arxiv.org/abs/1809.09125) [gr-qc].
- [51] Jonathan Blackman et al. “Numerical relativity waveform surrogate model for generically precessing binary black hole mergers”. In: *Phys. Rev. D* 96.2 (2017), p. 024058. doi: [10.1103/PhysRevD.96.024058](https://doi.org/10.1103/PhysRevD.96.024058). arXiv: [1705.07089](https://arxiv.org/abs/1705.07089) [gr-qc].
- [52] Isabella Verdinelli and Larry Wasserman. “Computing Bayes Factors Using a Generalization of the Savage-Dickey Density Ratio”. In: *Journal of the American Statistical Association* 90.430 (1995), pp. 614–618. ISSN: 01621459. URL: <http://www.jstor.org/stable/2291073>.
- [53] Abhirup Ghosh et al. “Testing general relativity using golden black-hole binaries”. In: *Phys. Rev. D* 94.2 (2016), 021101(R). doi: [10.1103/PhysRevD.94.021101](https://doi.org/10.1103/PhysRevD.94.021101). arXiv: [1602.02453](https://arxiv.org/abs/1602.02453) [gr-qc].

- [54] Abhirup Ghosh et al. “Testing general relativity using gravitational wave signals from the inspiral, merger and ringdown of binary black holes”. In: *Classical Quantum Gravity* 35.1 (2018), p. 014002. DOI: [10.1088/1361-6382/aa972e](https://doi.org/10.1088/1361-6382/aa972e). arXiv: [1704.06784](https://arxiv.org/abs/1704.06784) [gr-qc].
- [55] Michele Vallisneri et al. “The LIGO Open Science Center”. In: *J. Phys. Conf. Ser.* 610.1 (2015), p. 012021. DOI: [10.1088/1742-6596/610/1/012021](https://doi.org/10.1088/1742-6596/610/1/012021). arXiv: [1410.4839](https://arxiv.org/abs/1410.4839) [gr-qc].
- [56] B. P. Abbott et al. “Properties of the binary black hole merger GW150914”. In: *Phys. Rev. Lett.* 116 (2016), p. 241102. DOI: [10.1103/PhysRevLett.116.241102](https://doi.org/10.1103/PhysRevLett.116.241102). arXiv: [1602.03840](https://arxiv.org/abs/1602.03840) [gr-qc].
- [57] B. P. Abbott et al. “Characterization of transient noise in Advanced LIGO relevant to gravitational wave signal GW150914”. In: *Class. Quant. Grav.* 33.13 (2016), p. 134001. DOI: [10.1088/0264-9381/33/13/134001](https://doi.org/10.1088/0264-9381/33/13/134001). arXiv: [1602.03844](https://arxiv.org/abs/1602.03844) [gr-qc].
- [58] B. P. Abbott et al. “Observing gravitational-wave transient GW150914 with minimal assumptions”. In: *Phys. Rev. D* 93.12 (2016). [Addendum: *Phys. Rev. D* 94, no. 6, 069903 (2016)], p. 122004. DOI: [10.1103/PhysRevD.94.069903](https://doi.org/10.1103/PhysRevD.94.069903), [10.1103/PhysRevD.93.122004](https://doi.org/10.1103/PhysRevD.93.122004). arXiv: [1602.03843](https://arxiv.org/abs/1602.03843) [gr-qc].
- [59] B. P. Abbott et al. “Binary Black Hole Mergers in the first Advanced LIGO Observing Run”. In: (2016). arXiv: [1606.04856](https://arxiv.org/abs/1606.04856) [gr-qc].
- [60] J. Veitch et al. “Parameter estimation for compact binaries with ground-based gravitational-wave observations using the LALInference software library”. In: *Phys. Rev. D* 91 (4 Feb. 2015), p. 042003. DOI: [10.1103/PhysRevD.91.042003](https://doi.org/10.1103/PhysRevD.91.042003). URL: <http://link.aps.org/doi/10.1103/PhysRevD.91.042003>.
- [61] Norman Levinson. “The Wiener (Root Mean Square) Error Criterion in Filter Design and Prediction”. In: *Journal of Mathematics and Physics* 25.1-4 (1946), pp. 261–278. DOI: [10.1002/sapm1946251261](https://doi.org/10.1002/sapm1946251261). URL: <https://onlinelibrary.wiley.com/doi/abs/10.1002/sapm1946251261>.
- [62] J. Durbin. “The Fitting of Time-Series Models”. In: *Revue de l’Institut International de Statistique / Review of the International Statistical Institute* 28.3 (1960), pp. 233–244. ISSN: 03731138. URL: <http://www.jstor.org/stable/1401322>.
- [63] Eric Jones, Travis Oliphant, Pearu Peterson, et al. *SciPy: Open source scientific tools for Python*. [Online; accessed 16 April 2019]. 2001. URL: <http://www.scipy.org/>.
- [64] Peter Welch. “The use of fast Fourier transform for the estimation of power spectra: a method based on time averaging over short, modified periodograms”. In: *IEEE Transactions on audio and electroacoustics* 15.2 (1967), pp. 70–73. DOI: [10.1109/TAU.1967.1161901](https://doi.org/10.1109/TAU.1967.1161901).

- [65] Reinhard Prix. *Bayesian QNM search on GW150914*. Tech. rep. LIGO-T1500618. LIGO Scientific Collaboration, 2016. URL: <https://dcc.ligo.org/LIGO-T1500618/public>.
- [66] B. Farr and W. M. Farr. “kombine: a kernel-density-based, embarrassingly parallel ensemble sampler”. in prep. 2015. URL: <https://github.com/bfarr/kombine>.